UNIVERSITY OF EXETER

THE IMPACT OF TIDAL STREAM FARMS ON FLOOD RISK IN ESTUARIES

Submitted by

Miriam Garcia Oliva

to the University of Exeter as a thesis for the degree of Doctor of Philosophy in Engineering, March 2016.

I certify that all material in this thesis which is not my own work has been identified and that no material has previously been submitted and approved for the award of a degree by this or any other University.

.....

Miriam Garcia Oliva

Abstract

There is a growing interest in tidal energy, owing to its predictable nature in comparison to other renewable sources. In the case of the UK, its importance also lies on the availability of exploitable areas as well as their total capacity, which is estimated to cover more than 20% of the country demand. However, the level of development of this kind of technology is still far behind other types of renewable energy. However, several studies focused on a variety of individual devices, followed by more recent research on the deployment of large arrays or tidal farms.

Potential sites for energy extraction can be found in narrows between islands and the coast or estuaries. The latter present some advantages for the installation and the connection to the grid but estuaries are often prone to flood risk from tides and surges. Therefore, the objective of this thesis is to evaluate the effect that very large groups of turbines could have on peak water levels during flooding events in the case of being deployed in estuarine areas. For that purpose, a new methodology has been developed, which implies the use of a numerical model (MIKE 21 by DHI), and it has been demonstrated against a real case study in the UK: the Solway Firth estuary. Another objective has consisted of integrating in this thesis the results from detailed CFD modelling and optimisation techniques involved in the project. A literature review has been carried out in order to identify the current state of the art for the different subjects considered in the thesis. Different aspects of the numerical model used for this study (MIKE 21) have been presented and the modelling of the turbines within the code has been validated against experimental and CFD

data. The procedure to include large numbers of turbines in the code is also developed. An analysis has been done of the different estuaries existing in the UK suitable for tidal energy extraction, identifying their main geometrical features. Based on this, idealised models of estuaries have been used to assess the influence that the channel geometry could have on the impact of tidal farms under extreme water levels. The effect has been measured by comparing the results of the numerical model between the case with and without turbines under different flooding scenarios. Finally, the same methodology has been applied to a real case study selected from the previous group of estuaries namely the Solway Firth. An initial model has been created, according to the available data at the start of the research, which contained some errors related to the water depth at the intertidal areas in the upper estuary. Therefore, when a more realistic dataset became available, an improved model was created. The improved model has been used to assess the effects of tidal farms in the estuary under a coastal flooding event.

It is concluded that there is significant influence of the channel geometry over the locations where the maximum changes in water levels due to the tidal farms will happen. Nevertheless, the effects seem to be more relevant in terms of the decrease rather than the increase of peak water levels for all geometries and the maximum changes seem to be in the order of dm. This is in agreement with the results of the Solway Firth models and can be summarised as a positive net effect over flood risk. On the other hand, a concern has been raised about the impact on intertidal areas, which could be the subject of future research.

Acknowledgements

First, I wish to thank my supervisors, Prof. Slobodan Djordjeviç and Dr. Gavin Tabor, for their guidance and patience throughout these years. I have learned a lot from their expertise and I sincerely appreciate their understanding and human qualities.

I am very grateful to Dr. Mulualem Gebreslassie and Prof. Michael Belmont. Their knowledge and advice has been of great help many times during the PhD.

I would also like to thank my colleagues and friends at the University and the rest of the good people that I have met in Exeter. They have really made it a beautiful experience that I will always remember.

A mention to my great friends in Spain for being there all these years, encouraging me, despite the distance.

My deepest gratitude to my family, specially to my parents and brother. Their love and support accompanied me in the journey of this thesis.

I would like to acknowledge DHI for the MIKE 21 software licence and for the support received, specially from Stephen Flood and Suzie Clarke, who kindly assisted me on every consultation.

Finally, I also want to acknowledge the financial help received from the University of Exeter through the College of Engineering, Mathematics and Physical Sciences Research Scholarship because without it this study would not have been possible.

In memory of Petra and Josefa.

Contents

List of Figures

List of Tables

DECLARATION

I hereby declare that this PhD thesis report entitled

"THE IMPACT OF TIDAL STREAM FARMS ON FLOOD RISK IN ESTUARIES"

is written by me and that all material in this thesis which is not my own work has been identified and properly cited.

Student's Name: Miriam García Oliva

Signature _____ Date: _____

ABBREVIATIONS

GW GigaWatts 31

HDNS Horizontally Deployed Near Surface 32

2D two−dimensional 33

3D three−dimensional 33

CFD Computational Fluid Dynamics 33

MRL Momentum Reversal Lift 34

1D one−dimensional 48

0D zero−dimensional 48

AC Alternating Current 49

FDM Finite Difference Method 53

FVM Finite Volume Method 53

FEM Finite Element Method 53

BEM Blade Element Momentum 54

ADI Alternating Direction Implicit 55

ADCP Acoustic Doppler Current Profiler 55

M2 Principal lunar semi−diurnal harmonic constituent 60

S2 Principal solar semi−diurnal harmonic constituent 61

LIDAR Light Detection and Ranging 11

LMADT Linear Momentum Actuator Disk Theory 66

GIS Geographical Information Systems 77

DEM Digital Elevation Model 78

TVD Total Variational Diminishing 83

CFL Courant-Friedrich-Levy 83

List of Symbols

α	Correction factor
$\Delta\rho$	Density difference between fresh water and sea water
ΔD	Variation of the depth over the length of the estuary
Δt	Time step
ΔW	Variation of the width over the length of the estuary
Δx	Element width
$\Delta x, \Delta y$	Characteristic length scales
Δz	Element depth
ε	Turbulence dissipation rate
ζ	Tidal height
$\overline{\zeta}$	Static tidal height
η	Surface elevation
θ	Co-latitude
λ	Tidal wavelength
ν_t	Eddy viscosity
ν	Conversion factor for the thrust coefficient between the area of the rotor and the frontal area of the element
ϕ	Longitude
ρ_a	Density of air
ρ_o	Reference density of the water
ρ_m	Vertically averaged mean water density
ρ	Water density
$\vec{\tau}$	Bed resistance
τ_{bx}, τ_{by}	Bottom shear stresses
τ_s	Wind stress
τ_{sx}, τ_{sy}	Wind or ice stresses
ϑ	Estuarine shape number
ω	Angular velocity of Earth's rotation
Ω	Tide generating potential

a	Earth's mean radius
A	Horizontal eddy viscosity
A_e	Effective area of the turbine
a_j	Amplitude
A_t	Frontal area of the turbine
C	Chezy number
c_d	Empirical drag coefficient of the air
C_d	Turbine drag coefficient
c_d	Sea bed roughness drag coefficient
c_f	Bed resistance drag coefficient
C_l	Turbine lift coefficient
C_P	Power coefficient
c_s	Smagorinsky constant
C_S	Smagorinsky coefficient
C_T	Thrust coefficient
C_{100}	Empirical values of the sea bed drag coefficient 1 m above the bed
CFL	Courant-Friedrich-Levy number
d	Still water depth
D	Depth at the mouth of the estuary
D_h	Hydraulic diameter
D_H	Depth at the head of the estuary
D_M	Depth at the mouth of the estuary
D_{mean}	Mean depth of the estuary
D_{mouth}	Depth at the mouth of the estuary
E	Estuary number
E_D	Densimetric estuary number
F_o	Estuary Froude number
F_b	Distributed force per unit volume of the blades
F_d	Axial component of the turbine drag force

F_D	Densimetric Froude number
F_l	Transverse component of the turbine drag force
F_{RD}	Drag force over the blades
F_{RL}	Lift force over the blades
g	Gravitational acceleration
g_j	Phase lag on the equilibrium tide
h	Total water depth
I	Turbulence intensity
j	Generic constituent
k	Turbulence kinetic energy
$K(T)$	Frequency factor used in the calculation of extreme river discharge
l	Characteristic length in Smagorinsky model
L	Estuary length
M	Manning number (inverse of n)
n	Number of layers intersected by the turbine
p	Pressure
P	Power dissipated by the turbine
p_a	Atmospheric pressure
Per	Tidal period
P_t	Tidal prism
Q	Sample mean of the river discharge
Q_f	Fresh water discharge
$Q200$	200 year return period river discharge
S	Sources discharge
s_{ij}	Components of the radiation stress tensor
S_{ij}	Deformation rate
s_Q	Standard deviation of annual maximum river flows
T	Thrust force
u	Mean velocity

$\vec{u_b}$	Depth-averaged flow velocity
u_{b4}	Bypass flow velocity at station 4 (LMADT)
u_{cell}	Local cell velocity
u_f	Maximum flood tide velocity
u_s, v_s	Velocity components of the water discharged into ambient
u_t	Velocity at the turbine
u_{t1}	Turbine velocity at station 1 (LMADT)
u_{t4}	Turbine velocity at station 4 (LMADT)
$\vec{u_w}$	Wind speed 10 m above the sea surface
u, v	Velocity components in x and y direction
U, V, W	Mean velocity components
u', v', w'	Varying velocity components
u_0	Free flow velocity
v	Velocity of the flow incident into the turbine
V	Volume occupied by the turbine
V_j	Astronomical argument
W_H	Width at the head of the estuary
W_M	Width at the mouth of the estuary
X	Constraining force between the bypass flow and the streamtube formed by the turbine
y	Length parameter

Chapter 1

Introduction

1.1 Motivation

There have been increasing efforts in recent years to boost the deployment of tidal systems, to some extent this was due to the pressures to meet the 2020 and 2050 targets set by EU. Tidal energy is predictable and, in the case of the UK, its total capacity could represent around 50 % of the total European tidal resource. Nevertheless, compared with other schemes, such as wind farms, there are only a few examples of commercial devices in use. However, the scale of marine renewable energy schemes would need to reach installed capacities of the order of GigaWatts (GW) to provide a worthwhile contribution. That means that the development of tidal technologies should be moving towards the deployment of very large arrays formed by thousands of turbines.

Around the UK, high levels of resource can be found either at offshore sites or at estuaries. Although estuaries have been usually considered solely in terms of tidal range resources, because they do not present such high speeds of current as in the offshore locations, some cases would also be interesting for tidal stream energy extraction. Besides, the ease of sheltered conditions would provide benefits for the developers in terms of maintenance and operation as well as closeness to grid connections. However, many sites represent areas of natural protection where ecological and social concerns exist. Estuarine

environments are highly complex as they represent the transition zones between marine and fluvial ecosystems. In addition, they often suffer serious damages from flooding events. Concerns about flood risk are growing due to the high losses experienced in recent times. On top of that, since some of the locations with the highest resources, like the Bristol Channel, present tidal amplification towards the head of the estuary, some questions arise about energy extraction potentially aggravating this situation.

Although the adaptability of the devices to the shallow water and medium flow conditions in estuaries can be regarded as an issue, Horizontally Deployed Near Surface (HDNS) turbines could overcome those restrictions. Despite this idea, research on HDNS designs is still limited as most of the investigations have been focused on the traditional axial flow type. Nevertheless, given the fact that the kinetic energy is highest in the upper part of the water column, HDNS turbines supported by floating structures could be an option for the exploitation of an important resource that has not usually been taken into consideration.

Regarding the deployment of very large groups of tidal turbines, a good compromise has to be found between the magnitude of the energy extracted and the associated environmental impacts. It is necessary to address the hydro-environmental impact assessment of the tidal farms during their design and prior to their installation. Although there exist prototype test facilities with monitoring systems, such as the Europe Marine Energy Centre (EMEC), there is still a scarcity of commercial scale technologies operating in connection to the electrical grid. In order to provide complimentary information, computational models are being developed and validated against laboratory testing. Optimisation techniques are also being integrated in the process in order to find the solutions with maximum power output and minimum environmental impact. Flood risk can be a starting point in the assessment as it can be directly computed from the existing numerical models. Hydrodynamic models have been used to analyse impacts on water levels, although in some studies the flood risk is not the main focus and in others only tidal range schemes have

been considered.

From the aforementioned ideas it can be remarked that there is a need to create a methodology which allows the evaluation of the flood risk effects that very large tidal farms could have on peak water levels when they are installed in shallow estuaries.

1.2 Aim and Objectives

The aim of this thesis is to understand the effects that large groups of tidal stream turbines could have on flood risk levels when they are installed in estuaries.

This study is part of a broader research project which aims to investigate the optimisation of the design of large tidal stream farms for shallow estuaries. The objectives of the optimisation process are the maximum energy extraction and the minimum environmental impact from the tidal farm, the latter initially represented by the effect on flood risk.

The objectives of this thesis are described as follows:

- The development of a generic methodology for the assessment of the flood risk introduced by tidal stream farms in estuarine areas based on the use of a two−dimensional (2D) numerical model.
- The demonstration of the validity of the new methodology over a specific geographical area.
- A better understanding about the influence of different factors affecting the impact of tidal farms on flood risk in estuaries, such as:
  - Estuary geometry
  - Turbine loading
  - Array configurations
- The integration of the results from the detailed three−dimensional (3D) Computational Fluid Dynamics (CFD) model and experiments with the

Momentum Reversal Lift (MRL) turbine within the 2D estuary model.

- The integration of the results from the optimisation project related to the intra-array spacings.
- The calculations performed to provide results and define variables to be used in the optimisation project.

1.3 Structure

This thesis is divided into six chapters. First, a literature review is given in the present chapter. Chapter 2 describes model used for this study (MIKE 21), with details about the representation of tidal turbines and its validation with experiments and CFD. Chapter 3 presents a sensitivity analysis of the influence of the geometry on the impacts of tidal farms on water levels in idealised estuaries based on real cases in the UK. In Chapter 4, an initial model of a real estuary (Solway Firth) is presented together with the changes in peak water levels for three flooding scenarios and two different arrays and configurations. Chapter 5 describes an improved version of the Solway Firth model, in which new array layouts are tested under a coastal flooding event in terms of the impacts on peak levels. Chapter 6 includes a discussion of the results, the conclusions of this study and the ideas for future research. Finally, a Python script for the implementation of tidal farms in MIKE 21 and the results from Chapter 3 are given in the Appendices.

1.4 Review of previous work

The objective of this chapter is to analyse the existing methods for the assessment of: hydro-environmental impact of tidal technologies, flood risk in estuaries and estuarine characterisation.

1.4.1 Theory of tides

Tides are caused by the combination of the gravitational forces of the celestial bodies. The theory of gravitation, published by Newton in 1678 explained the main properties of tides [Ekman, 1993]:

- Main period (12 lunar hours or 12 hours and 25.2 minutes), which is associated with the effect of the Moon. Despite the difference in mass, the gravitational effect of the Moon over the Earth is stronger than the effect of the Sun due to their proximity.

- Spring-neap cycles, which depend on the relative position between the Earth, the Moon and the Sun. Spring tides occur at full and new moon (when the acting forces are almost aligned), whereas neap tides happen during first and last quarter of the lunar phase (when the forces tend to cancel) [DHI, 2012c]

- Diurnal inequality or variations in tidal elevations due to the declination of the Moon and the Sun as well as the latitude of the location where the tides are considered [Reeve et al., 2004].

However, according to Ekman [1993], Newton overestimated the lunar tidal force by a factor of 2.

The basis of the modern tidal theory is found in the theory developed by Laplace [Reeve et al., 2004], who was the first to treat the tides as a dynamic problem Ekman [1993]. Laplace's tidal equations are covered in the analysis given by Lamb [1932] (considered one of the main references in this field by several authors), who dedicates one chapter of his book 'Hydrodynamics' to the characterisation of tidal waves. The equations, given by Lamb [1932] with some changes in the original Laplace's notation, are:

$$\frac{\partial u}{\partial t} - 2\omega v \cos\theta = -\frac{g}{a}\frac{\partial}{\partial \theta}\left(\zeta - \overline{\zeta}\right) \tag{1.1}$$

$$\frac{\partial v}{\partial t} + 2\omega u \cos\theta = -\frac{g}{a \sin\theta \partial\phi}\left(\zeta - \overline{\zeta}\right) \tag{1.2}$$

$$\frac{\partial \zeta}{\partial t} = -\frac{1}{a \sin\theta}\left\{\frac{\partial (hu \sin\theta)}{\partial\theta} + \frac{\partial (hv)}{\partial\phi}\right\} \tag{1.3}$$

where: u, v are the velocity components, θ is the co-latitude, ϕ is the longitude, a is the Earth's mean radius, g is the gravity acceleration, ω is the angular velocity of Earth's rotation, h is the ocean depth, ζ is the tidal height or elevation of the disturbed surface above the surface of reference and $\overline{\zeta}$ is the static tidal height, given as follows.

$$\overline{\zeta} = -\frac{\Omega}{g} \tag{1.4}$$

where Ω is the tide generating potential.

Laplace differentiated three kinds of tides: long-periodical, diurnal and semi-diurnal. In addition to the equations for fluid motion in a rotating sphere, Laplace also calculated the generating tidal forces [Reeve et al., 2004]. According to Laplace's dynamic theory of tides the frequencies of the solutions of the equations are coincident with the frequencies from the acting forces [Hardisty, 2009]. Therefore, tides are periodic and the periods are determined by the positions of the celestial bodies.

Harmonic analysis

Given that periodic motions can be treated as a sum of a series of harmonic motions [Hardisty, 2009] tidal behavior can be described as the superposition of different harmonics related to periods of occurrence as a fraction of the day length. The frequency associated with these phenomena is called tidal constituent [Novák et al., 2010].

The basis for the definition of the harmonic frequencies is the Equilibrium Tide Theory, which considers three assumptions:

- water covers the whole Earth

- there is no inertia acting in the water
- water is in equilibrium.

The harmonic analysis of tides has been addressed by several authors, as described by Ekman [1993]. One of the main contributions to this field is the work by Doodson [1921], who developed the harmonic expression of the tidal potential in 1921, consisting of up to 386 components [Ekman, 1993]. According to Doodson's development [Doodson, 1921], tidal levels can be represented by a finite number of harmonic terms:

$$\sum_{j=0}^{N} a_j \cos\left(V_j\left(t\right) - g_j\right) \tag{1.5}$$

where: j is the generic constituent considered, a_j is the amplitude, V_j is the astronomical argument or angular position of the causal agent of the constituent and g_j is the phase lag on the equilibrium tide [DHI, 2012c].

According to Doodson [1921], the tidal constituents included in Table 1.1 represent up to 83% of the total generating tidal force [DHI, 2012c].

Constituents		Period (hrs)	Amplitude (M_2=100)
Name	Symbol		
Principal Lunar	M_2	12.42	100.0
Principal Solar	S_2	12.00	46.6
Larger Elliptical Lunar	N_2	12.66	19.2
Luni-Solar Declinational	K_2	11.97	12.7
Luni-Solar Declinational	K_1	23.93	58.4
Principal Lunar	O_1	25.82	41.5
Principal Solar	P_1	24.07	19.4

Table 1.1: Main tidal constituents

1.4.2 Tidal technologies

Tidal technologies can be classified as tidal range systems (barrages, lagoons) or tidal stream systems (turbines) [Kadiri et al., 2012]. In the case of tidal range systems, it is necessary to build a structure similar to a dam to create a difference between water levels. This structure consists of: embankments, turbines, openings with control gates and locks for ships. They have three different operating schemes: ebb, flood or two-way; each one comprising different combinations of the basic stages (filling, holding and generating) [Kadiri et al., 2012], [Xia et al., 2010b].

Tidal lagoons differ from barrages in that they are enclosed bodies whereas barrages cross the total width of the area. According to Cousineau et al. [2012], lagoons can be either offshore structures, consisting of a circular impoundment, or coastal lagoons, attached to the shore. At present, there are no built lagoons and only five operating barrages, in France, Russia, China, Canada and South Korea [Shapiro, 2011]. However, there are several proposed projects around the world [Kadiri et al., 2012]. Several studies present details about the design of the proposed Severn Barrage and its operating modes [B. Lin et al., 2010], [Xia et al., 2010a], [Xia et al., 2010b], [Xia et al., 2011], the Fleming Lagoon in the UK [Falconer et al., 2009], [Xia et al., 2010c], the lagoons proposed at the Bay of Fundy in Canada [Cousineau et al., 2012] and the more recent tidal lagoon project at the Swansea Bay in Wales [Waters & Aggidis, 2016].

For tidal stream schemes, different kind of devices, most of them consisting of turbines, are used to extract the power from the current. Such devices need to be robust in order to resist the forces induced by operating submerged in a harsh environment. There are several designs depending on the geometry and movement of the mechanism: horizontal or vertical axial and transverse flow turbines, ducted devices as well as oscillating hydrofoils and other designs, such as Archimedes screws or tidal kites(figure 1.1). A brief description of each system is given as follows:

- Axial flow turbines have their axis aligned with the flow, which causes the

rotation of the blades and generates power. The most popular designs are the horizontal axial flow turbines. They are very similar to the models commonly used for wind generators although, for the same capacity of a single device, dimensions are smaller as a consequence of the higher density of water. Some axial flow turbines incorporate a duct around the blades, which accelerates the flow passing through the turbine due to the Venturi effect. Other designs have an open-centre with the purpose of increasing the mass flux and decreasing the base pressure [Borthwick, 2016].

- In the case of the transverse or cross-flow turbines, the direction of the flow is perpendicular to the axis of rotation, which can be horizontal or vertical. Several designs have appeared with straight or helical blades, fixed or mobile.

- In the oscillating hydrofoils, the lift created by the tidal stream flowing either side of the wing produces an oscillation and generates power [Aqua-RET consortium, 2016].

- Regarding the Archimedes screw, it consists of a spiral covering a central cylindrical shaft. The flow moving through the helical surface turns the turbines [Aqua-RET consortium, 2016].

- Tidal kites consist of a wing which supports a turbine underneath. The movement of the device has a figure-of-eight shape and the device is attached to the seabed by a cable [Aqua-RET consortium, 2016].

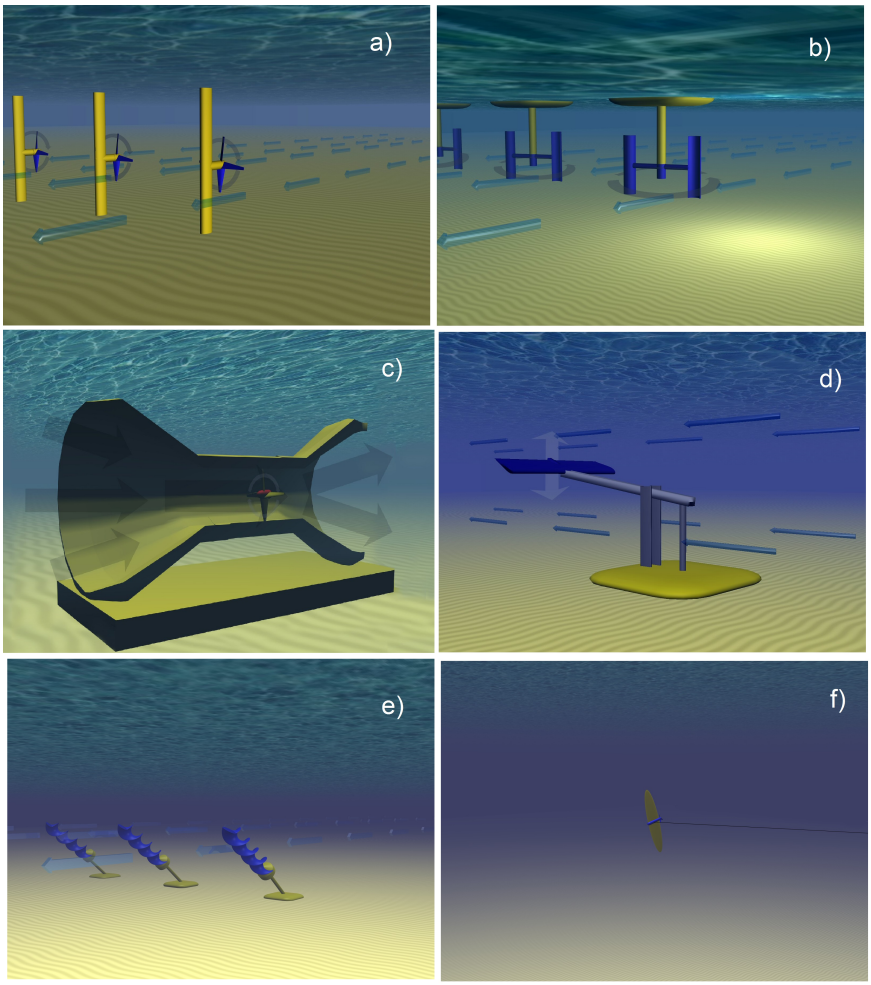

Figure 1.1: Examples of tidal stream energy devices (Source: Aquaret - Aquatic Renewable Energy Technologies) / a) Horizontal axis turbines; b) Vertical axis turbines; c) Venturi effect device; d) Reciprocicating hydrofoils; e) Archimedes screw; f) Tidal kite.

Examples of the aforementioned devices, as given by Borthwick [2016], are: the Atlantis AK 1000 axial-flow turbine, the Atlantis Solon-K ducted turbine, the Open-Hydro open-centre turbine, the Kepler transverse horizontal axis water turbine, the Edinburgh vertical axis cross-flow turbine, the bioSTREAM oscillatory-hydrofoil, the Flumill Archimedes screw and the Minesto deep sea tidal kite.

It is necessary to highlight that most of the tidal stream energy devices are still under development. Prototypes of some of the designs are being tested in

real world conditions. Examples of marine testing facilities can be found in the United Kingdom (European Marine Energy Centre - EMEC and WaveHub), Ireland, France, Holland and Canada. However, there are still few examples of single devices operating in connection to the electrical grid. SeaGen, a system consisting of two axial-flow turbines supported by a monopile structure, is the first commercial turbine supplying electricity out of a testing site [Roberts et al., 2016]. It was deployed at Strangford Lough (Northern Ireland) in 2008. Regarding the first tidal arrays, there are plans to connect two Open-Hydro devices to the electrical grid at Paimpol-Brehat (France) in the next months.

Current research is orientated towards the objective of extracting power at a GW scale, either by means of groups of vertical axis turbines with very large diameters [Salter & Taylor, 2007] or tidal farms including many hundreds of turbines with smaller dimensions. Regarding the latter, it is possible to distinguish two main types of tidal farms in terms of their geometry: tidal fences or arrays of turbines distributed along a line across the width of a channel (e.g. [Draper et al., 2010]), and block farms, where several rows of turbines cover an area in a certain location, not necessarily a channel (e.g. [Ahmadian & Falconer, 2012]).

1.4.3 Estuaries

Estuarine characterisation

First, a brief introduction on estuaries and their main features is given. Although there are several definitions of Estuary not all of them include the tidal concept. Due to the nature of this study it seems appropriate to present here the definition according to Fairbridge et al. [1980], (cited by Townend [2008]): an inlet of the sea reaching into a river valley as far as the upper limit of tidal rise.

Regarding the classification of estuaries into different types, in the case of the UK the criteria applied by Defra in 2002 take into account the origin of the estuary, which defines the behavioural type, as well as the existing geomorphic elements [Novák et al., 2010]. However, there are some components that are

common to all estuaries, such as intertidal areas, water mixing, sediment transport, temperature and salinity gradients, amongst others. Regarding the characterisation of an estuary, it is possible in a first instance to analyse several properties. As can be seen from table 1.2 , (adapted from Townend [2008]), some of these can be directly measured and give rise to other derived parameters, as will be explained below.

Measured Properties
Lengths
Plan Areas
Cross-sectional areas
Volumes
Widths and Depths
Tidal levels and range
Freshwater flows
Geology
Geomorphology
Sedimentology

Derived Properties
Form descriptions
Estuary number
Tidal wavelength (λ)
Tidal constituent ratio's
Tidal asymmetry
Hydraulic geometry relationships

Table 1.2: Estuarine properties

When analysing the geometry and sedimentology of an estuary it is necessary to take into account that the bathymetry or topography of the seabed [Novák et al., 2010] will be constantly changing due to the sediment transport as part of the balance function of the estuary [Townend, 2008]. Regarding the form descriptions, they refer to the variation of width, depth and cross-sectional area. Prandle & Rahman [1980] define shape functions for the exponential laws associated with the breadth and depth.

The estuary number (E) relates to the degree of stratification of the water density. It was defined by Harleman & Abraham [1966] as:

$$E = \frac{P_t {F_o}^2}{Q_f Per} \tag{1.6}$$

where P_t = volume of sea water entering the estuary on flood tide, Q_f = fresh water discharge, Per = tidal period and F_o = estuary Froude, given as follows:

$$F_o = \frac{u_f}{\sqrt{gD_{mean}}} \tag{1.7}$$

with u_f = maximum flood tide velocity and D_{mean} = mean depth of the estuary.

However Harleman & Thatcher [1974] indicated that the previous formulae could be only applied to estuaries with constant fresh water inflow and width and defined the densimetric estuary number (E_D) as:

$$E_D = \frac{P_t F_D}{Q_f Per} \tag{1.8}$$

where F_D = densimetric Froude number, given by:

$$F_D = \frac{u_f}{\sqrt{gD_{mean}\left(\frac{\Delta\rho}{\rho_m}\right)}} \tag{1.9}$$

with $\Delta\rho$ = density difference between fresh and sea water and ρ_m = vertically averaged mean water density.

The study by Harleman & Thatcher [1974] shows that values of the densimetric estuary number range approximately between 1 for stratified estuaries and 100 for well-mixed estuaries.

If the estuary is not strongly stratified it can be described by the barotropic mode, which implies a constant density value, otherwise it will be necessary to include a baroclinic mode, where the density depends on the temperature or salinity.

In reference to the tidal wavelength, as it will be shown later, this can give an initial idea about the existence of resonant effects in the estuary. The value can be obtained by the following equation [Prandle & Rahman, 1980]:

$$\lambda = (gD)^{1/2} Per \tag{1.10}$$

where λ is the tidal wavelength, g is the gravitational acceleration, D is the depth at the mouth and Per is the tidal period.

The tidal constituent ratio indicates the relation between diurnal and semi-diurnal constituents and gives an idea of the dominant duration of the cycle.

[Townend, 2008]

Tidal asymmetry occurs when the peak current for the flood tide is stronger than the one for the ebb tide, or *vice versa*. It can be determined by the phase relationship between tidal constituents if there is no other significant force acting [Novák et al., 2010]. It affects coarse and fine sediment transport and gives an indication of the type of tidal basin [Townend, 2008].

Tidal response

Lamb [1932] described the equations for tidal waves in a channel, which could be applied to certain geometries found in estuaries, amongst other numerous cases. Tidal response in an estuary can be described by means of the analysis of the water elevations and the speed of the current along the estuary and the existing phase difference between them. Usually, the maximum and minimum elevations would be coincident with zero velocities, at the point where the flow direction starts to change from ebb to flood situation or *vice versa*.

However, under certain circumstances the phase difference could be moved towards a state where the velocity at maximum or minimum elevations is not zero. This phenomenon is associated to the concept of tidal resonance, defined by Finlay et al. [2009] as the situation when the reflected wave coincides with the next tidal wave giving amplification as a result. In a simplified way, this will happen if the estuary length is one-quarter of the wavelength [Townend, 2008]. But it can be seen from Prandle & Rahman [1980], that tidal amplification depends on the geometry and it will increase towards the head unless the channel section changes abruptly or due to the effect of friction, river flow or non-linear effects. For example, Fallon et al. [2014] explore the effect of the funnel shape in the Shannon estuary on the amplification of tidal levels towards its head. Godin [1993] studies the resonance in the Gulf of California and Bay of Fundy through the analysis of the hydrodynamic equations and concludes that the one-quarter of the wavelength criterion is not the only requirement for resonance and the ocean bathymetry and friction also have an important

influence. Therefore it could be recommended to analyse resonant effects by using these theories, instead of using only the simplified quarter of wavelength condition. In the study from Prandle & Rahman [1980] the equations are presented in a dimensionless form by use of two parameters that can be applied to estuaries in general: the estuarine shape number (θ), and the length parameter (y). These parameters depend on the aforementioned shape functions. The same study by Prandle & Rahman [1980] shows that, as the parameter (y) is related to tidal frequency, for longer period tides there will be less amplification while for short periods amplification will happen at many locations. In addition, it gives a comparison for ten existing estuaries with and without including the effect of a barrage. Lane & Prandle [2007], analyse the resonant periods graphically for the case of a linear variation of the depth of the estuary and provide the conditions for the estuarine length and depth at the mouth that could have resonant effects. For the semidiurnal frequencies these values are: $D_M > 25(m)$ and $L > 150(km)$. Therefore, resonance for semidiurnal frequency in the United Kingdom can only be found in the Bristol Channel.

In terms of the effect of barriers on the resonant response of estuaries, it can be seen from Prandle & Rahman [1980] that this influence will depend on the barrier location within the estuary. Finlay et al. [2009], assessed the effect of the Severn barrage, concluding that resonance would be reduced if the barrage is constructed at the proposed location. It is interesting to consider the simplified scenarios used in this study to compare tidal curves of elevations and currents at the open, middle and close points of the estuary (figure 1.2). Results are compared, showing the influence of the shape and seabed in the resonance, the decrease in velocities with the barrage and the non-linear effects due to the intertidal areas in the real estuary.

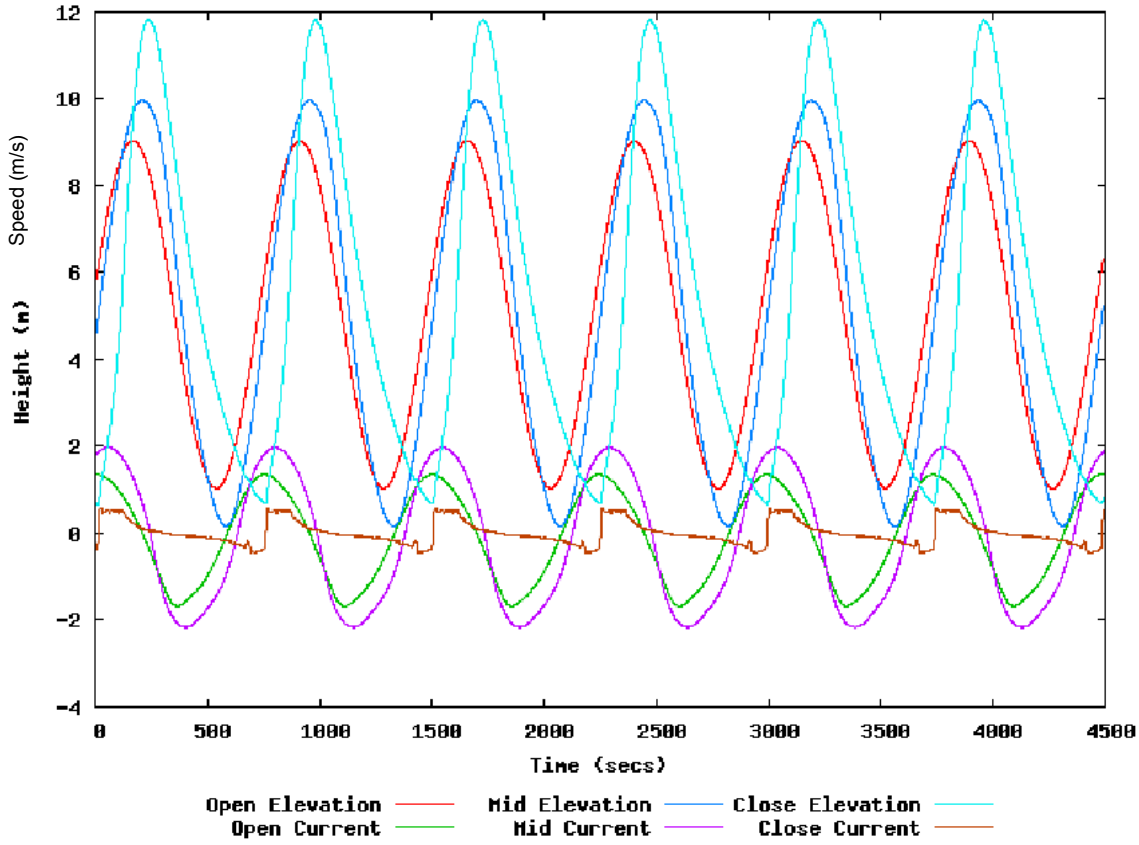

Figure 1.2: Surface elevation and current velocity for the Severn Estuary on a simulated spring tide, Adapted from Finlay et al. [2009]

1.4.4 Power extraction and hydro-environmental impact assessment

Due to the early stage of development of tidal stream energy systems, compared to other renewable schemes, several studies have appeared on a variety of individual devices, followed by more recent research on the deployment of large arrays or tidal farms. Some definitions of what represents a large array are given by Vennell et al. [2015], as a case where the channel-scale dynamics is influenced by the array or where the power extracted by each individual turbine is greater than 5% of the power available at the undisturbed flow.

To optimise the design of large arrays of turbines and prior to their deployment it is important to understand their effect on the hydrodynamic behaviour of the tidal flow because it will lead to changes in the different elements involved (morphological, ecological, sediment transport and water quality) [Kadiri et al., 2012]. Vennell et al. [2015] also mention the impacts on flow reduction and marine life as constraints for the design of tidal farms. Several studies have appeared in the last years with a main focus on the environmental impacts of tidal energy extraction. [Bonar et al., 2015] give a complete review of socio-ecological impacts of tidal energy developments that can be taken into consideration as a framework for future research. In terms of ecological impacts associated with changes in the hydrodynamics, the authors mention the effect of flow alteration on the structure of soft-sediment communities while changes to current patterns would affect the processes of erosion, deposition, scour, turbidity and water quality. In Leslie & Palmer [2015], the tools and data necessary to perform an ecosystem service assessment for marine energy systems are identified. The authors indicate that the ecosystem service assessment can help during project planning and monitoring by giving a description of the potential environmental and socioeconomic impacts on a project.

A full understanding of the ecological impacts of tidal energy schemes could be reached through the monitoring of installed prototypes [Bonar et al., 2015]. Due to the lack of installed devices, the use of models which replicate the physical trends and conditions in the potential locations of these developments is necessary to provide a tool for the environmental impact assessment of these technologies. These models are parameterised, calibrated and validated against real data in order to assure the accuracy of the results.

In this section, different types of models used for the purpose of evaluating tidal energy extraction and its environmental impacts are presented through several examples taken from the existing literature.

Analytical models

Analytical models have been used extensively to represent flow conditions in locations where tidal resource is available as well as the effects that the extraction could have on the hydro-environmental conditions and the remaining available power. One of the main reasons for using these models, when compared to numerical models, is the reduction in computational demand while giving an estimation of the desired results when a high degree of accuracy is not required. However it must be highlighted that in most of the studies these models are applied as a simplification of a much more complex problem and they are only valid under certain specific circumstances.

Draper et al. [2010] review one−dimensional (1D) models in this field. Xia et al. [2010b] describe previous models related to the Severn Barrage, such as a zero−dimensional (0D) model used to give an estimation of the extracted power for different types of turbines and a 1D model that is only valid under the assumption of constant water level and averaged velocity across a section. Another example is a 1D model of a wedge-shaped estuary which includes bed friction, developed by Robinson [1981] for the application to the case of a barrage in Bristol channel. The author indicates the use of this model for initial estimations of the changes to the tidal regime from power extraction happening at different locations.

Studies using analytical models in the context of electrical circuit analogies have been included here. It has been found to be a common approach for several authors to study tidal locations and their interaction with energy extraction systems.

As a starting point, Lighthill's analogy [Lighthill, 2001] for one dimensional waves under linearity assumptions has been used by several authors. Rainey [2009] uses it to analyse the extractable power from a barrage at different positions in Bristol Channel in combination with the analytical model given by Taylor [1921]. This defines the tidal flow at various locations along the estuary and extends Lamb's theory, [Lamb, 1932], to the case of uniform changes in

breadth and width, confirmed from observed measurements. More recently, P. F. Cummins [2013] applies the same electrical concepts to the assessment of the maximum available power and the change in the flow due to the installation of a tidal fence in a sub-channel of a split channel connecting a basin to the open sea.

The advantages of the linearised circuit analogy are mentioned by Miles [1971] who applies it to the study of the surface-wave resonant response to an incident wave of a harbour connected with the sea by a narrow mouth or channel. In a similar way, Garrett [1975] analysed the response of a gulf, modifying Miles approach to account for the tidal forces. Based on the aforementioned studies, Garrett & Greenberg [1977] apply the concept of impedance for the domain and surrounding region in a numerical model in order to analyse the effect that barrages could have on the open boundary with an example on the Bay of Fundy. In the same sense, Prandle [1980] studies the changes on the open boundary induced by barrages included in numerical models, varying the open boundary at different positions (River Thames) and comparing with the results from previous models (Bristol Channel). In this case, the author decides to use the electrical analogy for tides in a channel as an Alternating Current (AC) circuit, developed by Van Veen [1947] instead of Miles approach, [Miles, 1971], which is suitable only for the harbour case.

The electric circuit is presented in a simple way by Polagye & Malte [2011]. They define idealised numerical models with the purpose of analysing the resource availability and far-field effects of tidal energy systems. Different configurations of channel networks are compared to real sites. This study is based on the thesis by Polagye [2009], which highlights the spatial variability of the impacts of energy extraction on tidal regime, amongst other far-field effects.

It should be highlighted that some cases found in the literature (P. F. Cummins [2013]) are based on analogies which were established a long time ago under a different context and applied without giving a strong justification of their validity in the new scenario.

A more recent study carried out by Draper et al. [2014] justifies the use of the electrical circuit analogy for the representation of the Pentland Firth based on the analysis of the results of depth-averaged numerical models previously developed for the same area. The authors develop analytical models of tidal fences in a single channel and parallel sub-channels which give good agreement with the results of the simulations.

Numerical models

As a high level of detail is necessary during the initial phases of design of tidal stream turbines, effects inside and close to them are often studied by using a CFD 3D model. This is due to some extent to the difficulty of acquiring data from commercial demonstrations because of their confidential nature. These models have been widely applied and give accurate results with a high level of detail.

Most studies using CFD models focus on single devices or arrays with a small number of turbines, organised in two or three rows where spacing is varied in the lateral and longitudinal directions to observe the effect on the flow and power extraction. Croft et al. [2010] give an example of this for axial flow turbines. Other studies related to this kind of designs are the works carried out by Turnock et al. [2011], Masters et al. [2013] and Malki et al. [2014]. Turnock et al. [2011] analysed the effect of different spacing on a fixed number of turbines, showing that smaller lateral spacing with longer distances between downstream rows gives a higher power output and that longitudinal spacing can be reduced by staggering rows. Masters et al. [2013] evaluated the effect of head loss and related flow acceleration on turbine performance and wake development, concluding that faster flows lead to shorter regions of low velocity downstream the turbine, although the wake expansion is initially wider. Malki et al. [2014] analysed the results of simulations of 1, 2, 3 and 14 turbines with varying spacing and indicated that staggered arrangements can reduce wake interactions. Both studies use a BEM (Blade Element Momentum) model for the turbine coupled to a CFD model for the outer domain. In the BEM model the

turbine is divided by rings which extend from the centre to the tip of the blades. A circular region represents the influence of the blades in a time-averaged computation [Masters et al., 2013], which reduces the computational demand in solving the turbine rotation [Turnock et al., 2011]. In the CFD Reynolds-averaged NavierStokes (RANS) model, the turbine is represented as a cylinder and the coupling of the momentum and the drag and lift of the blade is achieved by an iterative approach [Turnock et al., 2011].

In the case of transverse flow types, studies are not so numerous. The study by Consul et al. [2013] analyses the effects of blockage, free-surface proximity and Froude number on the performance of a generic cross-flow turbine by means of FLUENT, a 2D CFD model which solves the RANS equations. In the work carried out by Stringer et al. [2016], a 2D RANS solver (ANSYS CFX) is also applied in order to model the straight-bladed version of the Transverse Horizontal Axis Water Turbine, developed at the University of Oxford. The model is validated against experiments and adapted to simulate different scales of the turbine up to a 10 m diameter scale. Regarding the MRL turbine, which has been the turbine design taken under consideration in this thesis the following results have been given by means of the CFD code OpenFOAM about:the wake characterisation [Gebreslassie et al., 2012], the calculation of the energy extraction [Gebreslassie et al., 2013a] as well as the analysis of the existing interactions between turbines (See Fig. 1.3) [Gebreslassie et al., 2013b], [Gebreslassie et al., 2015].

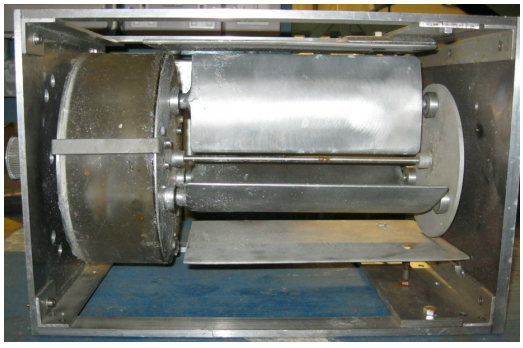

Figure 1.3: Momentum Reversal Lift (MRL) turbine (Source: Gebreslassie et al. [2013a])

As the influence of tidal technologies is not only restricted to the immediate area surrounding the system, it is necessary to analyse the far-field effects in the geographical area of the basin or estuary. Numerical models are used in order to take into account the complexity of the flow behaviour in the tidal physical environment and provide more accurate simulations than the aforementioned analytical models. Although the CFD models usually applied for the simulation of individual devices give more accurate results in terms of interactions within the arrays, they have some limitations for tidal basins applications in representing the far-field effects and adapting to changing boundaries during the tidal cycle. Therefore, shallow water equation solvers seem more appropiate for this purpose, as can be seen from the comparison of TideModeller and MIKE3 carried out by Waldman et al. [2014]. Hydrodynamic models also provide a basis for the use of applications related to other parameters involved, such as sediment transport, bed level change or water quality, as can be seen from Neill et al. [2009] and Kadiri et al. [2012]. Besides, the use of CFD models for spatial and temporal scales in the range of 10 to 1000 km and one tidal cycle to one year becomes unfeasible, given the computational limitations, and makes necessary the use of larger-scales coastal models [Masters et al., 2015]. The study by Masters et al. [2015] compares a BEM-CFD model and the coastal model MIKE3 of a simplified tidal fence close to a headland and highlights the difficulty in comparing time-varying conditions with the steady-state simulations. Some attempts have already been done to reduce the computational resources for CFD simulations, as shown in the study by Creech [2009], which gives a solution with lower computational demand by means of a parallel computing system. The use of this model for the simulation of a wind farm ([Creech et al., 2013]) demonstrates the ability to be scaled for large groups of turbines but any example of its application to tidal farms has been found at the moment.

Most of the hydrodynamic models applied in the context of coastal areas are two dimensional (2D), whereas for a larger scale (open sea locations or

regional ocean circulations), 3D solvers are more appropriate. One reason is that they account for the vertical mixing processes between waters with different salinity or temperature gradients that may occur in deeper waters. On the other hand, at coastal areas it is often necessary to reduce the size of the mesh in certain locations, above all in the vicinity of a tidal farm. Therefore, comparing this situation between a 3D and a 2D model, the latter would reduce significantly the computational time due to averaging the equations of momentum and conservation of mass over the water column.

In 2D models, the depth-averaged governing equations can be solved by means of different discretisation methods: Finite Difference Method (FDM), Finite Volume Method (FVM) or Finite Element Method (FEM). Regarding the generation of the computational mesh for the representation of the models domain, the choice is made between the use of a regular grid or an unstructured mesh.

Examples of different software and their characteristics of use in the field of tidal energy resource and environmental impact assessments can be seen in table 1.3. Their applications in related studies are illustrated below.

MODEL	DIMENSIONS	SOLVER	TYPE
MIKE21	2D-3D	FVM	Commercial
DELFT 3D	2D-3D	FDM	Open Source
DIVAST	2D	FDM	Commercial
TELEMAC	2D-3D	FEM	Open Source
ADCIRC	2D-3D	FEM	Open Source
FLUIDITY	2D-3D	FEM	Open Source
FVCOM	3D	FVM	Open Source
POLCOMS	3D	FDM	Licence-POL
SELFE	3D	Other	Open Source
ROMS	3D	Other	Open Source
POM	3D	Other	Open Source

Table 1.3: Comparison of existing numerical models

As an example of the use of FVM, Easton et al. [2010] used MIKE 21 in order to evaluate the effect of a tidal energy fence in the Pentland Firth (Scotland), concluding that a high level of power extraction could have a large effect on the speed of the currents at a regional scale although these changes would be acceptable for smaller capacities of the fence under a certain threshold. The model is based in the Reynolds-averaged Navier-Stokes equations, integrated over the depth. An application of MIKE 3 (the 3D version of MIKE 21) to the analysis of the effect of in-stream turbines on water levels in a river can be found in the work by Lalander & Leijon [2011]. Although the focus of this study is not the tidal energy extraction but hydrokinetic power from a regulated river it includes an interesting analysis done on the energy dissipated by the turbines as a sum of losses and absorbed energy. The authors also indicate the limitations of MIKE 3 to represent wake losses and the dependency of the results on the mesh resolution.

As an example of the use of a FDM scheme, DELFT 3D, was applied by Carballo et al. [2009] as a tool to identify the flow velocity and power density fields in the Ria de Muros (NW of Spain) with the objective of giving an estimation of the annual power that could be extracted from two potential locations. The governing equations in this model are the baroclinic Navier-Stokes and transport equations. In this case, it is not clear if the model was calibrated and, although there is a reference to the validation, both processes would be necessary to guarantee the accuracy of the model. A more recent example of the application of DELFT 3D can be found in the work by J. Lin et al. [2015], where the authors develop a model of the Zhaitang Island in the Yellow Sea and evaluate the velocity field around an individual turbine and a group of 8 turbines. The turbines are parameterised within the model governing equations as a momentum sink over the vertical plane of the rotor and the turbines' thrust varies with the local velocity according to the results of a Blade Element Momentum (BEM) model of an axial flow rotor validated against experiments. Another model using a FDM scheme is the DIVAST model (Depth

Integrated Velocity and Solute Transport),which was applied by Fallon & Nash [2012] and Fallon et al. [2014] to analyse the effect of power extraction from different configurations of arrays of turbines over the speed of currents and water elevations in the Shannon Estuary (Ireland). The model is based on an Alternating Direction Implicit (ADI) technique to solve the Navier-Stokes and continuity equations and has been mainly applied to address hydro-environmental impacts in coastal areas such as the Bristol Channel (UK), as can be seen in section 2.3.4.

Regarding the models using a FEM technique to solve the St Venant equations, Lalander et al. [2013] present a study of the fjord Skarpsundet (Norway) using the TELEMAC 2D model for the evaluation of the flow field around the area in terms of potential energy extraction. However they conclude that the results are not accurate enough compared to the Acoustic Doppler Current Profiler (ADCP) measurements due to the use of tidal range as the only input data. Luo et al. [2013] also apply the open source code TELEMAC 2D but, in this case, the aim of the study is the characterisation of the hydrodynamics and sediment transport in the estuaries of the rivers Dee, Mersey and Ribble (UK) in conjunction with the open sea. Another open-source FEM model is Fluidity, which was used by Martin-Short et al. [2015] to simulate the impacts of three different numbers of turbines in an array on the sediment transport and flow regime in the Inner Sound of the Pentland Firth. The impacts on sediment transport are approached indirectly in this study, through the analysis of the critical bed shear stress, which determines the finest size of the material which can start to be deposited. As an example of other FEM open-source codes, the model ADCIRC (Advanced Circulation Model), which solves the depth-integrated mass and momentum equations in the wave continuity form is used by Yates et al. [2013] to build a simulation of the west coast of the UK in order to analyse the power extraction from different combinations of barrages, represented in an external zeroth order model, in the main estuaries (Solway Firth, Morecambe Bay, Mersey, Dee and Severn), as

well as tidal lagoons, small arrays of tidal stream turbines and a proposed large farm between the Isle of Man and Scotland. In this case, despite the potential energy that could be extracted from the latter, it is surprising that they have not taken into consideration scenarios including large farms within the estuaries instead of barrages. Walkington & Burrows [2009] also use the ADCIRC model to simulate the impact of tidal stream farms in two cases: an estuary with idealised geometry and a scenario with several locations along the UK west coast (Mersey Estuary, Lynmouth, The Skerries and West Wales). The results in the second case are compared with the values obtained in previous works from the POLCOMS (Proudman Oceanographic Laboratory Coastal Ocean Modelling System) model. In a similar way, Wolf et al. [2009] evaluate the near and far-field environmental impacts from the major potential estuarine barrages in the Eastern Irish Sea by integrating a zeroth order and the 2D model ADCIRC. Another FEM solver found in the literature, although less frequently used together with tidal energy extraction, is the 3D model SELFE (semi-implicit Eulerian-Lagrangian finite-element model). In the study by W.-B. Chen et al. [2013], SELFE is used to model the energy resource and impacts on currents and water levels of a group of 55 turbines, represented as a momentum sink term, in the Penghu Channel in the Taiwan Strait. The authors concluded that the effects on current speeds were not significant in terms of affecting the energy production and the variations in water levels were negligible at all sites around the model domain.

Finally, in terms of Oceanic scale models, there is an example on the application of the FVCOM model (Finite-Volume Coastal Ocean Model) focused on the effects over the tides and power generated from a tidal farm in the Bay of Fundy and the Gulf of Maine (Canada) [Karsten et al., 2008]. The conclusion is that one would need to extract the maximum available power in order to produce a significant decrease of tidal elevations within the upper part of the Bay of Fundy although they could increase in the outer part. This area, connected to the Gulf of Maine, could be even closer to resonance. Similarly to

Easton et al. [2010], for smaller quantities of extracted power the effects would be much less important. It is necessary to highlight that this study is only focused on tidal fences, which justifies the applicability of certain simplified analytical models, whereas it would not be valid for the case of a block farm. Regarding the oceanic model POLCOMS, there is an example in the next section, related to the Bristol Channel [Shapiro, 2011]. Other examples on Ocean Circulation models can be seen from the work by Hasegawa et al. [2011], using the POM (Princeton Ocean Model) model with a nested-grid in order to analyse the far-field impact of tidal turbines in the Bay of Fundy and Gulf of Maine system with similar results to the ones presented by Karsten et al. [2008] and [Defne et al., 2011], with the model ROMS (Regional Ocean Modelling System), in order to identify the potential locations for tidal energy extraction and its effect on the hydrodynamic behavior of the estuaries along the Georgia Coast (USA).

Finally, a more recent example of the application of numerical models to environmental impact assessment of tidal energy extraction is found in the study carried out by van der Molen et al. [2016]. The 3D model GETM-ERSEM-BFM is used to analyse the effect that two arrays of tidal turbines installed at the Pentland Firth could have in the hydrodynamics and biogeochemistry conditions of a large scale model covering the North-West European Shelf around the UK. In relation to the geochemistry changes, the authors identify changes up to 10% happening at The Wash area due to the largest array (8 GW), therefore it suggests that far-field effects of this kind can happen for very high installed capacities. Based on the results, they also suggest investigation of the impact interactions from simultaneous schemes deployed at different areas.

Idealised models

Idealised models of estuaries are based on simplified physical formula, geometrical dimensions and applied forcing [Hibma et al., 2004]. In comparison

with complex models, which include sediment transport, currents and waves [Hibma et al., 2004], idealised models benefit from a reduction in computational demand, which allows the testing of numerous scenarios, and an easier identification of physical trends. [Hunt et al., 2015], [Moore et al., 2009]. Complex and idealised models can similarly explain some aspects, such as the influence of the basin length on tidal wave effects, as can be seen from Hibma et al. [2004], where examples of 1D, 2D and 3D complex and idealised models of estuaries are compared. Sometimes, large number of idealised models are used to evaluate one of the parameters involved in the estuarine behaviour and the results are contrasted against observed measurements or a complex model based on a real geometry.

Regarding the application of idealised models of estuaries two main groups of studies can be found: the projects related to the estuarine morphodynamics and the more recent research about the effects of tidal energy extraction in estuaries. In the first group, it can be found, in general, that the purpose is to analyse the effects of certain boundary conditions (wind, tides, waves, surges, river flows, etc.) or the combination of different parameters, such as: morphology, sediment transport, salinity, currents, stratification, etc. although sometimes they are also used to give a description of a full process happening in the estuary, like channel formation or flood-ebb dominance. Due to the development of tidal energy technologies, other studies have appeared with the aim of evaluating the power output from tidal farms and fences in different locations and the effects on hydrodynamics, amongst others. There are some examples of studies referred to morphodynamic analysis and the energy related works are presented in the next section.

An example of the use of idealised models to analyse the effects of wind and waves on tidal asymmetry in estuaries can be found in Hunt et al. [2015]. Four cases with an ellipsoidal domain related to a mesotidal estuary were created in Delft3D. The plan area and the thalweg depth or depth at the deepest part of the riverside are the same in all cases while the intertidal areas have been

varied from concave to convex shapes. The boundary conditions at the sea cover three cases: tides only, wind only and a combination of both. The results for the bed shear stresses from the subtidal and intertidal areas are compared with observations from a real case estuary. It can be seen that the relationship between the morphology and the tidal asymmetry is mainly non-linear. Three stable estuary states are identified depending on the dominating forcing: a convex shape of the intertidal area for dominating tides, a concave profile for winds and a flat surface in the case of tides and wind acting together.

The impact of sea-level rise on estuarine circulation is investigated by means of an idealized model in the study carried out by Chua & Xu [2014] by means of the 3D SUNTANS system. The geometry is based on San Francisco Bay and simplified as a rectangular channel for the estuary connected to an ocean basin. The boundary conditions are approximated to the M2 tidal constituent and a constant discharge for the river. The results are in agreement with previous studies cited in this work about the effect of sea-level rise resulting in higher salinity levels upstream and affecting the tidal currents.

In the study by J. Maskell et al. [2013], the authors analyse the interaction between storm surges and river flows in the inundation of well mixed macro-tidal estuaries. Two models are used, namely a detailed finite volume method model (FVCOM) and a simplified model (LISFLOOD-FP).

Three different cases are represented in FVCOM: a funnel-shaped estuary and two elongated and shallower estuaries with different slopes in the intertidal area. Results for the elevations are compared in the situation with the combined effects and in the case of summing the results from separate tidal and fluvial conditions acting individually. Another model is created in LISFLOOD-FP to be compared with FVCOM and there seems to be a good agreement although LISFLOOD-FP gives a smaller area of inundation. Regarding the results, it can be seen that in the funnel-shaped case there are non-linear interactions because the results of the combined situations are higher than the sum of the results for each case separately. In the case of the

elongated estuaries, the surge and river flows seem to have less interaction.

In the study by S.-N. Chen & Sanford [2009b], the 3D numerical model ROMS is used to simulate an idealised estuary-shelf system in order to investigate the lateral dynamics and related sediment transport in moderate and highly stratified estuaries. The authors included the shelf because the boundary conditions at the mouth of the estuary are not known and the salinity needs to become stable in the channel. The estuary is represented by a straight channel with triangular cross-section. (see Fig. 1.4) The Principal lunar semi−diurnal harmonic constituent (M2) tides are applied at the open boundary. The results are compared with the ones extracted from an analytical model and observed measurements from the river Hudson. From the results it can be seen that there is an important lateral circulation due to boundary mixing on a sloping bottom and that there are differences between the cross sectional sediment dynamics seaward and landward of the salt intrusion.

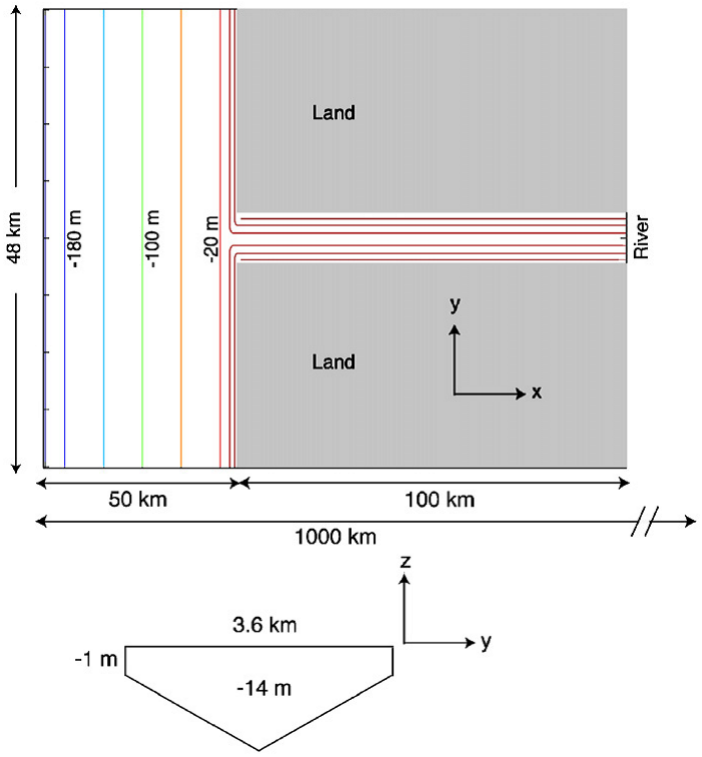

Figure 1.4: Plan view of the estuary-shelf system and cross section of the channel. (Source: S.-N. Chen & Sanford [2009b])

The same model in S.-N. Chen & Sanford [2009b] is slightly modified by the authors in S.-N. Chen & Sanford [2009a] to analyse the effect of axial wind on stratification and the related longitudinal salt transport in partially mixed estuaries. The model is compared against observed measurements from Chesapeake Bay. Regarding the stratification, the results show that there is a reduction in the case of up-estuary wind while for down-estuary wind an increase-decrease transition can happen. Regarding the salt transport, as it is related to shear dispersion due to wind, it can be seen that the dispersion is increased with moderate down-estuary winds and reduced always with up-estuary winds.

In the work by Hibma et al. [2003], an idealised estuary with a constant width is developed with a 2D depth averaged model and the results are compared with an analytical approach and field data in order to determine the ability of the model to reproduce the formation of shoals and channels in elongated, sandy, well-mixed and tide-dominated estuaries. The authors conclude that the results from the idealised model agree with realistic channel and shoal patterns but it is still a complementary tool to other approaches.

In the study by Moore et al. [2009], the authors analyse the ebb-flood dominance in the Dee estuary. Three cases were modelled with POLCOMS in the study, representing a funnel-shaped geometry related to the current bathymetry and the cases with deposition on the banks and erosion of the main channels (see LIDAR image in Fig. 1.5). The boundary conditions consist of the M2 and Principal solar semi−diurnal harmonic constituent (S2) tidal waves. The results show that the flood dominance occurs in the upper estuary in a high percentage of the estuary area and that the increase on the banks levels leads to an increase in the ebb dominance.

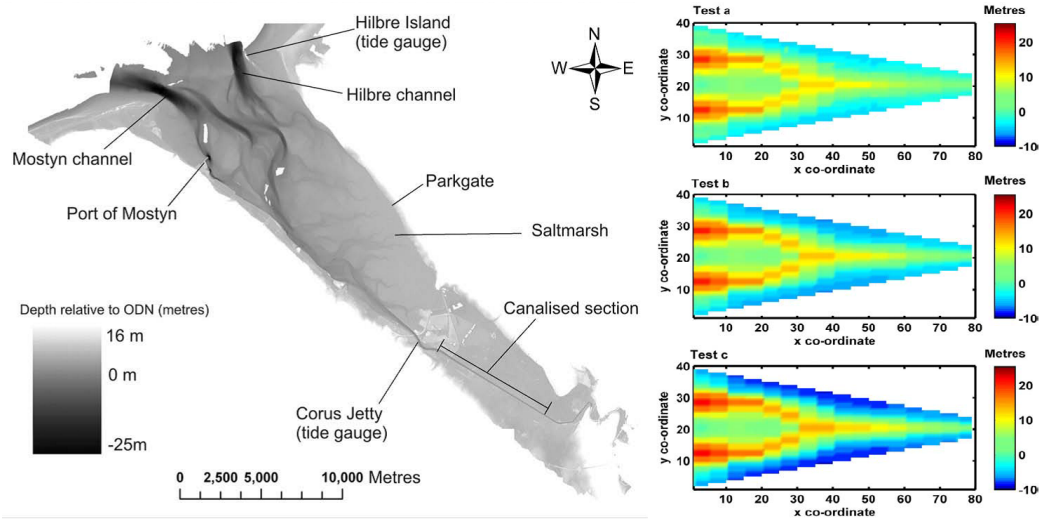

Figure 1.5: Left: Bathymetry of the Dee estuary from a LIDAR survey of 2003. Right: Grid used to represent a simple funnel-shaped idealised estuary (depths given are in metres). (Source: Moore et al. [2009])

Regarding the analysis of the effects of tidal energy extraction in estuaries, an example can be found in the thesis by Draper [2011], where a group of generic coastal geometries are used to identify the effects over the locations with a highest resource in the world. Numerical and analytical models are used to evaluate the extracted energy and the impact on available power due to the deployment of a tidal fence. The numerical models have been developed by means of the OxTide solver. There are four classes of geometries which mainly describe: straits between oscillating water bodies, oscillating bays, large currents between an island and a much larger land mass and accelerated flow around headlands. In the first class, the author considers both the cases without interconnected channels and with multiple interconnected channels in the strait. Similarly, in the second class, the author differentiates between enclosed bays and non-enclosed bays, including in the latter the case of estuaries. From the analysis of idealised models based on each class of geometry, it can be seen that there is a limit to the available power due to the feedback effect of the tidal fence on the currents, which are dependent on the geometry. Results also show that tidal currents and range are reduced in tidal

channels and enclosed oscillating bays while there is an increase in tidal range in non-enclosed bays with a sufficient length.

In the study by Y. Chen et al. [2014], the authors use a 3D idealised model of an estuary in order to evaluate the tidal energy extraction by horizontal axis tidal turbines which are represented by a momentum sink term in the governing equations. An area of interest is identified within the estuary where the minimum water depth and the velocity distribution are suitable for the deployment of tidal turbines. Two models were used with different mesh refinement. The first model used a refined mesh size to account for the thrust of an isolated turbine. The second model used a coarse grid, including five turbines in each cell. The thrust coefficient was reduced according to the increase of the area occupied by the tidal farm. In this case, the results showed that the extracted energy during the mid-ebb tide was different than in the refined model, therefore the authors applied a reduction of the thrust coefficient over several simulations until they obtain the same energy extraction as in the refined model. The authors also performed simulations with the coarse grid for a case with a tidal fence of 400 turbines and a multi-row farm formed by 10 rows and 4000 turbines in total covering the whole width of the estuary. They analysed the results for the effect on the water levels. These results are similar in both cases, consisting of an increase both in the high and low water levels in the order of cms, being the increase higher in the low levels.

The work carried out by Yang & Wang [2015] analyses the impacts of tidal energy extraction in the stratification and baroclinic circulation by means of an idealised model in FVCOM of an estuary and a narrow channel connecting it to the open sea. (Fig. 1.6) The dimensions of the idealised model are based on the Puget Sound, which is a tidally dominated estuary. The boundary conditions consist of the M2 and S2 tides in the open sea boundary and an idealised river flow based on the seasonal changes of the total inflow. Tidal energy extraction is included in the governing equations as a momentum sink term. By varying the turbine density in each element the authors develop a curve relating the

extractable power to the number of turbines. From this curve, it can be seen that there is a linear relationship between the extractable power and the number of turbines when the number of turbines is less than 10 % of the number of turbines corresponding to the maximum extractable power. Three different tidal farms were used in the model, consisting of 1500, 400 and 800 turbines, which represent 9, 2.4 and 5 % of the number of turbines for the maximum energy extraction (17000 turbines). Spacing is different for each scenario but all of them cover a similar area. When comparing the results between the situation without turbines and the case with 1500 turbines, the effect on tidal elevations in the channel is small and there is a phase lag in the surface current. There is also a reduction in the stratification and the two-layer circulation. The extractable power is calculated for each scenario and it can be seen that there is a reduction of the power output per turbine as the number of turbines increases. Results also show that stratification decreases with an increasing number of turbines but the effect is relatively small.

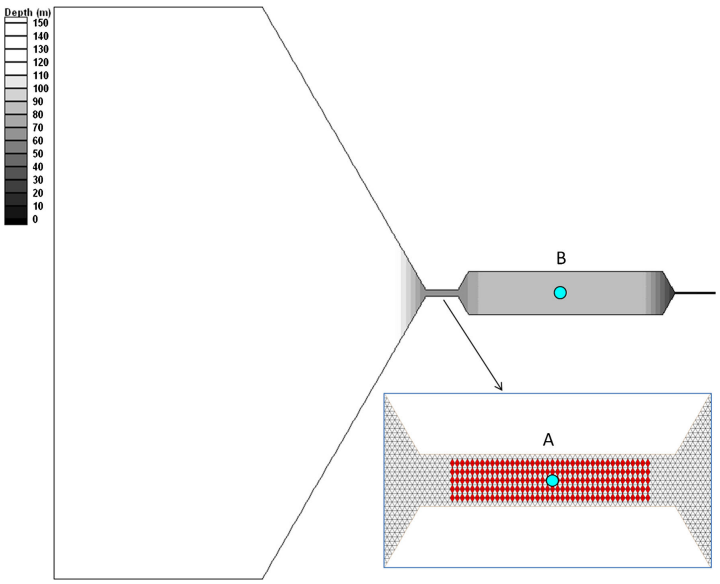

Figure 1.6: Model domain and bathymetry of an estuary connected to the coastal ocean through a channel. The inset image shows the unstructured model grid and tidal turbines. (Source: Yang & Wang [2015])

From the analysis of the literature in relation to idealised models including

tidal energy extraction in estuaries, it can be seen that there are only a few examples and they are either focused on tidal fences under different geometries or tidal farms in a specific estuary. Therefore, in relation to the objectives of this thesis, it seems necessary to address the effects of tidal farms on water levels in estuaries under different geometries by using idealised models.

Representation of tidal farms

The inclusion of the effect of tidal stream farms in the governing equations of the numerical models for the assessment of the maximum power extraction and changes over the flow has been treated from different perspectives by several authors in recent years. Representations vary from very simplified cases, where the farm is treated as a block over an area, to more accurate descriptions of the individual turbines within the farm.

Regarding the introduction of a tidal farm as a drag over the occupied area, Vennell [2012] presents a simplified 1D analysis of the energy losses in the flow where the results are given as non-dimensional values referred to the situation without the farm. Vennell uses the farm's gross drag coefficient based on its cross sectional area, including the power extraction and the effect of the support structures as well. In previous works, Vennell [2011] defines the farm's gross drag coefficient in terms of the sum of the drag coefficients for every row of untuned turbines in the farm applying the same non dimensional analysis to the 1D model. The purpose is to evaluate the optimal in-concert tunning in constricted channels or in farms with different densities between rows. The concept "in-concert" means here that in a multi-row farm each row of turbines need to be tuned with the others, apart from being tuned with the channel dynamics. The optimal tuning is defined previously [Vennell, 2010] as "the internal configuration of the farm required to maximise power production". In this study the author uses simplified models developed by P. Cummins & Garrett [2005], and Garrett & Cummins [2007] and combines them. In a more recent paper, Garrett & Cummins [2013] present a simplified analysis

combining analytical and numerical models to give the equations for the maximum power available from a tidal farm in steady and tidal flows in an unbounded location and use the local increase of a linearised bottom friction over the area of a circular farm. The same configuration of a circular farm in an open location is included in a previous 3D numerical model of the Celtic Sea as a drag over the water column by Shapiro [2011] in order to study the impact of energy extraction over the regional scale circulation.

It should be noticed that the use of a linearised drag, as can be seen from recent works ([Garrett & Cummins, 2013]) gives an unrealistic representation of the farms. Therefore, it would be recommended to use a quadratic law for the additional bottom friction, as can be found in the studies by Yates et al. [2013] and Easton et al. [2010]. Another example is the work by I. G. Bryden et al. [2004], who describe the energy extraction as a retarding force from the turbines and add a shear stress at the perimeter by the Chezy-Manning formula for friction on the bottom and sides of the channel.

In reference to the representation of individual turbines within optimisation processes, Funke et al. [2013] use a smooth increase in the bottom friction in the area of the turbine. This way they parameterise the friction function of every single turbine in order to be included in the adjoint technique. On the other hand, they highlight that there exist more sophisticated turbine parametrisations given by means of the actuator disk theory. Another document related to the optimisation of the arrays of turbines is the one presented by Divett et al. [2013] where the individual turbines are included in a numerical model as a depth-averaged drag (over an area of 20x5 m) in order to compare the energy capture and flow characteristics, such as the vorticity in the wake, in different configurations within a tidally reversing situation.

Regarding more detailed descriptions of turbines inside the models that calculate energy extraction from tidal stream farms, Draper et al. [2010] implemented the Linear Momentum Actuator Disk Theory (LMADT) in a shallow flow solver to represent a tidal fence. The LMADT was derived in the work by

Houlsby et al. [2008] and allows the study of the losses from turbulent wake mixing. As can be seen from figure 1.7 , this theory describes the rotor as a disk which extracts momentum and energy to the flow and five control sections are taken into account in the regions far and inmediately upstream and downstream of the turbine, as well as the area where the turbulent wake is formed. In figure 1.7, u_{b4} represents the bypass flow velocity at station 4, whereas u_{t1} and u_{t4} are related to the turbine velocity flow. In terms of the forces, T is the thrust force on the turbine and X is a constraining force between the bypass flow and the streamtube formed by the turbine.

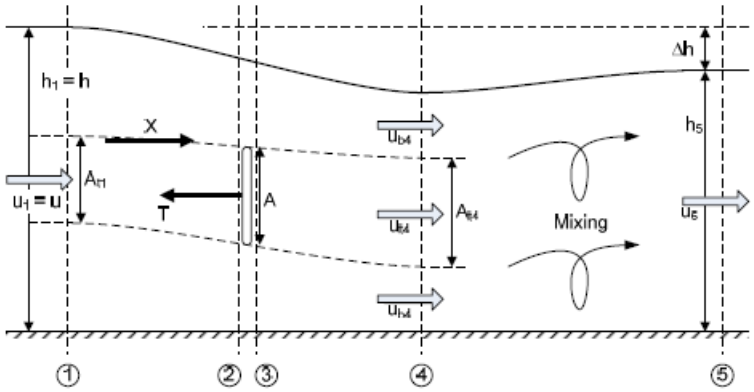

Figure 1: One dimensional linear momentum actuator disc theory in an open channel flow [16].

Figure 1.7: Control sections in the Linear Momentum Actuator Disk Theory (LMADT) (Source: [Houlsby et al., 2008])

Draper et al. [2010] differentiate between two cases for the introduction of tidal fences in 2D depth averaged numerical models: First, when the mesh size is larger that the turbine wake, the fence can be described as a line discontinuity either by means of a change in the numerical flux or by the LMADT. Second, when the wake length and the mesh size are of the same order, an increase in bed roughness would be more suitable, in agreement with Easton et al. [2010].

An example of the representation of partial blockage effects in tidal fences given by blockage coefficients according to the LMADT can be found in Nishino & Willden [2012b]. Finally, other examples using LMADT are given by Fallon & Nash [2012] and Fallon et al. [2014], where turbines are represented as a

momentum sink term from the thrust force in the governing equations and Roc et al. [2013], who extend the theory for a study at ocean scale. The methodology proposed in Roc et al. [2013] is demonstrated against a case study (Puget Sound) in the thesis by Roc [2013]. Another extension of actuator disk models is developed by Draper & Nishino [2014] in order to analyse the power extracted by closely spaced rows of turbines under parallel and staggered layouts. The authors assume that the lateral spacing is such that there is equal pressure across the flow, no significant wake mixing between rows as well as uniform flow without horizontal shear variations. The extended models are applied to the cases of 2 rows of turbines in a confined tidal channel and 2 arrays in a laterally unconfined flow.

Semi-empirical wake models have also been used to characterise the effects of tidal turbines. Of the existing studies in this subject one of the most recent examples, the work by Brutto et al. [2015], has been included here. This study analyses the influence of the thrust coefficient and the ambient turbulence over the wake of a tidal turbine. The authors used a numerical model validated against experiments with a porous disk in order to generate results of the wake expansion under different scenarios of the thrust coefficient and ambient turbulence. They observed that the wake is not influenced in a relevant way by the thrust coefficient whereas the ambient turbulence has a greater effect. Under the previous assumption, they modified the Vermeulen's empirical formulae and applied them in conjunction with the analytical model proposed by Jensen for a wind turbine in order to define the velocity in the wake as a function of the ambient turbulence. The resulting model was compared with the numerical model showing good agreement for the results of the velocity in the far wake region, although some improvements can be made in reference to the dependency on the turbulence length scale and the effect of the proximity of the free surface and the bottom. Regarding the latter, the study by Whelan et al. [2009] presents a one dimensional analytical model to account for the effects of the free surface and seabed proximity in the blockage of tidal

turbines. They described a method to incorporate the aforementioned effects in a BEM model. The theoretical results were compared with experiments carried out with porous disks and strips as well as two-bladed rotors. The results were also compared between the cases of an unblocked turbine and different levels of blockage. The performance of the turbine increases in the blocked case meaning that the power coefficient (C_P) and thrust coefficient (C_T) become higher. The power coefficient represents the proportion of the available power in the flow extracted as electricity by the turbine whereas the thrust coefficient is referred to the proportion of the mechanical power which is transferred from the flow to the turbine rotor [Baston et al., 2015]. For those cases where the tip speed ratio (or relationship between the rotational speed of the turbine and the free-stream velocity [Baston et al., 2015]) is high and the observations differ from the predictions of the free-surface proximity model, a correction of the thrust coefficient based on Maskells theory ([E. Maskell, 1963]) was incorporated. In the theory developed by Maskell it is assumed that the thrust and power coefficients respond as if the incident flow consisted of the bypass flow, accelerated by the effect of blockage and wake [Whelan et al., 2009]. The model presented by Whelan et al. [2009] assumes transversely averaged flow and is suggested by the authors for application in: closely packed arrays spanning the whole width of channels or other coastal features , cases where the array width is much larger than the water depth or devices producing significant pressure drops

As an example of the combined use of blockage and wake models for the representation of tidal turbines, there is the work carried out by Parkinson et al. [2012]. This study used an approach similar to the LMADT found in Draper et al. [2010], to represent the array. Assumptions were made on having negligible shear stress changes at the seabed. The blockage model was used to predict the changes induced in the local flow affecting adjacent devices. These changes were applied as a perturbation. The blockage model was based on Potential theory and the turbulence was assumed to be contained within a

bounding streamtube, represented by the Multipole method. An iterative approach was followed to modify the performance variables. Regarding the wake model, it was performed by means of a finite-difference model using the Navier-Stokes equations to calculate the velocity deficit in the far wake according to an eddy viscosity technique. An empirical turbulence intensity model was used to analyse the increase of loading on the downstream turbines. This model assumed that the changes in water elevation due to energy extraction were negligible and that the velocity deficit profile downstream the turbine could be approximated by a Gaussian profile.

Regarding the representation of tidal turbines in 2D depth-averaged models, it is common to parameterise the effects of the turbine based on results from a CFD model or experiments. As indicated by Kramer & Piggott [2016], the turbine thrust force implemented in some of these models as a drag force would be equivalent to an enhanced bottom drag. In depth-averaged models, the drag effect is acting over the water column, therefore the model velocity is an average of the turbine velocity plus the by-pass velocity above and below, and it is not the turbine velocity. If the cell that contains the turbine is not large enough the local velocity is affected significantly. This idea also applies to 3D models, even if the drag is acting over certain layers because they do not represent accurately the cross-section of the turbine. The authors provide a correction for the thrust coefficient based on actuator disk theory to account for the fact that models like MIKE 21 and Fluidity use the local velocity rather than the upstream velocity for the calculations of the turbine drag force.

Case studies.

The Severn Estuary presents one of the highest tidal ranges in the world and a strong velocity of current, up to 2.4 m/s in the spring tide. In addition, it has a complex bathymetry and flow regime, affected by the funnelling shape [Neill et al., 2009]. It has been widely studied and in some cases a 2D FVM model with an unstructured computational mesh is used ([Xia et al., 2010b], [Xia et

al., 2010a], [Xia et al., 2011]), whereas other studies apply a regular grid for both 2D DIVAST model coupled to a 1D FASTER (Flow and Solute Transport in Estuaries and Rivers) model ([B. Lin et al., 2010], [Croft et al., 2010], [Ahmadian & Falconer, 2012], [Ahmadian et al., 2012]) to allow the definition of a small grid size for the complex bathymetry in the riverine area [B. Lin et al., 2010].

For the representation of a barrage in the 2D FVM model a technique of domain decomposition and local refinement of the mesh close to the structure is used by Xia et al. [2010b], Xia et al. [2011] and Xia et al. [2010a] (figure 1.8). Xia et al. [2010a] indicate some references to problems that arose in previous hydrodynamic models due to large grid sizes or regular grids.

Regarding the representation of tidal stream turbines, there are several ways to introduce them in the model equations: as external forces representing the axial thrust reaction from the turbine and the drag force created by the pile supporting it ([Ahmadian et al., 2012], [Ahmadian & Falconer, 2012]) or as a momentum sink term of the power extraction coefficient factor obtained from a CFD model ([Croft et al., 2010]). Most of the existing studies on arrays of turbines in the Bristol Channel focus on axial flow types and a high number of turbines (hundreds or thousands) are commonly used to assess their effect [Croft et al., 2010], [Neill et al., 2009], [Ahmadian et al., 2012], [Ahmadian & Falconer, 2012].

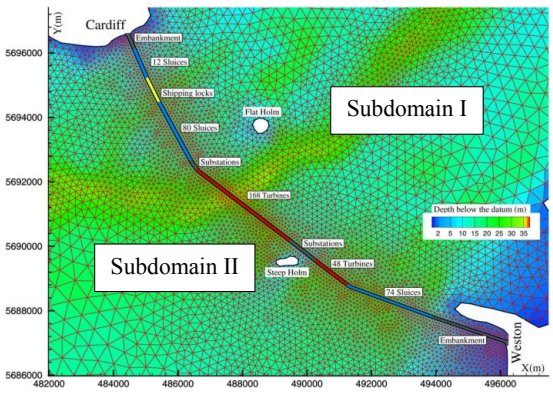

Figure 1.8: Domain decomposition and local refinement (adapted from Xia et al. [2010a])

Sediment transport, which is closely related to changes in current velocity and the sediment carrying capacity of the estuary, is often included in the hydrodynamic model [Kadiri et al., 2012], [Ahmadian et al., 2012].

Another parameter which has been taken into account only for the Severn Barrage case is the flood risk, directly related to the maximum water levels [Xia et al., 2010b] , [Xia et al., 2011], and also connected to the effect on low tide level changes over the groundwater and the drainage system [Xia et al., 2011]. An assessment of the effect of the Severn barrage on flood risk is presented by Xia et al. [2011], where three scenarios for the open seaward boundary conditions are analysed: the first scenario relates to tide levels predicted by the POL model, the second scenario includes the effect of sea-level rise and the third scenario includes the effect of a storm surge. The authors conclude that with the barrage the effects of extreme coastal flooding events would be reduced upstream, even with a future increase of the sea level.

A general overview of the results for tidal stream turbines is given by comparing the existing studies on the Bristol Channel. It can be seen that changes in water levels would be generally negligible [Ahmadian et al., 2012], [Ahmadian & Falconer, 2012]. For water velocities, the same studies indicate that the magnitude would be reduced inside the array as well as upstream and downstream, whereas it would increase on the sides.

Finally, Ahmadian & Falconer [2012] analyse the influence of the shape and density of the arrays by using 3 different configurations (a - parallel to the flow, b - perpendicular to the flow and c - sparser) with the same number of turbines. This shows that denser configurations would cause higher but more localised changes in water levels and velocities. Finally, sediment transport would be influenced by water velocities.

A more recent study with similar results was carried out by Fallon et al. [2014] in the Shannon Estuary in order to evaluate the effects of three arrays of turbines with different spacings and total capacity installed over the same area. In conclusion, impacts are more severe for the scenarios with a higher density

of turbines and extend to the far-field region. In relation to the tidal flows, water velocities are decreased within the farm and accelerated around it, which could increase the suspended sediment levels and have ecological impacts on flora and fauna, according to the authors. Regarding the water elevations, the effects consist of a decrease in the high water levels, with positive impact on flood risk, and an increase in the low water levels, which would mean a permanent inundation of certain inter-tidal areas. In addition, there are associated changes in the phase of both tidal flows and water elevations. The study also presents the consequences on kinetic fluxes at different cross-sections but these results can be obviously derived from the previous evaluation of changes in current speed. A further analysis about the impact on intertidal areas, flushing characteristics and tidal regime derived from the same model of the Shannon estuary can be found in Nash et al. [2014].

Although these studies give an initial idea about the hydro-environmental impacts associated with tidal farms in estuaries they are unable to represent the by-pass flows existing around the individual turbines. Therefore, three-dimensional models would be necessary to analyse the far-field effects associated with these flows.

1.4.5 Flood risk in estuaries

The term flood risk has been often defined as a combination of two variables: the probability and the consequences of an event happening. Szollosi-Nagy & Zevenbergen [2005] give a definition of risk based on the concepts of: a scenario, a probability and a damage index, citing the ideas presented by Kaplan and Garrick in the Journal of the Society of Risk Analysis in 1997. Balica et al. [2013] define the flood risk for their study as the product of probability and consequence, taking into account environmental, economic and social perspectives, according to the European Floods Directive 2007/60/EC.

Regarding the causes of flood risk, there are different sources as follows. Pluvial flooding is caused by local heavy rainfall and, therefore, it is necessary

to analyse extreme events and the associated return periods. In urban areas, the level of flood risk is increased when the drainage system is not capable of dealing with the runoff [Szollosi-Nagy & Zevenbergen, 2005; A. S. Chen et al., 2010]. Fluvial flood risk appears as a consequence of high water levels in rivers. Blocked culverts and bridges also increase the flood risk in these situations, [Great Britain Dept. for Communities and Local Government, 2009]. Frequently, pluvial and fluvial flooding happen together but the time scale and magnitude are usually bigger in fluvial flooding [A. S. Chen et al., 2010]. In coastal areas, the main cause of flood risk is the sea level rise due to a storm surge but several factors are involved in the resulting level of damage, such as the tidal, wind and wave conditions, the topography, the drainage system and the flood defences. Regarding the tidal conditions, they can be either astronomical or meteorological [Szollosi-Nagy & Zevenbergen, 2005], [Hardisty, 2007]. Finally, groundwater flooding, depends on the soil nature and it is closely correlated with fluvial flooding in riverine areas [Macdonald et al., 2012]. Whatever the source of flood risk, the extent of flooding will depend on the combination of the factors involved.

As previously mentioned, damages are part of the flood risk concept. They can be classified as direct or indirect damages. According to the possibility of measuring their monetary cost, they can be also classified as tangible or intangible damages [Szollosi-Nagy & Zevenbergen, 2005], [Hammond et al., 2012]. To estimate direct tangible damages it is necessary to get the flood characteristics and the information about land use as well as its maximum amount of damage and establish a stage-damage function [Szollosi-Nagy & Zevenbergen, 2005]. An example of this process is given by Hammond et al. [2012] in an urban area. Indirect tangible damages are evaluated in terms of the interconnections between the economic agents, adopted from urban and regional economic models or, sometimes, if sufficient data are not available, as a percentage of the direct damage [Szollosi-Nagy & Zevenbergen, 2005]. In the case of intangible damages it is more difficult to estimate the loss but there are

some methods, for example mortality functions or cultural loss assessment matrices. Burzel et al. [2012] introduce an integrated risk analysis to assess tangible and intangible damages by means of a spatial modelling approach through the use of utility functions and weighting factors to express the integrated risk as a non-monetary unit per year.

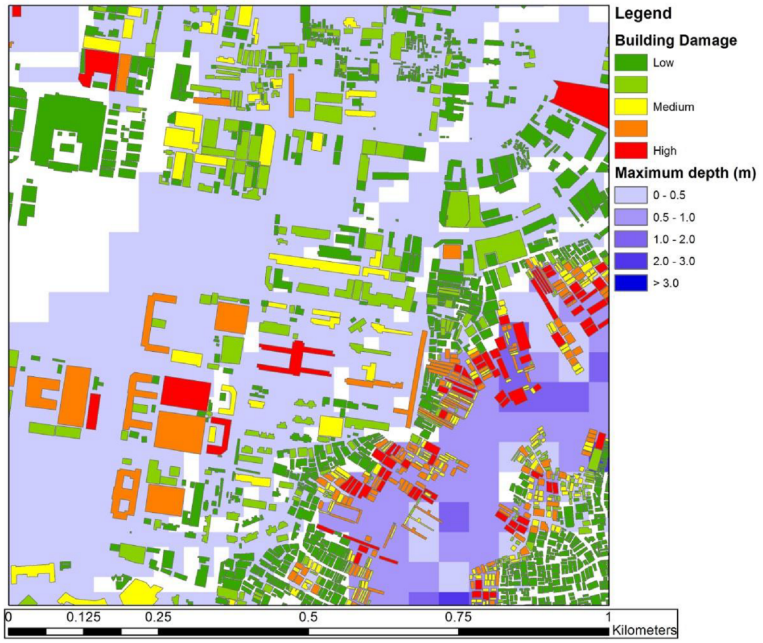

Figure 1.9: Damage per building (Source: Hammond et al. [2012])

As a result of the flood risk assessment process, flood-risk maps can be prepared. Hammond et al. [2012] provide a flood map for the area of study with a classification of the damage per building in terms of the water depth (See figure 1.9). Kalyanapu et al. [2012] give a flood risk map of the case study based on depth-velocity curves from dam break guidelines, used only for the demonstration purpose.

Balica et al. [2013] describe two main approaches for flood risk assessment: a deterministic approach and a parametric approach. Regarding the deterministic approach, data related to extreme events are analysed to build the scenarios that will be simulated in a computational model to give estimation about flood depth, elevation and velocity. In conctrast the parametric approach uses the scarce available parameters to estimate the flood vulnerability, defined

as the degree of sensitivity of a system to floods and the capacity to deal with and recover from these situations. Therefore, the parametric approach is aimed to be a tool for decision makers. More recently, probabilistic approaches have been used to introduce uncertainties that affect the results from the flood risk assessment [Kalyanapu et al., 2012], [Purvis et al., 2008], [Fontanazza et al., 2012], [Néelz & Pender, 2010].

(1) Name	(2) Developer	(3) Numerical scheme(s)[1]	(4)Shock Capturing	(5) 1D-2D Linkages	(6) Minimum recommended hardware specification
ANUGA	Geoscience Australia & Australian National University[2]	FV	Yes	No	Windows or Linux PC RAM: 512 MB
Flood Risk Mapper	Mouchel	FD (Explicit)	No	No	Not provided by supplier
FloodFlow	Micro Drainage	FD (ADI or Explicit)	No	Yes (River / overland flow link through a *vertical* link).	Processor: 1GHz RAM: 1 GB
Flowroute	Ambiental	FD (Explicit)	No	No	Processor: 1GHz RAM: 2GB
InfoWorks	Wallingford Software	FV (Roe's Riemann solver)	Yes	Yes. Integrated 1D-2D package	Processor: Pentium 4.1.5GHz RAM: 2GB
ISIS	Halcrow	FD (ADI or TVD)	Yes (TVD only)	Yes. Integrated 1D-2D package	Processor: Intel Pentium 4 or equivalent RAM: 100 MB
JFLOW-GPU	JBA	FD (Explicit)	No	No	The GPU should be a NVIDIA G80 series or a subsequent card. Any machine capable of supporting the graphics card.
MIKE FLOOD	DHI	FD (ADI)	No	Yes. Integrated 1D-2D package	Processor type: Intel or AMD Speed: 2.0 GHz RAM: 2.00 GB
RFSM (Direct)	HR Wallingford	N/A[3]	No	No	No specific needs - a standard recent computer.
RFSM (Dynamic)	HR Wallingford	FD (Explicit)	No	No	No specific needs - a standard recent computer.
SOBEK	Deltares	FD (Implicit - Staggered grid)	Yes	Yes. Integrated 1D-2D package[4].	Processor type: Pentium or compatible Processor speed: 1 GHz RAM: min 500 MB, recommended 2GB
TUFLOW	BMT WBM	FD (ADI)	No	Yes. Integrated 1D-2D package	Any PC
TUFLOW FV	BMT WBM	FV[5]	Yes	No	Any Windows or Linux PC
UIM	University of Exeter	FD (Explicit)	No	Yes. Integrated with 1D sewer network model (SIPSON)	Desktop PC

Table 1.4: Models included in the study by Néelz & Pender [2010]

Regarding the modelling techniques, basically, in the case of a river channel 1D models are commonly used whereas for a floodplain 2D models are required. According to Kalyanapu et al. [2012], there are some limitations of 1D models to represent complex flow patterns in urban areas.The advantages of 2D models are that they give a more realistic flow representation and that less pre- and post-

processing are required. Some examples of 2D models, both commercial and open source software, can be seen in table 1.4, adapted from the work by Néelz & Pender [2010] with the purpose of being a guidance for the benchmark tests required to compare the performance and accuracy of different flood inundation models.

Some tools, such as Geographical Information Systems (GIS), are used as a support to these models because of their advantages of data storage, display and maintenance [Szollosi-Nagy & Zevenbergen, 2005].

In the case of coastal flooding in estuaries, 2D models are more appropriate to represent the domain because it is a basin instead of a channel. The domain and boundary conditions are controlled by several constraints: wind, waves, tides, Coriolis force, evaporation, precipitation, sources and sinks, as well as temperature and salinity conditions [Szollosi-Nagy & Zevenbergen, 2005]. Shallow coastal areas and well mixed estuaries need accurate data to estimate the flood damage. A grid scale of 50 m or less is required to represent the domain with sufficient precision [Bates et al., 2005].

Bates et al. [2005] and Purvis et al. [2008] used a 1D/2D hydraulic model (LISFLOOD-FP) based on a raster grid, originally developed for the case of fluvial flooding. Bates et al. [2005], indicate that, as many coastal floodplains also contain channels, it is necessary to use the 1D model. The model is applied to local and regional scenarios with extreme events such as: storm surges, high tides, high waves and high water levels and it is validated against observed inundations, except for the scenario of an extreme sea level rise carried out in an estuarine area in order to demonstrate the capacity of the model for large calculations.

In order to analyse coastal flooding with combined heavy rainfall and tidal effects in an urban area, Shahapure et al. [2010] take into account the mass balance equation for the overland flow and the diffusion wave equation for the channel flow, solved by a Finite Element Model (FEM). Tidal variations are introduced as downstream boundary conditions by means of an equation for

the semi-diurnal stage of the tide. For the case study, the Digital Elevation Model (DEM) and the remote sensing data were analysed by using a GIS tool. Different rainfall events with tidal variations were taken into account.

As an example of previous studies about coastal flood risk in estuarine areas, Purvis et al. [2008] assess the flood risk in Somerset. A probabilistic methodology is applied to take into account the uncertainty over the sea level rise. DEM data are obtained from LiDAR (Light Detection and Ranging) from the Environment Agency, also used by Macdonald et al. [2012]. The LISFLOOD-FP model, previously described, is used with an adaptive time step to simulate the wave propagation. On the seaward boundary, the peak levels from the astronomic tide plus the surge for several recurrence periods are determined. These values are interpolated along the coast and the effect of the funnel shape on water levels increasing inland was noticed. Land use and depth-damage curves are used to determine the monetary damage. The flood depths resulting from the model are represented on a map for each return period as well as the probability of inundation and the spatial variation of flood risk in monetary terms.

Burzel et al. [2012] carry out a flood damage assessment in an estuarine area, the Hamburg-Wilhelmsburg quarter in the Elbe Estuary, highly influenced by the tidal effect from the North Sea and previously protected by flood defences. As aforementioned, an integrated risk analysis is applied, taking into account the risk Source-Pathway-Receptor concept [Burzel et al., 2012], [Great Britain Dept. for Communities and Local Government, 2009]. The scenario is described as an increased storm surge curve from a past extreme event. Different numerical models are used both for representing the water levels and waves effect in the flood defence (Kalypso 1D/2D and SWAN) and the hinterland flooding (MIKE 21). Damages are assessed by means of a Cell-based risk assessment which allows the consideration of several parameters associated to each cell. The spatial domain is divided into a uniform grid with different resolutions. The data are first associated with each cell. Then, the models are applied to calculate

each type of damage and, finally, the results can be visualised in the form of risk maps.

1.4.6 Conclusion

This chapter aims to provide an insight into the existing theoretical framework associated with the subject of this thesis and to identify the points that would need to be included in future research lines. Tidal stream technologies appear to be in an early stage and, therefore, most of the studies were found to be very recent; on the other hand, in order to achieve a better understanding of a process integrating different scales of interactions between tidal farms and environment, the chapter has been divided into several sections and subsections.

In an array of turbines it is necessary to take into account the configuration and density of the arrays because the results would vary significantly [Ahmadian & Falconer, 2012]. Axial flow turbines have been extensively studied whereas there are no current studies on the hydro-environmental effect from other designs of turbines being developed, such as transverse flow turbines. It can be also noticed that 2D FVM hydrodynamic models have not been used yet for the assessment of the impact of tidal stream turbines, despite their advantages. In relation to the flood risk assessment in estuarine areas, deterministic analysis has been extensively applied, presenting a good scientific base and providing an estimation of the flooding extent with high resolution (according to Bates et al. [2005] it is necessary to use a grid scale less than 50 m). For the purpose of representing the domain 2D models appear to be sufficient. In reference to locations with tidal resonance, the existing studies for tidal stream farms do not analyse the potential effect on flood risk although it could be even aggravated.

Finally, these considerations justify further studies on turbine arrays focusing on the flood risk effect of transverse flow types by using a 2D FVM hydrodynamic model with a flexible mesh. It is also necessary to assess the effect of the tidal stream farm on tidal amplification with respect to the associated flood risk levels.

Chapter 2

Hydrodynamic modelling

This chapter includes first a rationale for the use of the hydrodynamic model MIKE 21 by DHI in this thesis and a description of the aforementioned program. It also presents a comparison of results between experiments and CFD models of individual turbines and the MIKE 21 simulations based on them. The purpose is to check that the turbine is accurately implemented in the model and that the downstream wake generated by the device is realistically replicated in order to achieve an accurate computation of the energy dissipated and its hydrodynamic impacts.

2.1 MIKE 21

An existing numerical model, MIKE 21 has been chosen for this project. MIKE 21 is a commercial software developed by DHI (Danish Hydraulic Institute) which has been extensively used for coastal and other applications. The versions of the software launched in 2012 and 2014 have been used for this thesis. It was chosen because it makes possible to analyse both the energy extraction and the effect on flood risk within the same model. When compared to other programs, it shows the advantages of including a specific structure for turbines and it also benefits from a user-friendly interface.

MIKE 21 FM is a two-dimensional (2D) system. Traditionally, 2D models have

been used to evaluate the levels of flood risk. Besides, the use of a 2D model rather than a 3D version, such as MIKE 3 (by DHI), is preferred in this study due to the reduction in computational demand, which will be required in the future integration of the outcomes of this project within the optimisation of tidal farms.

The specific version of MIKE 21 with a flexible mesh (MIKE 21 FM) has been used. For the spatial discretisation of the governing equations, MIKE 21 FM applies a cell-centred finite volume method over an unstructured mesh (figure 2.1).

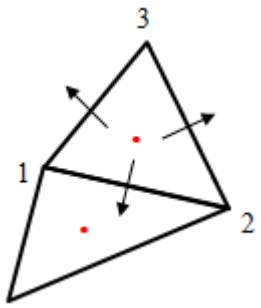

Figure 2.1: Elements in the cell-centred volume method scheme.

In the unstructured mesh the elements can be triangular or quadrilateral and their size can be refined according to different criteria, e.g. larger water depth requires larger mesh element. One of the advantages of the flexible mesh is the adaptability to bathymetry changes.

2.2 Governing equations

The governing equations consist of the 2D incompressible Reynolds averaged Navier-Stokes equations subject to the assumptions of Boussinesq and of hydrostatic pressure distribution. [DHI, 2012b]

The mass conservation equation (2.1) and momentum conservation equation (2.2), (2.3) are represented as follows, after integration over depth $h = \eta + d$.

$$\frac{\partial h}{\partial t} + \frac{\partial h\overline{u}}{\partial x} + \frac{\partial h\overline{v}}{\partial y} = hS \tag{2.1}$$

$$\begin{aligned}\frac{\partial h\overline{u}}{\partial t}+\frac{\partial h\overline{u}^2}{\partial x}+\frac{\partial h\overline{uv}}{\partial y}&=f\overline{v}h-gh\frac{\partial \eta}{\partial x}-\frac{h}{\rho_o}\frac{\partial p_a}{\partial x}\\ -\frac{gh^2}{2\rho_o}\frac{\partial \rho}{\partial x}+\frac{\tau_{sx}}{\rho_o}-\frac{\tau_{bx}}{\rho_o}-\frac{1}{\rho_o}&\left(\frac{\partial s_{xx}}{\partial x}+\frac{\partial s_{xy}}{\partial y}\right)\\ +\frac{\partial}{\partial x}\left(hT_{xx}\right)+\frac{\partial}{\partial y}&\left(hT_{xy}\right)+hu_sS\end{aligned} \tag{2.2}$$

$$\begin{aligned}\frac{\partial h\overline{v}}{\partial t}+\frac{\partial h\overline{uv}}{\partial x}+\frac{\partial h\overline{v}^2}{\partial y}&=f\overline{u}h-gh\frac{\partial \eta}{\partial y}-\frac{h}{\rho_o}\frac{\partial p_a}{\partial y}\\ -\frac{gh^2}{2\rho_o}\frac{\partial \rho}{\partial y}+\frac{\tau_{sy}}{\rho_o}-\frac{\tau_{by}}{\rho_o}-\frac{1}{\rho_o}&\left(\frac{\partial s_{yx}}{\partial x}+\frac{\partial s_{yy}}{\partial y}\right)\\ +\frac{\partial}{\partial x}\left(hT_{xy}\right)+\frac{\partial}{\partial y}&\left(hT_{yy}\right)+hv_sS\end{aligned} \tag{2.3}$$

Where $\eta =$ surface elevation above mean water level, $h =$ water depth, $u, v =$ velocity components, respectively, $f =$ Coriolis parameter ($f = 2\Omega \sin\phi$, $\Omega =$ angular velocity and $\phi =$ latitude), $g =$ gravitational acceleration, $\rho_o =$ reference density of the water, s_{ij} = components of the radiation stress tensor, p_a = atmospheric pressure, $\tau_{bx}, \tau_{by} =$ bottom shear stresses, $\tau_{sx}, \tau_{sy} =$ wind or ice stresses, T_{ij} the lateral stresses including viscous friction, turbulent friction and differential advection, S the discharge from sources and u_s, v_s the velocity components of the water discharged into ambient. [DHI, 2012b]

The depth averaged values are given by equations (2.4), (2.5) and the lateral stresses are represented by (2.6), (2.7) and (2.8).

$$h\overline{u} = \int_{-d}^{\eta} u dz \tag{2.4}$$

$$h\overline{v} = \int_{-d}^{\eta} v dz \tag{2.5}$$

$$T_{xx} = 2A\frac{\partial \overline{u}}{\partial x} \tag{2.6}$$

$$T_{xy} = A\left(\frac{\partial \overline{u}}{\partial y}+\frac{\partial \overline{v}}{\partial x}\right) \tag{2.7}$$

$$T_{yy} = 2A\frac{\partial \overline{v}}{\partial y} \tag{2.8}$$

Where $d =$ mean water depth and $A =$ horizontal eddy viscosity [DHI, 2012b].

The spatial discretisation of the governing equations over the domain can be applied following a first order or second order scheme. An approximate Riemann solver is applied in the calculation of the convective fluxes at the cell interface. A linear gradient reconstruction technique is used to provide the second order accuracy and the numerical oscillations are avoided by means of a Total Variational Diminishing (TVD) slope limiter [DHI, 2012b].

For the time integration both a low order method (first order explicit Euler method) or a higher order method (second order Runge-Kutta method) can be applied [DHI, 2012b]. In order to provide stability the time step varies according to the restriction of having a Courant-Friedrich-Levy (CFL) number less than a critical value, usually 1. The CFL number is given by:

$$CFL = \left(\sqrt{gh} + |u|\right)\frac{\Delta t}{\Delta x} + \left(\sqrt{gh} + |v|\right)\frac{\Delta t}{\Delta y} \tag{2.9}$$

Where h is the total water depth, u and v the velocity components in the x and y directions, Δt the time step and $\Delta x, \Delta y$ the characteristic length scales, which are determined by the minimum edge length at each element [DHI, 2012a].

2.3 Parameters

2.3.1 Density

According to DHI [2012a], the value of the density is given by the UNESCO's standard equation of state for sea water presented in Intergovernmental Oceanographic Commission [2010].

2.3.2 Bed resistance

The bed resistance $\vec{\tau}$ is included in the governing equations by the bottom stress terms ([DHI, 2012b]):

$$\frac{\vec{\tau}}{\rho_0} = c_f \vec{u_b} |\vec{u_b}| \tag{2.10}$$

Where $\vec{u_b}$ is the depth-averaged flow velocity and c_f is the drag coefficient, which can be defined in terms of the Chézy (C) or Manning (M) numbers:

$$c_f = \frac{g}{C^2} \tag{2.11}$$

$$c_f = \frac{g}{\left(M h^{1/6}\right)^2} \tag{2.12}$$

Where g is the gravitational acceleration and h is the total water depth. It is necessary to note that the Manning number (M) here represents the inverse of the Manning's n most commonly used [DHI, 2012a].

2.3.3 Coriolis force

As shown in section 2.2, the Coriolis Force is included in the governing equations. There are two different ways to define the effect of the Coriolis force: constant or varying along the domain. In the varying Coriolis force option it is calculated according to the geographical information of the computational mesh [DHI, 2012a].

2.3.4 Wind stress

The wind stress (τ_s) is represented by:

$$\vec{\tau_s} = \rho_a c_d \left|u_w\right| \vec{u_w} \tag{2.13}$$

being ρ_a the density of air, c_d the empirical drag coefficient of the air (according to J. Wu [1980] and J. Wu [1994]) and $(\vec{u_w}) = (u_w, v_w)$ the wind speed 10 m above the sea surface [DHI, 2012b].

2.3.5 Turbulence

There are two options for the definition of the turbulence in the horizontal scale of the model [DHI, 2012a]:

1. Constant viscosity: A constant value of the eddy viscosity coefficient, usually calibrated against observed data, is applied throughout the domain.

2. Smagorinsky viscosity (A): It is related to a characteristic length and provides a sub-grid scale value according to the following formula [DHI, 2012a].

$$A = c_s^2 l^2 \sqrt{2 S_{ij} S_{ij}} \tag{2.14}$$

where c_s is constant, l is the characteristic length and S_{ij} is the deformation rate defined by:

$$S_{ij} = \frac{1}{2}\left(\frac{\partial u_i}{\partial x_j} + \frac{\partial u_j}{\partial x_i}\right) \tag{2.15}$$

$(i, j = 1, 2)$

The model also covers the equations for temperature, salinity and density. Some of these aspects are not treated in this document because they were not included in the simulations for this project. Therefore, more information can be found in the Scientific Documentation provided with the software [DHI, 2012b].

2.3.6 Flood and dry conditions

The model allows the treatment of moving boundaries by the specification of parameters such as a wetting depth, a flooding water depth and a drying water depth. When the depths are smaller than the wetting depth the momentum fluxes are set to zero and when the depths reach a value under the drying depth the related elements are removed from the calculations [DHI, 2012a]. The approach followed by the wetting and drying fronts problem is taken from the work by Sleigh et al. [1998] and Zhao et al. [1994].

2.3.7 Boundary conditions

The boundaries in the model can be specified according to seven different conditions [DHI, 2012a]:

- Land (zero normal velocity): full slip conditions.
- Land (zero velocity): no slip condition, zero values for both normal and tangential velocity components.
- Specified velocities.
- Specified fluxes.
- Specified levels
- Specified discharge
- Flather condition: it consists of velocities and water levels, although an additional discharge condition can also be included.

The specified velocities, fluxes and levels can be defined by three different options [DHI, 2012a]:

- Constant (in time and along boundary).
- Variable in time and constant along boundary.

- Variable in time and along boundary.

The level boundary can be also given by a rating curve, as well as the discharge boundary. The latter can be alternatively defined as constant (in time) or variable in time [DHI, 2012a].

The Flather condition has transmissive properties, as indicated by Baston et al. [2015], that is, it allows the outgoing waves to pass through the open boundary avoiding the creation of an error wave by reflection. More details about the Flather boundary can be found in the work by Flather [1976].

2.4 Representation of tidal turbines in MIKE 21

Turbines are modelled as sub-grid structures by reducing the flow velocity due to an additional resistance which increases with the flow speed. Based on the idea that structures are generally smaller than the extent of the mesh element, the sub-grid technique allows using basic equations to calculate the overall impact in the cell instead of performing detailed modelling.

The effect of turbines is introduced in the governing equations as an additional shear stress component from the drag force imposed to the flow, in a similar way to the wind or radiation stress components. The axial and transverse components of the drag force (F_d , F_l) are given by equations:

$$F_d = \frac{1}{2}\rho\alpha C_d A_e v^2 \tag{2.16}$$

$$F_l = \frac{1}{2}\rho\alpha C_l A_e v^2 \tag{2.17}$$

Where α is a correction factor, C_d and C_l the drag and lift coefficients respectively, A_e the effective area of the turbine and v the velocity of the flow incident into the turbine. The velocity is the current value in the element wherein the turbine is positioned. This value is influenced by the former time steps in the calculation and is affected by the presence of the turbine but it is not to be interpreted as the current speed through the turbine [DHI, 2012a].

2.4.1 Turbine structure in MIKE 21

The input data necessary to define the turbines through the graphical interface of MIKE 21 are: the coordinates of the turbine in the map projection, the diameter of the turbine, the drag and lift coefficients and the correction factor.

It can be noted that the diameter of the turbine is used to calculate the frontal area involved in the formula of the resistance force exerted by the turbine on the flow. In the case of an axial flow turbine the diameter of the turbine can be directly used whereas in a cross flow type a conversion has to be done to find an equivalent diameter. The approach adopted in this study for a horizontal cross flow turbine will be explained in the following section.

The drag coefficient can be fixed or tabulated with the lift coefficient as a function of the angle of orientation of the turbine referred to the north and the current speed. The correction factor can be given either by a constant value or by a set of values varying in time.[DHI, 2012a]

2.4.2 Correction for mesh dependency

Kramer & Piggott [2016] and Kramer et al. [2014] have identified the dependency of the effect of the tidal turbine in MIKE 21 on the mesh resolution. Traditionally, in methods such as the actuator disk, the free flow velocity is used to compute the thrust induced by the turbine on the flow. However, in MIKE 21 the reference velocity used for that purpose is the velocity at the cell of the turbine. The force representing the turbine in MIKE 21 is extended over the cell where the turbine is positioned, resulting in a lower value of the flow velocity at the cell of the turbine with finer meshes because the reduction of the flow speed due to the turbine has more impact on the free flow velocity over the region of the cell. [Kramer et al., 2014]. In order to avoid these effects, a correction has been proposed for MIKE 21 by Kramer et al. [2014] based on the fact that actuator disk theory can be used to estimate the velocity drop from the free-stream value. Kramer & Piggott [2016] focus on the use of an increased bottom stress for the representation of energy extraction by turbines in depth-averaged models, following the theory

presented in Kramer et al. [2014] to avoid the mesh dependency of the results. The authors treat the implementation of the corrections to the enhanced drag in the case of quadrilateral and triangular meshes and extend the analysis to the computation of the extracted power.

Following the aforementioned approaches, Waldman et al. [2015] analyse the mesh dependency of the results in MIKE 3 models including tidal turbines showing that this effect can be negligible in the absence of turbines while a correction factor is necessary in the definition of the turbine to avoid underestimating the energy extracted when the mesh size is reduced. The authors run a simple MIKE 3 model with an unstructured triangular mesh under constant boundary conditions and four different mesh refinements applied in the area of the turbine in order to identify a correction factor, based on the Actuator Disk Theory, which is applied to the thrust force exerted by the turbine.

As a summary, the correction factors defined by Waldman et al. [2015], based on the work by Kramer & Piggott [2016] and Kramer et al. [2014], can be calculated according to:

$$\alpha = \frac{{u_0}^2}{{u_{cell}}^2} = \frac{4}{\left(1+\sqrt{1-\nu}\right)^2} \tag{2.18}$$

$$\nu = \frac{C_d A_e}{n \Delta x \Delta z} \tag{2.19}$$

Where α is the correction factor u_0 is the free flow velocity, u_{cell} is the local cell velocity, C_d is the thrust coefficient of the turbine, A_e is the effective area of the turbine rotor, Δx and Δz are the width and the vertical dimension of the mesh and n is the number of layers intersected by the turbine.

Waldman et al. [2015] also developed a MATLAB code which aims to facilitate the implementation of the correction factor in MIKE 3 by using an iterative process. Different positions of the turbine in the domain are considered to check that there is a small sensitivity of the results. However, it is recognised that some limitations arise due to the fact that the correction factor needs to be calculated at each time step to account for the changes of water levels and

current direction in a real case (the current version of MIKE 3 does not include this correction internally).

The study by Waldman et al. [2015] concludes that there is also some remaining mesh dependency after applying the correction may be due to different factors, such as the wake mixing effects, the nature of the actuator disk theory or the definition of the cell width.

2.5 Comparison with experiments

In order to give a more detailed description of the turbine structure in MIKE 21, the results of two models based on the work carried out by Mycek et al. [2014] and Bahaj et al. [2007] have been compared with the experimental data showed in the aforementioned studies. The purpose of the first comparison is to check that the thrust force of the turbine is accurately implemented in the model in order to achieve an accurate computation of the energy dissipated by the device, being this idea mentioned by Kramer & Piggott [2016]. In the second comparison, the accuracy of the model in representing the flow field at some positions inside the wake structure downstream the turbine is analysed.

2.5.1 Thrust force

The study by Mycek et al. [2014] analyses the performance and wake characteristics of a prototype of an axial flow turbine of 0.7 m diameter under two different conditions of the ambient turbulence intensity representing low and high levels of turbulence. The experiments were carried out in the IFREMER flume tank, with dimensions of 18 m length, 4 m width and 2 m depth at the working section. The blockage ratio was around 4.8 %. Different upstream velocities were used and the relationships between the power and thrust coefficients and the tip speed ratio of the turbine were measured for each set of velocities. The main features of the wake behind the turbine were also delimited, such as the axial velocity deficit, the turbulence intensity and the

Reynolds shear stress. It can be highlighted that the axial velocity deficit at the turbine wake in the study has been defined in terms of a disk-integrated velocity rather than the usual centre-line velocity deficit in order to provide a representative value of the area of influence of the turbine and take into account the effect over a potential turbine located downstream.

The numerical model in MIKE 21 is based on the domain of the IFREMER tank working section and two different scenarios taken from the sets of experiments. The boundary conditions in the first scenario consist of a turbulence intensity of 3% and an upstream velocity of 0.8 m/s, whereas these values are 15% and 0.83 m/s, respectively, in the second scenario. The upstream velocity has been implemented as a uniform vertical profile due to the little variation observed in the experimental measurements.

The turbulence intensity (I) is given by the root-mean-square of the turbulent velocity fluctuations and the mean velocity, according to the formula:

$$I = \frac{\sqrt{\frac{1}{3}(\overline{u'^2} + \overline{v'^2} + \overline{w'^2})}}{\sqrt{U^2 + V^2 + W^2}} \tag{2.20}$$

where U, V, W are the mean velocity components and u', v', w' refer to the difference between the mean and instantaneous velocity or varying components [Bahaj & Myers, 2013]. Given the fact that the turbulence intensity cannot be defined directly in the turbulence formulation in MIKE 21, a related eddy viscosity coefficient has been used, following the equation:

$$\nu_t = C_\mu k^2/\varepsilon \tag{2.21}$$

where ν_t is the eddy viscosity, C_μ is equal to 0.09 ([Sun, 2008]), k is the turbulence kinetic energy and ε is the turbine dissipation rate, which are calculated according to the formulae in Harrison et al. [2010] as follows.

$$k = (3/2)\, I^2 u^2 \tag{2.22}$$

$$\varepsilon = k^{(3/2)}/(0.3 D_h) \tag{2.23}$$

being I the turbulence intensity, u the mean velocity and D_h the hydraulic diameter.

The resulting values for the eddy viscosity in MIKE 21 are 3.17x10^{-3} and 1.64x10^{-2} m^2/s for the turbulence intensities of 3% and 15% respectively.

As will be explained, several simulations have been set up covering a period of 200 time steps of 6 seconds in all of them. The requirement for the Courant-Friedrich-Lévy (CFL) number has been adjusted to be equal or below 0.8. A higher order scheme has been used for the spatial and temporal discretisation of the governing equations. For the upstream boundary, a Flather condition consisting of the free flow velocity and a water level equal to zero has been used whereas in the downstream boundary a zero water level has been applied.

A flexible mesh has been used in the MIKE 21 model for the purpose of refining the mesh size and quadrilateral elements used in the region of interest around the turbine whereas an unstructured triangular mesh is applied outside. The use of quadrilateral elements implies more complexity during the pre-processing of the model but it seems to be closer to the concept of the area of influence of each individual turbine than the triangular mesh.

The blockage effects are considered to be negligible in this case and no correction has been used in that sense. However, the correction for mesh dependency proposed by Waldman et al. [2015] presented in section 2.4.2 has been applied to the turbine structure in the model. The results have been compared between the uncorrected and corrected case for a mesh including square elements of 0.7 x 0.7 m along the axis of the flume and a maximum size of 0.21 m^2 for the triangular mesh on both sides (figure 2.2).

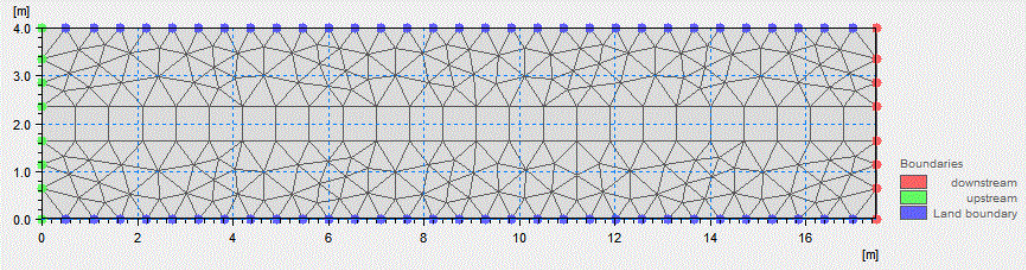

Figure 2.2: Flexible mesh representing the working section of the IFREMER tank.

The thrust force calculated by MIKE 21 without the correction with a drag coefficient equal to a thrust coefficient of 0.78, measured with 3% turbulence intensity and upstream velocity of 0.8 m/s, is approximately 13% smaller than the thrust exerted by the turbine (T) in the experiments, calculated according to the formula:

$$T = \frac{1}{2} C_T \rho A_t {u_0}^2 \tag{2.24}$$

where C_T is the thrust coefficient obtained in the experiments, ρ is the density of the water, A_t is the frontal area of the turbine and u_0 is the free flow velocity.

When the correction factor based on equation (2.18) is applied, the error between the modelled and the experimental thrust forces in the same case (C_d=0.78) reduces up to approximately 4%. The thrust forces in MIKE 21 under both scenarios (I=3%, u_0=0.8 m/s and I=15%, u_0=0.83 m/s) covering some values of C_T obtained from measurements have been compared with the thrust forces from the experiments, calculated based on equation 2.24, in order to define the range of error between them after applying the correction for mesh dependency. The comparison of results can be found in tables 2.1 and 2.2

I= 3%, u_0= 0.8 m/s			
Thrust coefficient, C_T	Experimental thrust, T_{exp} (N)	Modelled thrust, T_{M21} (N)	Difference, ΔT (%)
0.53	66.08	63.86	3.36
0.73	90.80	87.07	4.11
0.83	103.34	98.57	4.62
0.84	104.78	99.71	4.83
0.78	96.54	92.73	3.94

Table 2.1: Difference between experimental and modelled thrust forces for several turbine loadings in the case of low turbulence intensity

I= 15%, u_0= 0.83 m/s			
Thrust coefficient, C_T	Experimental thrust, T_{exp} (N)	Modelled thrust, T_{M21} (N)	Difference, ΔT (%)
0.33	44.13	43.58	1.25
0.66	87.71	86.16	1.77
0.78	104.30	101.50	2.68
0.78	104.68	101.50	3.04
0.71	95.04	92.56	2.61

Table 2.2: Difference between experimental and modelled thrust forces for several turbine loadings in the case of high turbulence intensity

Nevertheless, Waldman et al. [2015] indicated that some mesh dependency would still remain after the correction. For that reason, a sensitivity analysis has been carried out by using different values of the cell length given a fixed cell width and vice-versa on the quadrilateral mesh.

The dimensions of the different meshes, the corrections applied and the

results for the thrust forces computed in MIKE 21 can be seen in table 2.3. Figure 2.3 and figure 2.4 give the errors between the experimental and the modelled thrust for each simulation being the former related to a fixed element width of $0.7m$ and presenting the latter a fixed length of 0.7 m.

Quadrilateral elements		**Triangular elements**	**Correction factor**	**Modelled Thrust (N)**
Width (m)	**Length (m)**	**Maximum size (m^2)**		
0.70	0.35	0.05	1.124	92.39
0.70	0.70	0.21	1.124	92.73
0.70	1.03	0.46	1.124	93.99
0.70	1.35	0.79	1.124	95.50
0.70	1.75	1.33	1.124	94.79
0.70	1.94	1.63	1.124	98.25
0.70	2.19	2.08	1.124	98.14
0.70	2.50	2.71	1.124	98.21
0.70	2.92	3.69	1.124	98.05
0.70	3.50	5.30	1.124	97.80
0.70	4.38	8.29	1.124	101.82
0.70	5.83	14.73	1.124	101.82
0.70	8.75	33.15	1.124	101.77
0.70	17.50	132.61	1.124	101.86
0.70	0.70	0.21	1.124	92.73
1.05	0.70	0.21	1.079	95.03
1.40	0.70	0.21	1.057	96.16
1.75	0.70	0.21	1.045	96.73
2.10	0.70	0.21	1.037	97.06
2.45	0.70	0.21	1.032	97.34
2.80	0.70	0.21	1.028	97.56
3.15	0.70	0.21	1.025	97.71
3.50	0.70	0.21	1.022	97.81
4.00	0.70	0.21	1.019	98.05

Table 2.3: Element dimensions, correction factors and modelled thrust forces

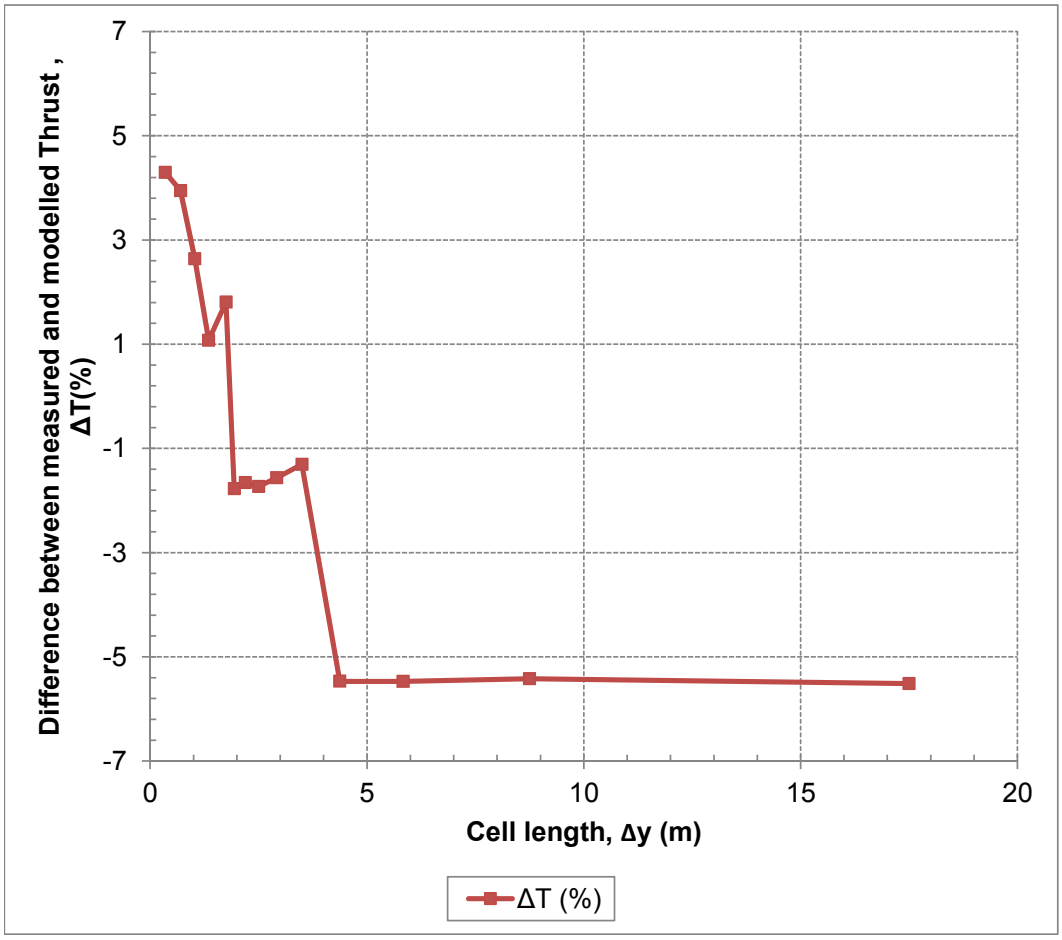

Figure 2.3: Variation in the difference between experimental and modelled thrust with the element length.

In figure 2.3 the differences seem to become stable around -1.5 % for cell lengths between approximately 2.0 m and 3.50 m. For smaller cell lengths the differences increase up to around a 4 % value for the finer mesh, with cell length equal to 0.35 m (1/2 of the turbine diameter), therefore it would indicate an over-refinement of the mesh.

A similar effect can be found in figure 2.4 for the case of having a cell width of 0.7 m (turbine diameter), which results in an increase of the differences up to approximately 4 % whereas for the rest of the cell widths used in the anaysis the differences are in the range of $(\pm)1.5\%$.

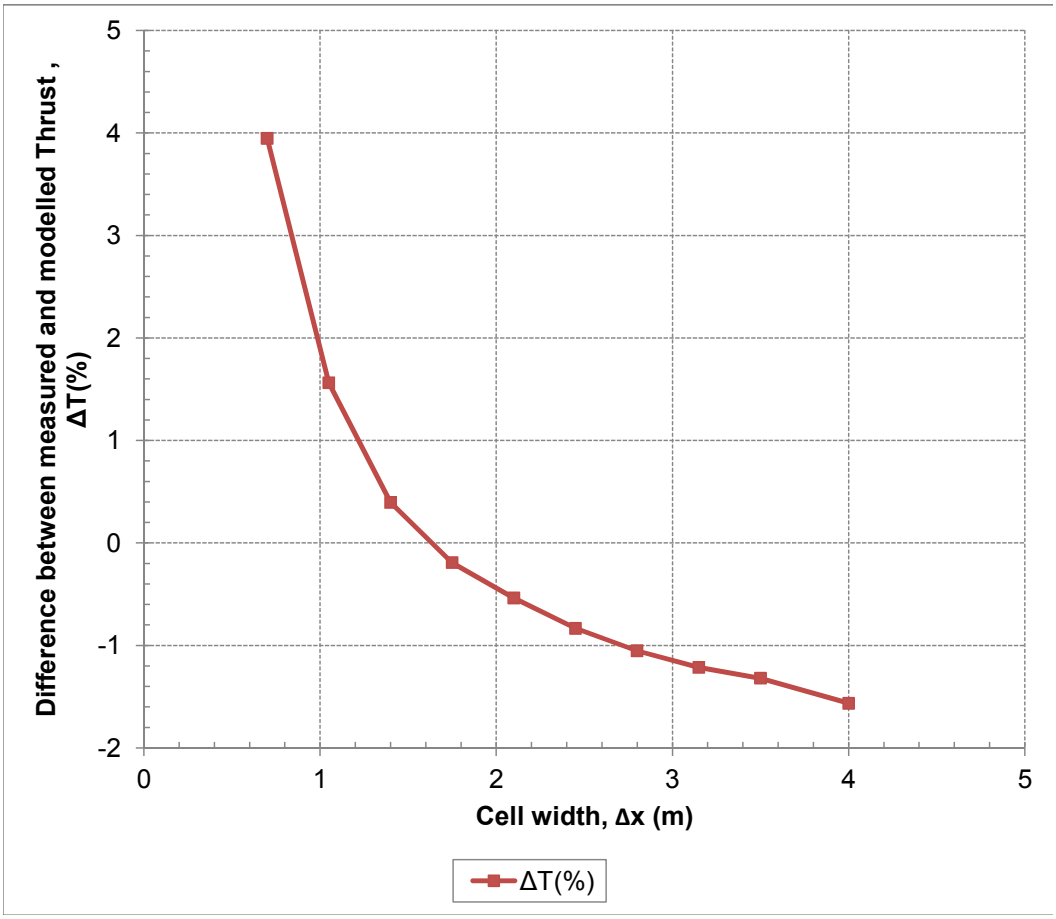

Figure 2.4: Variation in the difference between experimental and modelled thrust with the element width.

From the previous results it can be concluded that the difference between the experimental measurements and the thrust force modelled in MIKE 21 with the correction proposed by Waldman et al. [2015] and Kramer & Piggott [2016] is small, being the maximum values in the order of 5%.

2.5.2 Wake velocities

A numerical simulation has been created in MIKE 21 in order to provide a better understanding of the representation of the wake structure downstream of a turbine within the model by comparison with experimental measurements. The experiment which has been used as a base for the simulation is described in Bahaj et al. [2007]. It was carried out in the Chilworth flume at the University of

Southampton, with dimensions of 21 m in length, 1.37 m in width and 0.5 m in depth. For this experiment, a porous disk was used to emulate the presence of an individual turbine. The disk diameter was 0.1 m and the thrust coefficient was 0.95. The porous disk was installed in the centre of the water column, which covered 0.3 m depth for the purpose of the experiment. The flow velocity and turbulence intensity were obtained at different positions consisting of 8 vertical measurements at each location along the flume centreline (from 2.5D to 20D downstream the turbine) and laterally (from 3D to 7D downstream). Acknowledgment is included here to the authors of Bahaj et al. [2007] for sharing the data used in this study.

For the comparison between the experimental data and the results of the MIKE 21 model the observed measurements have been averaged over the depth and averaged again horizontally between lateral and longitudinal positions in order to match the volume averaged values obtained in the simulations. Based on the available data and the averaging process, the computational mesh in the model (figure 2.5) included square elements with an area of 2Dx2D m^2 (where D is the turbine diameter). The model domain represents a section of the flume with 3.0 m length, 1.37 m width and 0.3 m for the water depth.

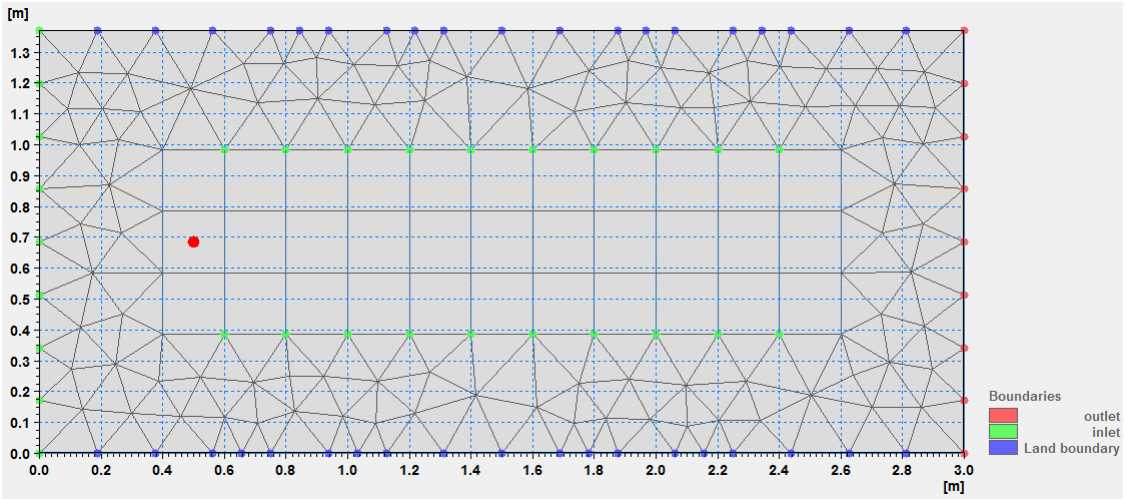

Figure 2.5: MIKE 21 mesh of the Chilworth flume experiment. The red dot indicates the position of the turbine

The simulation period was 20 minutes and both the spatial and temporal discretisation of the governing equations was carried out by means of a higher order scheme, with minimum and maximum time steps of 0.01 and 6 seconds, respectively, and a critical CFL number of 0.8. No bed resistance was included in the model and the turbulence conditions were defined by an eddy viscosity value of 1.2x10^{-4}m$^2/s$. The eddy viscosity has been calculated according to equations 2.21 to 2.23, with equal to 0.09 ([Sun, 2008]) and turbulence intensity I = 1.46 %, which has been averaged from observations. A Flather condition has been used at the upstream boundary, consisting of a zero water level and a horizontal velocity of 0.289 m/s (average of the measured velocities at the same position in the experiment). The initial conditions consisted of the same specifications as the ones given for the Flather boundary. The velocity conditions have been implemented as a uniform vertical profile. A zero depth has been defined at the downstream boundary. Regarding the turbine, a correction factor has been included in order to account for the mesh size dependency of the turbine effect. A value of 1.067 for the correction factor has been calculated following equations 2.18 and 2.19, taken from Waldman et al. [2015].

The results of the flow speed from the last time step of the model at four elements have been compared with the averaged observations from the experiment. The comparison can be found in table 2.4, where the elements are defined by the longitudinal and lateral positions of their centre with respect to the turbine centre.

Element	Velocity experiments (m/s)	Velocity MIKE21 (m/s)	Difference (%)
4D - 0D	0.279	0.283	-1.57
4D - 2D	0.299	0.301	-0.90
6D - 0D	0.281	0.283	-0.74
6D - 2D	0.296	0.301	-1.40

Table 2.4: Differences between modelled and averaged experimental results.

It can be noticed that the maximum difference is around 1.6 %, which gives a good agreement between the modelled and the experimental values.

2.6 Comparison with detailed CFD model

The representation of a tidal turbine in MIKE 21 has been compared with simulations carried out in the studies by Gebreslassie et al. [2015] and Gebreslassie et al. [2016] by means of a detailed numerical model (OpenFOAM) which has been validated with experiments . The thrust force exerted by the turbine into the flow and the velocity values at different positions are the metrics chosen for the comparison.

2.6.1 Representation of the MRL turbine in OpenFOAM

As explained in Chapter 1, this study is part of a research project called “Optimal Design of Very Large Tidal Stream Farms: for Shallow Estuarine Applications” based on the MRL turbine design developed by Aquascientific Ltd. in collaboration with the University of Exeter. The MRL turbine is a horizontal cross flow turbine consisting of three blades which rotate over their individual axis 180 degrees at the same time as the whole turbine rotates around the central axis 360 degrees (See figure 2.6). The combination of the

drag and lift forces acting over the blades is used to extract energy. Scale prototypes of the MRL turbine are being tested experimentally to optimise its performance [Gebreslassie, 2012].

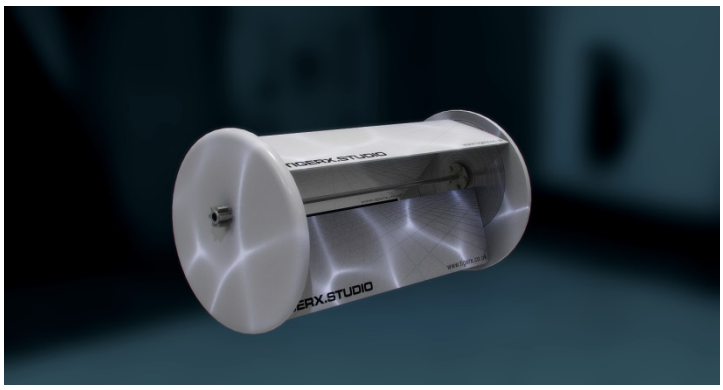

Figure 2.6: MRL turbine (Courtesy of Aquascientific Ltd.)

In the work by Gebreslassie et al. [2016], a detailed numerical model of the MRL turbine has been created in the Computational Fluid Dynamics (CFD) software OpenFOAM (Open Field Operation and Manipulation) and validated with experiments carried out at the facilities of the University of Edinburgh.

For the representation of the MRL turbine in OpenFOAM, the Immersed Body Force (IBF) approach has been used, as described in the work by Gebreslassie [2012]. The resistance of the turbine to the flow is represented by a distributed force per unit volume of the blades (F_b) applied in the cells where the blades would be located. This force is the reaction to the drag and lift forces ($\overline{F_{RD}}$, $\overline{F_{RL}}$) acting over the blades (see eqn. (2.25) and figure 2.7)

$$\overline{F_b} = \overline{F_{RD}} + \overline{F_{RL}} \tag{2.25}$$

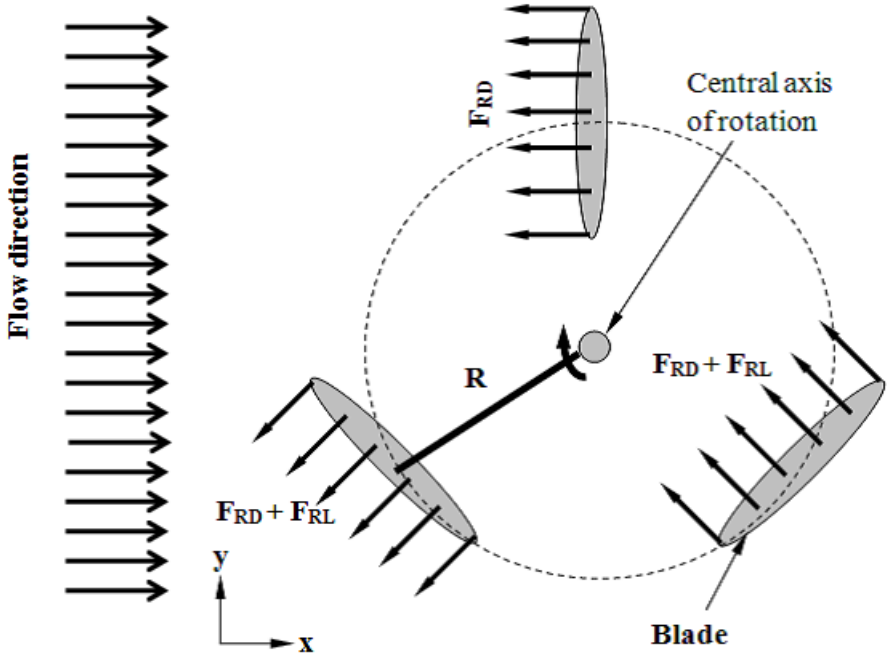

Figure 2.7: Body forces applied by each blade (source: [Gebreslassie, 2012])

One of the advantages of this method is the similarity with the actuator disk in terms of the use of a porous region rather than blocking the flow with solid blades. Although the mechanical power extracted by the turbine generator cannot be calculated without the solid blades, this method allows estimation of the energy loss including not only the useful power at the generator but also the effect of the wake downstream the turbine [Gebreslassie et al., 2015]. In order to account for the contribution of the pressure drop in the longitudinal direction over the performance of the turbine in a constrained flow, indicated by [Gebreslassie et al., 2015] the Conservation of Linear Momentum (COLM) was applied over a control volume containing the turbine. (See figure 2.8)

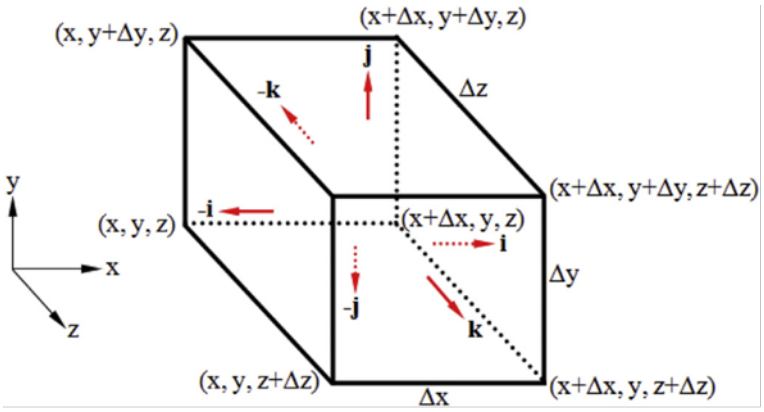

Figure 2.8: 3-D representation of a control volume housing the turbine (source: [Gebreslassie et al., 2015])

Thus, applying this technique the thrust force from the flow acting over the turbine is given by:

$$T = \int_{A_{yz}} [(p)|_x - (p)|_{x+\triangle x}]\, dA + \int_{A_{yz}} [(\rho u_x u_x)|_x - (\rho u_x u_x)|_{x+\triangle x}]\, dA + \int_{A_{xz}} [(\rho u_y u_x)|_y - (\rho u_y u_x)|_{y+\triangle y}]\, dA + \int_{A_{xy}} [(\rho u_z u_x)|_z - (\rho u_z u_x)|_{z+\triangle z}]\, dA \tag{2.26}$$

where p= pressure

The power (P) dissipated by the turbine in the flow is given by the product of the thrust force (T) and the velocity at the turbine (u_t):

$$P = T\overline{u_t} \tag{2.27}$$

It is important to note that the velocity at the turbine here is averaged over the volume occupied by the turbine (see eqn. (2.28)) in order to account for the non-uniform forces in the turbine region, instead of using the velocity averaged over the area of the rotor, like in the actuator disk theory [Gebreslassie et al., 2015].

$$\overline{u_t} = \frac{1}{V}\int_V u_x dV \tag{2.28}$$

2.6.2 Thrust force

Model set-up

In the study by Gebreslassie et al. [2015], an individual turbine and a group of seven turbines are analysed under different loading scenarios with the same boundary conditions and ambient turbulence in terms of the flow profiles and performance curves (thrust and power coefficients related to the induction factor). The model includes two phases: air and water. The turbulence scheme used in the aforementioned study is the Large Eddy Simulation (LES) scheme and the one-equation eddy viscosity model for the sub-grid scale with coefficients C_k, C_c and σ_k equal to 0.094, 1.0 and 1.0, respectively. The turbine dimensions are 0.2 m diameter and 0.3 m length. The blockage ratio is 2.1 %. figure 2.9 illustrates an example of the computational mesh used in one of the CFD models, with approximate location of the turbine inside (red dashed lines).

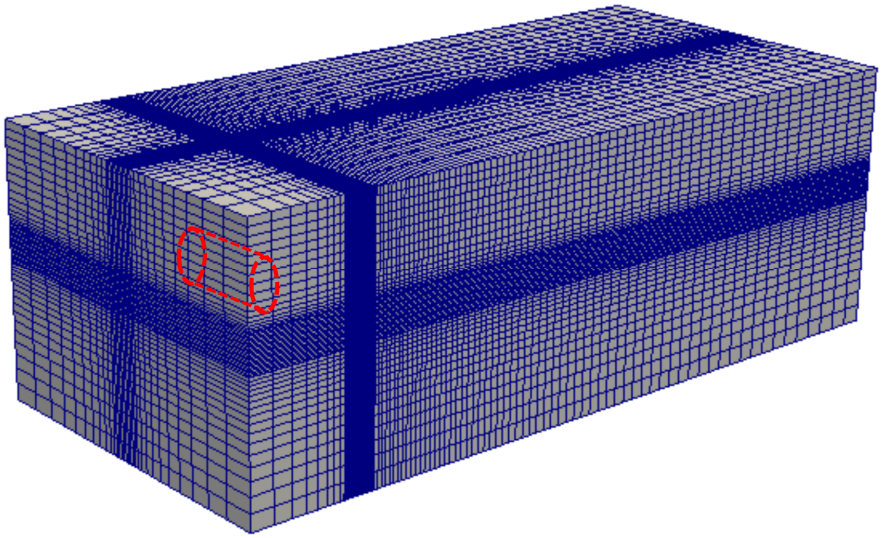

Figure 2.9: Example of computational mesh used in the CFD models (Adapted from Gebreslassie [2012])

A MIKE 21 model has been created based on the case for the individual turbine in the CFD model developed by Gebreslassie et al. [2015]. The domain presents a length of 7.2 m, a width of 2.3 m and a water depth of 1.26 m. A

flexible mesh has been used, consisting of quadrilateral elements with 0.2 m length and 0.3 m width in the area of influence of the turbine whereas an unstructured triangular mesh with a maximum size of 0.04 m^2 has been applied outside. (See figure 2.10)

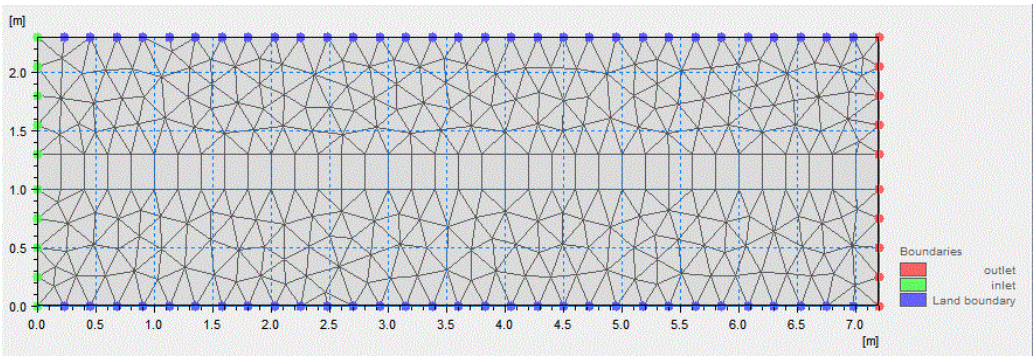

Figure 2.10: Flexible mesh used in the MIKE 21 model

The period of the simulation covers 200 time steps of 6 seconds, in which the results become convergent, being the critical CFL number equal to 0.8. Both the spatial and temporal discretisation of the shallow water equations follow a higher order scheme. The initial conditions consist of a horizontal velocity of 0.85 m/s implemented in a uniform vertical profile, being that value the current speed at the input of the CFD model. For the upstream boundary, a Flather condition consisting of a horizontal velocity of 0.85 m/s (vertical uniform profile) and a water level equal to zero has been implemented while in the downstream boundary a specific water level of zero has been used.

As the LES and Sub−grid Scale (SGS) one-equation eddy viscosity models cannot be implemented in MIKE 21 at the moment, a constant Smagorinsky coefficient (C_S) of 0.1 has been used, based on the following formula from Yoshizawa & Horiuti [1985], which relates some of the parameters from the schemes used in the CFD:

$$C_S = \left({C_k}^3 / C_\varepsilon\right)^{(1/4)} \tag{2.29}$$

where C_ε is expressed by:

$$C_\varepsilon = {a_K}^{-3/2} \tag{2.30}$$

with $a_k = 0.665$ m according to Yoshizawa & Horiuti [1985].

Regarding the parameters involved in the definition of the turbine in MIKE 21, an equivalent diameter of 0.276 m has been used in order to represent the frontal area of the turbine. The thrust coefficient used as drag coefficient in the MIKE 21 model has been obtained according to equation 2.24 and the free flow velocity of 0.85 m/s. Any correction has not been included regarding the blockage effects due to the small blockage ratio. Nevertheless, in order to avoid the dependency of the results on mesh size, a correction factor has been calculated for each thrust coefficient in the CFD and the mesh dimensions based on the formula 2.18 from Waldman et al. [2015], as can be seen in table 2.5.

Thrust modelled in CFD, T_{CFD} (N)	Thrust coefficient, C_T	Correction factor, α
28.51	1.30	1.119
21.70	0.99	1.087
16.45	0.75	1.064
11.95	0.55	1.046
7.39	0.34	1.028

Table 2.5: Thrust force obtained in the CFD model and related thrust coefficient and correction factors applied to the MIKE 21 model

Results

The results for the thrust force (or drag force) in MIKE 21 have been compared to the thrust force computed in the OpenFOAM model and the difference is shown in table 2.6

Thrust modelled in CFD, T_{CFD} (N)	Thrust modelled in MIKE21, T_{MIKE21} (N)	Difference, ΔT (%)
28.51	26.44	7.29
21.70	20.44	5.82
16.45	15.68	4.68
11.95	11.63	2.73
7.39	7.27	1.58

Table 2.6: Difference between the thrust force obtained in the CFD model and the MIKE 21 model

The differences increase with the thrust and the maximum difference is in the order of 7% for the maximum thrust force, which gives an accurate enough approximation. However, it is necessary to remark that in a real application, the turbine loading would be preferably closer to the value which gives the maximum power which does not mean to be the highest loading.

2.6.3 Flow velocities

Model set-up

In the work by Gebreslassie et al. [2016], a CFD model is created based on an experiment carried out with a prototype of the MRL turbine at the IFREMER tank. The study presents the calibration and validation of the CFD model against the experimental measurements of the flow field in the tank. Three different loadings are used for the turbine in the model and the results of the velocities along the central axis of the channel are compared in order to identify the case which gives a better agreement. For that case, the vertical profiles of the velocities are also compared with the observed measurements showing a good performance of the model in terms of the representation of the wake behaviour.

The conditions of the experiment consisted of an inlet velocity of

approximately 1.0 m/s and a turbulence intensity of 3 %. The turbine prototype had a dimensions of 0.164 m in diameter, 0.3 m in length and 0.095 m in blade chord, incorporating two plates at the top and bottom. The tank had a width of 4 m, a length of 18 m and a depth of 2 m. The velocities were measured at different points downstream the turbine with a laser Doppler velocimeter.

As the number of measurements from the experiments were not enough to be used in the comparison with the MIKE 21 model, the results from the CFD model, validated with those experiments, were used for that purpose. In the CFD model the domain covered a section of the tank with a length of 24 times the diameter of the turbine in order to reduce the computational demand. A finer mesh was used in the region of interest within the model domain, based on the sensitivity analysis presented in Gebreslassie et al. [2015]. The velocity at the upstream boundary was approximated to the experimental values by means of a power law profile. The free surface was excluded from the model given that the focus was on the wake analysis.

Regarding the MIKE 21 model based on the aforementioned CFD model, the domain had a length of 25 times the diameter of the turbine whereas the width and depth were the same (4 m and 2 m, respectively). Quadrilateral elements were used in the centre of the domain with 0.164 m length and 0.3 m width, based on the turbine size, whereas triangular elements with a maximum area of 0.03 m^2 were applied outside. The computational mesh can be seen in figure 2.11, where the red dot represents the centre of the turbine. A higher order scheme was selected for the time and space discretisation of the governing equations with minimum and maximum time steps of 0.001 and 1 seconds, respectively. The critical CFL number was set to a value of 0.85 and the period of the simulation covered 55 seconds. The initial conditions consisted of a zero level and a uniform vertical profile for the velocity, averaged from the CFD model (0.984 m/s). The upstream boundary was forced by a Flather condition formed by a zero level and the averaged velocity of 0.984 m/s whereas at the downstream boundary a zero level was imposed. In terms of the

turbulence, due to the difficulty of finding an equivalence between the CFD parameters and the options available in MIKE 21, the experimentally measured value of the turbulence intensity (3 %) was used instead. Formulas 2.20 to 2.23 were used to calculate an eddy viscosity value of 3.91 x 10^{-3} m^2/s.

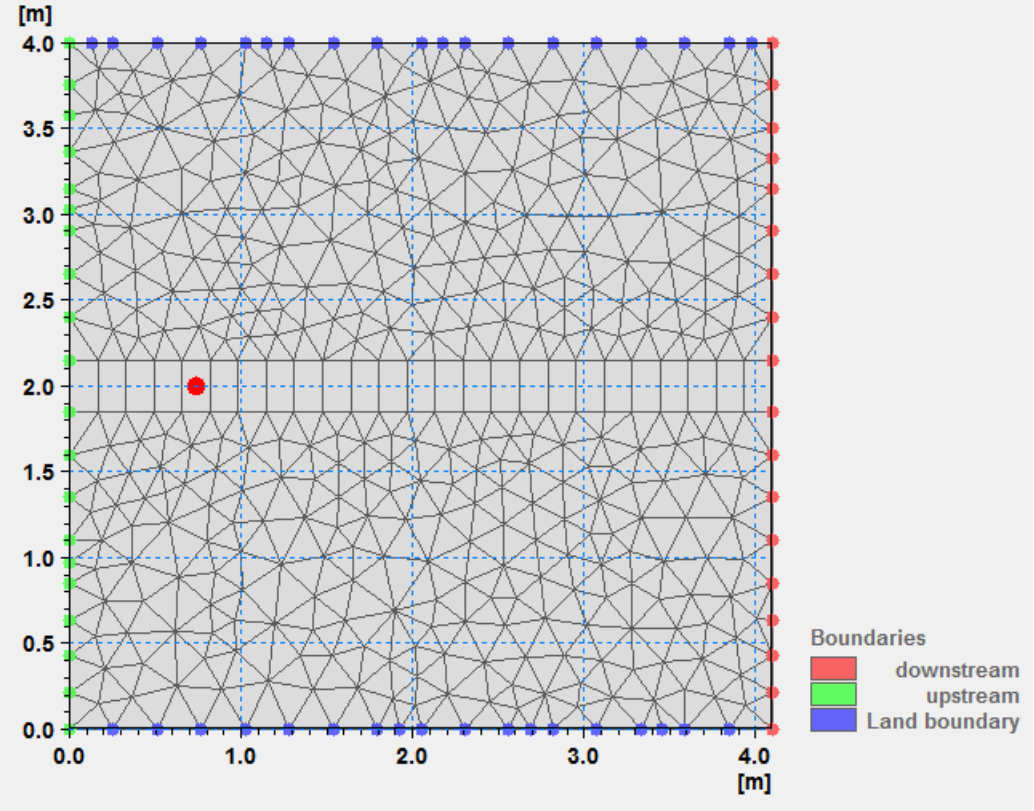

Figure 2.11: Flexible mesh used in the MIKE 21 model

Based on the information provided by the authors of Gebreslassie et al. [2016] about the values of the thrust force corresponding to two of the loadings applied in the study, the thrust coefficients were calculated and implemented in the turbine structure within MIKE 21. According to equation 2.24, the resulting thrust coefficients are the values shown in table 2.7, where the correction factors calculated following equations 2.18 and 2.19 from Waldman et al. [2015] have also been included.

Thrust modelled in CFD, T_{CFD} (N)	Thrust coefficient, C_T	Correction factor, α
16.68	0.693	1.029
17.39	0.722	1.031

Table 2.7: Thrust forces in the CFD model and related thrust coefficients and corrections factors used in MIKE 21

Results

In order to compare the results of the CFD model with the ones from MIKE 21, the values of the velocities from the CFD at several positions inside the domain were averaged over the volume occupied by the cells in MIKE 21. Acknowledgement is included here to the main author of Gebreslassie et al. [2016] for sharing the datasets of the CFD from which the results for the comparison have been extracted. Initially, vertical lines consisting of 100 points were extracted from the mean velocity results of the CFD at several positions along the central axis of the domain: -3.5D, -3D, -2.5D, -0.5D, 0D, 0.5D, 1.5D, 2D, 2.5D, 18.5D, 19D and 19.5D (indicating the distance in turbine diameters from the centre of the turbine). Besides, lateral results were obtained in the same way at 0.25L and 0.5L (L: turbine length) at both sides of the previous positions. These results were first averaged vertically for each line and then horizontally, between the lines included in a same element of the MIKE 21 model. The resulting values have been compared with the MIKE 21 velocities for the two turbine loadings, and the differences between them can be found in tables 2.8 and 2.9. Only the horizontal components of the velocities in the streamwise direction have been used in the comparison given the small magnitude of the other components.

Element	Velocity experiments (m/s)	Velocity MIKE21 (m/s)	Difference (%)
-3D	0.980	0.979	0.04
0D	0.965	0.966	-0.10
2D	0.951	0.967	-1.63
19D	0.967	0.969	-0.22

Table 2.8: Depth averaged velocities from the CFD and MIKE 21 models and differences between them for a thrust force of 16.68 N.

Element	Velocity experiments (m/s)	Velocity MIKE21 (m/s)	Difference (%)
-3D	0.980	0.979	0.05
0D	0.965	0.965	-0.01
2D	0.949	0.966	-1.81
19D	0.968	0.969	-0.04

Table 2.9: Depth averaged velocities from the CFD and MIKE 21 models and differences between them for a thrust force of 17.39 N.

The comparison aims to provide an idea about the behaviour of the model at several key positions, that is, upstream the turbine, at the turbine, just downstream and far downstream the turbine. It can be noticed that the highest value of the difference is found just downstream the turbine. Nevertheless, the maximum error found between the models reaches 1.8 % for the highest loading, which means that the results are in good agreement.

2.7 Summary and conclusions

2.7.1 Summary

This chapter explained the benefits of the use of the 2D model MIKE 21 for this thesis and described its main features, such as the governing equations and the different parameters involved. The representation of tidal turbines in the numerical model was explained in detail, together with proposed corrections for the mesh dependency of the results found in recent literature.

The last part of the chapter related to the comparison of the results for individual turbines between MIKE 21, experiments and CFD models. The aim was demonstrating that the energy dissipated by the turbine and the downstream wake were accurately modelled. First, the thrust force in the MIKE 21 model was compared with experimental values obtained in the study by Mycek et al. [2014] for a prototype of an axial flow turbine. Similarly, the flow conditions around the turbine were contrasted with experiments carried out by Bahaj et al. [2007] with a porous disk. Then, the same parameters (thrust force and flow field) from CFD models of the MRL turbine performed in Gebreslassie et al. [2015] and Gebreslassie et al. [2016] were compared with the results in the equivalent MIKE 21 simulations.

2.7.2 Conclusions

The main conclusion of this chapter is that the representation of individual turbines in MIKE 21 with the correction for mesh dependency described in subsection 2.4.2 is realistic to a large extent for the static conditions represented in laboratory and CFD tests.

This chapter shows that the agreement between the modelled thrust and the experiments and CFD is slightly better for the axial flow turbine than for the MRL turbine, maybe due to the fact that the correction applied to the turbine loading is based on the actuator disk theory. Regarding the comparison of the flow field results, the maximum differences between the MIKE 21 model and the

experiments and CFD are very similar for the axial flow device and the MRL design.

However, some limitations of the correction factor have been found related to the fact that in a real tidal flow its value will depend on the water levels, which change at each time step. Therefore, the correction factor would need to be implemented internally in future versions of the software.

Chapter 3

Idealised estuaries

3.1 Introduction

As can be seen from the report by McCall et al. [2007], in general, estuarine areas in the UK show the highest tidal ranges while the strongest tidal currents occur in offshore locations. However, some estuaries present tidal currents over 1 m/s and spring values over 2 m/s have been indicated by Liang et al. [2014] at certain locations within the Severn estuary. Macro-tidal estuaries, in which the tidal range is in excess of 4 m and tidal currents dominate the inter-tidal processes [EA & DEFRA, 2015], could benefit from the combined energy extraction from tidal stream and range resources. On the other hand, given the environmental relevance of the estuarine regions, the use of tidal technologies must be considered carefully. In that regard, an analysis of the effect of tidal schemes in the hydrodynamic behaviour of the estuary has to be done in the initial stages of the projects planning.

Analytical and numerical models have been used extensively to determine the hydrodynamic impacts of energy extraction in estuaries and coastal areas. Various examples about them were given in Chapter 1.4. Nevertheless, it must be highlighted that the results from these models are site-specific and depend on the bathymetry, boundary conditions, bed roughness and other intrinsic parameters, following I. Bryden et al. [2007]. Focusing on the geometrical

aspect, this Chapter aims to provide a better understanding about the effect that channel dimensions and also geometry have on the impact of tidal farms in estuaries.

The analysis followed is described in more detail throughout the Chapter but a brief overview is included here. First, several estuaries suitable for tidal energy extraction in the UK have been selected and classified according to their geometrical parameters. Idealised models based on the classified dimensions have been created and a sensitivity analysis has been performed over the variation of the geometrical parameters in those models. Finally, the results related to the impact on water levels have been analysed and some conclusions have been found in relation to the impact on flood risk levels and changes in intertidal habitats.

3.2 Classification of estuaries

Initially, the information in the report carried out by McCall et al. [2007] was used to identify the main estuaries in the UK with high tidal resource. The report distinguishes between locations with high tidal ranges and high tidal streams, as can be seen from figures 3.1 and 3.2.

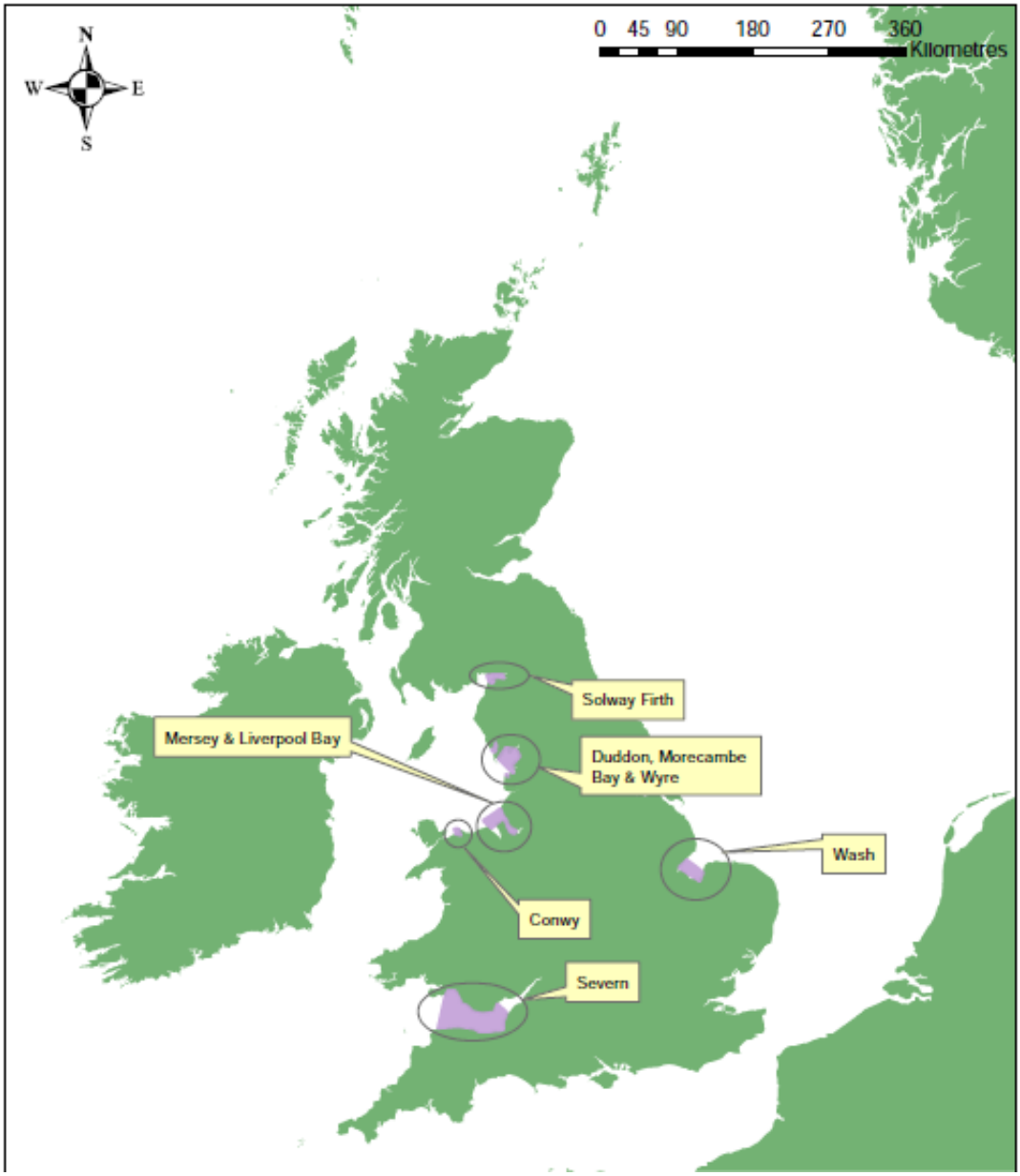

Figure 3.1: Tidal range resource locations.(Source: [McCall et al., 2007])

Figure 3.2: Tidal stream resource locations.(Source: [McCall et al., 2007])

Except for the Bristol Channel, most of the tidal stream resources are located in offshore areas whereas for the tidal range resources most of the locations are estuaries. However, tidal range schemes such as barrages or lagoons are not the only options for estuaries because tidal in-stream turbines could be also installed. Information extracted from ABPmer [2014] (figure 3.3) shows that in some estuaries current speeds at spring tides are in the order of 1m/s, reaching up to 2 m/s for the peak flows in a few cases.

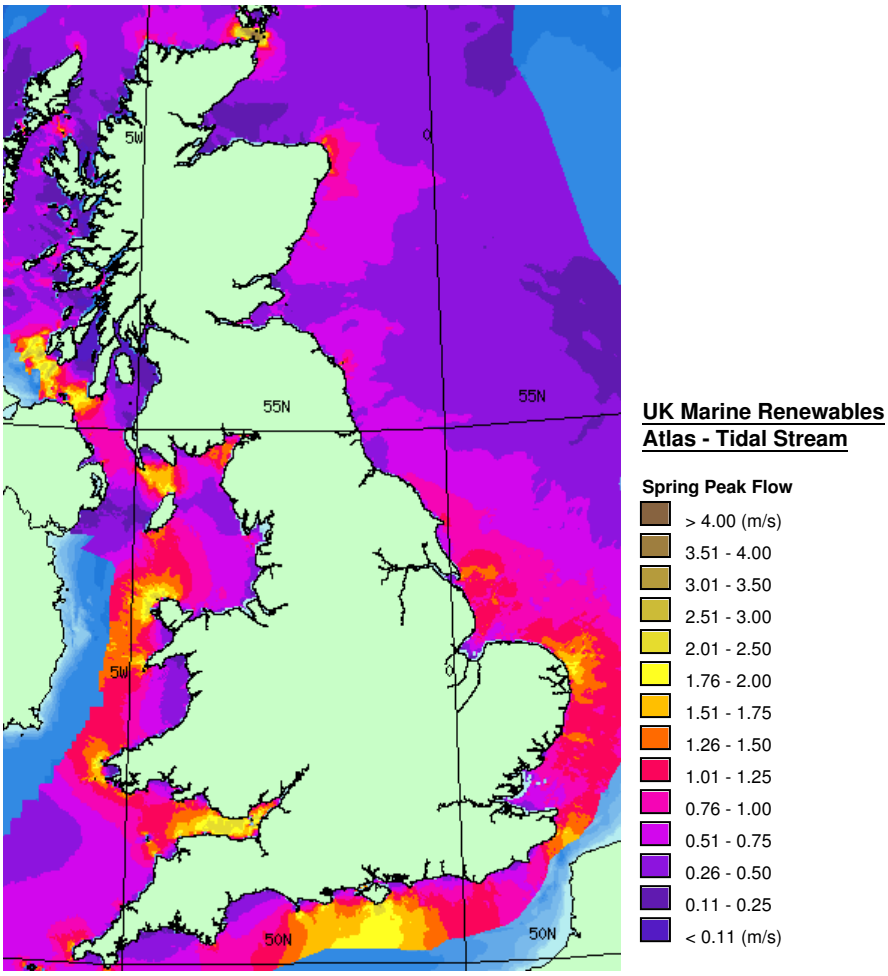

Figure 3.3: Spring peak velocities (m/s). Source: [ABPmer, 2014]

Apart from the estuaries included in figure 3.1, other macro-tidal estuaries were identified by means of EA & DEFRA [2015]. The list of the initial selection of estuaries obtained in this process can be found in table 3.1. Then, the peak flows existing in this group of estuaries were analysed with the information given by ABPmer [2014] and the existing literature ([Ahmadian et al., 2012], [Attrill, 1998], [CEFAS, 2008], [North West Coastal Group, 2012], [Flather & Heaps, 1975], [Aldridge, 1997], [Ridgway et al., 2012], [Scott, 1994], [Hofschreuder, 2012], [Y. Wu et al., 1999], [Shell, UK, 1987] and [EMEC, 2013]) in the cases where the aforementioned source did not have coverage. Information about tidal ranges of the estuaries has been obtained from EA & DEFRA [2015]. After the analysis of tidal ranges and velocities the main features for each estuary are

described in table 3.1.

Estuaries	Tidal range (m)	Maximum speed (m/s)	Literature
Severn	12.3	2.0	[Ahmadian et al., 2012]
Thames	6.5	1.4	[Attrill, 1998]
Medina	4.2	0.5	[CEFAS, 2008]
Ribble	7.9	1.5	[N.W.C.Group, 2012] and [ABPmer, 2003]
Duddon	8.1	1.2	[N.W.C.Group, 2012]
Morecambe Bay	8.4	1.0	[Heaps, 1975] and [Aldridge, 1997]
Mersey	8.9	2.0	[Ridgway et al., 2012]
Conwy	7.1	0.6	[Scott, 1994]
The Wash	6.5	1.2	[Hofschreuder, 2012]
Plymouth Sound	4.7	1.5	[Chen et al., 2012]
Humber Estuary	7.2	3.0	[Shell, 1987]
Solway Firth	8.4	2.5	[EMEC, 2013]

Table 3.1: Macro-tidal estuaries suitable for energy extraction in the UK. Initial selection.

Given the fact that the power is related to the velocity cubed, only the locations with current velocities above 1 m/s would be feasible for energy extraction. Therefore, the group of estuaries on which this analysis is focused result in the list shown in table 3.2. It has been taken into account that one of the aims pursued by some next generation tidal stream devices is to be able to operate under lower flow conditions in shallower waters.

The work by Draper et al. [2014] shows that the power potential of a tidal channel cannot be estimated solely on the basis of kinetic flux because it is referred to the undisturbed state without turbines and that two out of three parameters (flow rate, channel geometry and natural drag) would be necessary to calculate the power potential. In this case, the kinetic flux concept has been used as a tool for the initial assessment of potential resources given the complexity of characterising such parameters for all the estuaries considered in the study.

Estuaries	Tidal range (m)	Max current speed (m/s)
Severn	12.3	2.0
Thames	6.5	1.4
Ribble	7.9	1.5
Duddon	8.1	1.2
Morecambe Bay	8.4	1.0
Mersey	8.9	2.0
The Wash	6.5	1.2
Plymouth Sound	4.7	1.5
Humber Estuary	7.2	3.0
Solway Firth	8.4	2.5

Table 3.2: Tidal range and maximum speed of current (approximate value) in the selected estuaries.

3.3 Geometrical characterisation of estuaries

The importance of channel geometry was indicated by I. Bryden et al. [2007] in terms of the sensitivity of the channel to energy extraction and it was also highlighted by Draper [2011] in relation to the location of the optimal place for a tidal fence in order to maximise the available power in a non-enclosed bay. Therefore, a sensitivity analysis is conducted here about the influence of the geometry over the effect of a tidal array with the same size and number of turbines in all cases. The dimensions of the estuaries selected for this study were obtained from the literature and analysed to construct the generic cases that will be described in the next section. The dimensions considered in this study are the length as well as the widths and depths at the mouth and head of the estuary.

The length of the estuaries has been taken from Davidson & Buck [1997]), included in the study by Prandle [2010]. The width at the mouth has been also derived from the report by Prandle [2010]. Several studies have provided the values for the width at the head of the estuaries ([EA & DEFRA, 2015], [Xia et al., 2010a], [Attrill, 1998], [Scott, 1994], [Lane & Prandle, 2007], [Villars & Delvigne, 2001] and [Shell, UK, 1987]). The mean depth of the estuaries has been obtained from the data derived by Prandle [2010]. Formula 3.1 from Prandle [2010], which relates the mean depth to the depth at the mouth of the estuary, has been used to determine the values in the cases where this information was not available. These dimensions are grouped in table 3.3.

$$D_{mouth} = 1.8 D_{mean} \tag{3.1}$$

Estuaries	Length (km)	Width at mouth (m)	Width at head (m)	Mean depth (m)	Depth at mouth (m)	Depth at head (m)
Severn	111.2	6836	200	35.30	63.54	7.06
Thames	82.5	2191	90	24.10	43.38	4.82
Ribble	28.4	3129	-	4.90	8.82	0.98
Duddon	22.6	2094	50	4.60	8.28	0.92
Morecambe Bay	40.3	13493	-	4.40	7.92	0.88
Mersey	45.6	1706	150	15.80	28.44	3.16
The Wash	90.2	19360	50	11.60	20.88	2.32
Plymouth Sound	34.1	2533	20	8.30	14.94	1.66
Humber Estuary	144.7	7366	500	10.50	18.90	2.10
Solway Firth	46.3	7091	80	8.60	15.48	1.72

Table 3.3: Approximated main dimensions of the estuaries considered in this study. (- : information not available)

By analysing the dimensions shown in table 3.3, three ranges were defined (small, medium and large) for each parameter in the sensitivity analysis, as can be seen from table 3.4. The variation of the width and the depth over the length of the estuary (ΔW , ΔD) has been calculated according to equations 3.2 and

3.3.

Length (km)	Small	0 - 50
	Medium	50 - 100
	Large	100 - 150
Width at the mouth (m)	Small	0 - 7000
	Medium	7000 - 14000
	Large	14000 - 21000
Depth at the mouth (m)	Small	0 - 20
	Medium	20 - 40
	Large	40 - 60
Width variation (1/km)	Small	0 - 0.0007
	Medium	0.0007 - 0.0014
	Large	0.0014 - 0.0021
Depth variation (1/km)	Small	0 - 0.0016
	Medium	0.0016 - 0.0032
	Large	0.0032 - 0.0048

Table 3.4: Ranges of dimensions, based on the estuaries analysed in this study

$$\Delta W = \frac{W_H}{W_M L} \tag{3.2}$$

$$\Delta D = \frac{D_H}{D_M L} \tag{3.3}$$

where the subscripts H and M relate to the head and the mouth of the estuary, respectively, and L refers to the total length of the estuary.

Based on the ranges of values shown in table 3.4, fifteen different synthetic geometries (case 1.a to case 3.iii) were created for the sensitivity analysis, that is, varying one of the parameters while fixing the rest.

3.3.1 Longitudinal depth and width variation

Two more geometries (cases 3.i-ii and 3.ii-iii), related to the longitudinal depth variation, were included afterwards, in order to provide a more detailed analysis. As will be explained in the next sections, this parameter had a higher influence on the water levels than others.

3.3.2 Cross section influence

The aforementioned geometries present rectangular cross sections or vertical walls on both sides of the channel. However, it is expected that the shape of the cross section will also have some influence in the results. Therefore, another six cases (case 4.a to case 5.c) were defined, covering rectangular, trapezoidal or triangular shapes of the cross section. In these cases, either the width or the depth were fixed and three different sizes of the lateral slopes in the channel walls were used with the same cross sectional area. The lateral slope here is calculated as the ratio between the horizontal and vertical dimensions, therefore a smaller slope means that the sides are closer to a vertical wall.

Finally, three more cases (case 6.a to case 6.c) were defined based on the triangular cross section representing different lateral slopes with the same area. Triangular cross sections have been previously used by S.-N. Chen & Sanford [2009b] and S.-N. Chen & Sanford [2009a] in numerical models of idealised estuaries.

3.3.3 Resonant case

In the analysis carried out by Draper [2011] for non-enclosed bays by means of a 1D simplified analytical model, it was indicated that an increase in the tidal range could happen in those cases on a length scale larger than the resonant length when a fence is deployed at one quarter of the wave-length (λ) from the mouth of the bay. This idea is extracted from a model which neglects bed friction and considers a rectangular shape of the bay. All the rectangular geometries

described previously (cases 1.a to 1.c, 2.a to 2.c and 3.a to 3.c) are shorter than their theoretical resonant length ($\lambda/4$) and so would be non-resonant according to the $\lambda/4$ theory. Therefore, it was found of interest to create a geometry long enough to test the idea given in Draper [2011] with a tidal farm in MIKE 21.

Based on the depth and width values used in case 1.b (D = 30 m, W = 10.5 km) the resonant length ($\lambda/4$) has been calculated according to the following formula from Prandle [2009]:

$$\lambda = Per(gD)^{1/2} \tag{3.4}$$

where Per is the tidal period and D is the depth.

In this case the tidal period for the principal lunar semi-diurnal constituent or M2 (12.42 h) has been considered and the resonant length was approximately 192 km. Therefore, the length of the resonant case has been set to 250 km, which is bigger than the resonant length where the tidal farm will be positioned.

3.3.4 Solway Firth case

An idealised model of the Solway Firth estuary has been carried out, based on the dimensions given in table 3.3:

- Length = 46.3 km
- Width at mouth = 7091 m
- Width at head = 80 m
- Depth at mouth = 14.94 m
- Depth at head = 1.72 m

The purpose is to compare the results from this model with a fully detailed numerical model of the estuary, which will be described in Chapter 5.

3.3.5 List of geometrical cases

A complete list of all the geometrical parameters for every case used in the sensitivity analysis of the geometry is shown in table 3.5.

Case	Length (km)	Width at mouth (m)	Width variation (1/km)	Depth at mouth (m)	Depth variation (1/km)	Lateral slope (1/m)	Cross section
1.a	**25**	10500	0.0000	30	1.0000	0.000	Rectangular
1.b	**75**	10500	0.0000	30	1.0000	0.000	Rectangular
1.c	**125**	10500	0.0000	30	1.0000	0.000	Rectangular
2.a	75	**3500**	0.0000	30	1.0000	0.000	Rectangular
2.b	75	**10500**	0.0000	30	1.0000	0.000	Rectangular
2.c	75	**17500**	0.0000	30	1.0000	0.000	Rectangular
2.i	75	10500	**0.0018**	30	1.0000	0.000	Rectangular
2.ii	75	10500	**0.0011**	30	1.0000	0.000	Rectangular
2.iii	75	10500	**0.0004**	30	1.0000	0.000	Rectangular
3.a	75	10500	0.0000	**10**	1.0000	0.000	Rectangular
3.b	75	10500	0.0000	**30**	1.0000	0.000	Rectangular
3.c	75	10500	0.0000	**50**	1.0000	0.000	Rectangular
3.i	75	10500	0.0000	30	**0.0040**	0.000	Rectangular
3.i-ii	75	10500	0.0000	30	**0.0032**	0.000	Rectangular
3.ii	75	10500	0.0000	30	**0.0024**	0.000	Rectangular
3.ii-iii	75	10500	0.0000	30	**0.0016**	0.000	Rectangular
3.iii	75	10500	0.0000	30	**0.0008**	0.000	Rectangular
4.a	75	10500	0.0000	**60**	1.0000	**87.500**	Triangular
4.b	75	10500	0.0000	**40**	1.0000	**65.625**	Trapezoidal
4.c	75	10500	0.0000	**30**	1.0000	**0.000**	Rectangular
5.a	75	**21000**	0.0000	30	1.0000	**350.000**	Triangular
5.b	75	**15750**	0.0000	30	1.0000	**175.000**	Trapezoidal
5.c	75	**10500**	0.0000	30	1.0000	**0.000**	Rectangular
6.a	75	**21000**	0.0000	**30**	1.0000	**350.000**	Triangular
6.b	75	**16601**	0.0000	**38**	1.0000	**218.750**	Triangular
6.c	75	**10500**	0.0000	**60**	1.0000	**87.500**	Triangular
Resonant	**250**	10500	0.0000	30	1.0000	0.000	Rectangular

Table 3.5: Dimensions for the different geometries used in the sensitivity analysis (bold numbers indicate the parameters that are not fixed on each case).

Note that some of the cases are equivalent (have the same dimensions) and they have been included in the list for the purpose of comparison in the sensitivity analysis.

3.4 Idealised models

Based on the geometries described in the previous section, idealised models of the estuaries were built in MIKE 21 in order to evaluate the changes introduced by a tidal farm on each case. As it was mentioned in subsection 1.4.4, there are benefits in the use of idealised models in terms of the reduced computational demand and the ease of identification of physical trends [Hunt et al., 2015]. In this study, given the numerous cases which need to be tested, idealised models provide a good solution compared to more detailed models.

In subsection 1.4.4, examples of numerical models of idealised estuaries can be found, several of them being related to morpho-dynamic studies while the more recent ones explore the introduction of energy extraction. However, there are no previous studies about the effect of geometry on the impact of energy extraction in estuaries using 2D numerical models. The only study which gives some insight into the subject is the Chapter related to non-enclosed oscillating bays in the PhD thesis by Draper [2011], where a 1D analytical model has been used to describe the phenomena in relation to tidal fences.

3.4.1 Models set-up

Regarding the details about the numerical model (MIKE 21), used to create the simulations of the idealised estuaries, a full description can be found in section 2.1

The geometries given in table 3.5 as well as the dimensions of the Solway Firth estuary in table 3.3 were used to define the boundaries of the domain and the bathymetry over which the computational mesh is constructed. The other features of the models were the same in all cases. Rectangular cell elements were used in the unstructured flexible mesh, with a maximum size of 1 km^2. The simulation, carried out in MIKE 21 Flow model FM (version 2012), covered a period of 6 days. The maximum and minimum time steps were set to 900 and 0.01 seconds, respectively, and the Courant-Friedrich-Levy (CFL) number was

limited to a maximum value of 0.8. The relationship between time step and CFL number was given in equation 2.9. Both the time and spatial discretisation of the shallow water equations were performed using a higher order scheme.

In order to remove the cells from the calculation when the depth is very small (dry elements), a flood and dry function was activated in all the models. The parameters defining this function consisted of a drying depth of 0.005 m, a flooding depth of 0.05 m and a wetting depth of 0.1 m.

A uniform bed roughness was used over the domain, given by an inverse value of the Manning coefficient equal to 40 $m^{1/3}/s$, related to a sandy type of seabed, which has been taken as an indicative value for every model. Two models were run without bed roughness, one of them based on the geometry of case 1.b and the other representing the resonant case, in order to replicate the conditions used in the study by Draper [2011] and allow the comparison of the results. Regarding the turbulence scheme, a constant Smagorinsky's coefficient of 0.28 was used throughout the domain, taken from the recommendations in DHI [2012a]. Given the simplified nature of the idealised models, the Coriolis force was not included in the simulations.

Regarding the specifications at the boundaries, these were similar to the ones applied in the study by Draper [2011] for the non-enclosed bay model. A description of the different boundary options available in MIKE 21 was given in Chapter 2. At the open sea boundary, the conditions consisted of a zero velocity and a tidal curve approximated as a cosine function of the M2 tide with an amplitude of 9 m. The Flather condition, available in MIKE 21, was selected, considering the appropriateness of transmissive boundaries for the avoidance of error waves reflected by the tidal farms [Baston et al., 2015]. Accordingly, the river discharges were not included in the models.

3.4.2 Tidal farms

Details about the representation of tidal turbines in MIKE 21 can be found in section 2.4. In this study, the same tidal farm has been used in every model

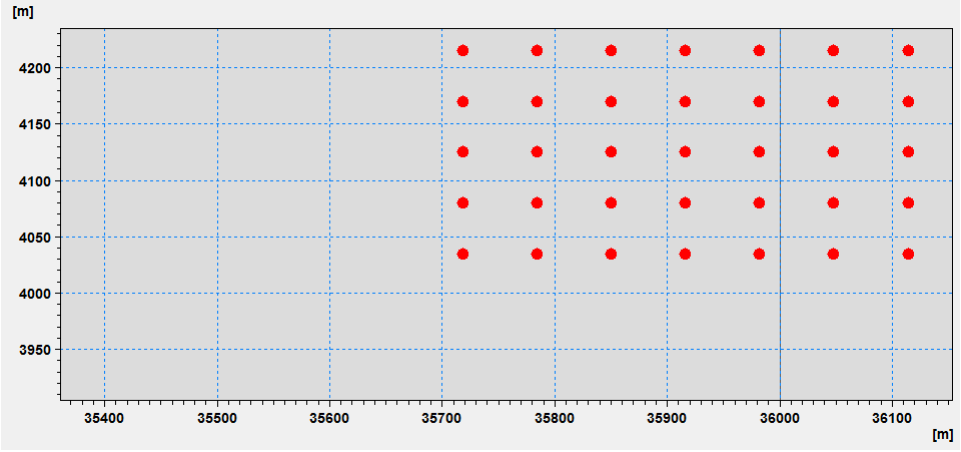

Figure 3.4: Detail of tidal turbines arranged in a parallel configuration

to allow comparing the effect of the geometry on the results. The tidal farm consisted of 3025 turbines distributed in 55 rows by 55 columns under a parallel configuration, as can be seen from figure 3.4. The farm was installed in the central area of each model except for the resonant case, where it was located at one quarter of the wavelength distance from.the mouth.

The MRL turbine design has been chosen because it presents some advantages, such as the adaptability of the floating support structure to the water levels and the suitability of its dimensions to shallower areas. The MRL turbine was described in subsection 2.6.1. The turbine diameter has been limited to 6 m, which corresponds to 70 % of the water column for the minimum depth (8.6 m) recorded at the model without turbines in the shallowest case. The length of the turbine is 30 m, according to a hypothetic value of 1:5 for the aspect ratio of a commercial device mentioned by the developers. Considering a power coefficient of 0.5 [Gebreslassie, 2012], the maximum installed capacity of the farm would be approximately 1.1 GW in the case of a peak current speed of 2m/s.

Within the array, the lateral spacing between the edges of the turbines was set to 0.5 times the turbine length whereas the longitudinal spacing between consecutive rows of turbines was 10 times the turbine diameter. The lateral spacing value was suggested by the main author of Gebreslassie et al. [2013b]

as the minimum distance that could allow the flow to pass between the turbines. The longitudinal spacing was based on the values given by Gebreslassie et al. [2015] for a group of seven turbines. The idea here was to represent a closely packed configuration.

Regarding the turbines parameters in MIKE 21, an equivalent diameter of 15.14 m was introduced in the model, which provides the same frontal area as a rectangle of 6x30 m in the MRL turbines. In terms of the resistance of the turbines to the flow, a drag coefficient of 0.9 has been applied, based on the information from Gebreslassie [2012]. This value is in agreement with experiments carried out in the studies by Bachant & Wosnik [2014] and Bachant & Wosnik [2015] for other cross-flow designs, such as the Vertical axis turbine UNH-RVAT and the Gorlov Helical Turbine (GHT). For simplicity, a fixed drag coefficient and zero lift coefficient were applied. Regarding the correction factor α from equations 2.16 and 2.17, it was set equal to an initial value of 1.0. However, in order to evaluate the effect of the drag coefficient in the results, four more cases were used based on the geometry of case 1.b with different drag coefficients (1.0, 2.0, 5.0 and 10.0). Although the larger values can be regarded as unrealistic the purpose here is to delimit the influence of the drag coefficient.

3.5 Results

3.5.1 Maximum changes in high and low tides

Before comparing the water levels between the models with and without turbines, the results for the last half of the simulation were extracted, in order to account for the warm-up period. Then the statistical analysis tool in MIKE 21 was used to calculate the maximum and minimum values of the water levels (high and low tides) in the domain. Following this, the differences between the water levels for the high and low tides in the situations without turbines and with the tidal farm were calculated for each case. An example of these differences calculated for case 1.a can be found in figure 3.5. The plots for all the cases can be found

in Appendix B. The analysis of the differences between water levels allowed determining the maximum increase and decrease in the water levels over the domain with and without turbines present, which are summarised for each case in table 3.6.

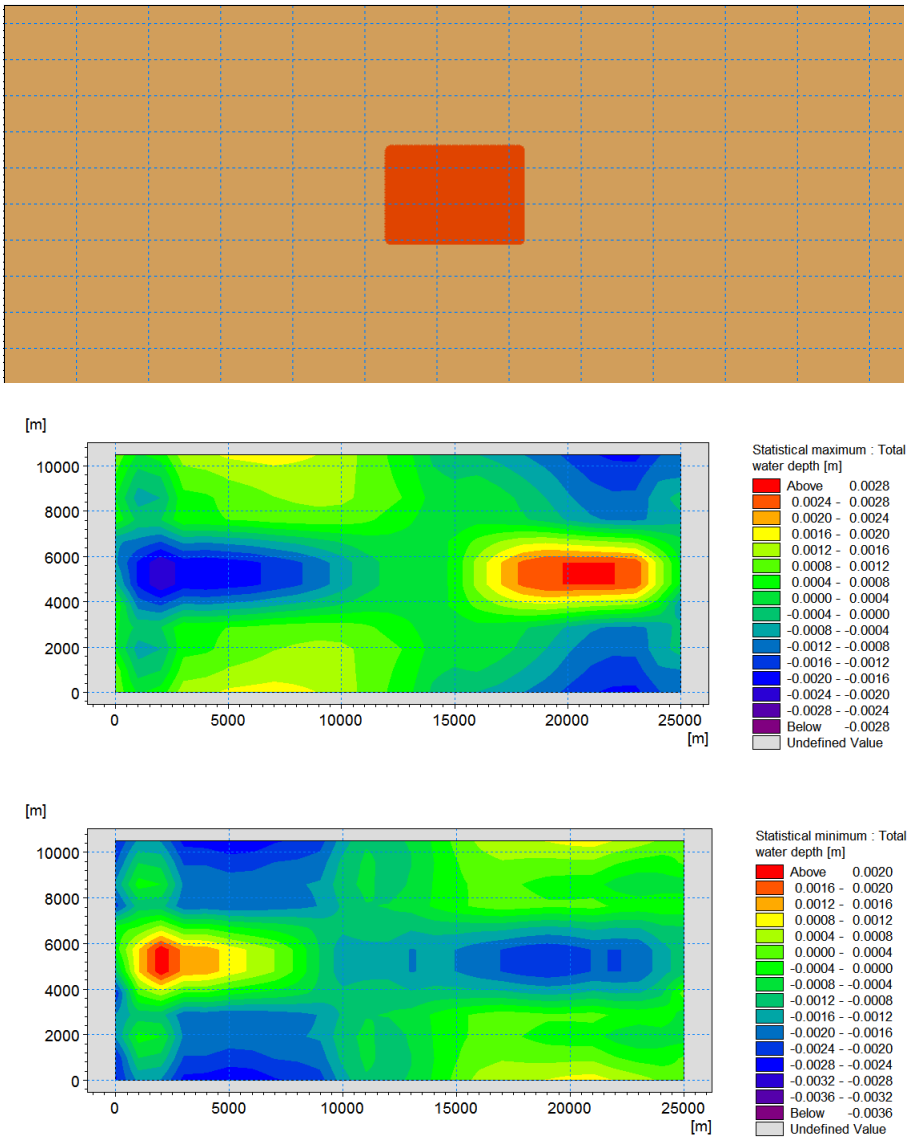

Figure 3.5: Case 1.a / Upper image: Computational domain and tidal farm; Central image: Difference in high water levels with and without turbines present; Lower image: Difference in low water levels with and without turbines present.

Case	Difference low tides (m)		Difference high tides (m)	
	Max increase	Max decrease	Max increase	Max decrease
1.a	0.003	0.004	0.003	0.003
1.b	0.026	-	-	0.019
1.c	0.038	0.011	0.016	0.046
2.a	0.133	-	-	0.124
2.b	0.026	-	-	0.019
2.c	0.016	-	-	0.013
2.i	0.017	-	0.006	0.006
2.ii	0.015	-	0.005	0.005
2.iii	0.013	0.002	0.004	0.005
3.a	0.052	0.020	0.080	0.051
3.b	0.026	-	-	0.019
3.c	0.007	0.002	0.002	0.004
3.i	0.102	0.007	-	0.076
3.i-ii	0.122	0.008	-	0.084
3.ii	0.142	0.007	-	0.089
3.ii-iii	0.160	0.006	-	0.090
3.iii	0.178	0.005	0.012	0.091
4.a	0.054	0.002	-	0.040
4.b	0.043	0.003	-	0.031
4.c	0.026	-	-	0.019
5.a	0.077	0.033	0.046	0.063
5.b	0.076	0.014	-	0.200
5.c	0.026	-	-	0.019
6.a	0.077	0.033	0.046	0.063
6.b	0.072	0.023	-	0.142
6.c	0.054	0.002	-	0.040

Table 3.6: Maximum differences (m) in tide levels with and without turbine present over the models domain.

For the geometries with different longitudinal depth variation (cases 3.i to 3.iii) the results were plotted in figure 3.6. It can be seen that the effect over the increase of low tide levels is bigger than the one for the high tides and it follows

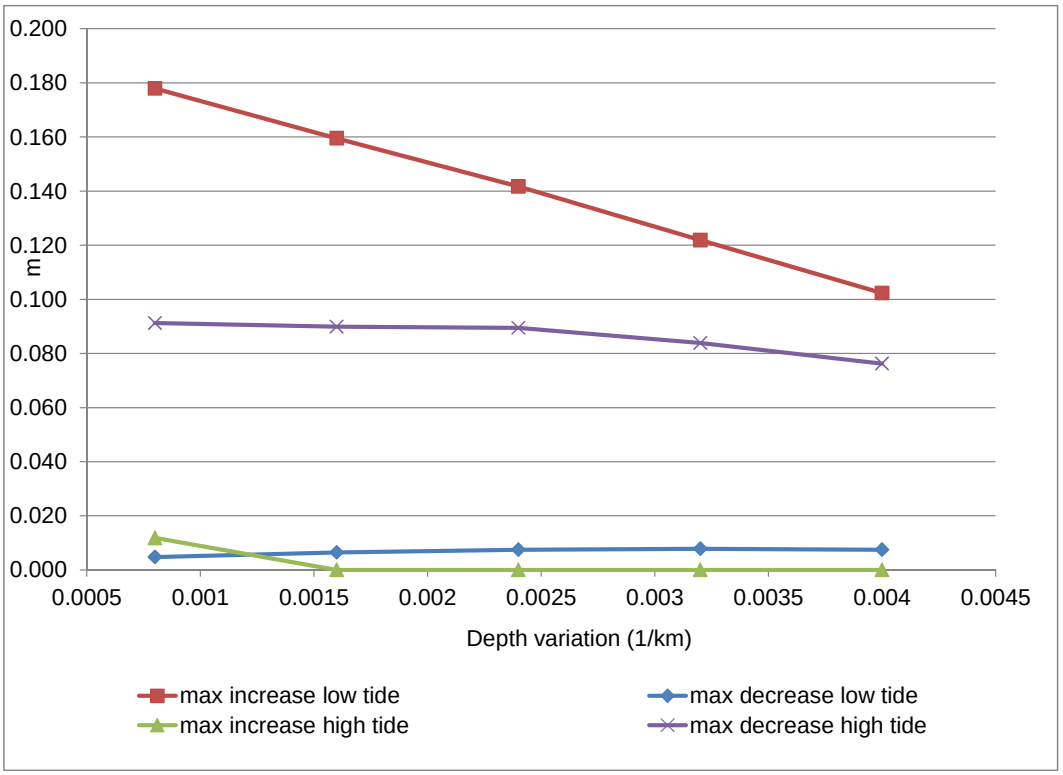

Figure 3.6: Maximum differences (m) in tide levels with and without turbine present, for cases with longitudinal depth variation

an almost linear variation.

Locations of maximum changes in high and low tides

Another aspect that has been addressed is the analysis of the locations where the maximum increase and decrease happen both for the low and high tides with and without the turbines present. This would be an important subject during the planning for the deployment of tidal farms in places with environmental issues or other kind of constraints. Those locations have been given for each case in table 3.7 in the form of an Index, following the scheme of the estuary in figure 3.7.

Case	Difference low tides - location		Difference high tides - location	
	Max increase	Max decrease	Max increase	Max decrease
1.a	I	O	O	I
1.b	D	-	-	S
1.c	D	O	M	S
2.a	I	-	-	M
2.b	D	-	-	S
2.c	D	-	-	S
2.i	S	-	I	S
2.ii	S	-	I	S
2.iii	S	H	I	S
3.a	D	U	O	S
3.b	D	-	-	S
3.c	O	S	U	S
3.i	D	M	-	M
3.i-ii	D	M	-	M
3.ii	D	M	-	S
3.ii-iii	F	M	-	S
3.iii	F	M	M	S
4.a	U	E	-	M
4.b	D	U	-	M
4.c	D	-	-	S
5.a	D	M	M	O
5.b	D	M	-	M
5.c	D	-	-	S
6.a	D	M	M	O
6.b	D	M	-	M
6.c	U	M	-	M

Table 3.7: Locations of the maximum increase and decrease of high and low tide levels within the estuary. (figure 3.7 defines the meaning of the capital letters).

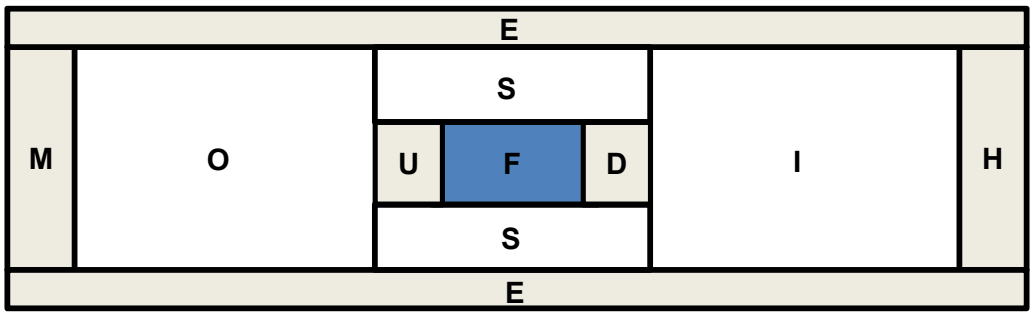

Figure 3.7: Scheme of the estuary (M: mouth of the estuary; O: outer area; U: area upstream the farm; F: tidal farm: S: sides of the farm; D: area downstream the farm; I: inner area; H: head of the estuary; E: edges of the estuary)

3.5.2 Changes in time for high and low tides

Changes due to the presence of the tidal farm to the times when the high and low tides happen is another aspect that can be evaluated, given its potential impact on navigational activities in some of the estuaries. For this purpose, the time series of the water levels over the last half of the simulation were obtained at a point located on the longitudinal axis at a distance of one quarter of the length from the head of the estuary. From the study carried out by Fallon et al. [2014] on the effect of tidal turbine arrays in the Shannon estuary it can be seen that changes in times of low and high tides were more noticeable at the inner part of the estuary.

The results from the idealised models presented here showed that there was no appreciable change in time for the high and low tides. The occurrence of the high and low tides at the same time for the situations with and without tidal farm has been checked in a spreadsheet. As an example, the results for case 1.b have been plotted in figure 3.8.

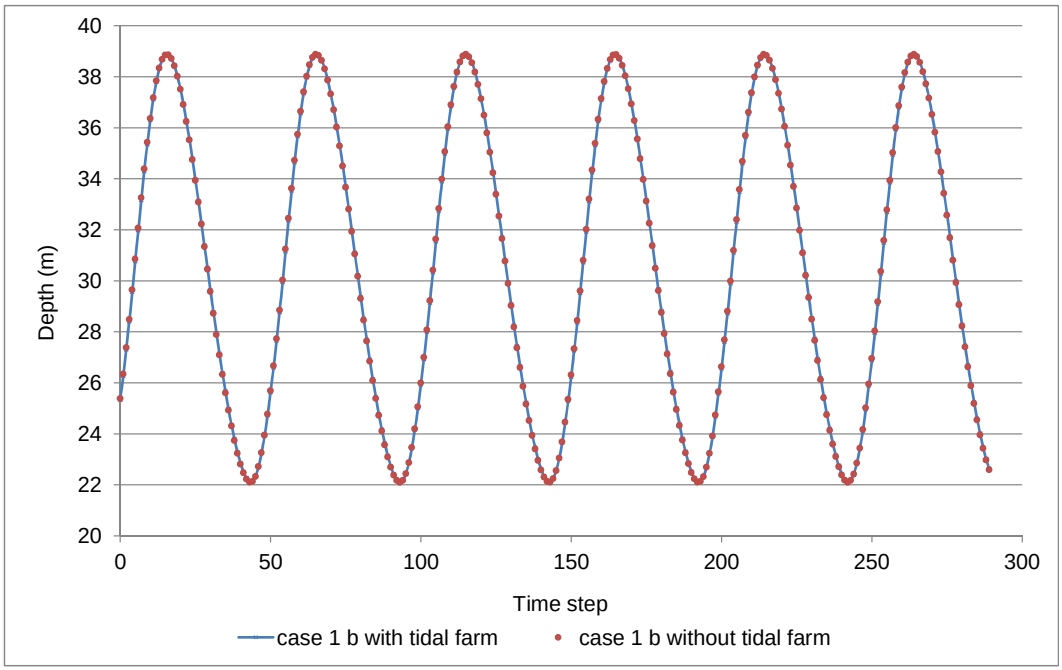

Figure 3.8: Water level time series for Case 1.b with and without the tidal farm present, at (x,y)= (3L/4, W/2), where L is the estuary length and W the estuary width.

3.5.3 Influence of drag coefficient

As it was mentioned, a group of simulations were run with the same geometry but a different drag coefficient of the turbines, in order to study the influence of this parameter on the results. The maximum increase and decrease in the low and high tide levels due to the effect of the tidal farm were identified. These results can be found in table 3.8 and a plot is provided in figure 3.9 to visualise the trend of each change.

Case	Difference low tides (m) Max increase	Max decrease	Difference high tides (m) Max increase	Max decrease
1.b Cd 0.9	0.026	-	-	0.019
1b Cd 1.0	0.027	-	-	0.020
1b Cd 2.0	0.034	-	-	0.029
1b Cd 5.0	0.044	-	0.010	0.042
1b Cd 10.0	0.056	-	0.020	0.053

Table 3.8: Maximum increase and decrease of low and high tide levels with a tidal farm with different drag coefficient for the turbines in case 1.b.

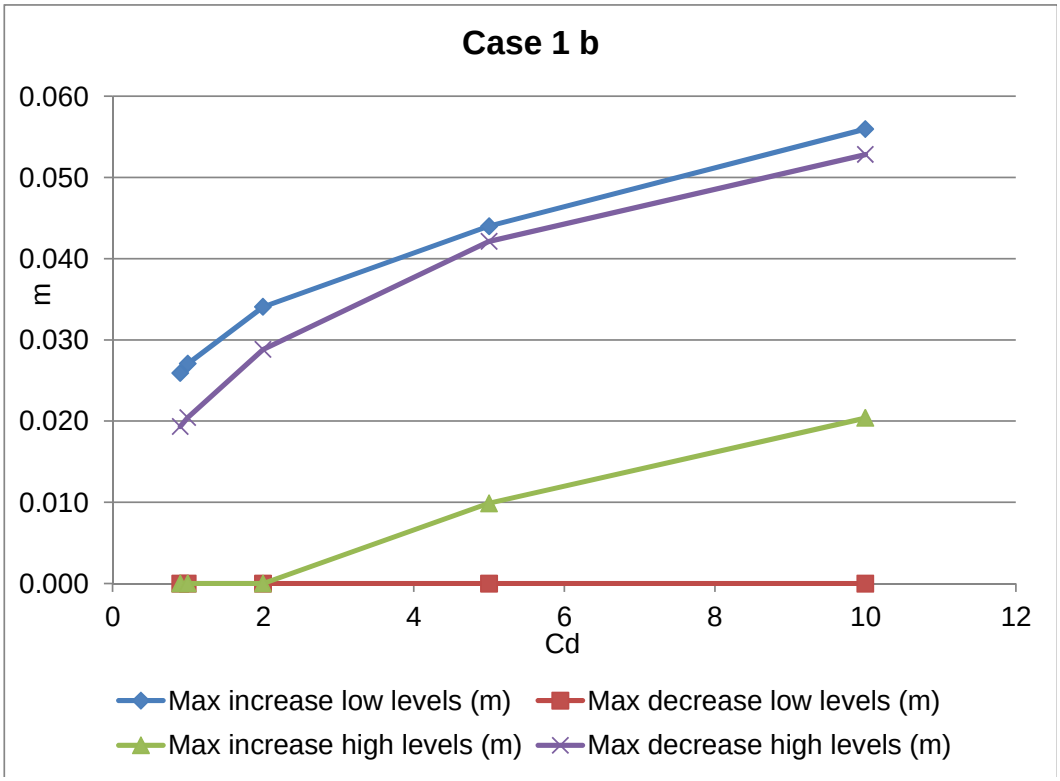

Figure 3.9: Maximum increase and decrease of low and high tide levels in case 1.b with different drag coefficients of the turbines in the tidal farm.

3.5.4 Resonant case

As it was explained previously, two cases without bed friction have also been tested: a case with non-resonant length based on case 1.b and a resonant case.

Initially, the results for the water elevations and currents at a point located at one quarter of the total length of the estuary from the mouth were extracted from the models without turbines in order to observe the resonance effects. The aforementioned time series can be seen in figures 3.10 and 3.11. In the resonant case there is a clear phase shift of the current speed and the maximum and minimum values of the elevations are not coincident with current speed zero, as in the non-resonant case.

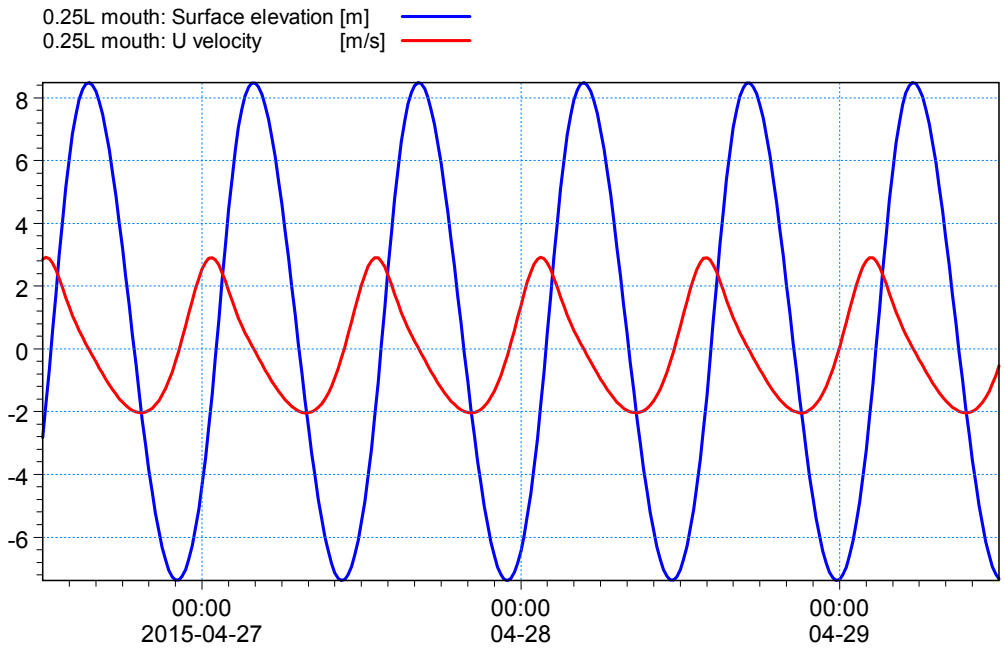

Figure 3.10: Surface elevation (m) and current speed (m/s) at a point located at L/4 from the mouth in the axis of the estuary in case 1b (non-resonant) without friction

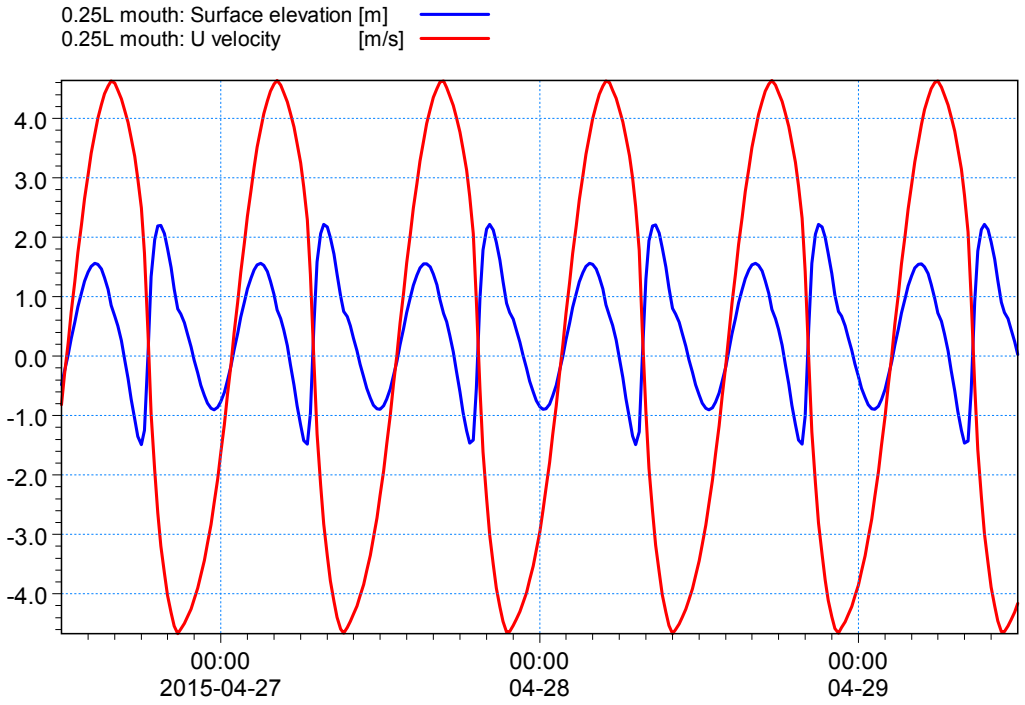

Figure 3.11: Surface elevation (m) and current speed (m/s) at a point located at L/4 from the mouth in the axis of the estuary in the resonant case without friction

As for the other cases, the maximum changes in high and low water levels were obtained. The results can be found in table 3.9.

Case (no bed friction)	**Difference low tides (m)**		**Difference high tides (m)**	
	Max increase	**Max decrease**	**Max increase**	**Max decrease**
1.b	0.023	-	0.015	0.013
Resonant	0.200	0.015	0.030	0.130

Table 3.9: Maximum increase and decrease of low and high tide levels with a tidal farm in case 1.b. (non-resonant) and the resonant case without bed friction.

The maximum changes in tidal range for both cases have also been calculated, as shown in table 3.10 and plotted in figures 3.12 and 3.13 in order to contrast the effect with the ideas mentioned by Draper [2011] for a tidal fence, as will be explained in the next section.

Case (no bed friction)	Difference tidal range (m) Max increase	Max decrease
1.b	0.004	0.028
Resonant	-	0.316

Table 3.10: Maximum increase and decrease of tidal range with a tidal farm in case 1.b (non-resonant) and the resonant case without bed friction.

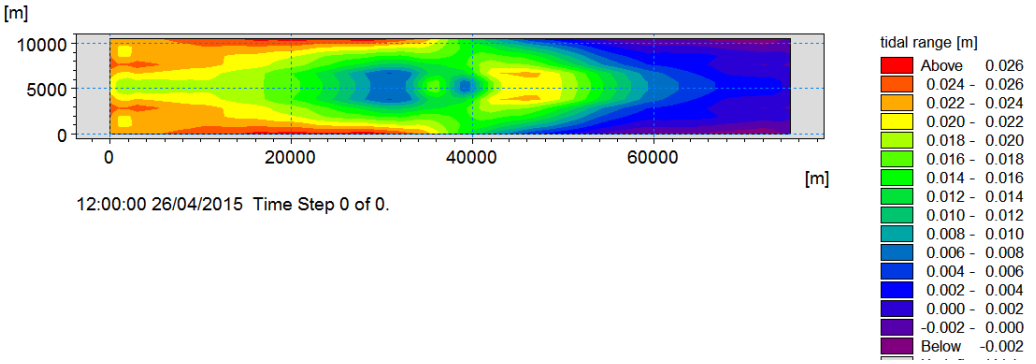

Figure 3.12: Changes in tidal range in case 1.b due to a tidal farm deployed in central location.

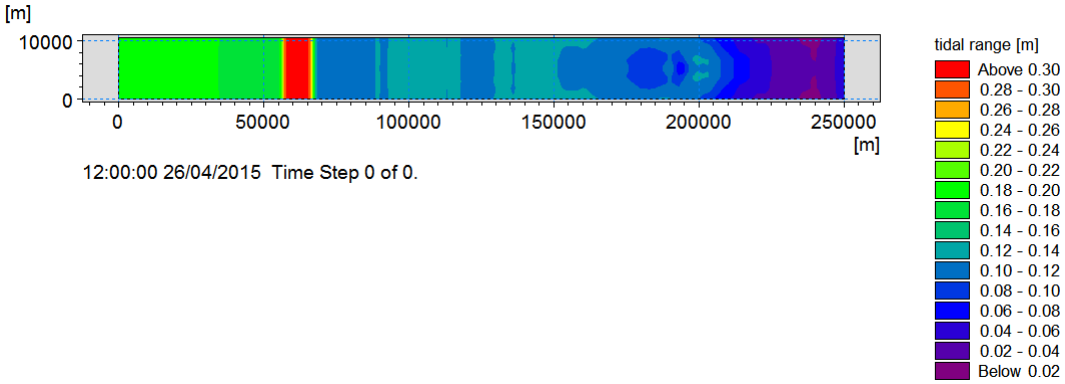

Figure 3.13: Changes in tidal range in the resonant case due to a tidal farm deployed at one quarter of the wavelength from the mouth of the estuary.

3.5.5 Solway Firth case

The maximum differences in low and high tide levels with and without turbines present and the locations where these changes happen have been calculated in the same way as in the other cases considered in this study. Those results can be found in table 3.11 and they will be contrasted with results from a highly detailed numerical model of the estuary in Chapter 5.

	Difference low tides		**Difference high tides**	
	Max increase	**Max decrease**	**Max increase**	**Max decrease**
Max changes (m)	0.014	0.667	0.076	0.418
Locations	I	F	M	H

Table 3.11: Maximum changes of low and high tide levels due to a tidal farm and their locations

3.6 Discussion of the Results

The results for each case in terms of maximum changes to the high and low tidal levels from table 3.6 are included in table 3.12 with a colour scale indicating the highest values with the darkest colour for each column to facilitate the discussion of the results.

Case	Difference low tides (m)		Difference high tides (m)	
	Max increase	Max decrease	Max increase	Max decrease
1.a	0.003	0.004	0.003	0.003
1.b	0.026	-	-	0.019
1.c	0.038	0.011	0.016	0.046
2.a	0.133	-	-	0.124
2.b	0.026	-	-	0.019
2.c	0.016	-	-	0.013
2.i	0.017	-	0.006	0.006
2.ii	0.015	-	0.005	0.005
2.iii	0.013	0.002	0.004	0.005
3.a	0.052	0.020	0.080	0.051
3.b	0.026	-	-	0.019
3.c	0.007	-	0.002	0.004
3.i	0.102	0.007	-	0.076
3.i-ii	0.122	0.008	-	0.084
3.ii	0.142	0.007	-	0.089
3.ii-iii	0.160	0.006	-	0.090
3.iii	0.178	0.005	0.012	0.091
4.a	0.054	0.002	-	0.040
4.b	0.043	0.003	-	0.031
4.c	0.026	-	-	0.019
5.a	0.077	0.033	0.046	0.063
5.b	0.076	0.014	-	0.200
5.c	0.026	-	-	0.019
6.a	0.077	0.033	0.046	0.063
6.b	0.072	0.023	-	0.142
6.c	0.054	0.002	-	0.040

Table 3.12: Maximum changes of water levels at low and high tides due to a tidal farm (darker colours: higher values)

From an initial analysis of the results in terms of each geometrical dimension, it can be generally noted that:

- The effects of length are inverse to those from width or depth. The magnitude of the maximum changes in the estuary increase with increasing length and decrease with increasing width and depth.
- Longitudinal width variation has a smaller effect on the maximum increase

of low tides than the equivalent case with constant width (case 2.b).

- Longitudinal depth variation has a stronger overall effect on the maximum changes than the case with constant depth (case 3.b).

- A smaller lateral slope gives higher maximum changes over low and high tidal levels than a steep slope.

From a deeper analysis, focusing on the results for the increase and decrease of low and high tidal levels separately (columns in tables 3.7 and 3.12), it was observed that:

- Regarding the maximum increase in low tidal levels, the most relevant change appears in case 3.iii at the inner area and downstream of the farm, being of the order of 18 cm. Case 2.a, which relates to the narrowest case in the study, also shows a significant value of the maximum increase in low tides, reaching up to 13 cm in the outer area of the estuary. Basically, longitudinal depth variation and width have stronger effects than the other parameters over the increase of low tidal levels, which can be associated with the permanent submersion of intertidal areas.

- In relation to the maximum decrease of low tidal levels, the highest value (approx. 3 cm) happens in cases 5.a and 6.a at the mouth of the estuary. These cases present a more horizontal lateral slope. It can also be noticed that in some other cases the value of the decrease is almost imperceptible. One of the implications of a decrease of the low tidal levels would be the increase of the extension of intertidal areas.

- The increase of high tidal levels would have consequences for the flood risk and the extension of intertidal areas. In this regard, the overall highest value (8 cm) appears in the outer area of the shallowest case (case 3.a) followed by cases 5.a and 6.a, with approximately 5 cm for the maximum value happening at the mouth of the estuary. The rest of the cases have small changes in this sense.

- In reference to the maximum decrease over the high tidal levels, case 5.b (trapezoidal cross section) reaches 20 cm at the mouth of the estuary, which is the absolute maximum change in all situations. Case 6.b also shows a significant maximum decrease in the mouth of the estuary (approximately 14 cm). On the other hand, the width of the estuary seems to have some impact, being the effect at the inner part in case 2.a (narrowest case) higher than in cases 2.b and 2.c. The decrease of high tidal levels would imply the reduction of intertidal areas, which become permanently dry areas.

Although some of the locations where the highest changes appear have been commented on in the previous paragraph, there are other conclusions which can be extracted from table 3.7:

- In general, when one of the parameters is varied, the maximum effects seem to move to different parts of the estuary. For example, in cases 1.a and 1.c the maximum increase of low tidal levels and decrease of high tidal levels move from the outer part to different locations, including both sides of the tidal farm.

- In cases with longitudinal variation of the width and depth (cases 2.i to 2.iii and 3.i to 3.iii), the maximum changes usually happen in different areas to those in the equivalent case with a constant depth or width over the length.

- Counting the number of times in table 3.7 that each location from figure 3.7 registers a maximum change it was found that most of them happen at the mouth of the estuary, followed by the outer part and the area upstream the tidal farm. In the cases with triangular and trapezoidal cross sections these maximum changes happen more commonly at the mouth of the estuary.

3.6.1 Changes in time for low-high tides

From the analysis of the time series extracted at a point located at L/4 distance from the estuary head in all cases it has been found that the high and low tides

occur during the same time step with and without the tidal farm. The time step used for the results was 15 minutes, therefore any change is less than this value.

3.6.2 Influence of the drag coefficient of the turbines

By comparing the results from the cases based on case 1.b with different values of the drag coefficient, it seems that the maximum increase in low levels and decrease in high levels follow a similar trend (see figure 3.9) and there is no noticeable decrease in low levels for any case.

3.6.3 Resonant case

From comparing the results relating to the maximum changes in high and low tides between the resonant and non-resonant cases without bed friction it can be noticed that the most significant increase happens for the low tides in the resonant case, which would be associated with the permanent inundation of some regions previously regarded as inter-tidal areas. In reference to the high tides, the effect is stronger for the maximum reduction of water levels. This could be regarded as beneficial in terms of the flood risk.

In relation to the effects on tidal range, it can be seen that there is no increase of the tidal range in the resonant case whereas in the non-resonant case it was rather small (order of mm). However, the reduction of tidal range is significant in the resonant case (close to 30 cm). These results are different from the ones derived by Draper [2011] from its analytical model with a tidal fence. Several aspects could have an influence on that difference. For example, the fact that here a 2D model has been used instead of a 1D model and that the tidal farm concept is a block array rather than a tidal fence consisting of one row crossing the entire width of the estuary.

3.6.4 Solway Firth case

From the results of the idealised model of the Solway Firth estuary, given in table 3.11, it can be seen that the most significant effect of the turbines is the decrease of low tide levels within the farm itself. This would lead to the creation of new intertidal areas. The other important effect is the decrease of high tide levels at the head of the estuary, which would provoke loss of intertidal areas and would also have positive effects for the flood risk levels at this part of the estuary.

A validation of these results with a more realistic model of the estuary will be presented in Chapter 5.

3.7 Conclusions

Some conclusions can be drawn from the results of this chapter:

In general, with the inclusion of the tidal farm, the decrease in high tidal levels happens to be more frequent than the increase. This would mean that the net effect on the flood risk could be positive. On the other hand, intertidal areas could become permanently dry.

It could be also mentioned that, when comparing all geometries, the effect of the farm seems higher in terms of permanently submerging the intertidal areas (increase in low tidal levels) rather than increasing the extension of intertidal areas (decrease of low tidal levels).

The locations of the maximum changes in low and high water levels happening due to the influence of the tidal farm are strongly dependent on the geometry.

There are negligible effects on the time of high/low tides derived from the introduction of the farm in all cases.

There is an increase of the effects, in general, with a higher drag coefficient. Nevertheless, the decrease of low tide levels is negligible for all cases with a different drag coefficient in case 1.b.

Finally, it seems necessary to highlight that the analysis of the maximum

changes in peak and low levels provides a better understanding of the effects of tidal farms over flood risk levels and intertidal areas, and its use seems preferable than only the evaluation of the differences in tidal range.

Chapter 4

Solway Firth Estuary - Initial model

4.1 Introduction

In order to demonstrate a methodology allowing the identification of the impact of tidal farms on flood risk in estuaries, numerical modelling of a real case study has been carried out using MIKE 21. Due to the fact that the data available at the beginning of the project had some inconsistencies, the initial model created based on that data was modified later, when new datasets, which give a more realistic representation of the estuary, became available.

This Chapter describes the process of selecting the real case study (Solway Firth estuary), creating the input parameters for the initial model and analysing the results. Regarding the numerical simulations, several points, such as the analysis of the mesh size, the calibration and validation as well as the adaptation of the tidal farms to the model, have also been covered here.

4.2 Methodology

The methodology followed in this study to delimit the effects of very large groups of tidal stream turbines on flood risk levels in estuaries consists of the following parts:

- The creation of a detailed numerical model of the estuary in the

undisturbed state with boundary conditions representing the extreme water levels.

- The analysis of the hydrodynamic conditions of this model in terms of the locations with higher energy resources and sufficient clearance for the deployment of the turbines with the purpose of identifying the extension of the tidal farm.
- The characterisation of the tidal farm (turbines loading, configuration and spacings in the array layout).
- The simulation of the previous numerical model with the tidal farm included in the same flooding scenario.
- The analysis of the results of peak water levels in the domain of the models with and without turbines present.
- The calculation of the differences on peak water levels between both models and location of maximum changes in the estuary.
- The assessment of the effects on flood risk levels.

Figure 4.1 provides a scheme summarising the methodology.

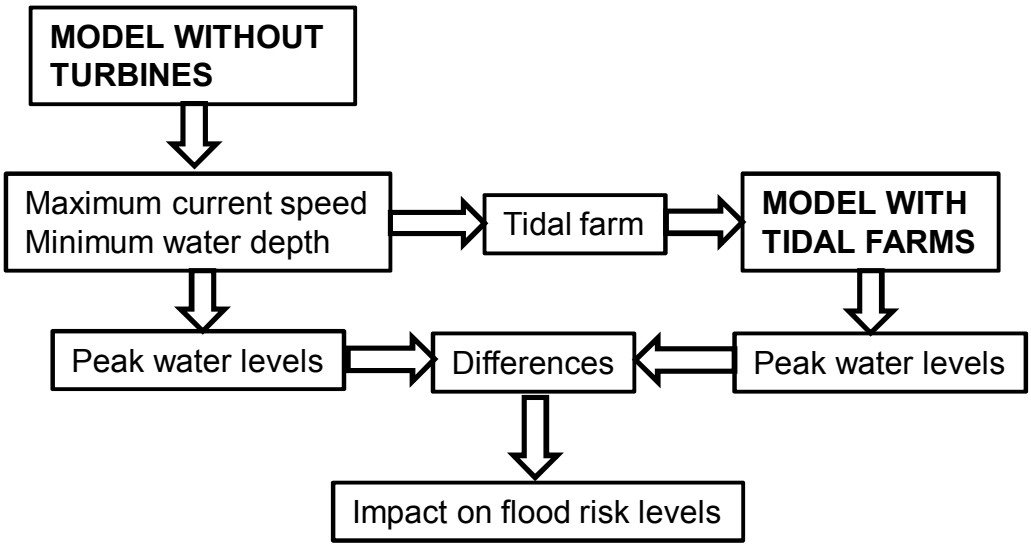

Figure 4.1: Methodology for the impact assessment of tidal farms on flood risk in estuaries

4.2.1 Case study selection

Based on the group of estuaries suitable for tidal energy extraction in the UK, identified in Chapter 3, and the existence of high levels of flood risk, the Solway Firth has been selected as a representative case for the analysis of the impact of tidal farms on flood risk in estuaries. The Solway Firth is located between Cumbria and Dumfries and Galloway.

As can be seen in figure 4.2 from ABPmer [2014], the annual percentage of exceedance of the velocities over 1 m/s at some areas inside the estuary can reach up to 50 %. On the other hand, the levels of flood risk in some locations around the coastline in the estuary are regarded as significant, according to the flood maps provided by Environment Agency [2015] and Scottish Environment Protection Agency [2015], shown in figures 4.3 and 4.4. Table 4.1 gives the return periods used to define the flood risk levels at each area in the flood risk maps.

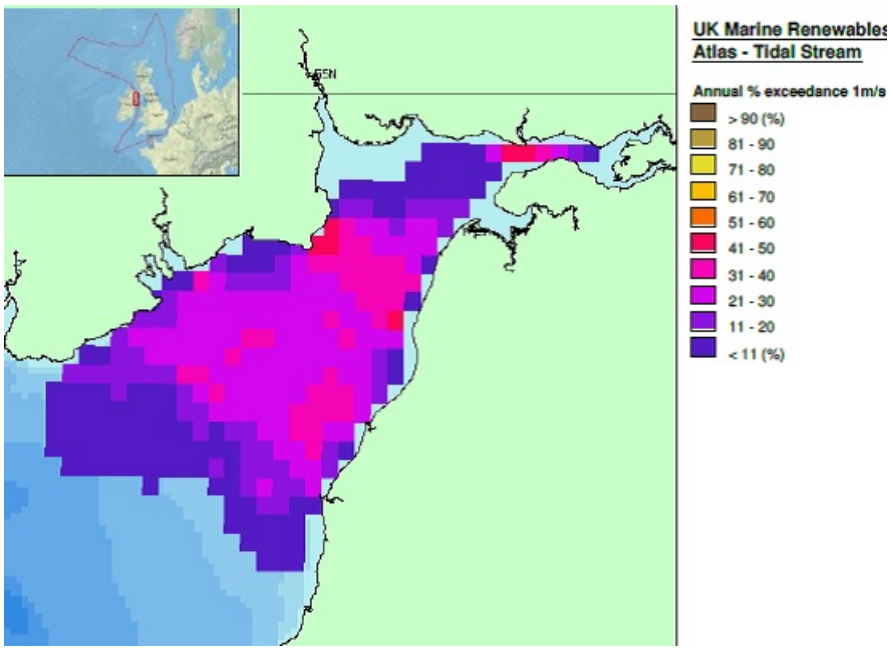

Figure 4.2: Annual percentage of velocities over 1 m/s.(Source: UK Atlas of Marine Renewable Energy Resources. [ABPmer, 2014]

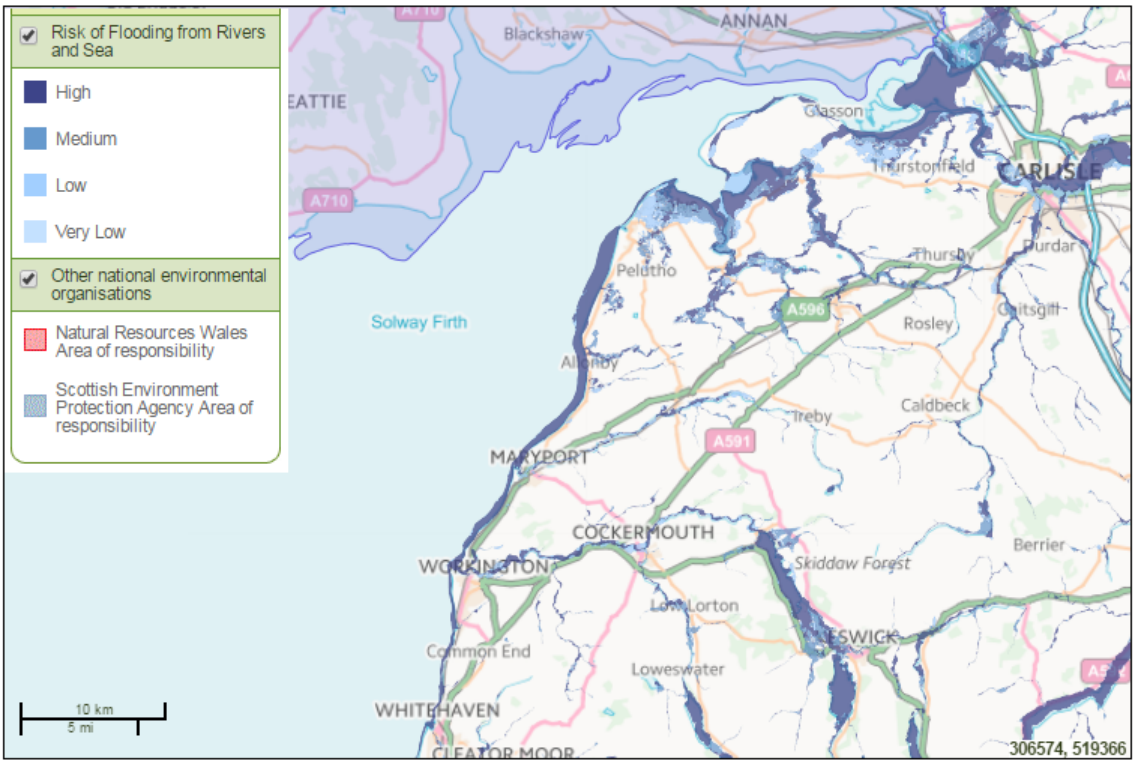

Figure 4.3: Risk of flooding from rivers and sea along the English coastline of the Solway Firth estuary (Source: [Environment Agency, 2015]

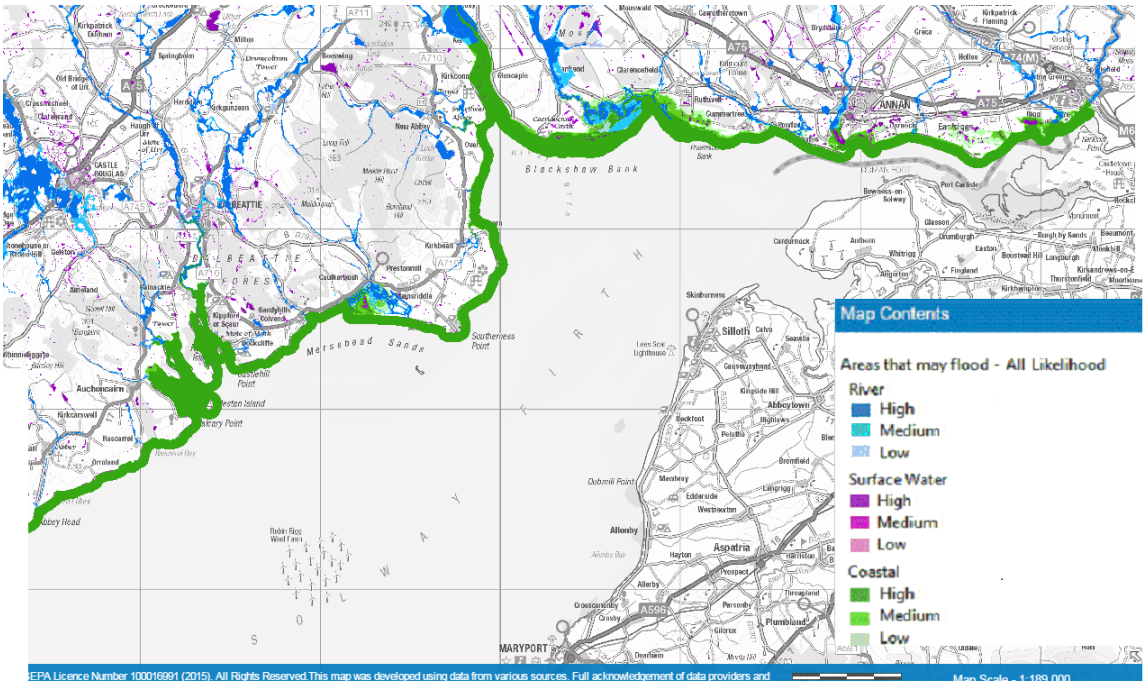

Figure 4.4: Risk of flooding from rivers, surface water and sea along the Scottish coastline of the Solway Firth estuary (Source: [Scottish Environment Protection Agency, 2015]

Level of flood risk	Return Period (years)	
	E.A.	S.E.P.A.
High	< 30	10
Medium	30 - 100	200
Low	100 - 1000	1000
Very low	> 1000	-

Table 4.1: Return periods associated with each level of flood risk in the Environment Agency and the Scottish Environment Protection Agency flood maps

4.2.2 Numerical models

In order to study the effect of the tidal turbines on the flood risk levels in the estuary, hydrodynamic models of the Solway Firth have been built using MIKE 21 FM (flexible mesh), which was described in Chapter 2. An unstructured triangular mesh has been used for the spatial discretisation of the domain. The bathymetry was created by interpolation of the measured depths over the nodes of the computational mesh. The different data sources for the bathymetry in the area of the estuary were analysed in order to find the most accurate ones to be applied in the model. The available sources of gridded bathymetry are shown in table 4.2 with details about their resolution, where BODC stands for the British Oceanographic Data Centre and EMODNET for the European Marine Observation and Data Network.

Bathymetry	**Source**	**Resolution**
GEBCO_1	BODC	1 arc-min
GEBCO_08	BODC	0.5 arc-min
CELTIC SEAS	BODC	0.5 arc-min
EMODnet	EMODnet	0.25 arc-min
Gridded bathymetry 6 arcsec	SeaZone	6 arc-sec
Gridded bathymetry 1 arcsec	SeaZone	1 arc-sec

Table 4.2: Different sources and resolutions of bathymetry in the Solway Firth area

From table 4.2 it can be seen that the highest resolution is provided by the Seazone gridded bathymetry with 6 arc seconds resolution. However, due to the fact that this dataset is based on the information provided by the Admiralty Charts, the inner part of the estuary was not surveyed because it is too shallow for navigation. Figure 4.5 has been taken from the Admiralty Chart 1346, covering the Solway Firth area, and shows details about the unsurveyed area.

Regarding the other sources of bathymetry, it can be noticed that the GEBCO08 dataset gives unrealistic depths of the order of 150 meters in the inner part of the estuary. In this case, depths in shallow waters, where there was no data available from measurements, have been created as an artefact during the interpolation of the grid, as reported by BODC [2015]. Similarly, the inner part of the estuary in the EMODnet dataset is not covered entirely because there are extensive intertidal areas which are not permanently submerged and thus not considered as part of the bathymetry. Regarding the Celtic Seas bathymetry provided by BODC, the coverage of the estuary is complete although the report by Brown et al. [2001] indicates the existence of errors in the regions of intertidal areas, mentioning the Solway Firth, due to the difficulty of modeling and validating the wetting and drying patterns. Therefore, due to the lack of better data sources at the initial stages of the research, the Celtic Seas bathymetry was used to create the computational mesh for several MIKE 21 simulations providing preliminary results. Several improvements to the model were applied afterwards, given the availability of another bathymetry dataset covering the intertidal areas in more detail and new data sources for the calibration and validation. The so-called initial model is described in this Chapter and its improvements are included in Chapter 5.

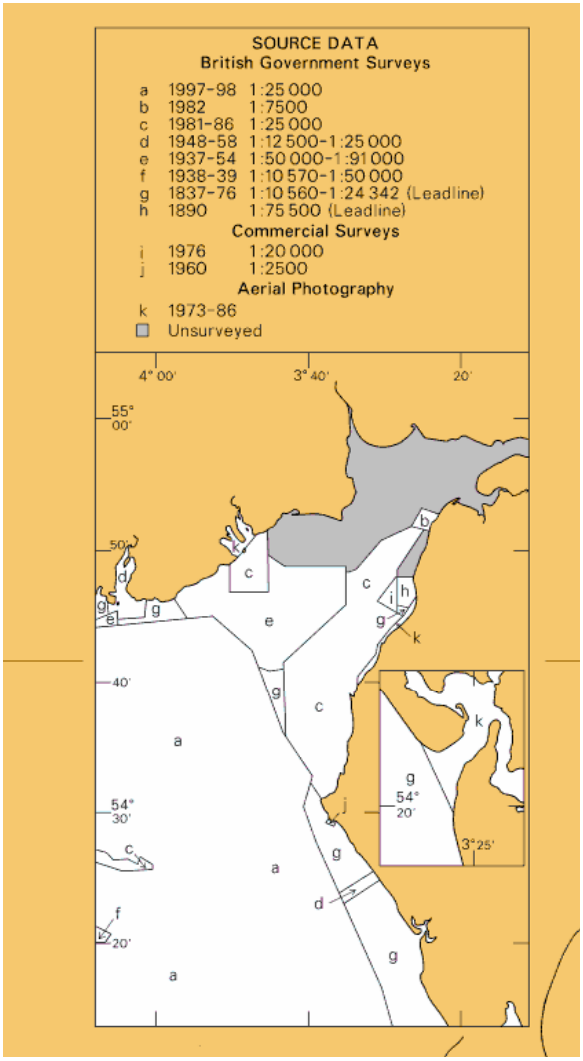

Figure 4.5: Unsurveyed areas in the Admiralty Chart 1346, Solway Firth area. (Source: TIFF geospatial data, Scale 1:250000, Tile: 1346−0 w, Updated: 6 December 2013, Seazone, Using: EDINA Marine Digimap Service, http://digimap.edina.ac.uk, Downloaded: 2015-08-11 18:39:12.268)

4.3 Initial model

4.3.1 Domain

The domain of the initial model was delimited by the inland boundary to the North-East, close to the convergence of the rivers Esk and Eden, and by the open sea boundary in the South-West, between Abbey Head (Kirckcudbright

Bay) and St Bee's Head (Workington), as can be seen from figure 4.6.

Figure 4.6: Solway Firth initial model domain. (Source: Digimap)

As will be demonstrated in the next sections, the extent of the domain was large enough to avoid the reflection on the boundary of the wave generated by the tidal farm as an obstacle to the incoming tidal wave, despite not having used a non-reflective boundary condition.

The domain is covered by an unstructured flexible mesh created through the interpolation of the bathymetry provided by the British Oceanographic Data Centre, which is described by Brown et al. [2001]. The bathymetry dataset, called Celtic Seas' bathymetry, has a resolution of 30 arc seconds for the latitude and 1 arc minute for the longitude.

Sensitivity Analysis of the Mesh Size

A sensitivity analysis was carried out by using different element sizes within the same model in order to determine the effects of the mesh size on the results. It was also used to reach a good compromise between the computational demand

and the accuracy of the results. The maximum element size for each mesh used in the sensitivity analysis can be seen in table 4.3.

Mesh	Max size (km^2)
1	5.00
2	2.50
3	1.00
4	0.75
5	0.50
6	0.25

Table 4.3: Maximum element size for different meshes in the sensitivity analysis of the initial model of the Solway Firth

The period of the simulation covered 276 time steps. The time integration and spatial discretisation of the governing equations followed second order schemes, with a minimum time step of 0.01 seconds and a maximum time step of 600 seconds, with the critical CFL number set to a value of 0.8. The model was forced at the open sea boundary with the water levels predicted by means of the Global Tide Model (GTM) included in the MIKE 21 toolbox during the period between 30th April at 19:00 h and 2nd May of 1977 at 17:00 h, with a resolution of 0.25° x 0.25°. The flood and dry function was used, with the drying, flooding and wetting depths equal to 0.005, 0.05 and 0.1 m, respectively. For simplicity, the river discharges were not included in the simulations, neither was the effect of the wind. Uniform bed roughness and horizontal eddy viscosity were used over the domain with values of 22 and 0.28 $m^{1/3}/s$ for the inverse of the Manning's number and the Smagorinsky coefficient, respectively.

The computational time for these simulations varied from 21 minutes for the greater mesh size to 3 hours and 18 minutes for the smaller one, run on a 3.2 GHz Intel core i5 (4 cores) processor.

The results of the water levels at a point inside the domain, located at coordinates (306445, 558483) (Easting, Northing), were compared between the different meshes by extracting the results of the model with coarser meshes from the one with the finest mesh (mesh 6). Table 4.4 shows the mean absolute error and the error standard deviation for each case. It can be seen that the difference between the results for the coarser and finer mesh is not significant.

Mesh	MAE (m)	STDEV (m)
1	0.007	0.006
2	0.007	0.007
3	0.005	0.004
4	0.004	0.003
5	0.001	0.001

Table 4.4: Statistical errors computed as difference in results with Mesh 6

4.3.2 Model Calibration and Validation

According to Bartlett [1998], “Calibration is to be taken as meaning the adjustment of certain internal model parameters so as to optimise the simulation of reality in comparison with a set of measurements.”

The calibration of the initial model was carried out with observed current speeds provided by the British Oceanographic Data Centre (BODC) from a station located at coordinates (-3.8833, 54.7333) (longitude, latitude) during the period between 26th March and 4th May of 1977. The parameters involved in the calibration of the model were the bed roughness and the eddy viscosity.

The location of the station where the data for the calibration were observed is shown in figure 4.7, along with other features of the simulation of the estuary which will be described in next sections.

Figure 4.7: Location of the stations for the calibration, validation, river conditions, boundary reflection analysis and tidal farm in the initial model of the Solway Firth.

A maximum element size of 1 km^2 was used for the unstructured mesh over which the 'Celtic Seas' bathymetry was interpolated. The simulation comprised 552 time steps of 600 seconds with a critical CFL number of 0.8. The boundary conditions at the open sea were predicted by means of the Global Tide Model toolbox in MIKE 21 for the period from 30th April 1977 at 19:00 h until 4th May 1977 at 15:00 h. The effect of the rivers and wind was neglected. The flood and dry function was activated, with a drying depth of 0.005 m, a flooding depth of 0.05 m and a wetting depth of 0.1 m.

First, a Smagorinsky coefficient of 0.28 (default value provided in MIKE 21), uniform over the domain, was used for the simulations while the bed roughness, defined by the inverse of the Manning's number, was varied over the values

shown in table 4.5. The first value used, M=40 $m^{1/3}/s$, was intially calculated according to sediment maps in the area as follows. Information about sediments in the estuary was extracted from Davies & Lawrence [1995] and the Nature Conservation Committee [2014], as can be seen from figure 4.8. Bed sediments in the Solway Firth area seem to consist mostly of sand.

Following the study by Lambkin D. [2016], Manning's coefficient for sea bed roughness can be defined as a function of the drag coefficient (c_d), which is derived from the empirical values 1 m above the bed (C_{100}) for different sediment types. The formula that relates C_{100} to the drag coefficient is:

$$c_d = \left(\frac{1}{0.32h}\right)^{1/7} C_{100} \tag{4.1}$$

h being the water depth.

A water depth equal to 17.5 m has been assumed, as an average of the bathymetry in the estuary, which ranges from 0 to 35 m. For Mud/Sand types the value of C_{100} is equal to 0.003. Therefore, the result for the drag coefficient in this case is 0.0023.

On the other hand, the formula that relates the Manning's roughness with the drag coefficient is:

$$M = \sqrt{\left(\frac{g}{c_d h^{1/3}}\right)} \tag{4.2}$$

Including the previous values in the formula, the result for M is 40.13 (approx. 40) $m^{1/3}/s$.

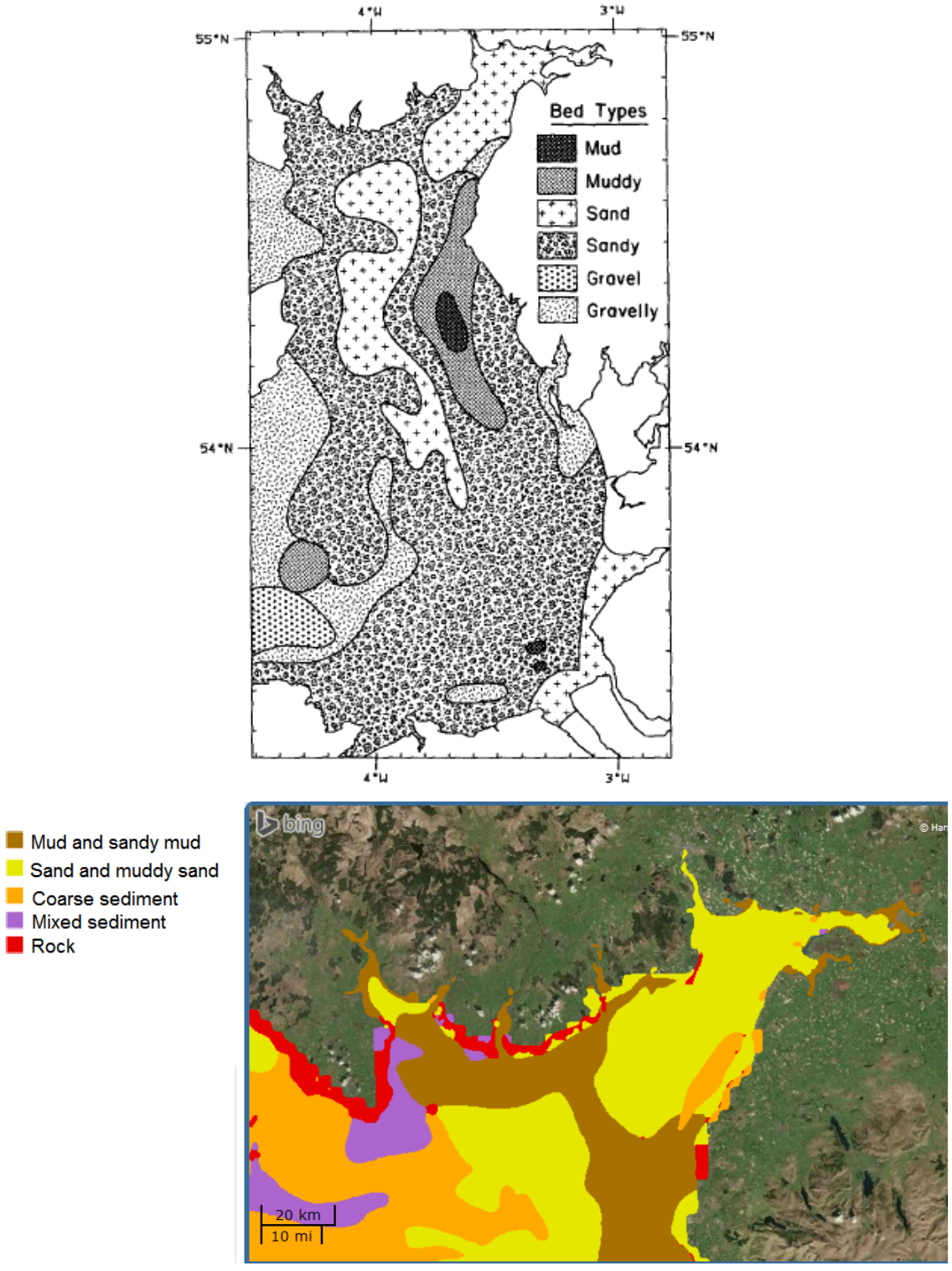

Figure 4.8: Schematics showing the spatial variation of bed types, adapted from Davies & Lawrence [1995] (top) and Nature Conservation Committee [2014] (bottom)

For the comparison with the observed current speeds, the requirement of having differences within (+/-) 0.2 m/s at 90 % of the positions/times observed, as indicated by Bartlett [1998] has been considered. It has been found that this requirement is fulfilled at different levels depending on the Manning coefficient used. The percentage of time steps that meet the previous requirement for each case, listed in table 4.5, is approximately: 31.6 %, 97.5 %, 99.3 % and 98.5 %. The mean errors between the observed and modelled speeds have also been calculated and are included in table 4.5. It can be seen from the previous parameters that the best agreement with the observed measurements is found for the results from the simulation with M = 22 $m^{1/3}/s$.

Simulation	**M (1/n)**	**Mean error (m/s)**
1	40	-0.322
2	25	-0.053
3	22	-0.007
4	20	0.024

Table 4.5: Bed roughness values employed in the calibration of the initial model and mean errors obtained by comparison with observed velocities

The graphical comparison between the results for each simulation and the observed measurements can be found in figure 4.9.

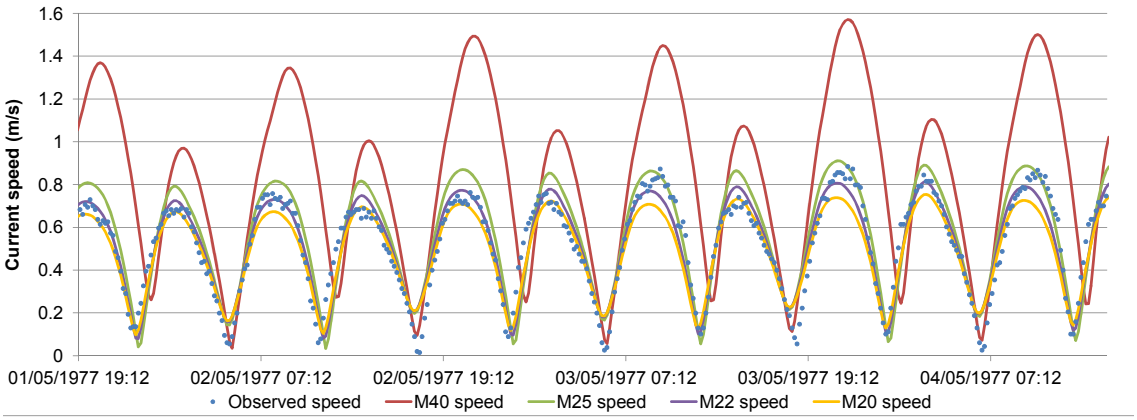

Figure 4.9: Comparison between observed current speed and modelled results with different bed roughness

Considering the dependence of the Smagorinsky coefficient on different flow regimes, indicated by Pope [2000], the calibration of the aforementioned coefficient was included in this study. Different values of the Smagorinsky coefficient were used (see table 4.6 with a fixed bed roughness represented by M = 22 $m^{1/3}/s$. These values are between the range of 0.2 and 1.0, as recommended in DHI [2012a]. The details of the simulations and comparisons with observed measurements are the same as in the case of the calibration of the bed roughness. Regarding the percentage of time steps that meet the requirement of errors in velocity within +/- 0.2 m/s, it was found the same value (99.3 %) for all cases. The mean errors, shown in table 4.6 also show very similar values. Therefore, the default value of 0.28 for the Smagorinsky coefficient was chosen and used for the validation of the model.

Simulation	Smagorinsky coefficient	Mean error (m/s)
I	0.25	-0.007
II	0.28	-0.007
III	0.50	-0.007
IV	1.00	-0.008

Table 4.6: Values of the Smagorinsky coefficient and mean errors obtained in the calibration of the initial model

Figure 4.10 shows the modelled current speed and the observed measurements at the location of the BODC current meter station.

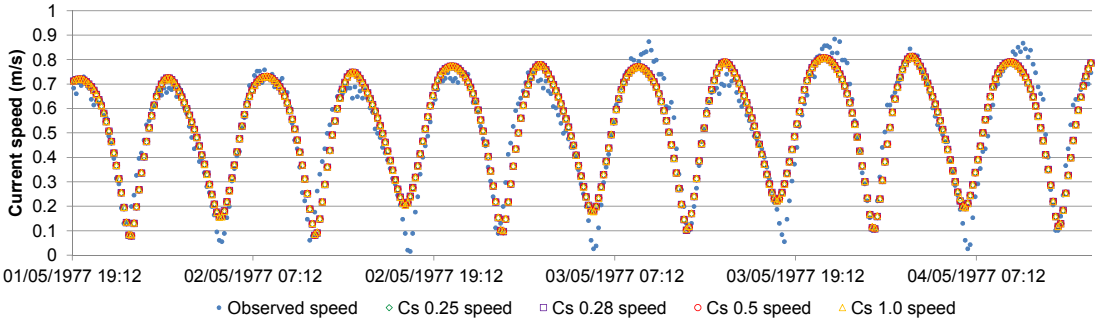

Figure 4.10: Comparison between observed current speed and modelled results with different eddy viscosity

Validation

"Validation is to be taken as meaning the testing of the calibrated models in comparison with new sets of measurements." [Bartlett, 1998]

The results from the simulation with a bed roughness parameter (M) equal to 22 $m^{1/3}/s$ and a Smagorinsky coefficient equal to 0.28 were validated against observed measurements during the period from 9^{th} February 2013 at 10:00 h until 9^{th} March 2013 at 10:00 h. The simulation period allowed covering both the spring and neap tides. The information of the observed water levels has been

extracted from the tidal gauge at Workington Port, which is shown in figure 4.7, and provided by the British Oceanographic Data Centre (BODC).

The graphical comparison between the observed and modelled values can be found in figure 4.11

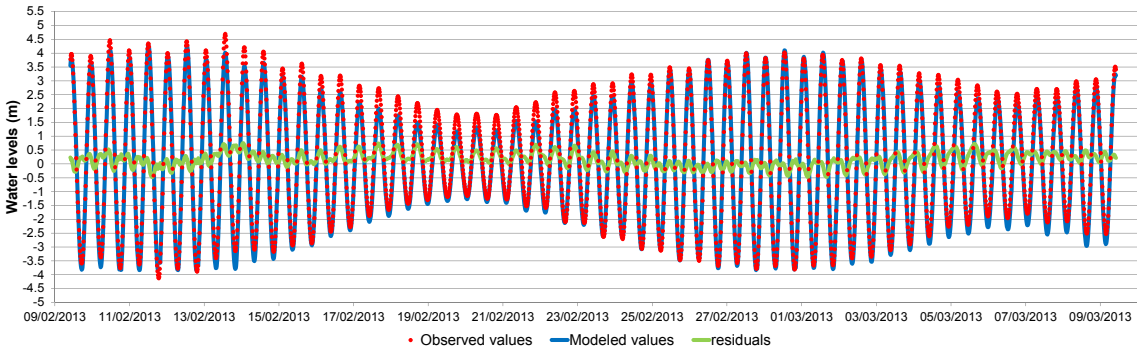

Figure 4.11: Comparison between observed water levels and modelled results at Workington port for the validation of the model

Table 4.7 shows the percentage of difference between the observed and modelled spring and neap ranges. It can be seen that the adjustment is better in the spring tides than in the neap tides.

Difference spring range (%)	8.08
Difference neap range (%)	16.55

Table 4.7: Statistical parameters describing the adjustment of the model in the validation

The percentage differences between the model and the measurements in spring and neap tidal ranges fulfill the recommendations given by Bartlett [1998] for estuarine models (15% for spring range and 20% for neap range).

4.3.3 Flooding Scenarios

The boundary conditions at the open sea consisted of water levels while the rivers flowing into the estuary were represented by their discharges. The stations for the discharges of the rivers in the model can be found in figure 4.7 from section 4.3.2. The monthly conditions for the wind acting over the domain were obtained from Carlisle airport.

In order to analyse the effect of tidal farms on flood risk levels in the estuary, the boundary conditions in the initial model were adapted to three different flooding scenarios:

- The first scenario represented a coastal flooding with a 200-year return period event happening at the open sea, formed by a storm surge and the highest astronomical tide. The water levels in this case were determined following the process indicated by the Environment Agency for the design of flood defences [McMillan et al., 2011]. First, the values for the 200-year return period elevations and their confidence intervals at the edges of the open boundary (Kircudbright Bay and Whitehaven) were obtained from the GIS information provided by the Environment Agency [McMillan et al., 2011]. The confidence intervals are included because there is some uncertainty due to the fact that the data have been developed by means of the skew surge joint probability method according to records covering a period of less than 100 years. The values of the aforementioned parameters are given in table 4.8.

LOCATION	GIS ID	T200 (m)	CONFIDENCE (m)
Kirkcudbright Bay	752	5.58	0.3
Whitehaven	686	5.75	0.3

Table 4.8: 200-year return period elevations (T200) and confidence intervals at the edges of the open boundary

Then, a base astronomical tide curve was created by using the information from the United Kingdom Hydrographic Office [2012]. A standard port was identified in the area, being in this case Liverpool port, in order to define a high tide level. This level (9.9 m Chart Datum (CD)) was taken as an average between the highest astronomical tidal level from table V (10.3 m CD) and the mean high water springs level from Part II of the Admiralty Tide tables (9.4 m). Afterwards, a date and time when this level would occur (11th February 2013 at 11:45 h) was identified in Part I of the Admiralty Tide tables. This date and time was used to determine the base tidal curve at the open sea boundary covering a period of four days by means of the MIKE 21 toolbox for the prediction of tidal heights. This tool is based on the works of Doodson [1921] and Godin [1972] on tidal analysis. A least squares method is used to calculate the amplitudes and phases. The Doodson's [Doodson, 1921] tidal potential is the basis for the calculations of frequencies, nodal factors and astronomical arguments of the tides. During the prediction of tidal elevations, tidal constituents have been taken from the Global Tide Model (Andersen [1994] and Andersen [1999]), provided by DHI, with a resolution of 0.125 degrees.

In order to produce the resultant curve including the high tide plus the storm surge, first, the peak base tide levels for both edges of the boundary are taken from the peak of the predicted tidal curve, as can be seen in table 4.9.

LOCATION	**Base tide (m OD)**
Kirkcudbright Bay	4.09
Whitehaven	4.23

Table 4.9: Peak base tidal levels at boundary edges

The surge curve '31: Workington' (see figure 4.12), covering the Solway Firth area, was identified in the information provided by McMillan et al. [2011]. This curve was added to the base tide levels at each edge of the boundary during the highest tide, occuring in the central part of the time series. The surge shape was then scaled in order to target the 200-year event value (see figure 4.13). The scaling factors shown in table 4.10 were applied to every location. Finally, the boundary conditions at both edges were interpolated over the line of the open boundary and used as an input to the MIKE 21 model.

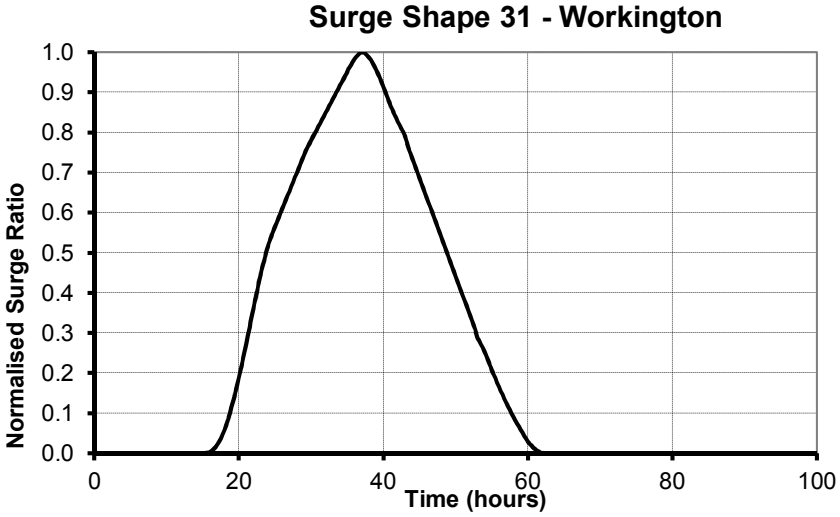

Figure 4.12: Surge curve 31: Workington/ Haverigg Point to Isle of Whitorn (incl. Solway Firth, Wigtown Bay), Source: [McMillan et al., 2011]

LOCATION	Scaling factor (m OD)
Kirkcudbright Bay	5.58-4.09 = 1.49
Whitehaven	5.75-4.23 = 1.52

Table 4.10: Scaling factors for peak tidal levels at the edges of the open boundary.

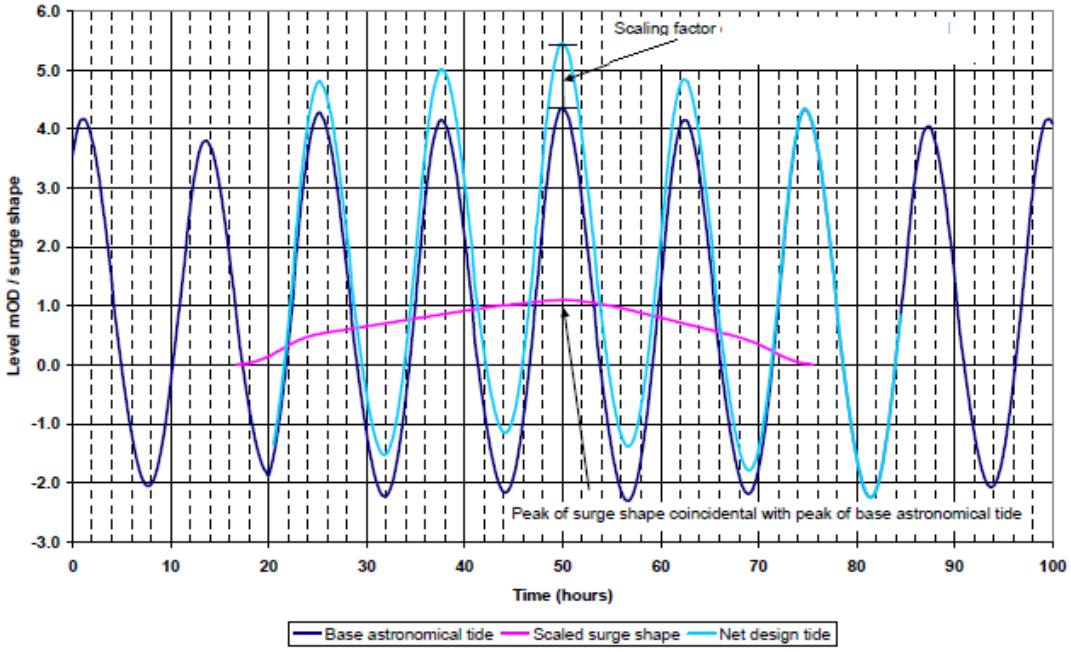

Figure 4.13: Peak surge occurring two hours before peak base tide, (Adapted from McMillan et al. [2011])

The discharges of the main rivers in the estuary have been included as boundary conditions. The river discharges have been represented as point sources with a constant discharge given by the average annual values from the study by Gurbutt [1993], as can be seen in table 4.11.

River	Discharge (m^3/s)
Urr	5
Nith	40
Lochar water	5
Annan	28
Esk	34
Eden	45
Wampool	2
Waver	3

Table 4.11: Mean annual river discharges in the Solway Firth model. (Source: [Gurbutt, 1993]

Figure 4.14 shows the rivers flowing into the Solway Firth basin.

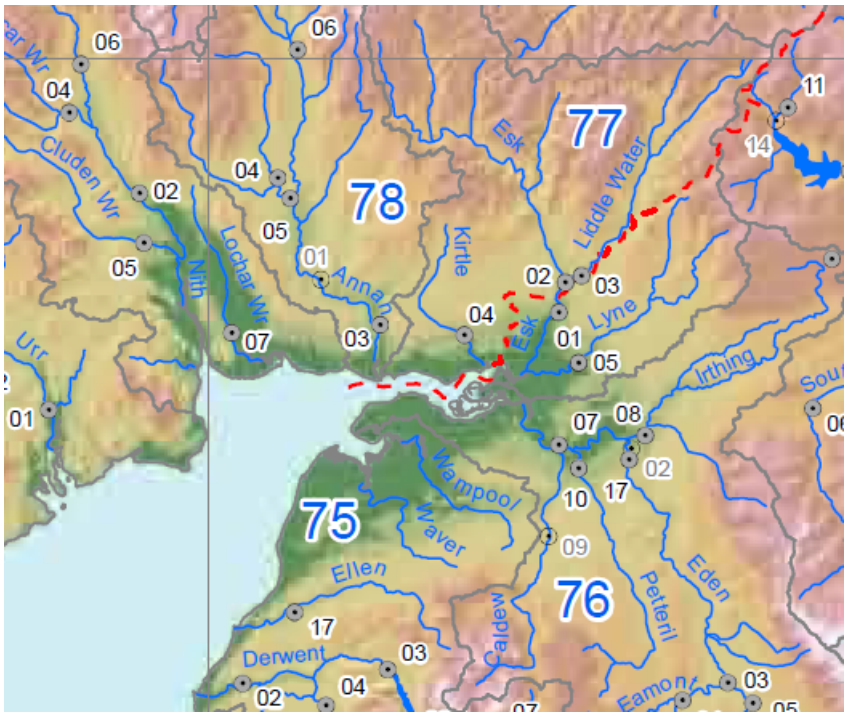

Figure 4.14: Rivers in the area of the Solway Firth estuary. (Source: [Centre for Ecology and Hydrology, 2013])

- In the second scenario, related to fluvial flooding, the boundary conditions at the open sea consisted of the water levels given by the MIKE 21 toolbox for the prediction of tidal heights during the period of the simulation while the conditions at the rivers were the discharges for the 200-year return period event obtained as follows.

  First, the discharges for the 200-year return period event were identified for each river in the dataset provided by the CEH (Centre for Ecology and Hydrology) in ascii format. ArcMap was used to find the values in the locations close to the estuary, which are included in table 4.12. The technique applied by the CEH in order to produce these discharges is explained in Morris [2003].

River	Q200 CEH (m^3/s)
Annan	863
Esk	1458
Urr	236
Kirtle Water	124
Eden	1553
Ellen	161
Derwent	419

Table 4.12: 200-year return period discharges in several rivers from CEH values

In the case of the river Nith, it was difficult to identify such discharge, therefore a Gumbel type distribution was applied to the Annual Maximum (AMAX) series provided by SEPA (Scottish Environment Protection Agency), covering 56 years, in order to calculate the discharge for the 200-year return period according to the indications given by Shaw [1994] for river flow records over 25 years. An estimate of $Q200$ (200-year return period discharge) may be obtained from:

$$Q200 = Q + K\,(200)\,s_Q \tag{4.3}$$

Where Q is the sample mean, s_Q the standard deviation of annual maximum flows and $K(T)$ the frequency factor. For the Gumbel type 1 distribution K(200) is equal to 3.68 [Shaw, 1994]. Therefore, applying this method to the Nith AMAX serie the discharge results to be as shown in table 4.13.

River	Q200 (m^3/s)
Nith	1020

Table 4.13: 200-year return period discharge in river Nith

These values are introduced in the model as sources with the coordinates that can be seen in table 4.14.

River	Coordinates (Easting, Northing)
Urr	(283400, 554304)
Nith	(301465, 562791)
Annan	(319417, 563545)
Kirtle Water	(331650, 565568)
Esk	(331650, 565568)
Eden	(330908, 561127)
Ellen	(302093, 537618)
Derwent	(297904, 529969)
Lochar water	(309836, 564841)
Wampool	(318015, 556892)
Waver	(317000, 554690)

Table 4.14: Coordinates of the point sources representing the rivers in the model

- The third scenario represented a situation with coastal and fluvial flooding happening at the same time, with a combination of the boundary conditions from the first scenario at the open sea and the river discharges from the second scenario, both for the 200-year return period event.

4.3.4 Tidal farms

Tidal farm locations

The analysis of the potential locations of the tidal farms focused on two main constraints:

- The minimum water levels, which restrict the size of the turbine that could be deployed and thus the installed capacity.
- The existence of current speeds over 1 m/s, given the fact that the velocity is cubed in the calculation of the available power.

In order to define the minimum water levels in the estuary, a simulation was run covering the scenario of a generic Mean Spring tide. At the open sea, the boundary conditions were created by the interpolation of the water levels between the edges of the open boundary, which were approximated to a sinusoidal function. The minimum and maximum values for the tidal elevations at the edges of the sea boundary are related to the Mean Low Water Spring (MLWS) and Mean High Water Spring (MHWS) tide, respectively, which were obtained from United Kingdom Hydrographic Office [2012] for the closest secondary ports (Kircgudbright and Whitehaven). The minimum water levels in the estuary would be related to the Mean Low Water Spring situation. The simulation was run covering a period of 400 time steps of 15 minutes and the same features as in the validation of the model in subsection 4.3.2. The same simulation was used to characterise the maximum current speeds in the estuary.

The results for the water levels and current speeds in the model domain were extracted for the whole period of the simulation. However, for the statistical analysis of the results, the values corresponding to the warming-up period, here considered as the first 100 time steps, were removed. The statistical tool in MIKE 21 was used to calculate the minimum values of the total water depths as well as the maximum current speeds, as can be seen in figure 4.15 and 4.16.

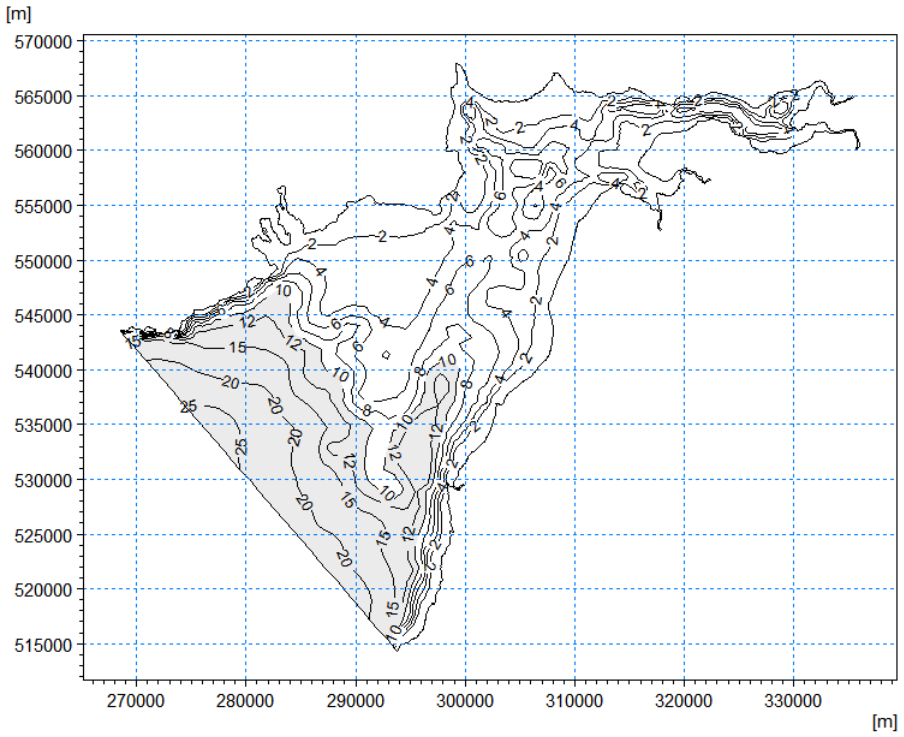

Figure 4.15: Minimum water depths in the estuary model during a mean spring tide

In terms of the maximum current speeds, there are three locations of interest for the tidal farm where the maximum current speeds are higher than 1 m/s, indicated with red elipses in figure 4.17. However, if we take into account the minimum water depths at those locations, it can be noticed that the narrow in the inner part of the estuary would be too shallow for the turbines deployment. The other two areas are deeper, although the area in the central part of the estuary shows faster velocities than the one closer to the mouth of the estuary. Therefore, the location surrounded by the red rectangle in figure 4.18 has been considered for the implementation of the tidal farm in the model, which will be described as follows.

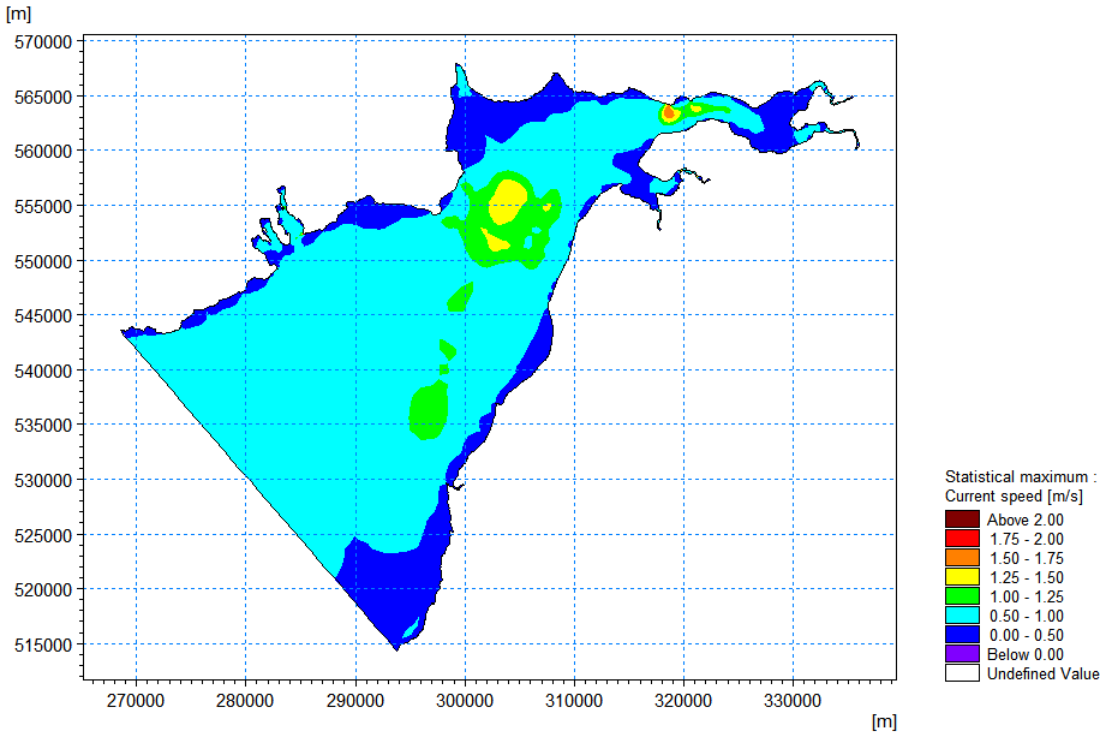

Figure 4.16: Maximum current speeds in the estuary model during a mean spring tide

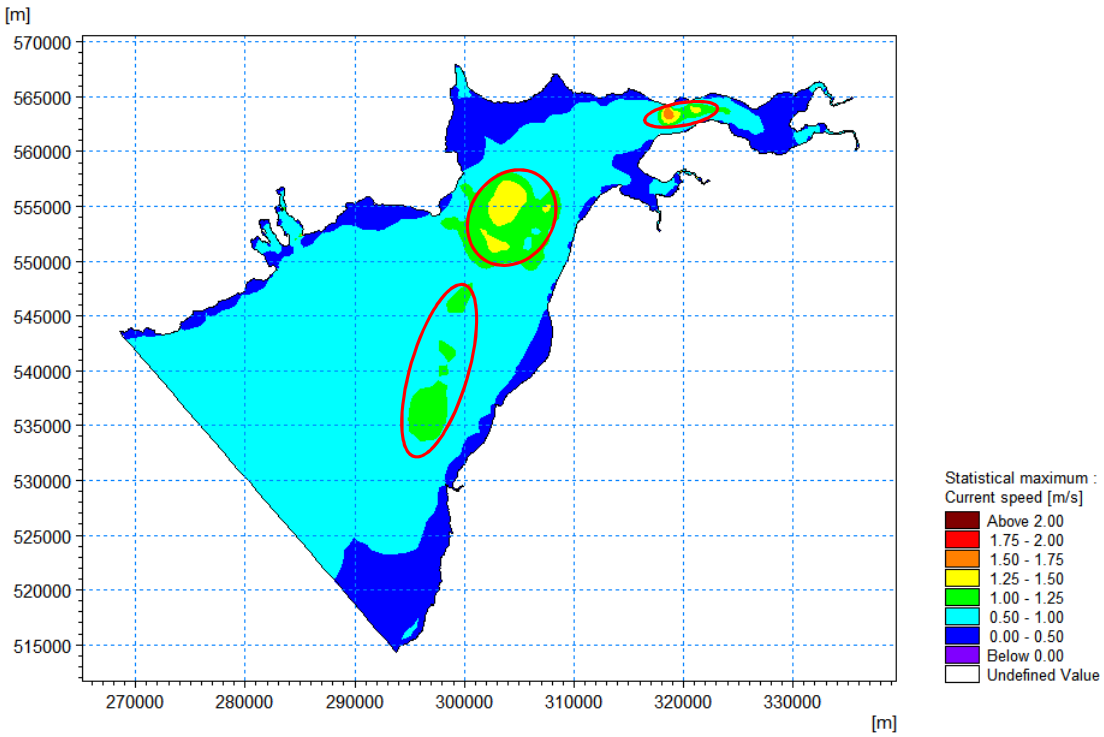

Figure 4.17: Potential locations of the tidal farms according to the maximum current speed criteria

Tidal farm characterisation

With the purpose of evaluating the impact of tidal stream farms on the existing flood risk levels in the estuary, a tidal farm was introduced in the MIKE 21 model, previously described, as follows.

The area occupied by the tidal farm consists of a rectangle with several rows of turbines with their axis positioned at a right angle to the main current direction in the region of interest. The rectangular shape of the farm was chosen because it would facilitate and reduce the cost of the deployment and arrangement of cabling, compared to other geometries. A main current direction of 0.942 radians with respect to the West-East axis, approximately, was identified as the most frequent value appearing in the results of the hydrodynamic model at a point within the potential location of the farm.

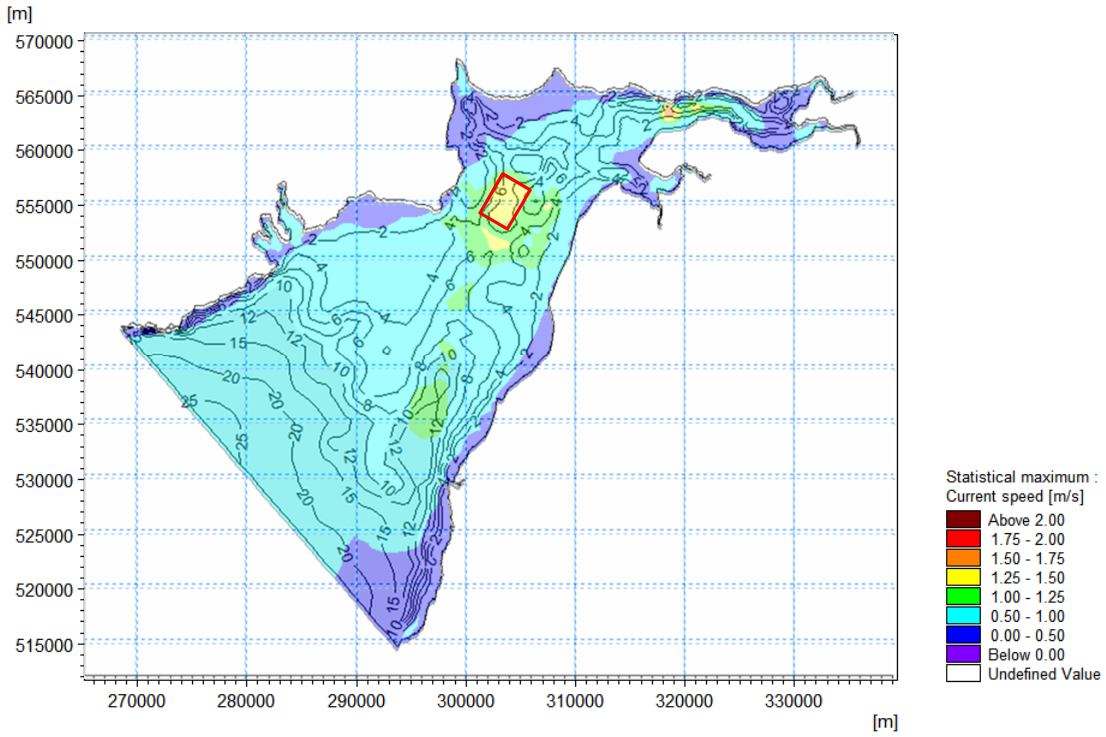

Figure 4.18: Combination of minimum water levels and maximum current speeds to identify the location of the tidal farm (red rectangle)

As shown in figure 4.18, the potential location of the farm would be the available space in the region of the estuary with maximum speed of the current

above 1 m/s with minimum depths over 6 m. Taking into account the clearance between the turbine and the bottom and free surface of the sea, 5 m diameter turbines could be considered for the proposed tidal farm.

The MRL turbine design, described in previous Chapters, has been considered for this study. The aspect ratio for a commercial device has been suggested by the team working on the development of the prototype to be around 1:5 (diameter: length). According to the power formula and considering a power coefficient of 0.5, taken from experimental results by Gebreslassie et al. [2013b], for a turbine with a capacity of 250 KW in a flow at 2 m/s the dimensions would be 5 meters diameter and 25 meters length approximately. Regarding the spacing between turbines inside the farm, a lateral distance of 0.5 times the length of the turbine has been used while a distance of 10 times the diameter has been considered for the longitudinal spacing between rows. The lateral spacing has been taken as the minimum value which allows the flow to pass between the turbines and the longitudinal spacing is based on the work by Gebreslassie et al. [2015].

Two different farm sizes have been considered in order to represent their impact on the estuary:

- A tidal farm consisting of 32 rows and 32 columns of turbines (1024 turbines in total), which would represent a very large tidal farm.
- A tidal farm consisting of 84 rows and 48 columns of turbines (4032 turbines in total), representing an extremely large tidal farm. The approximate extension of this farm is shown in figure 4.7 from section 4.3.2.

Rows are orientated in a perpendicular direction to the flow while columns are parallel to the main direction of the flow. Although such a large number of turbines does not seem realistic given the current state of the art, the purpose of it here is the theoretical demonstration of the effect of the turbines in the estuarine hydrodynamics.

Based on the idea that different configurations of the turbines would provoke different impacts on the current speeds and water levels, two layouts have been used for every tidal farm, covering two extremes in terms of the shifting between turbines in different rows:

- A parallel configuration, where each turbine in the downstream row is located in front of the turbine in the same position within the precedent row. (See figure 4.19)
- A staggered configuration, being the turbines in the downstream rows displaced in reference to the turbines in the same position within the precedent row. (See figure 4.20)

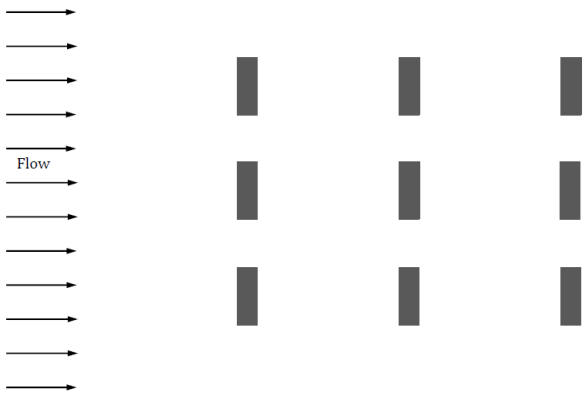

Figure 4.19: Parallel layout

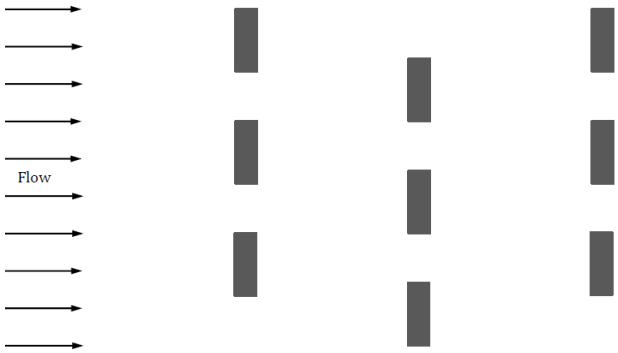

Figure 4.20: Staggered layout

Given the fact that the farms are formed by very numerous groups of turbines and that every turbine is treated as an individual structure in MIKE 21 (version 2012) and thus, must be introduced manually through the use of the graphical interface, a new method was created in order to include the tidal farm in the model in a faster way. A python script is used to write the turbines section in the MIKE 21 model, opened as a text file. Details of the python script are included in Appendix A. It is only necessary to modify the header of the file, introducing the requested parameters and destination files before running the script in order to get a list of the turbines that can be directly copied into the corresponding turbines section of the MIKE 21 model.

For the definition of the aforementioned tidal farms in the intial Solway Firth model, the following coordinates have been used to define the centre of the first turbine on each python script (see table 4.15)

All the turbines in the tidal farm have the same features, for simplicity reasons. Turbines in the MIKE 21 model have been represented by an equivalent diameter of 12.62 m, which gives the same area as a rectangle of 5 m (diameter) by 25 m (length) in the real turbine. A constant drag coefficient of 0.9 has been used to represent the retarding force of the turbine against the flow. Due to the lack of experimental data, this value has been taken from the study by Bachant & Wosnik [2015] for a crossflow Gorlov's turbine because its design is closer to the MRL turbine than the axial ones. The correction factor, described in subsection 2.4.2, was being investigated at this stage of the research and no correction was introduced during these simulations. It was assumed that the increase of the drag coefficient due to the correction in this case would not provoke significantly higher effects. The maximum value of the correction factor would be given by the minimum depth, which is around 6 m, and it would result in an approximate value of 1.37. From table 3.8 in section 3.6 it can be seen that the differences in the maximum effects of a tidal farm over the water levels in an idealised estuary for values of C_d between 0.9 and 1.37 are in the order of mm.

Tidal Farm	Number of turbines	Layout	Coordinates 1st turbine (Easting, Northing)
1A	1024	Parallel	303284.63, 553225.16
1B	1024	Staggered	303468.97, 553158.10
2A	4032	Parallel	303122.88, 551982.65
2B	4032	Staggered	303576.05, 551658.26

Table 4.15: Coordinates of the first turbine on each tidal farm

Analysis of the boundary reflections

As indicated by Baston et al. [2015], when using ”clamped” boundary conditions, such as water levels, in numerical models of coastal areas with tidal farms, the latter can provoke a wave opposite to the tidal wave which cannot propagate beyond the boundary producing artificial changes in the hydrodynamics of the model. Lewis et al. [1994] also mention the suitability of clamped boundary conditions only for those cases with negligible reflection of the tidal wave from the shoreline and bathymetry at the open boundary. In order to avoid these reflections of the tidal wave the domain of the model must be large enough. An example of the application of this method can be found in Adcock et al. [2013].

In order to check that the domain of the model was large enough to avoid reflection of the wave generated by the tidal farm in the open boundary, the results of the simulations with and without the tidal farm were compared at the boundary line in the scenario of fluvial flooding with the tidal farm consisting of 4032 turbines. The approximate location of the nodes in the boundary line can be seen in figure 4.7 from section 4.3.2.

It was found that the maximum differences between the situations with and without turbines were 2.4 % for the current speed and 0.7 % for the current direction, and that 30% and 70 % of the nodes at the boundary showed an error below 0.5% for each parameter, respectively.Therefore, it was considered that the reflection at the boundary was small enough and it would not provoke substantial changes to the model results.

Figure 4.21 shows the aforementioned differences at the open boundary and it can be noted that the highest values appear in the fist half of the domain. This effect may be due to the existence of a shallower area and a constriction in the Scottish shoreline, close to Southerness (see circle around the area in figure **??** , which could provoke a reflection of the tidal wave to some extent

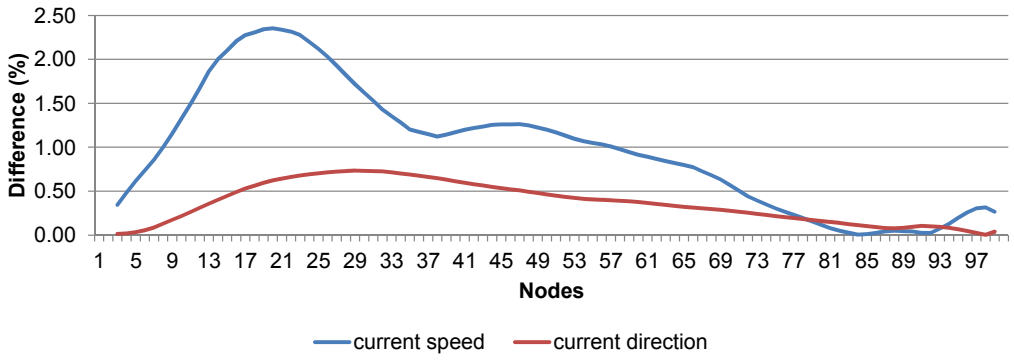

Figure 4.21: Differences of current speed and direction at the open boundary with and without turbines present in the Solway Firth initial model.

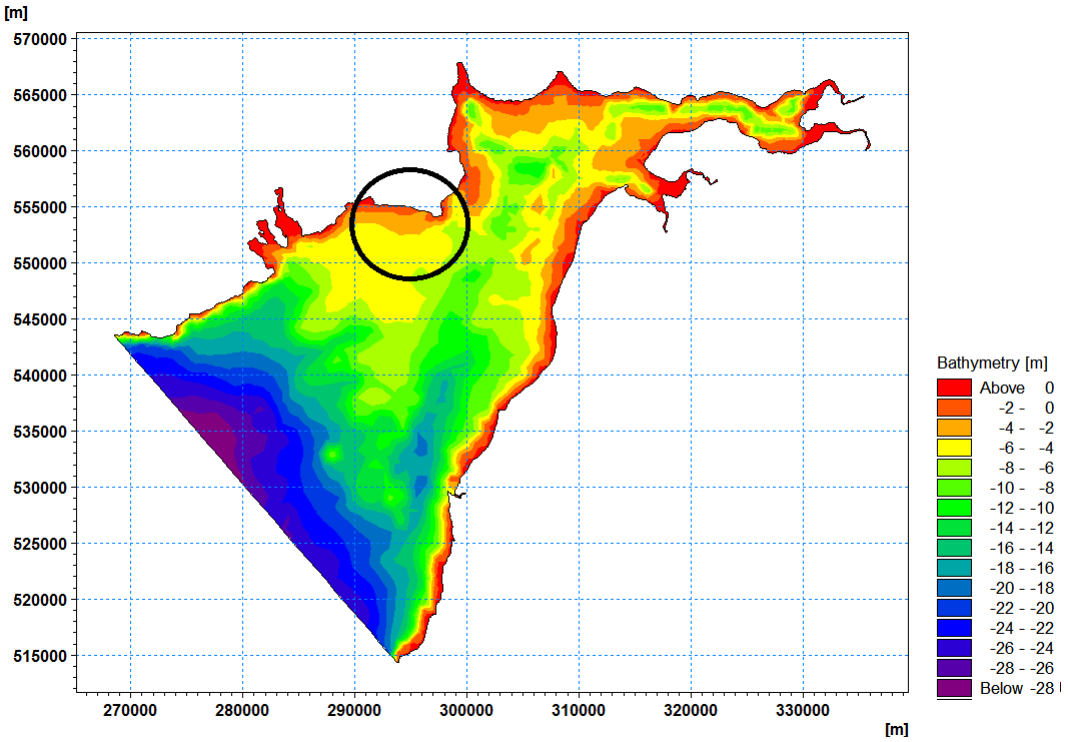

Figure 4.22: Bathymetry from BODC (depths related to MSL)/ Circle: shoreline constriction and shallow bathymetry around Southerness.

Graphical results are included in figures 4.23 and 4.24, related to two points close to the open boundary, which illustrate the comparison of surface elevation, current speed and direction in the second scenario with and without the tidal farm 2A.

Model with tidal farms

In the MIKE 21 model with the tidal farms the computational mesh has been modified to include quadrilateral elements surrounding each turbine, which give a more intuitive representation than the triangular mesh about the effect of every individual turbine in the flow field. The quadrilateral elements have a size of 37.5 m in width and 50 m in length, according to the turbine spacings. The triangular mesh around the farm has been divided into subdomains with maximum element sizes of 10^4 and 10^5 m^2, as can be seen in figure 4.25.

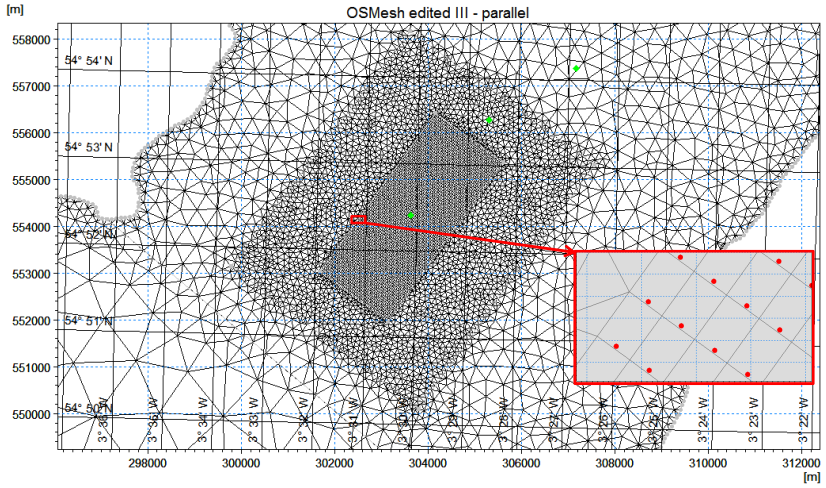

Figure 4.25: Different mesh refinements in and around the area of the tidal farm. The red dots indicate the location of each turbine

The main parameters of the four models with the tidal farms (named 1A, 1B, 2A and 2B in table 4.15) are the same and can be found in table 4.16.

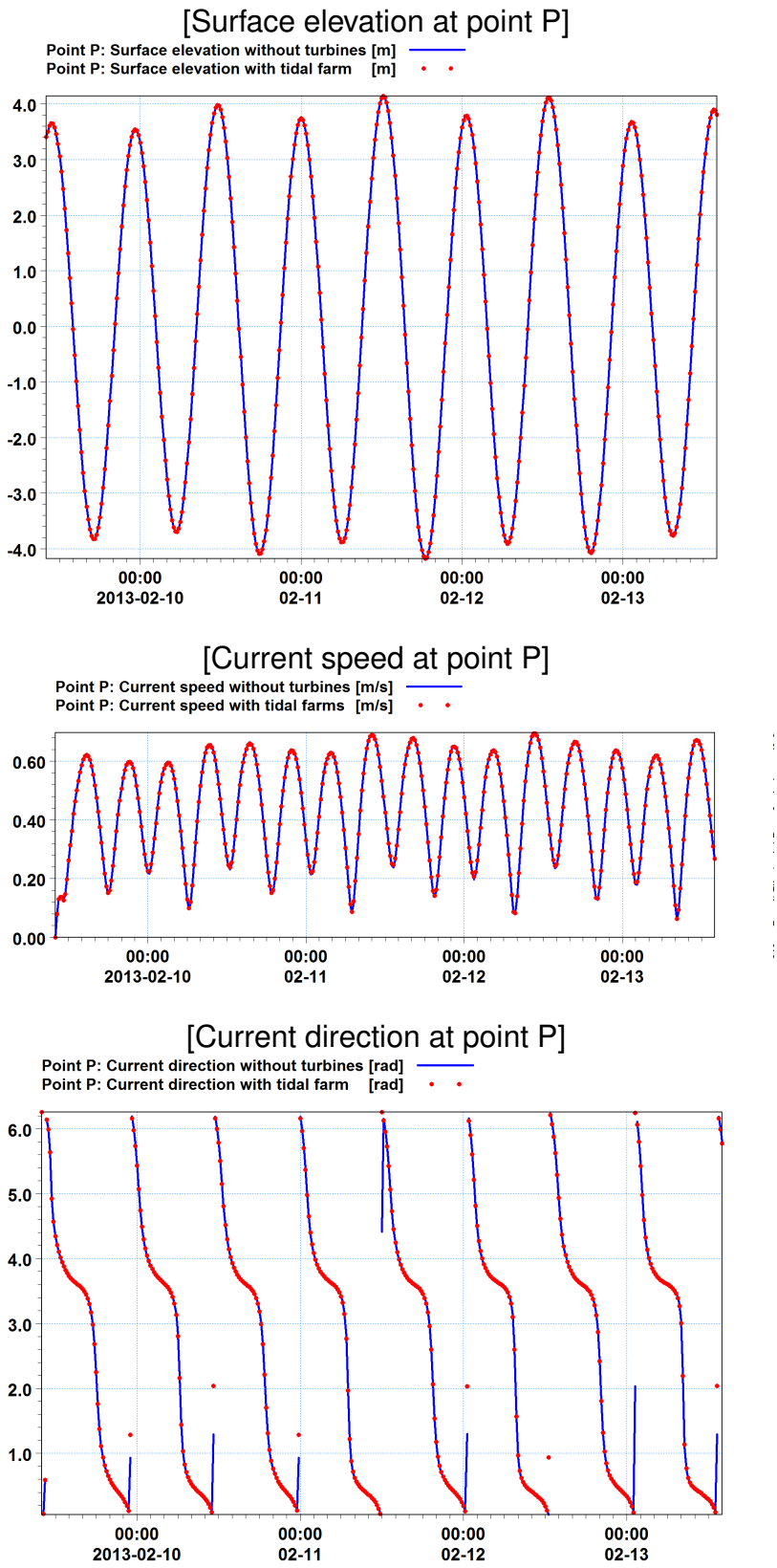

Figure 4.23: Comparison of results at point P (278032.79, 533233.46) in the fluvial scenario with and without the tidal farm 2A

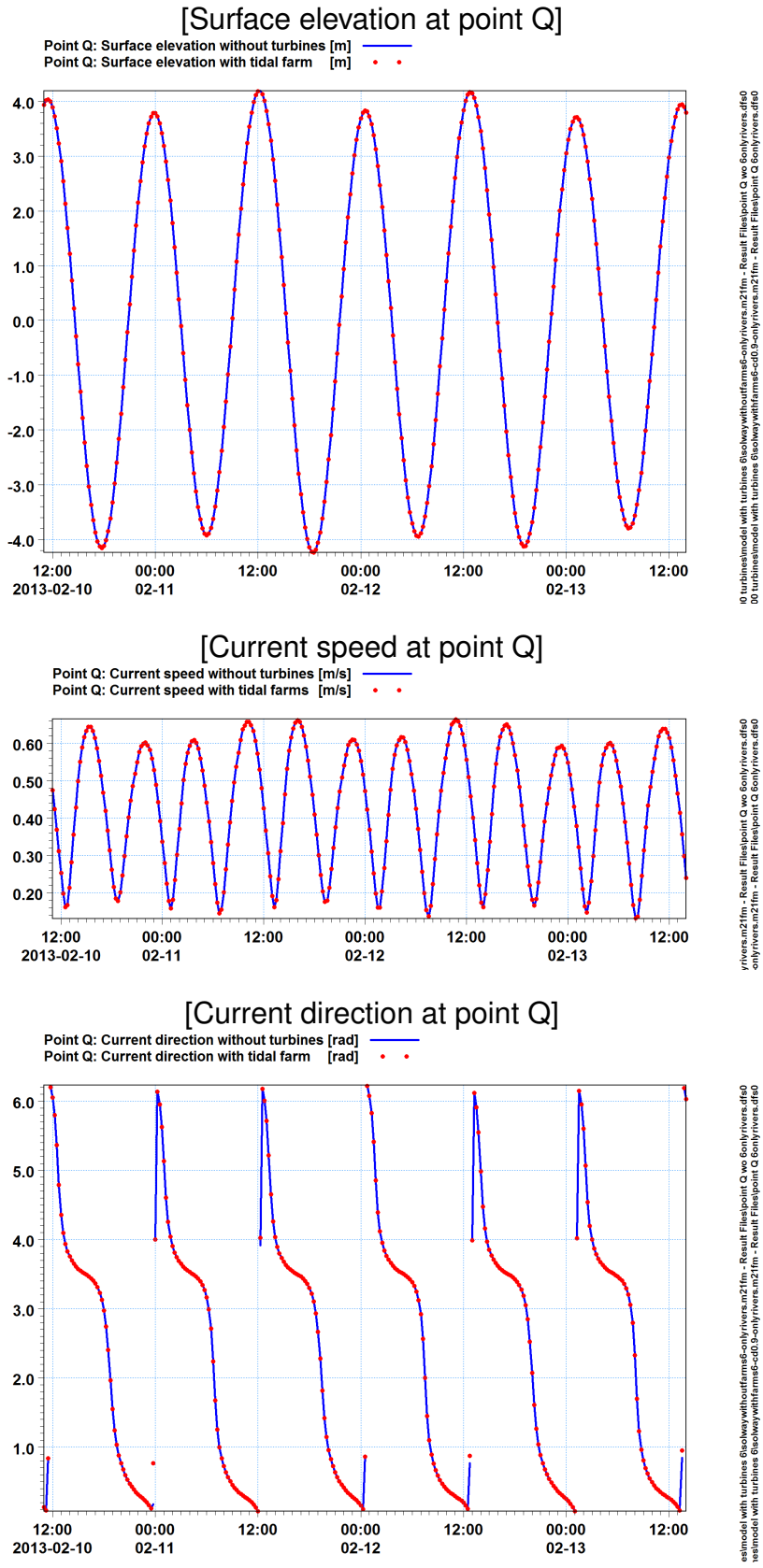

Figure 4.24: Comparison of results at point Q (288913.43, 520093.59) in the fluvial scenario with and without the tidal farm 2A

Simulation period	100 h
Time step	900 sec
Elements	20278 (staggered layout)
	21184 (parallel layout)
Maximum mesh size	1 km^2
Bed Roughness (1/n)	22 $m^{1/3}/s$
Smagorinsky coeff.	0.28

Table 4.16: Parameters of the initial model of the Solway Firth with tidal farms

4.3.5 Results

The simulations with tidal farms were run and the results of the water levels in the estuary were extracted and compared with the ones of the model without tidal farms:

- Initially, the results of the water levels in the model of the estuary without turbines were obtained for the last 300 time steps, because it was considered that the results in the first 100 time steps would be related to the warming up period. The same process was followed for the results of water levels in the different models with tidal farms.
- Then, the statistics tool in MIKE 21 was used to calculate the maximum values of the water levels during the period of the simulation on each model (with and without turbines).
- Finally, the effects of the tidal farms on the existing levels of flood risk in

the estuary were calculated as the difference between the model with tidal farm and the model without turbines under the same scenario. Therefore, negative values of the difference would indicate a decrease in the maximum water levels while positive values would be related to an increase of the water levels.

The differences between the models with and without turbines for each tidal farm on every scenario have been plotted in figures 4.26 to 4.37

In order to have a more comprehensive idea about the effect of the tidal farms over the extreme water levels in the estuary, the maximum increase and decrease between the situation without the turbines and with the tidal farms have been calculated for each case and presented in tables 4.17 to 4.19.

The locations where these maximum changes appear inside the estuary, taking into account figure 4.38, have also been included in the analysis.

It can be highlighted from the results that:

- The maximum reduction in peak water levels happens at the inner part of the estuary in all cases whereas the maximum increase of peak water levels occurs in the outer area.
- The maximum increase in water levels is of the order of centimeters whereas the maximum decrease is of the order of decimeters.
- The highest values of the maximum increase and decrease of water levels happen in scenario 2 and 1, respectively. Therefore, the influence on the results seems to be case specific to the type of flooding.
- In general, tidal farms with the staggered layout have a bigger impact than farms with a parallel layout comprising the same number of turbines and same spacings.
- The effect of increasing the number of turbines (from 1024 to 4032 turbines) is more noticeable in relation to the reduction of the peak water levels at the inner estuary.

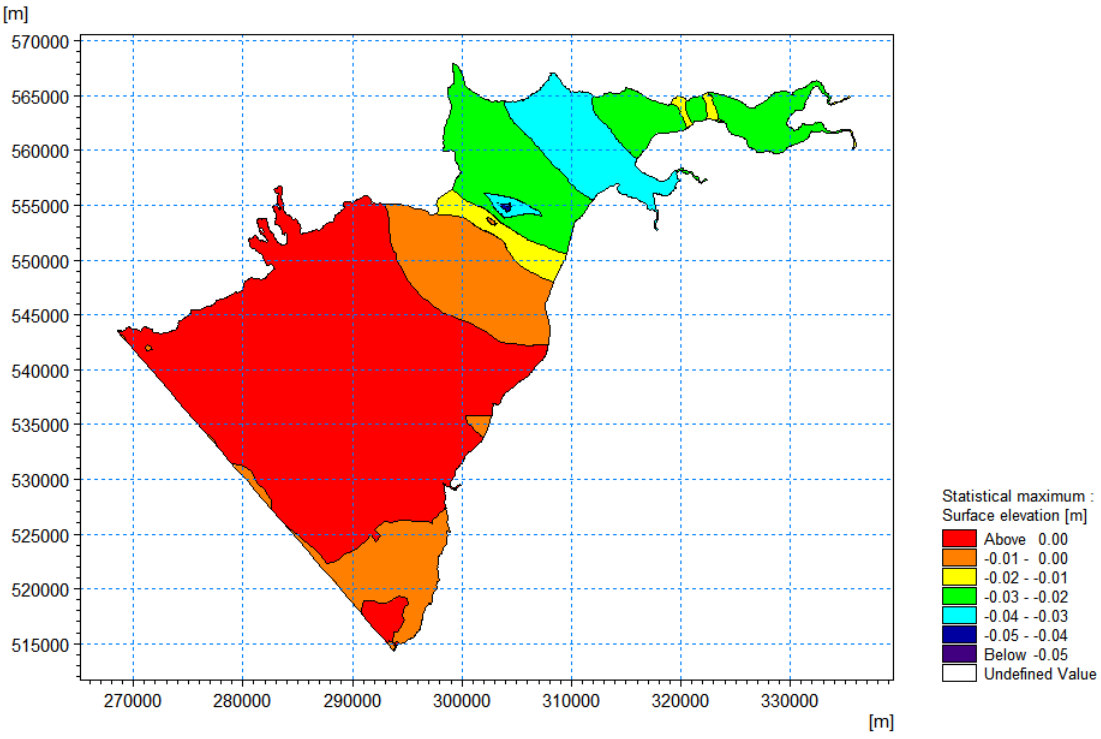

Figure 4.26: Difference in maximum water levels with tidal farm 1A (32x32 turbines arranged in parallel layout) under coastal flooding scenario.

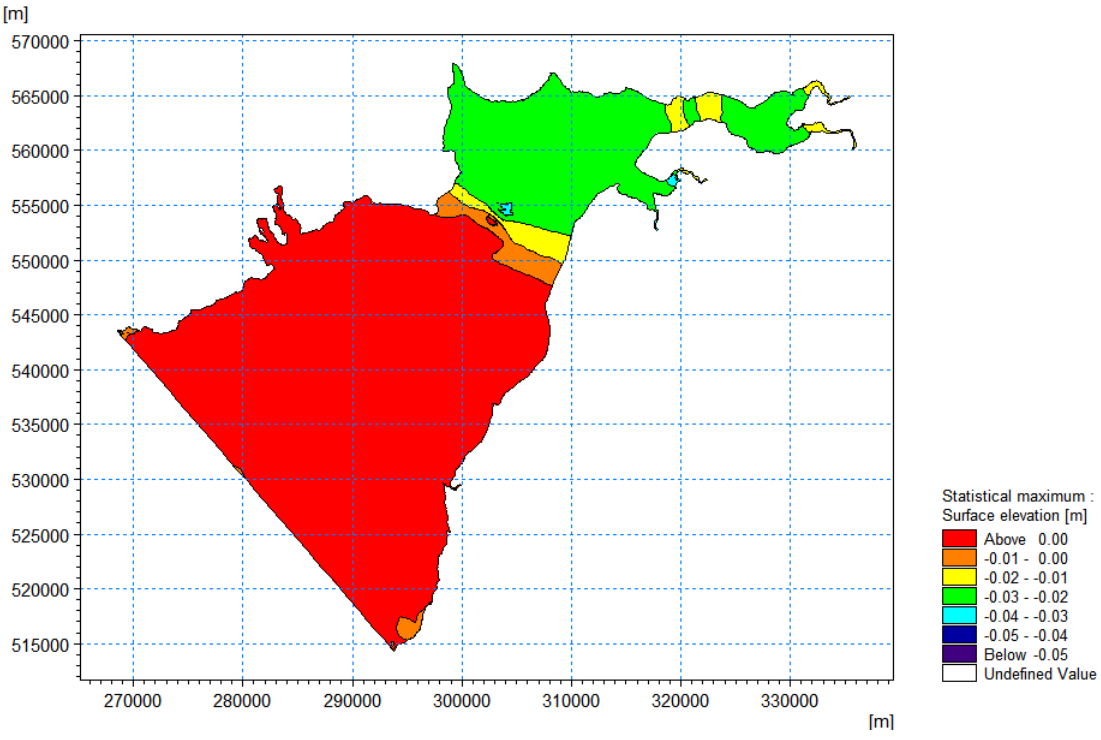

Figure 4.27: Difference in maximum water levels with tidal farm 1A (32x32 turbines arranged in parallel layout) under fluvial flooding scenario.

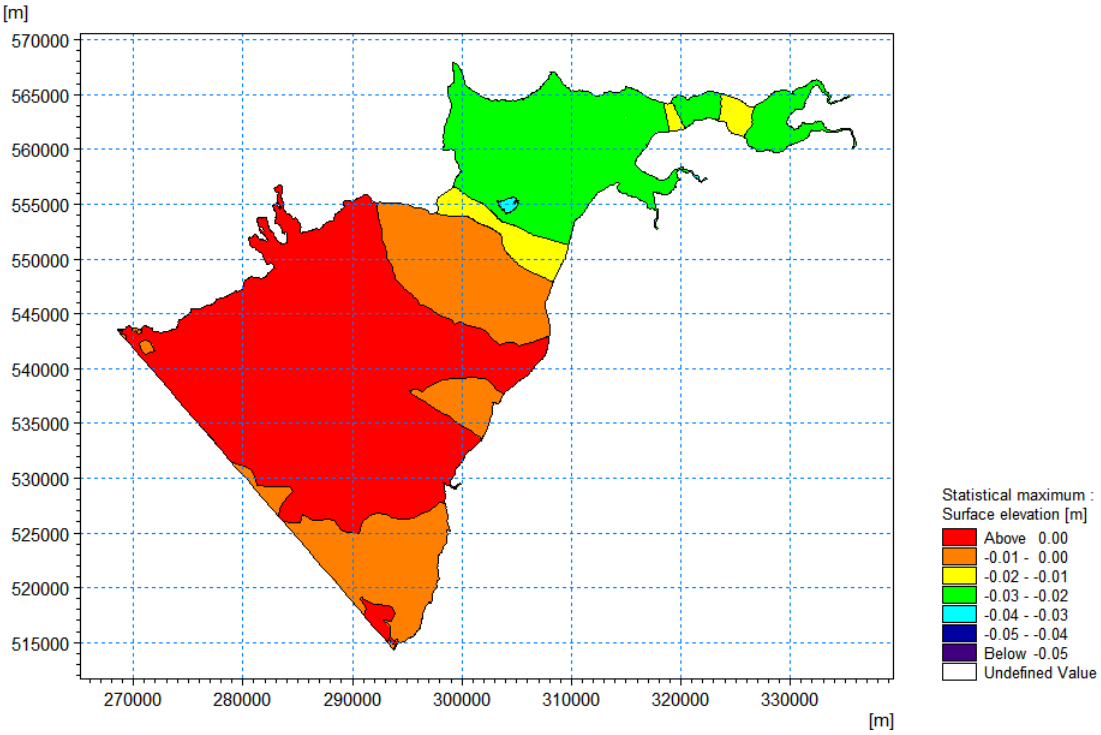

Figure 4.28: Difference in maximum water levels with tidal farm 1A (32x32 turbines arranged in parallel layout) under coastal and fluvial flooding scenario.

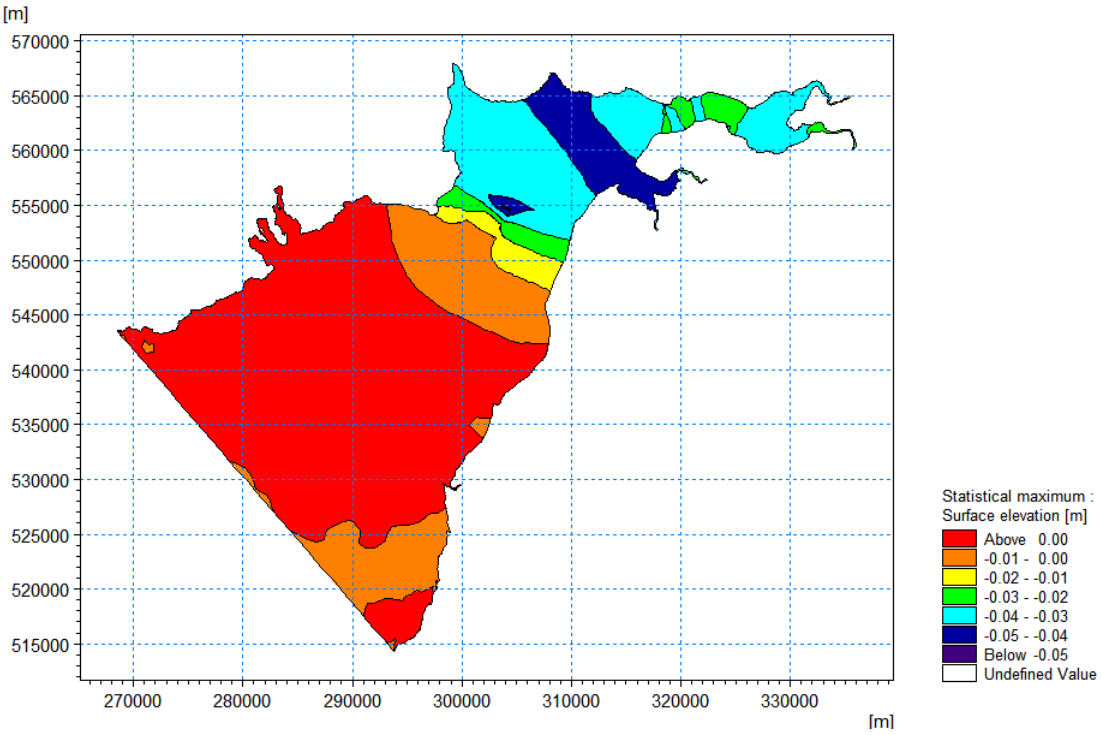

Figure 4.29: Difference in maximum water levels with tidal farm 1B (32x32 turbines arranged in staggered layout) under coastal flooding scenario.

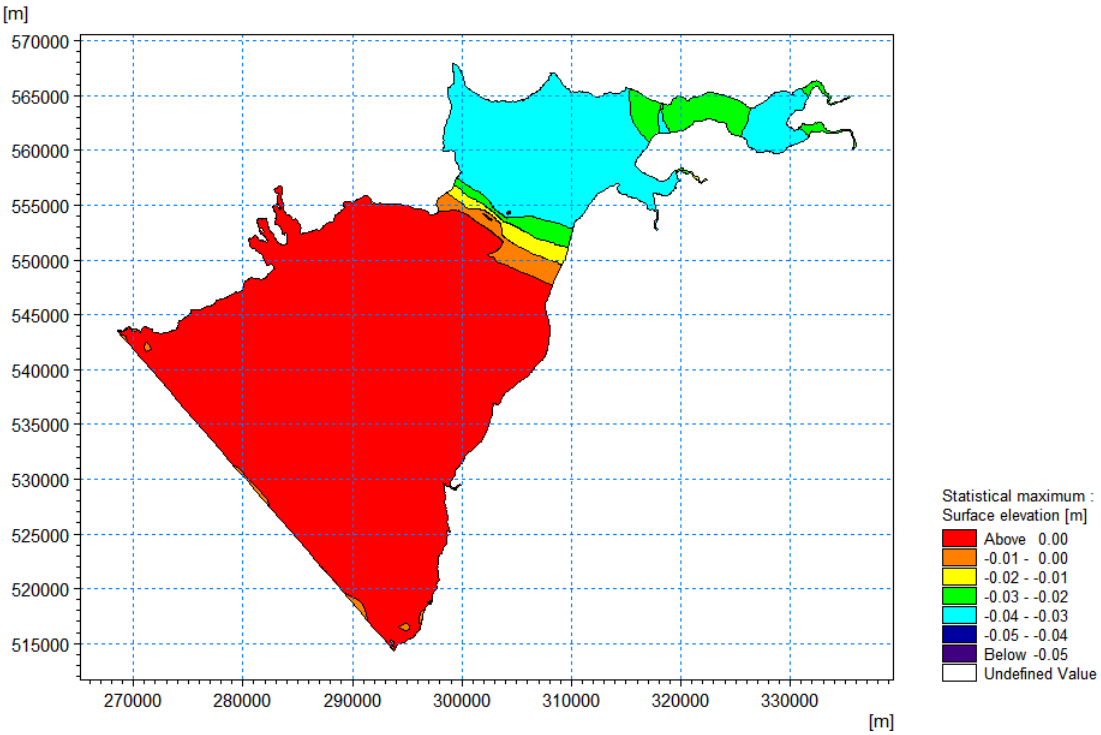

Figure 4.30: Difference in maximum water levels with tidal farm 1B (32x32 turbines arranged in staggered layout) under fluvial flooding scenario.

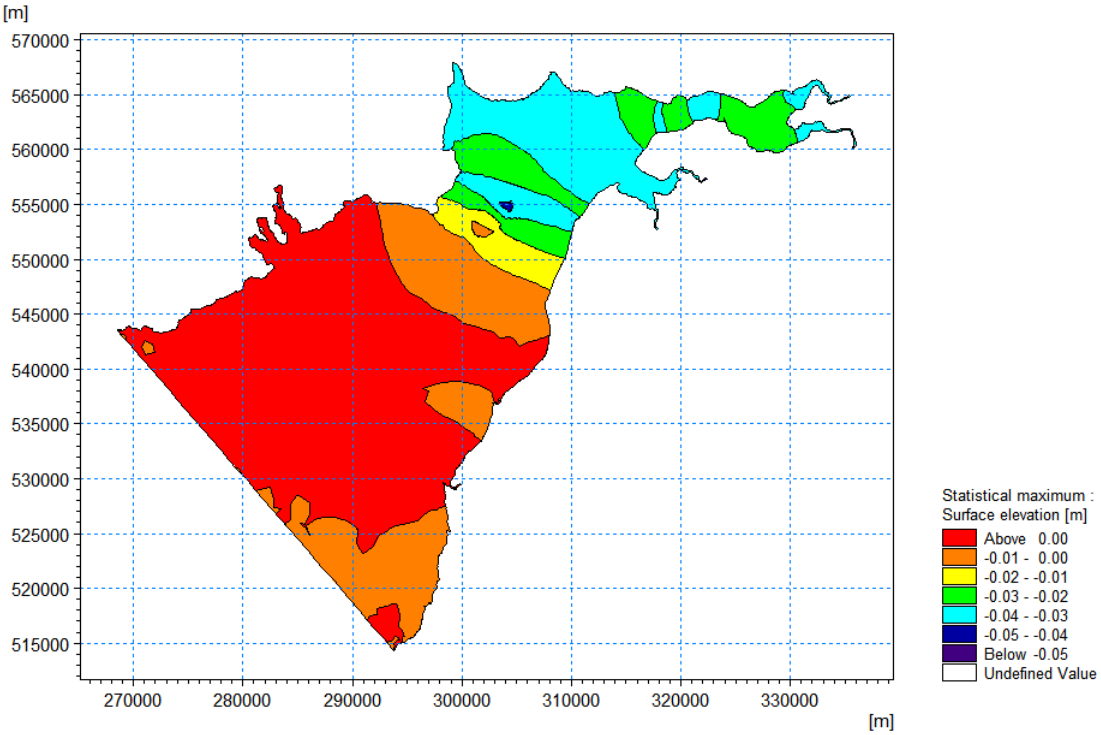

Figure 4.31: Difference in maximum water levels with tidal farm 1B (32x32 turbines arranged in staggered layout) under coastal and fluvial flooding scenario.

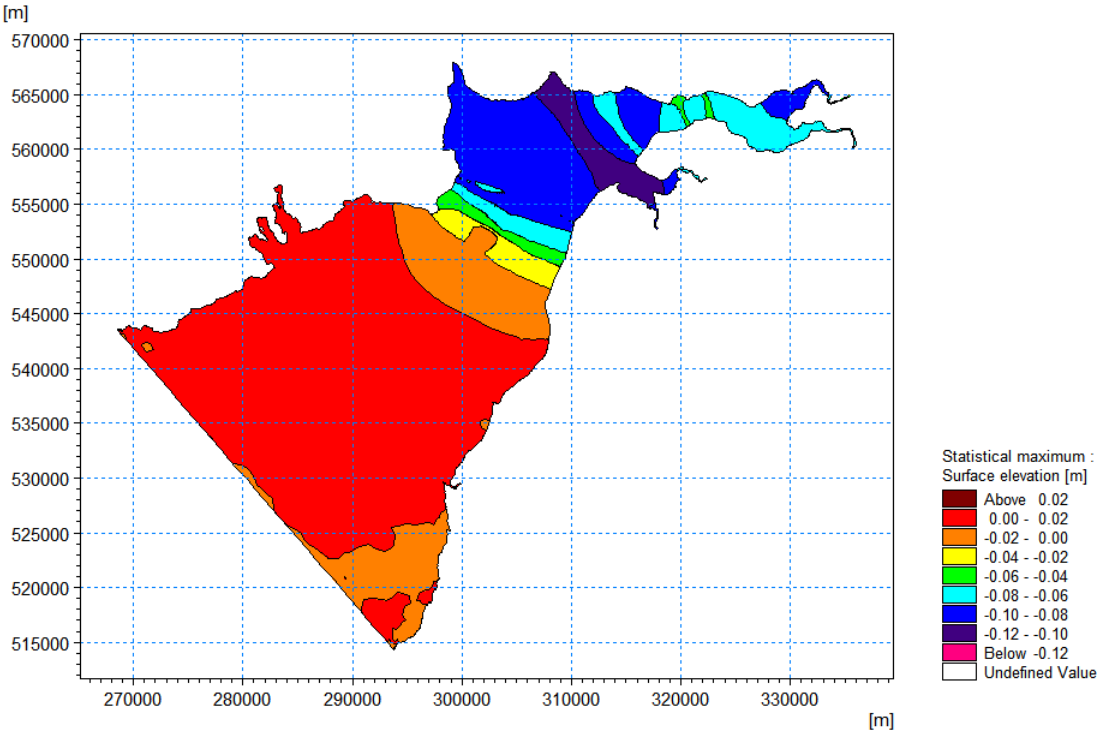

Figure 4.32: Difference in maximum water levels with tidal farm 2A (84x48 turbines arranged in parallel layout) under coastal flooding scenario.

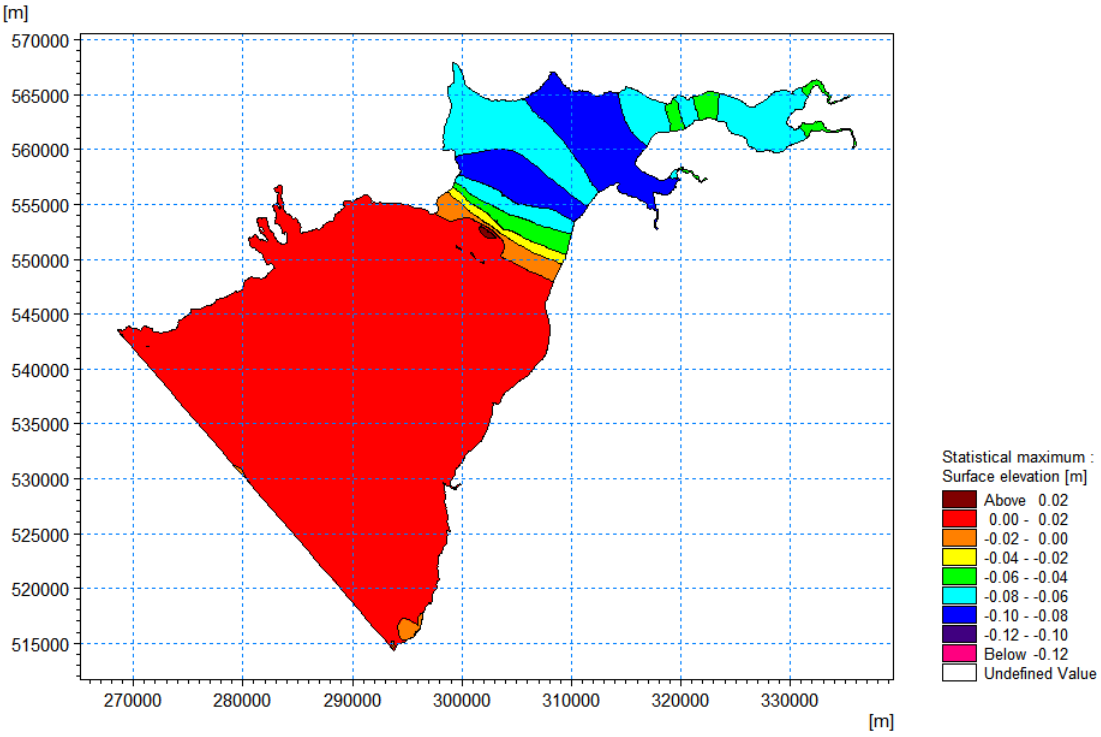

Figure 4.33: Difference in maximum water levels with tidal farm 2A (84x48 turbines arranged in parallel layout) under fluvial flooding scenario.

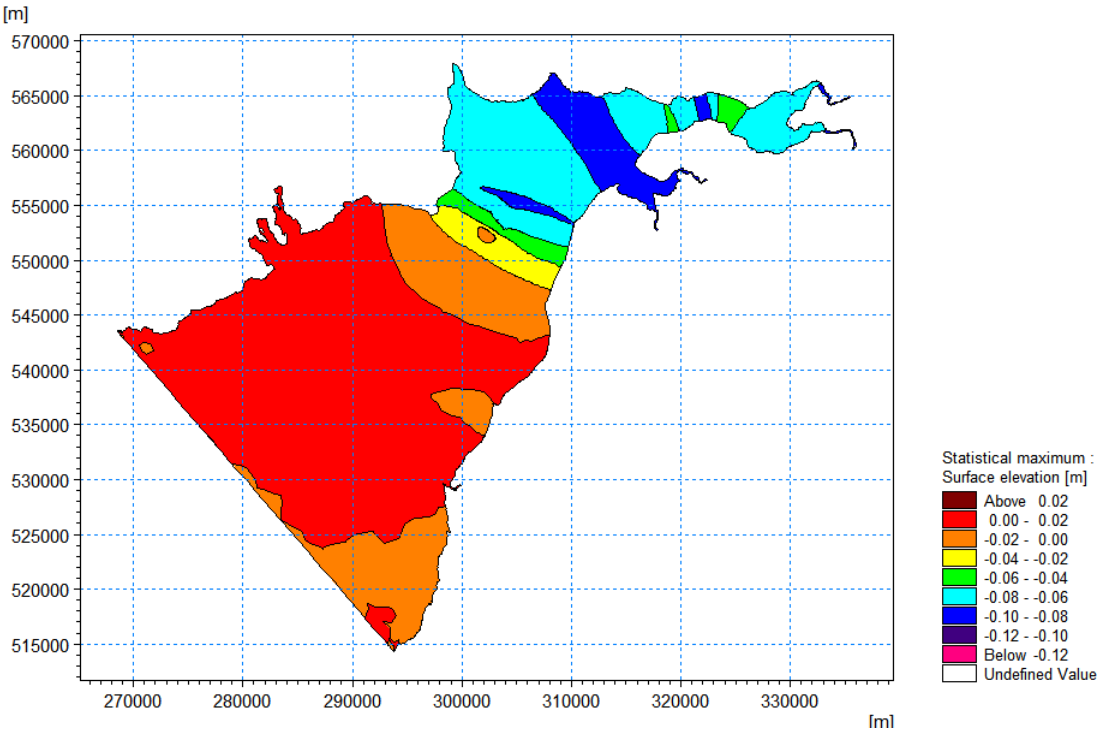

Figure 4.34: Difference in maximum water levels with tidal farm 2A (84x48 turbines arranged in parallel layout) under coastal and fluvial flooding scenario.

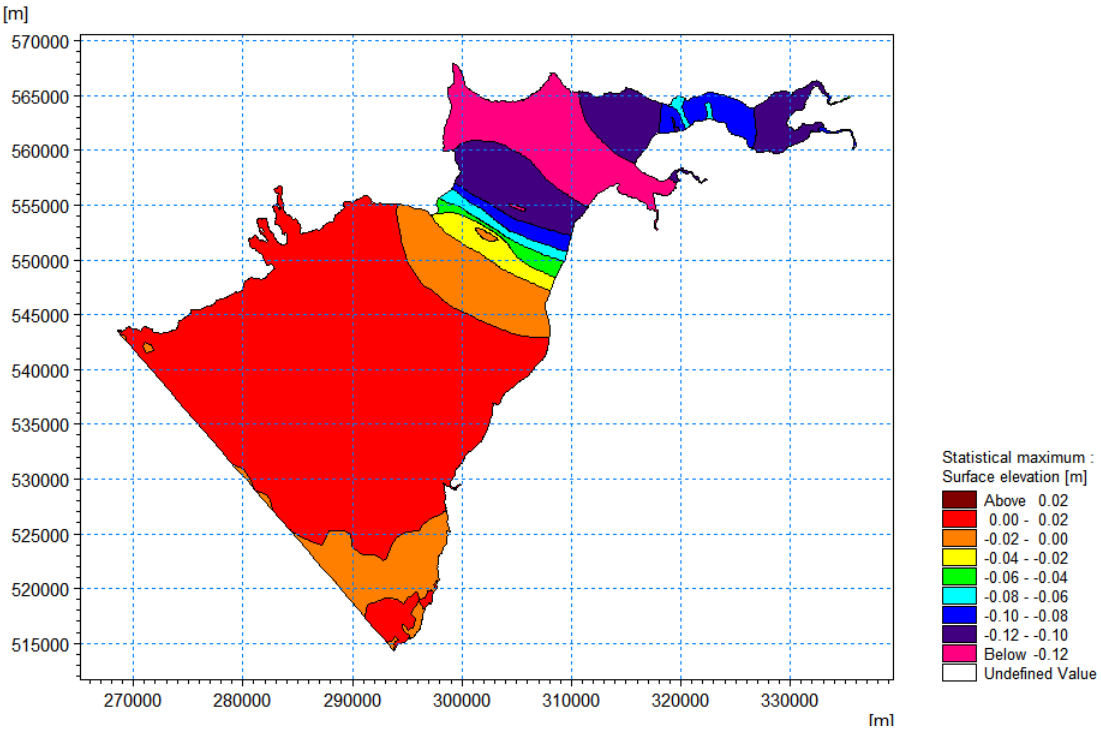

Figure 4.35: Difference in maximum water levels with tidal farm 2B (84x48 turbines arranged in staggered layout) under coastal flooding scenario.

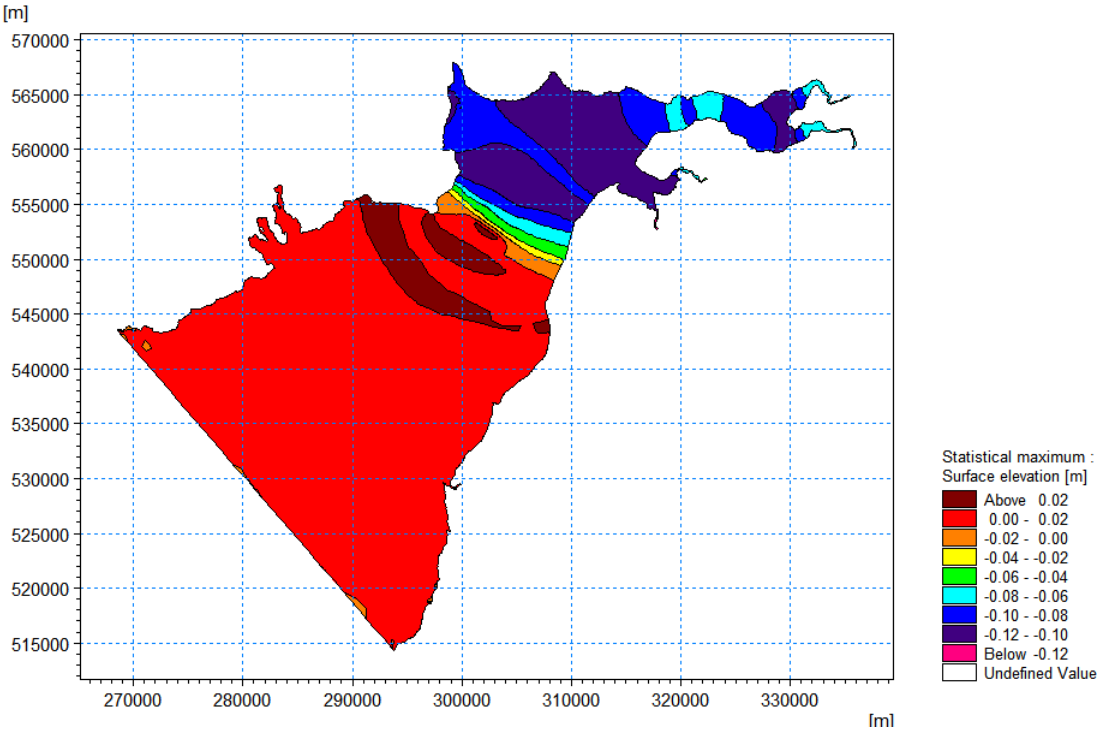

Figure 4.36: Difference in maximum water levels with tidal farm 2B (84x48 turbines arranged in staggered layout) under fluvial flooding scenario.

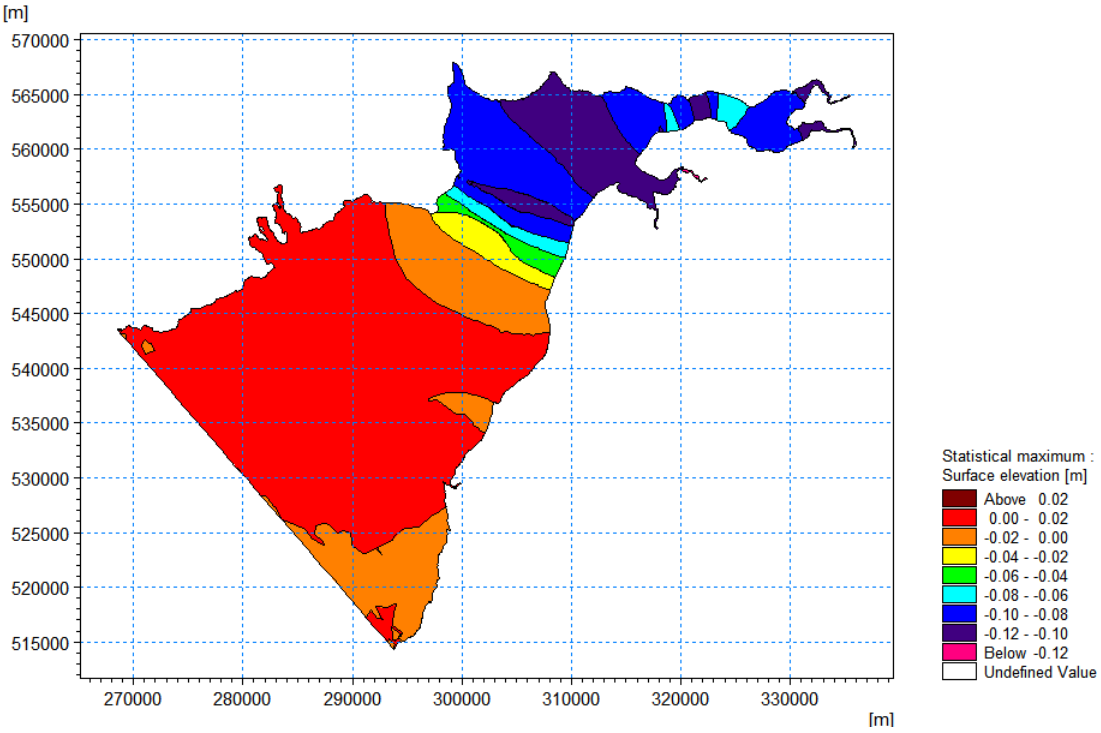

Figure 4.37: Difference in maximum water levels with tidal farm 2B (84x48 turbines arranged in staggered layout) under coastal and fluvial flooding scenario

Tidal farm	Number of turbines	Layout	Scenario 1			
			Max increase /	Location	Max decrease /	Location
1A	1024	Parallel	0.002	Outer part	-0.047	Inner part
1B	1024	Staggered	0.003	Outer part	-0.052	Inner part
2A	4032	Parallel	0.007	Outer part	-0.104	Inner part
2B	4032	Staggered	0.010	Outer part	-0.136	Inner part

Table 4.17: Maximum increase and decrease (m) of peak water levels and their locations in the coastal flooding scenario

Tidal farm	Number of turbines	Layout	Scenario 2			
			Max increase /	Location	Max decrease /	Location
1A	1024	Parallel	0.002	Outer part	-0.038	Inner part
1B	1024	Staggered	0.009	Outer part	-0.042	Inner part
2A	4032	Parallel	0.031	Outer part	-0.094	Inner part
2B	4032	Staggered	0.028	Outer part	-0.122	Inner part

Table 4.18: Maximum increase and decrease (m) of peak water levels and their locations in the fluvial flooding scenario

Tidal farm	Number of turbines	Layout	Scenario 3			
			Max increase /	Location	Max decrease /	Location
1A	1024	Parallel	0.002	Outer part	-0.038	Inner part
1B	1024	Staggered	0.002	Outer part	-0.043	Inner part
2A	4032	Parallel	0.005	Outer part	-0.098	Inner part
2B	4032	Staggered	0.007	Outer part	-0.128	Inner part

Table 4.19: Maximum increase and decrease (m) of peak water levels and their locations in the combined coastal and fluvial flooding scenario

Figure 4.38: Parts of the estuary with respect to the location of the tidal farm

4.4 Conclusions

This Chapter shows that the Solway Firth estuary can be regarded as a valid example for demonstrating the methodology proposed for the assessment of the impact on flood risk derived from tidal farms in estuaries. There is a relevant tidal stream resource in the estuary and high levels of flood risk.

It can be also remarked that several difficulties have been found regarding the available datasets for the creation of the numerical model. Generally, in the shallower parts of the estuary, there is a lack of coverage of the bathymetry, related to the navigational purposes of some of the data sources, as well as errors, which have been identified in the other available information. Therefore, new data covering those areas was necessary in order to identify the locations of the tidal farms and their impacts on the peak levels in a more realistic way. Similarly, after producing this Chapter, it was found that the current speed values used for the calibration of the model were not averaged over the total depth but they were only related to a point at a certain depth where the measurements were taken . Thus, it does not provide a representative current speed profile and

the calibration of the model would have to be done against alternative data. For all these reasons, it can be concluded that there is a need for more accurate data, in terms of bathymetry and observed measurements, in order to provide a model closer to the real conditions in the estuary.

Anyway, from a theoretical point of view, the following conclusions can still be extracted from the results presented in this Chapter for this specific model of the Solway Firth:

- For all cases and scenarios, the maximum decrease of peak levels due to the tidal farm is higher than the maximum increase and the locations where these maximum changes happen are similar. This would mean a loss of intertidal areas due to permanent submersion at some locations whereas the effect could be beneficial for the flood risk levels at some other places around the coastline.

- The impact of the farm depends on the flooding type, although a similar order of magnitude can be found for the maximum effects of the same cases under different events.

- There is no linear relationship between the maximum effects on peak levels and the number of turbines in the farm.

Chapter 5

Solway Firth Estuary - Improved model

5.1 Introduction

As was mentioned in subsection 4.2.2, the bathymetry used in the initial model (Celtic Seas dataset provided by BODC) features some errors in the intertidal regions [Brown et al., 2001]. On the other hand, these regions are very important for the estuarine behaviour as they represent the third-largest area of continuous mudflats and sandflats in the UK [Joint Nature Conservation Committee , 2016]. Therefore, when a more realistic bathymetry of the area of interest was found the model was modified to include it and consequently this led to other changes, related to the design of the tidal farms.

In this Chapter, the improved model is described in terms of the input parameters involved as well as the new process of calibration and validation necessary due to the significant changes introduced with respect to the initial model. In this regard, the size and location of the tidal farms have varied according to the energy resource analysis and other constraints in the outer estuary. As a result, the domain of the model has been enlarged in order to avoid reflections of waves created by the tidal farms at the boundary. Finally, the results for the effect of the tidal farms on peak water levels under a coastal

flooding scenario are explained and some conclusions are derived from them.

5.2 Improved model

5.2.1 Bathymetry

The bathymetry used for the improved model was obtained from the study by Natural Power [2015] for the deployment of an offshore wind farm in the estuary. Being based on surveys carried out in the estuary between 2001 and 2002, it provided a more realistic representation of the inner part of the estuary than the dataset used in the initial model. According to Natural Power [2015], surveys were taken accross the windfarm licensed area with spacings between readings of 150 and 300 m as well as along the cable route and several transects covering regular distances along the main channels and across the estuary. This information was digitised in order to be used in MIKE 21.

Due to the need for a more detailed bathymetry around the area of the station used for the validation of the model (Workington port), the data from EDINA Marine Digimap Service [2015c], with a scale of 1:10000, have also been digitised and incorporated to the model. Previously, a conversion of the units for the depths from Chart Datum (CD) to Mean Sea Level (MSL), according to table III of United Kingdom Hydrographic Office [2012], was carried out. For the same reason, the shoreline has been defined by means of the information provided by EDINA Marine Digimap Service [2015a], which was updated in 2014. The resulting bathymetry map after interpolation of the mesh of the model over the new datasets can be found in figure 5.1. The bathymetry used in the initial model is included in figure 5.2 in order to appreciate the differences between both datasets at the inner estuary.

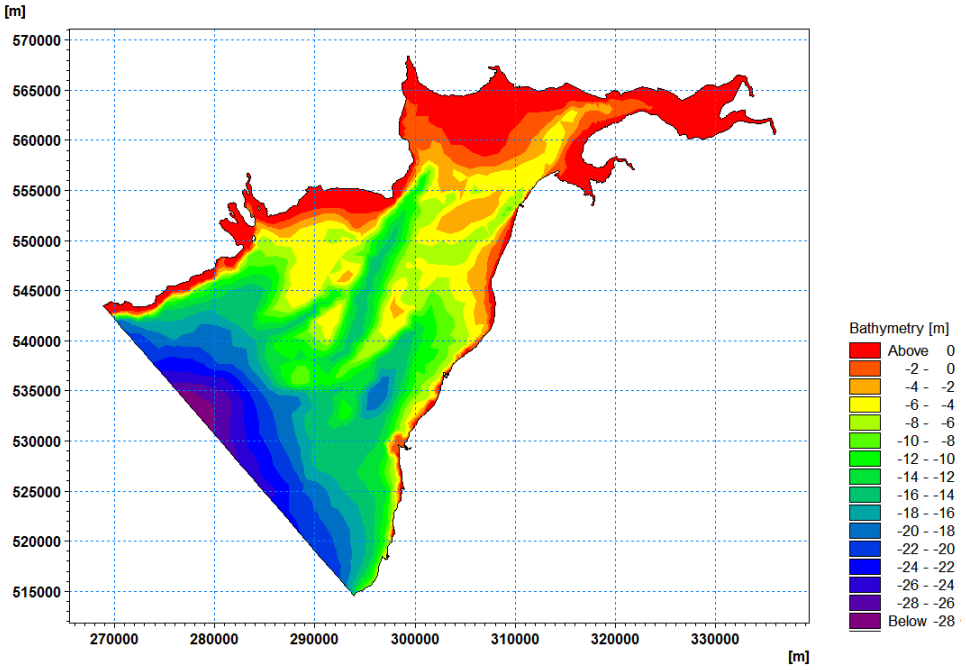

Figure 5.1: Bathymetry created in MIKE 21 through interpolation of data from Natural Power [2015] and EDINA Marine Digimap Service [2015c] over the computational mesh. Depths in MSL

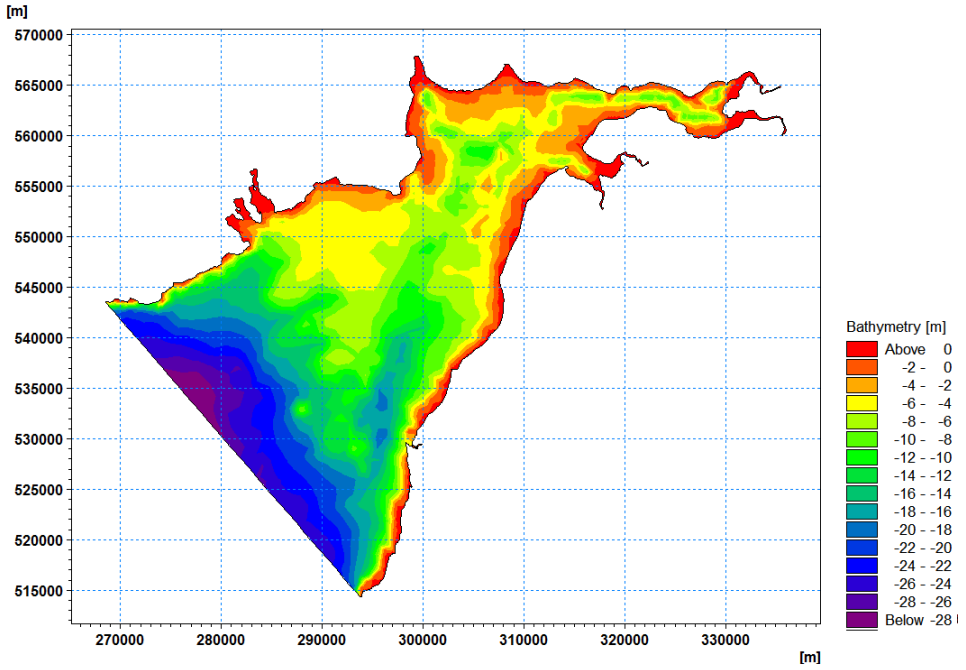

Figure 5.2: Bathymetry extracted from the BODC Celtic Seas dataset, depths related to MSL.

5.2.2 Sensitivity analysis of the mesh size

The domain of the model covered the same extension as the initial model and before interpolating the computational mesh over the new bathymetry, a sensitivity analysis of the mesh size was carried out in order to find a good compromise between the resolution and the computational time of the simulations. Five different simulations were used in the analysis, with details as shown in table 5.1, where mesh size refers to the maximum area of the elements allowed in the domain. The simulation period covered 480 time steps of 900 seconds over the period between 1st and 6th august of 2004 at 00:00 hours. Figure 5.3 gives an idea about the different resolutions for each simulation.

Mesh ID	Mesh size (x10^3 m^2)	Number of elements	Number of nodes	Elapsed time
1	100000	23562	13263	7h 56min
2	250000	14414	8620	3h 54min
3	500000	11481	7178	3h 5min
4	750000	10544	6706	2h 52min
5	1000000	10137	6502	2h 34min

Table 5.1: Simulation features for the sensitivity analysis of the mesh size.

Regarding the other parameters of the simulations, a uniform coefficient of 32 $m^{1/3}/s$ (default value of the inverse of Manning's coefficient in MIKE 21) was used for the bed roughness and a constant Smagorinsky's coefficient of 0.28 was used to represent the turbulence. The open boundary was forced by water levels predicted during the period of the simulation at the boundary with the MIKE 21 Toolbox, based on the Global Tide Model by Doodson [1921] with a resolution of $0.125°$ by $0.125°$. The flood and dry function was activated, with drying depth of 0.005 m, flooding depth of 0.05 m and wetting depth of 0.1 m.

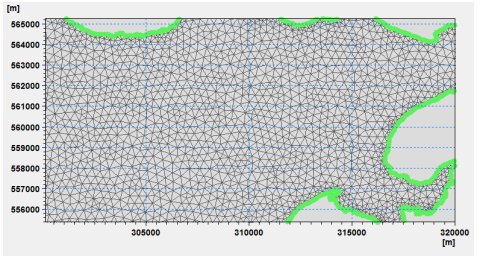

(a) Mesh 1

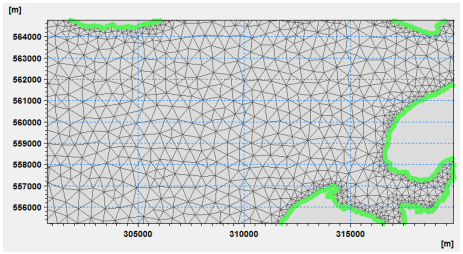

(b) Mesh 2

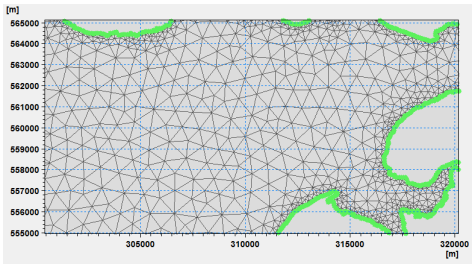

(c) Mesh 3

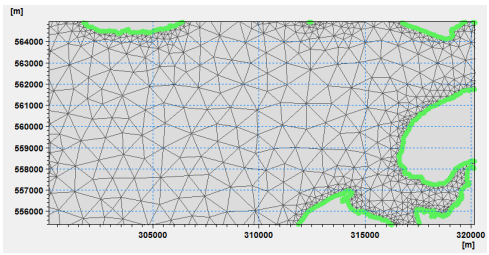

(d) Mesh 4

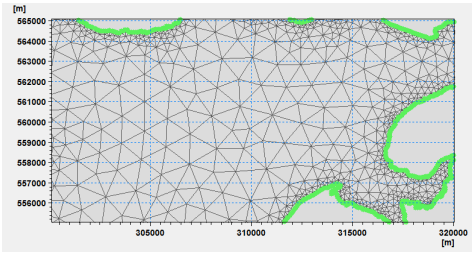

(e) Mesh 5

Figure 5.3: Different mesh sizes used in the sensitivity analysis of the mesh size.

The critical Courant-Fiedrich-Levy number was set to 0.8.

The results of water levels from these simulations where compared at a point with coordinates (298865.306, 529553.265) m (Easting, Northing). The results from the coarser mesh sizes were subtracted from those on the finest mesh size (mesh 1). The mean absolute error and standard deviations of these differences are presented in table 5.2. For the coarsest mesh, errors are in the order of those obtained in the work by Ahmadian et al. [2010]. Therefore, there is not a significant error introduced by the use of a coarser mesh, which provides a faster solution.

Mesh ID	Water levels (m)		Current speed (m/s)	
	MAE	STDEV	MAE	STDEV
2	0.007	0.012	0.004	0.006
3	0.007	0.012	0.004	0.006
4	0.011	0.012	0.004	0.006
5	0.026	0.024	0.013	0.013

Table 5.2: Mean absolute error and Standard deviation from sensitivity analysis of the mesh size

5.2.3 Calibration

For the calibration of the model, two parameters were modified: the bed roughness, represented by the Manning's formula, and the turbulence. The Smagorinsky coefficient was fixed to a uniform value of 0.28 over the domain while the inverse of the Manning coefficient was varied between 20 and 40 $m^{1/3}/s$. The simulations were run over a period of one month (August 2004) and the time step was 900 seconds. Higher order schemes both for the time and space discretisation were used with a critical CFL number of 0.8. Based on the results from the sensitivity analysis of the mesh size, the maximum element size used for the interpolation of the bathymetry over the computational mesh was chosen equal to 1 km^2. Water levels predicted with the Global Tide Model tool in MIKE 21 were used at the open boundary, being the initial conditions given by the average level at the boundary.

The results from the simulations with a fixed Smagorinsky's coefficient and a different bed roughness were compared with observed water levels at Workington Port. The data were developed through the UK Tide Gauge Network project, provided by the British Oceanographic Data Centre and

funded by the Proudman Oceanographic Laboratory. The location of Workington Port station is approximately given by a squared symbol in figure 5.4, in which other locations of interests for the next sections of this chapter are also represented.

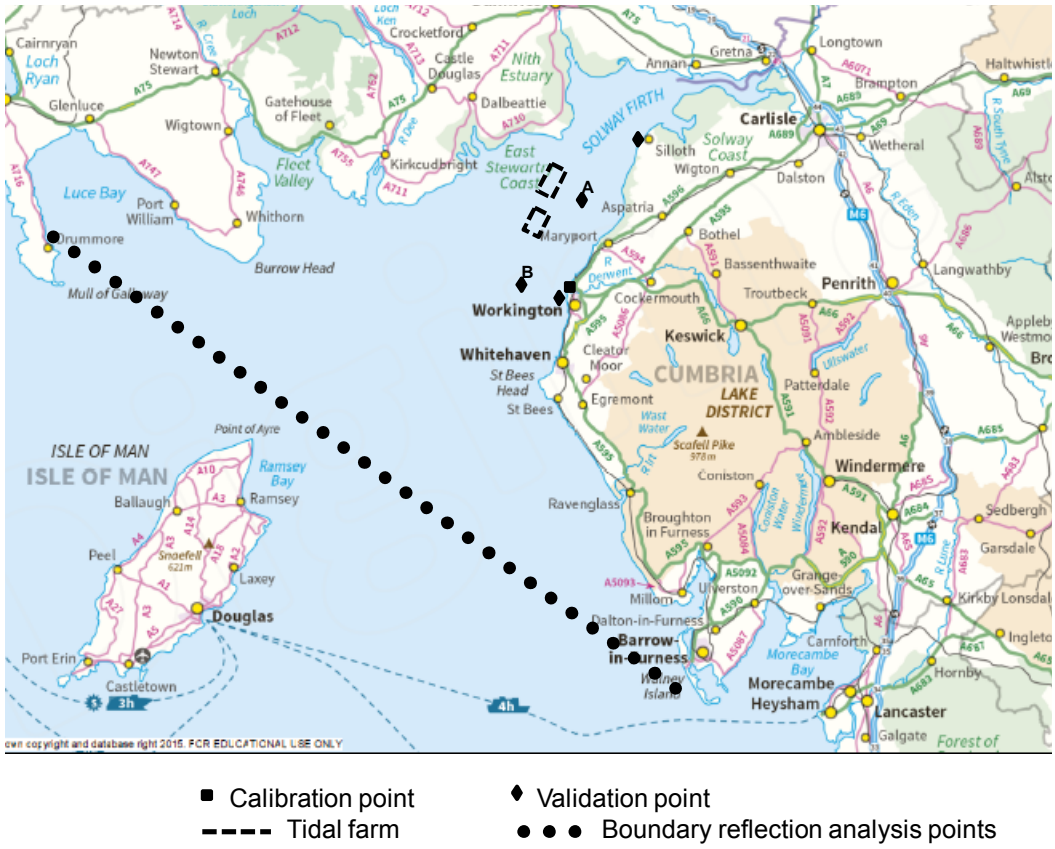

Figure 5.4: Location of the stations for the calibration, validation, boundary reflection analysis and tidal farms in the improved model of the Solway Firth.

Following the guidelines for estuarine modelling given by Bartlett [1998], the spring and neap tidal ranges were obtained during the one month period. The differences between the observed and modelled values for each range of parameters can be found in table 5.3. These differences are in agreement with the requirements of water levels being within 15% for spring tidal range or 20 % for neap ranges, indicated by Bartlett [1998].

Manning's M ($m^{1/3}/s$)	Difference (%)	
	Spring range	Neap range
20	1.957	15.785
25	0.830	15.541
32	0.089	15.421
40	-0.016	15.348

Table 5.3: Differences between observed and modelled results for water levels at Workington port obtained during the calibration of the bed roughness.

As can be seen from table 5.3, the differences are bigger for the neap tides than for spring tides. Taking this into account, M = 40 $m^{1/3}/s$ gives the smaller difference in neap tidal ranges.

The value of M = 40 $m^{1/3}/s$ was calculated in section 4.3.2 according to sediment maps in the area. Therefore, taking into account this fact and the results from the calibration this value has been chosen to perform the rest of the simulations of the improved model.

Regarding the calibration of the Smagorinsky's coefficient representing the turbulence in the model, five values have been used, from 0.2 to 1.0, which are the values recommended by DHI [2012a]. The simulations for the turbulence calibration had a fixed bed roughness coefficient of 40 $m^{1/3}/s$, as aforementioned, and the rest of the features were the same as in the simulations for the calibration of the bed roughness. The differences with the observed measurements produced the values shown in table 5.4, which are in agreement with the requirements of Bartlett [1998] for estuarine modelling.

Smagorinsky's coefficient	Difference (%)	
	Spring range	Neap range
0.20	-0.020	15.355
0.28	-0.016	15.348
0.50	-0.013	15.356
0.80	0.900	15.465
1.00	0.969	15.472

Table 5.4: Differences between observed and modelled results for water levels at Workington port obtained during the calibration of the turbulence.

As can be seen from table 5.4, the differences are similar but Cs = 0.28 gives a slightly smaller error in the neap tidal levels, thus it has been chosen for the rest of the simulations of the improved model in this Chapter.

5.2.4 Validation

For the validation of the model, a period of one month, between 9th February and 9th March of 2013 was used to compare the improved model with observed measurements of water levels at Workington port and Silloth dock as well as with the current directions at the tidal diamonds inside the domain. The locations of the aforementioned stations can be found in figure 5.4 from the previous section. The observations at Workington port were recorded at a bubbler tide gauge by the UK Tide Gauge Network project, provided by the British Oceanographic Data Centre and funded by the Proudman Oceanographic Laboratory. Water levels data at Silloth harbour were obtained through the Environment Agency. Regarding the comparison with velocities, tidal diamonds A and B from EDINA Marine Digimap Service [2015b] were found inside the domain which provided information about current speeds and directions, related to high tide times at Liverpool port. However, the current speed is difficult to compare because the

speed is only measured on the first 10 m [Blunden, 2009]. Therefore, only the current direction has been compared in this case.

The simulation for the validation of the model consisted of 3072 time steps of 900 seconds, allowing for a warm-up period of 3-4 days before the period indicated in the previous paragraph. The time integration and space discretisation of the governing equations followed high order schemes with a critical CFL number of 0.8. The flood and dry function was activated using 0.005 m, 0.05 m and 0.1m for the drying, flooding and wetting depths, respectively. The density parameter was set up as barotropic, given the well-mixed nature of the estuary and that the Coriolis forcing was variable inside the domain. Regarding the turbulence scheme and bed roughness, values of 0.28 and 40 $m^{1/3}/s$ were used for the Smagorinsky coefficient and the inverse of Manning's coefficient, according to the results from subsection 5.2.3. The model was forced by water levels predicted for the period of the simulation by means of the MIKE 21 tool, which is based on the theory by Doodson [1921]. The initial conditions consisted of water levels as an average of the predicted values for the first time step and zero velocity.

Figure 5.5 shows the time series of observed and modelled water levels during the period of the validation of the model at Workington port and Silloth dock.

Following the recommendations of Bartlett [1998], the differences between the spring and neap tidal ranges from the model and the observations were compared, as can be seen in table 5.5. The results are within the range of 15 % for spring tides and 20 % for neap tides, as indicated by Bartlett [1998] for estuaries.

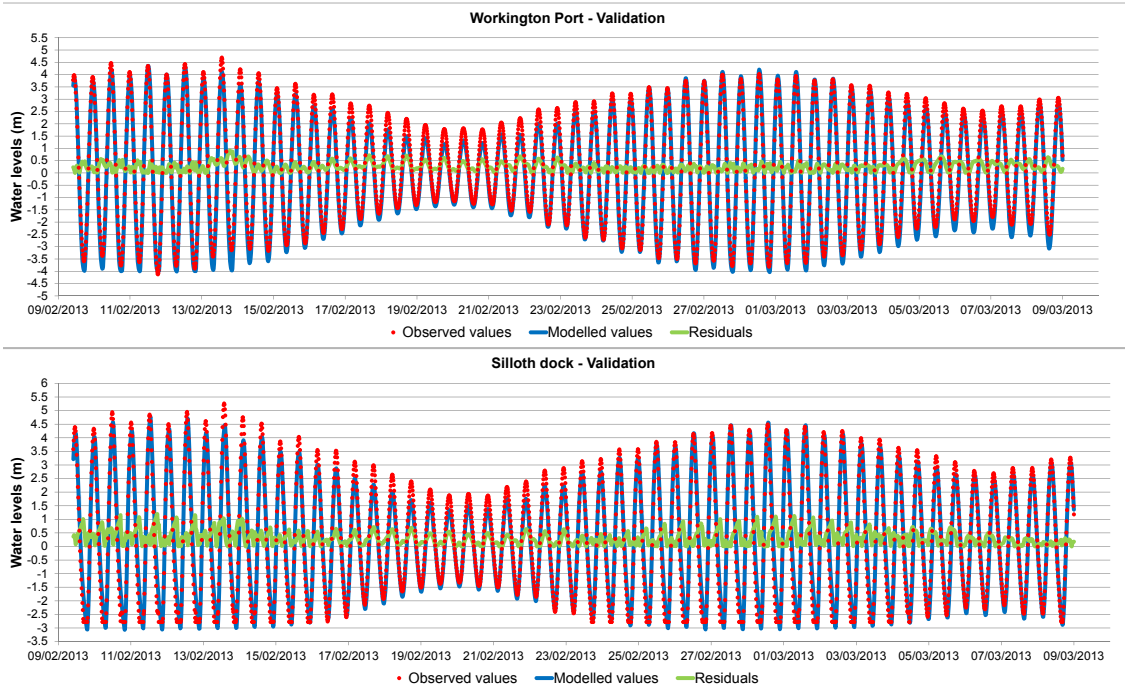

Figure 5.5: Comparison between observed water levels and modelled results at Workington port (upper graph) and Silloth dock (lower graph) for the validation of the model

Station	Difference (%)	
	Spring range	Neap range
Silloth dock	2.468	12.035
Workington port	4.871	15.918

Table 5.5: Differences between observed and modelled results for water levels at Silloth dock and Workington port obtained during the validation of the improved model.

Regarding the comparison with current directions from the Admiralty Chart diamonds, the graphical results can be seen in figures 5.6 and 5.7. The modelled values are close to the ones provided by the Admiralty Charts in the area of the estuary.

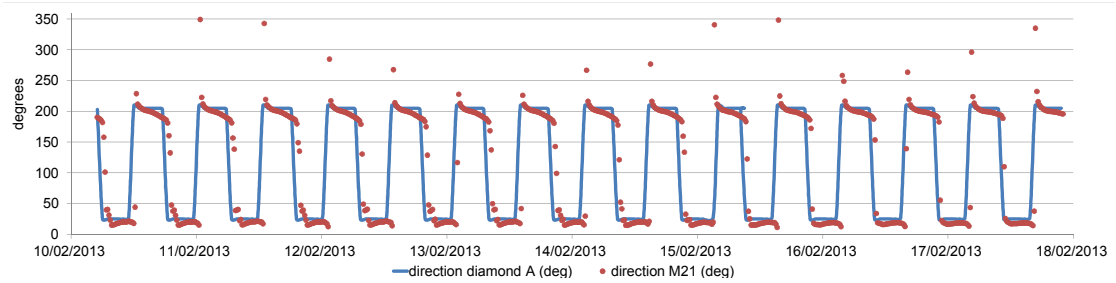

Figure 5.6: Current directions at tidal diamond A from Admiralty Chart 1346-0 and modelled results (red dots) obtained during the validation of the improved model.

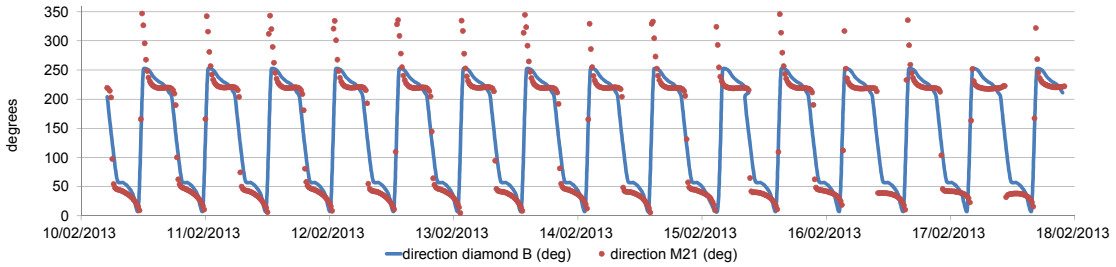

Figure 5.7: Current directions at tidal diamond B from Admiralty Chart 1346-0 and modelled results (red dots) obtained during the validation of the improved model.

5.2.5 Tidal farm locations

In order to identify the potential locations of the tidal farms in the improved model, first, the values for the maximum speed of the current were analysed during the period of the simulation used for the validation of the model. The statistics tool in MIKEZero Data Manager allowed the calculation of the maximum speeds over the domain, as shown in figure 5.8.

Considering that velocities over 1 m/s are more interesting for energy extraction, figure 5.8 shows that the areas in the central part or the main channels of the estuary could be potential areas for the deployment of instream tidal turbines. However, it is also necessary to take into account the turbines size and the related limitation of the minimum water depth at those sites.

Considering that all the turbines in the tidal farm have the same size, for simplicity reasons and reduction of the manufacturing costs, the turbine diameter has been set up to 5 m. Sustainable Energy Ireland [2005] indicates that up to 70% of the depth of the flow field might be occupied by the tidal energy devices. Therefore, locations with a minimum water depth of 7 m would be desirable, according to the previous idea.

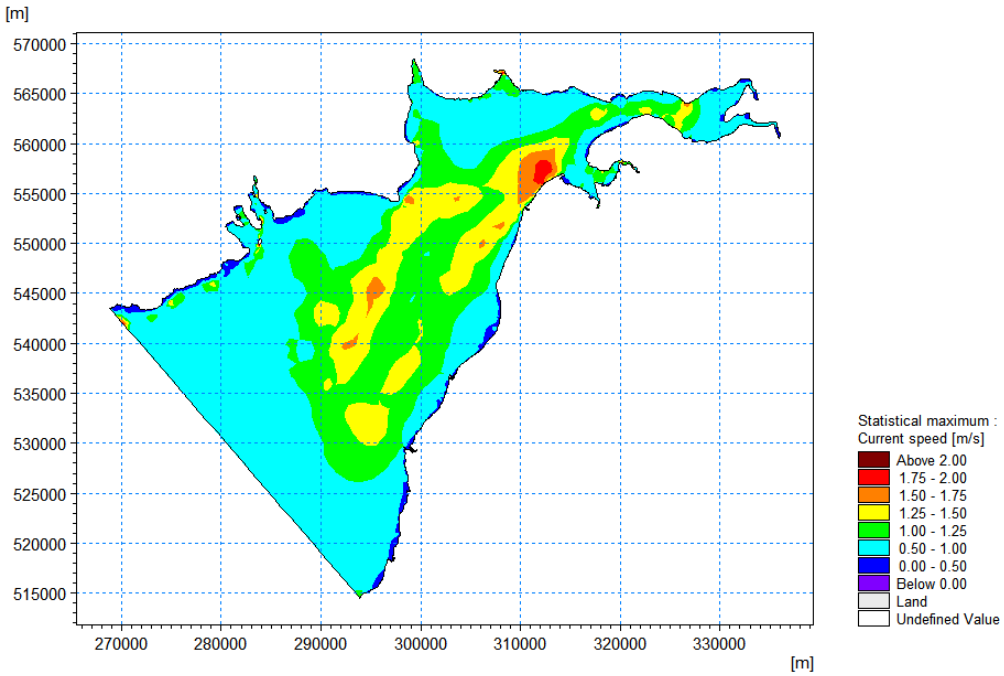

Figure 5.8: Maximum current speed (m/s) at the domain of the improved model during one month simulation.

The minimum water depths over the month period in the improved model are shown as isolines in figure 5.9. Figure 5.10 shows a combination of both requirements (current speed over 1 m/s and minimum water depths above 7 m) and it gives a better idea about the potential locations of the tidal farms according to the improved model. However, there are also other constraints related to the real situation at the estuary that affect the location of the turbines in a practical sense. Figure 5.11 from Natural Power [2015] shows the existence of navigational channels and an offshore wind farm already deployed in the area of interest, amongst others.

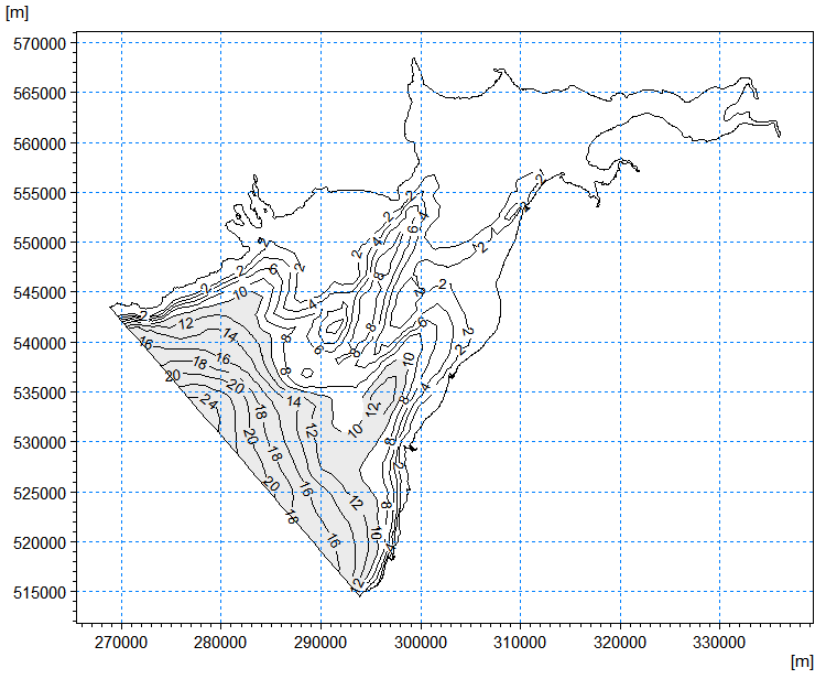

Figure 5.9: Minimum water depths (m) at the domain of the improved model during one month simulation.

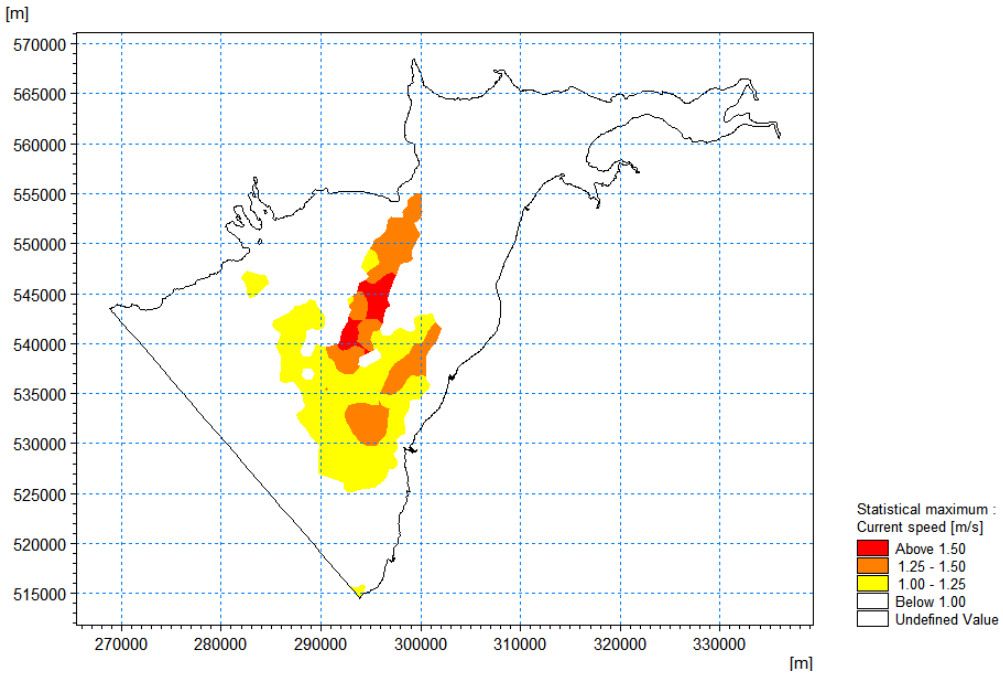

Figure 5.10: Minimum water depths above 7 m and current speeds over 1 m/s at the domain of the improved model during one month simulation.

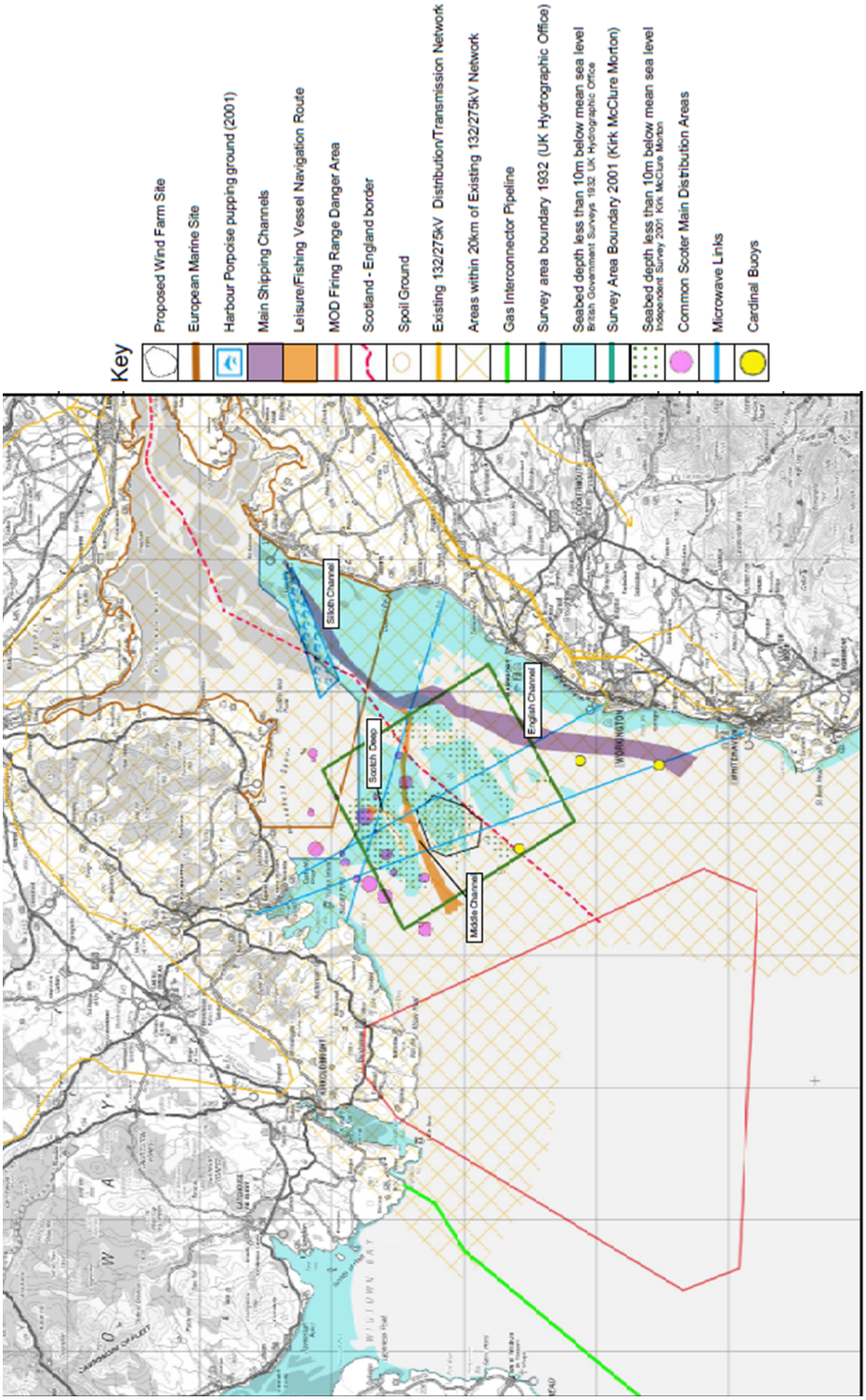

Figure 5.11: Constraints to site selection. (Source: [Natural Power , 2015]

Taking into account the navigational channels and the area occupied by the wind farm together with the information from figure 5.10 two locations have been identified for the deployment of tidal farms with the aforementioned features (5 m diameter turbines). These locations can be found represented by rectangles in figure 5.12, covering the areas with the highest speed of currents where possible.

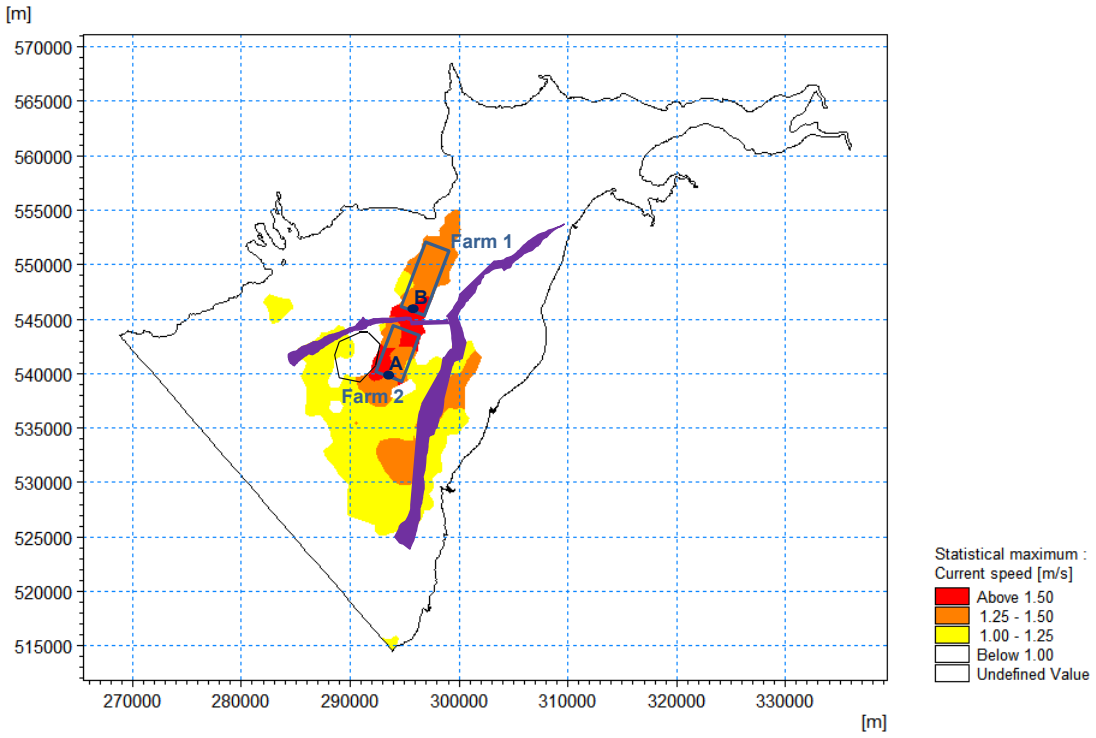

Figure 5.12: Proposed locations for tidal farms. The purple areas indicate the existing navigational channels and the polygon represents the Robin Rigg wind farm.

In order to characterise the flow field in those areas, snapshots of the current speeds have been taken at different times during the spring and neap cycles, as can be seen in figures 5.13 to 5.16

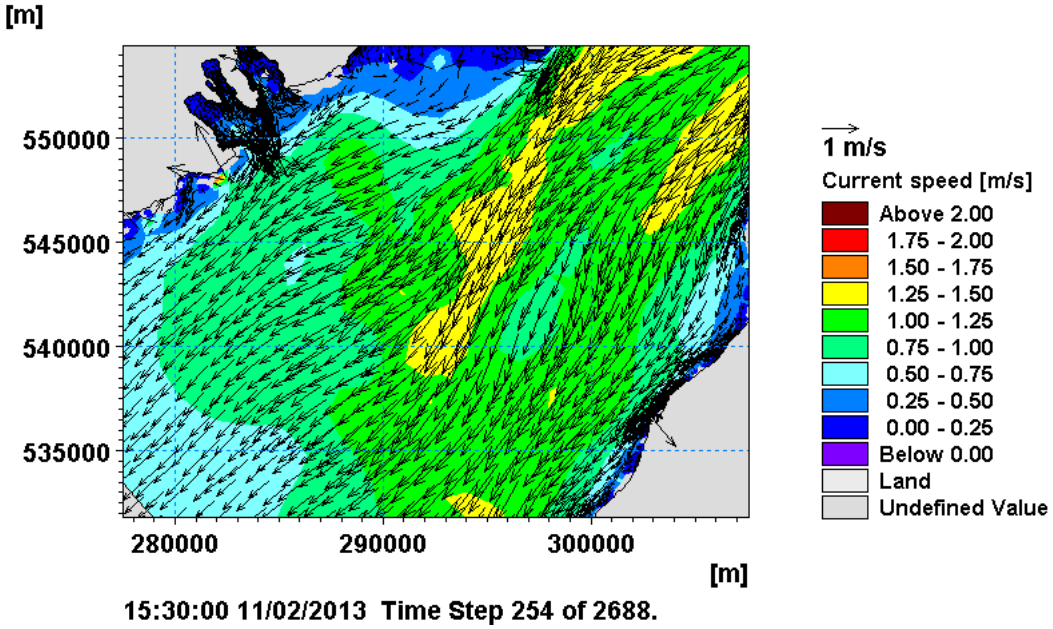

Figure 5.13: Flow field during mid-ebb spring tides in the area of interest.

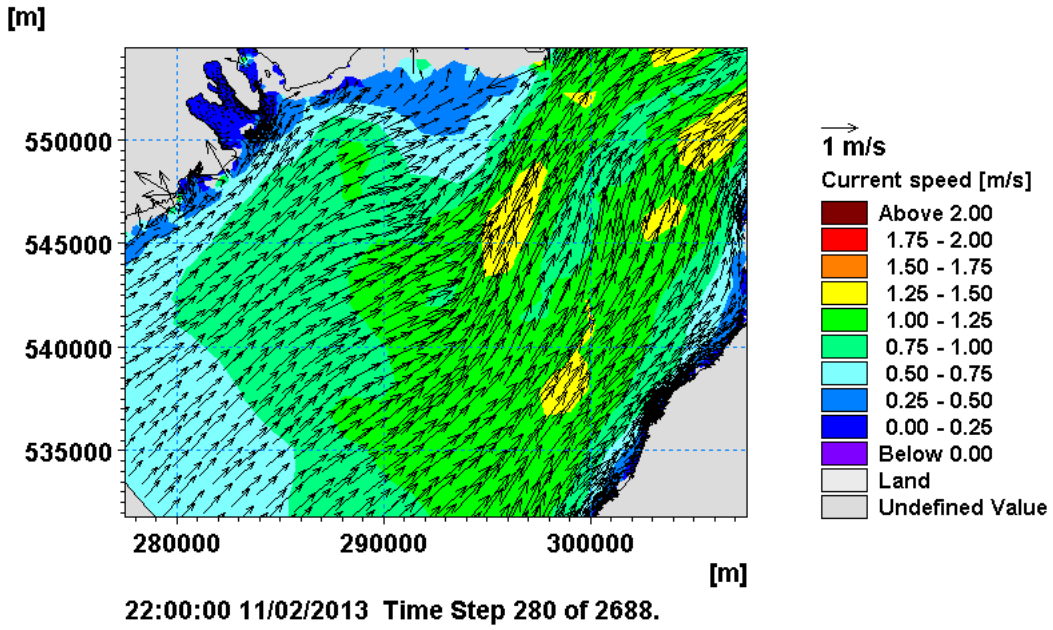

Figure 5.14: Flow field during mid-flood spring tides in the area of interest.

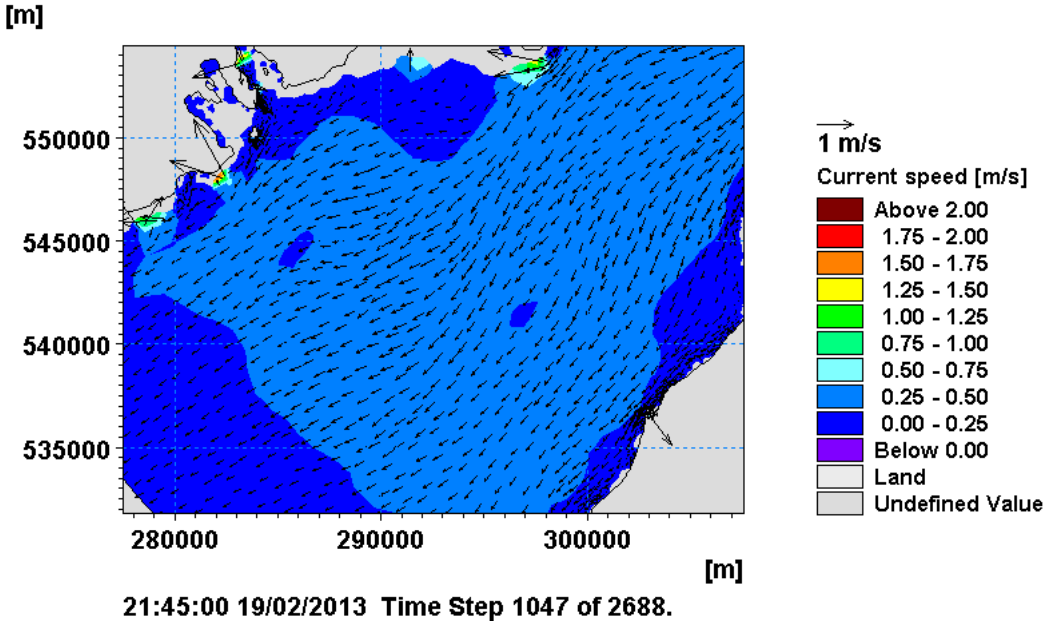

Figure 5.15: Flow field during mid-ebb neap tides in the area of interest.

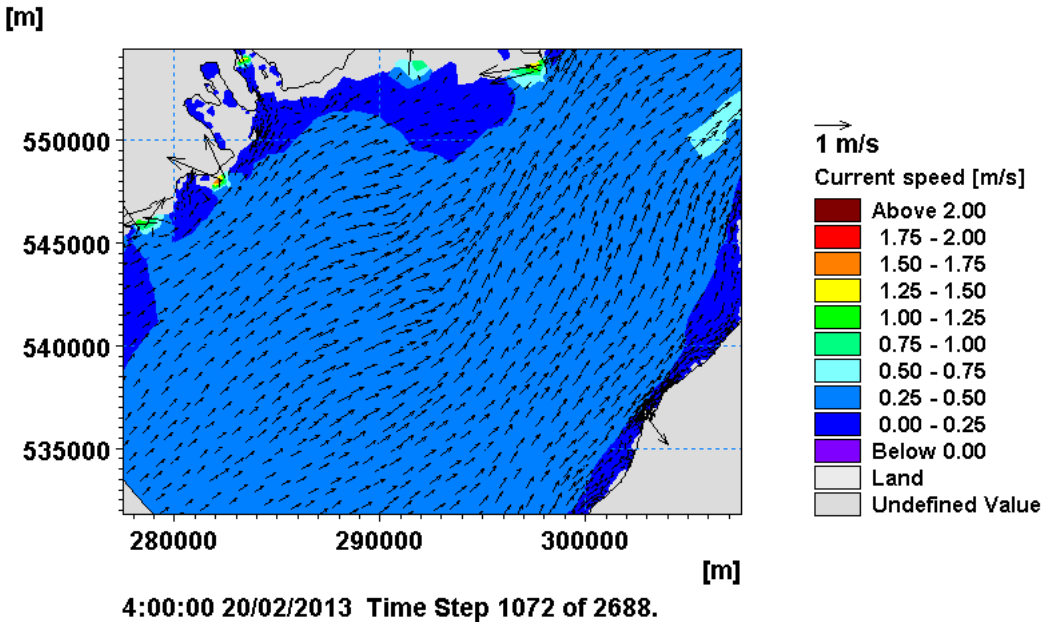

Figure 5.16: Flow field during mid-flood neap tides in the area of interest.

It can be noticed that the current speed is higher for the spring tides than the neap tides.

5.2.6 Tidal farms characterisation

Tidal farms in the improved model have been defined by several rows of turbines covering rectangular areas in the aforementioned locations, being the longitudinal axis of the farm parallel to the main current direction. The latter has been identified from the results of the validation of the model as the average between the current directions during the mid-flood and mid-ebb spring and neap tides at points A and B in figure 5.12. Following this process, the main current directions referred to the geographical North direction result to be approximately $31.73°$ at point A and $26.11°$ at point B.

The turbines have the same dimensions as those considered in section 4.3.4 with 5 m blade diameter and 25 m length. In terms of the spacings between turbines, a lateral spacing of 6 times the diameter and a longitudinal spacing of 10 times the diameter between the edges of consecutive turbines have been considered here, following the dimensions applied in the study by Gebreslassie et al. [2015] for a group of seven MRL turbines.

The rectangular areas where turbines could be deployed, shown in figure 5.12, have been analysed in order to estimate the number of turbines that could be deployed within them either in a parallel or a staggered configuration. The same number of turbines approximately covering the same area have been considered for both configurations in order to establish comparisons of the results between them. The estimated numbers of turbines for each tidal farm as well as the coordinates of the first turbine in the farms used to create the python script included in Appendix A can be seen in table 5.6. Turbines in farm 1 are distributed in 78 rows x 54 columns while farm 2 consists of 106 rows x 42 columns, the rows being perpendicular to the flow direction while the columns are parallel to the current. The approximate extension of the tidal farms is shown in figure 5.4 from section 5.2.3.

Tidal Farm	Number of turbines	Coordinates 1st turbine (Easting, Northing)
1	4212	294644.61, 539144.59
2	4452	296789.31, 545078.35

Table 5.6: Characteristics of tidal farms in the improved model of Solway Firth.

The turbines are implemented in the MIKE 21 model by means of the python script described in Appendix A, modified according to the geometry and size of the turbines and farms. Figures 5.17 and 5.18 show a scheme about the dimensions used in the python script and the cell sizes around the turbines for each layout.

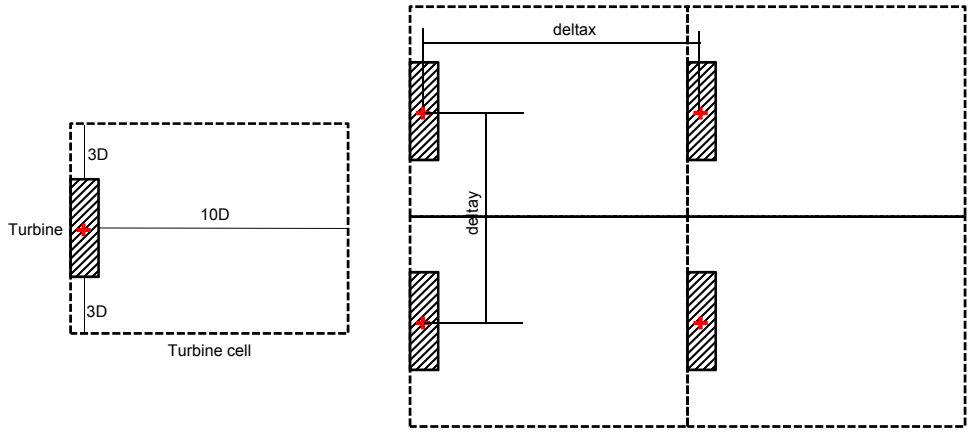

Figure 5.17: Cell sizes and separations between turbine centres in the parallel layout.

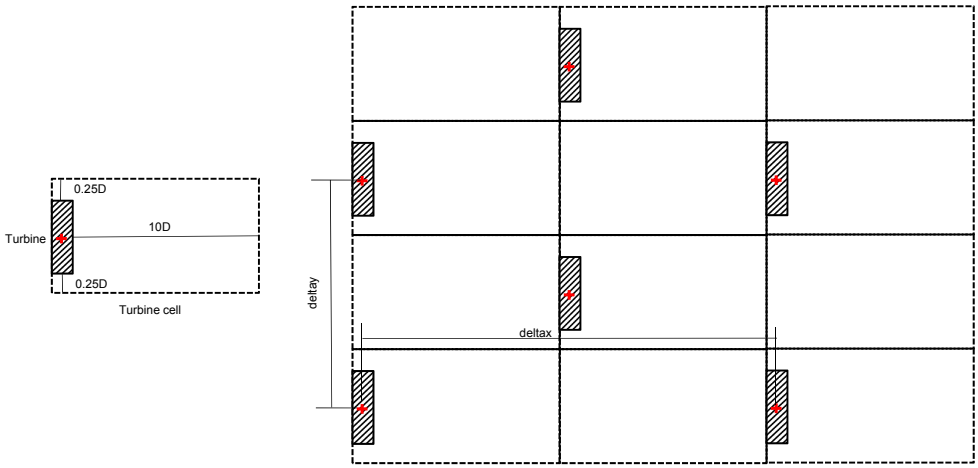

Figure 5.18: Cell sizes and separations between turbine centres in the staggered layout.

The computational mesh has been refined with quadrilateral elements in the area of the farms, surrounded by rectangular subdomains with maximum element sizes of 10000 and 100000 m^2, as shown in figure 5.19.

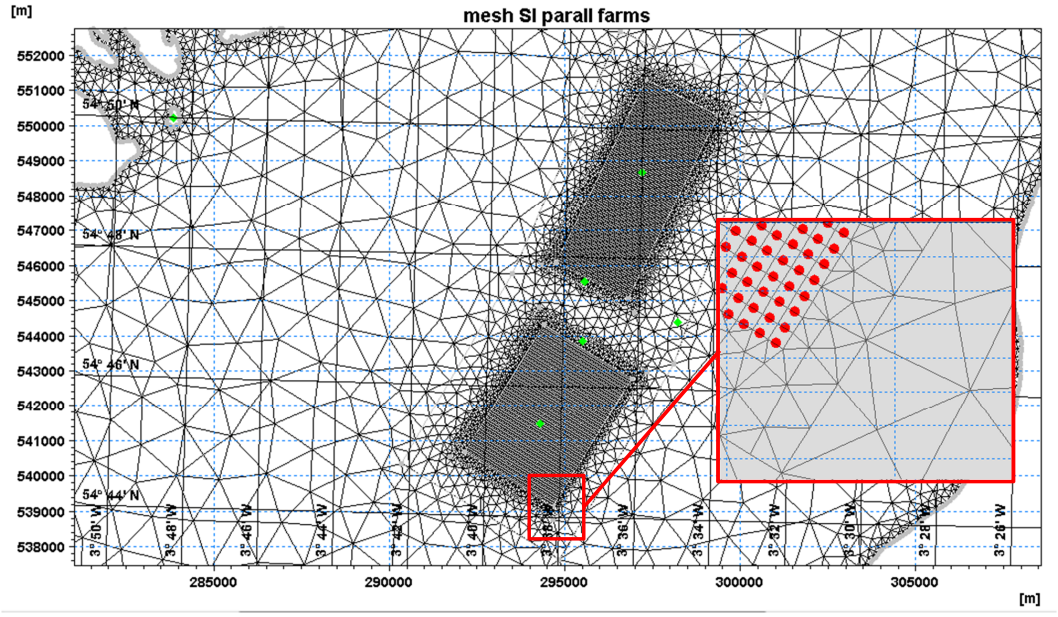

Figure 5.19: Subdomains around the turbines location in computational mesh for the parallel configuration. (Red dots representing the centres of individual turbines

Although the extremely high number of turbines used in this study can be regarded as unfeasible, given the current state of the technology, it has been used here for the purpose of demonstrating in a theoretical way the methodology proposed in this thesis.

5.2.7 Analysis of the boundary reflections

In order to check if there is any influence of the tidal farms described in subsection 5.2.6 over the open boundary of the improved model the results of the model with turbines have been compared with the ones from the model without turbines along the line of the open boundary. The location of the nodes at the open boundary is represented in an approximate way in figure 5.4 from section 5.2.3.

During the simulation of the model with tidal farms the correction factor for mesh dependency has been set up equal to 1 (no correction) for simplicity. The purpose is to demonstrate if there is reflection from the tidal farm at the boundary. The rest of the model features are the same as in the validation of the model. When comparing the results extracted at the boundary line it was found that the maximum errors between the model with and without tidal farms for the current speed and current direction were 1.4 and 8.5 %, respectively, and that 33% of the nodes in the open boundary showed errors above 0.5% for both magnitudes. Therefore, it means that the domain would need to be enlarged to avoid a reflection of the wave from the tidal farm at the boundary.

Several attempts for different extents of the model domain were carried out by displacing the open boundary from the initial locations (close to Kirckudbright bay and Whitehaven) over various points along the shoreline up to points near Portpatrick and Barrow-in-Furness. Finally, a good compromise between reduction of the reflections at the boundary and computational demand was found for the domain shown in figure 5.20. The edges of the open boundary in this case have been located close to Drummore, to the Northwest of the domain, and Barrow-in-Furness, to the Southeast.

Figure 5.20: Extent of the enlarged domain for the improved model of the Solway Firth estuary. The red line indicates the open boundary (Adapted from: EDINA Digimap)

For the creation of the computational mesh the same bathymetry datasets as in the smaller domain have been used together with the Celtic Seas bathymetry, mentioned in Chapter 4 and the Seazone bathymetry, these last two datasets being used to cover the extension of the domain out of the “small” domain. The Celtic Seas bathymetry in that region does not present the errors in the intertidal areas found in the inner estuary. The Seazone bathymetry has been used only in the area around Drummore to provide a better resolution necessary to represent the complex topography of the seabed present in that area. The results of the interpolation of the bathymetry over the mesh in MIKE 21, with a maximum element size of 10 km^2 in the extended part and 1 km^2 in the “small” domain, can be seen in figure 5.21.

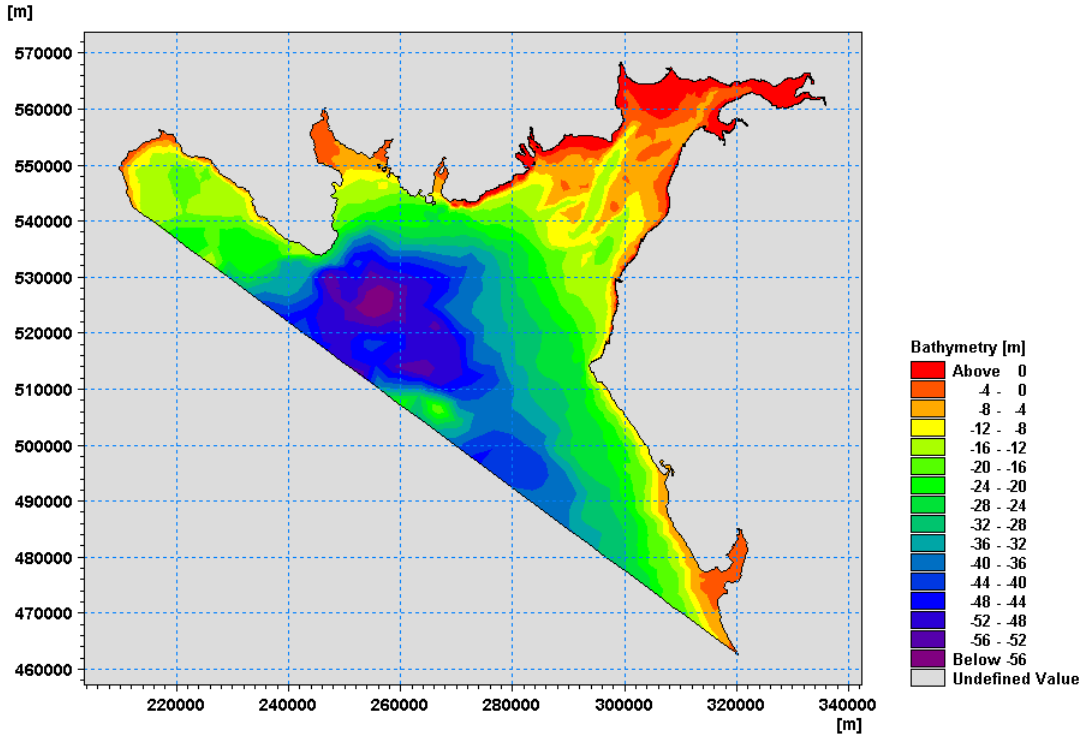

Figure 5.21: Bathymetry of the extended domain for the improved model of Solway Firth

Having applied significant changes to the model domain it was sensible to check the validation of the model again. Thus, the same features than in the simulations for the validation of the "small" domain, described in subsection 5.2.4, were used and the datasets from observed measurements and Admiralty chart diamonds were considered. The stations used for the validation of the enlarged model are located in figure 5.4 from section 5.2.3.

The comparison between the modelled and observed data can be found in table 5.7 and figures 5.22 and 5.23. It can be noticed that the modelled results are still suitable according to the guidance given by Bartlett [1998] for estuarine modelling. The comparison between modelled current directions and the ones from the tidal diamonds given in the Admiralty Charts also show good agreement.

Station	Difference (%)	
	Spring range	Neap range
Silloth dock	5.522	11.134
Workington port	6.709	14.785

Table 5.7: Differences between observed and modelled water levels during the validation of the improved model with enlarged domain.

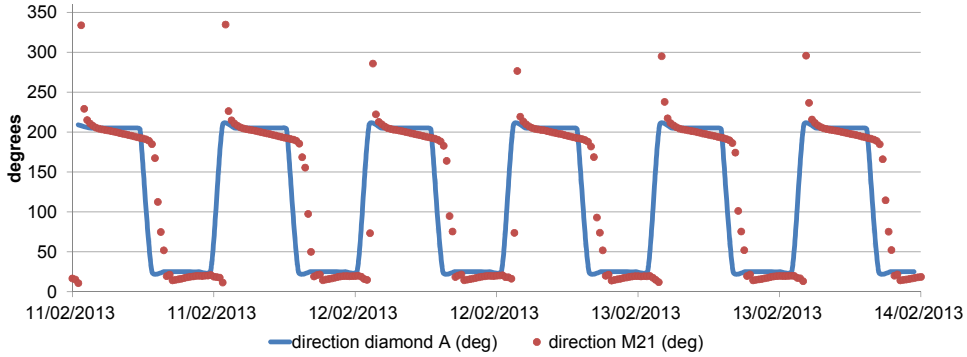

Figure 5.22: Current directions at tidal diamond A from Admiralty Chart 1346-0 and modelled results obtained during the validation of the improved model with extended domain

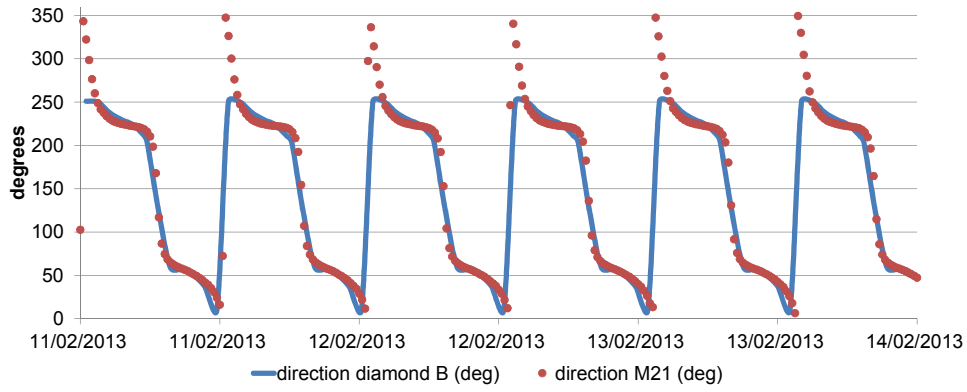

Figure 5.23: Current directions at tidal diamond B from Admiralty Chart 1346-0 and modelled results obtained during the validation of the improved model with extended domain

After the validation of the model with the new domain, it was necessary to check if the reflections from tidal farms in the open boundary had reduced to the point of being considered negligible. The tidal farms were introduced in the same way as in the model with the "small" domain, being the only difference the use of a maximum correction factor of 4.0 for all the turbines, in order to cover the worst case scenario.

As described in subsection 2.4.2, in order to avoid underestimation of the energy extracted when the mesh size is reduced, a correction factor is necessary [Waldman et al., 2015]. As can be seen from the formulation of the correction factor in equations 2.18 and 2.19, the correction factor has an upper limit of 4 when ν is approaching a value of 1. That would happen when the frontal area of the cell where the turbine is positioned becomes too close to the frontal area of the turbine multiplied by the drag coefficient, that is, when the water depth is becoming too small.

After running the simulation with the new domain with tidal farms over the period of the validation it was effectively concluded that the reflection had decreased significantly. The maximum errors for the current speed and direction at the open boundary between the model with and without tidal farms were 1.4% and 3.5 % respectively. 86 % of the nodes in the open boundary showed errors below 0.5% both for the current speed and direction. Therefore, it was considered that the new domain could be used for the rest of the study.

5.2.8 Sensitivity of energy extraction to boundary location

Adcock et al. [2013] indicated that the energy extraction in a numerical model of a coastal area could be affected by the choice of the location of the open boundaries, therefore it is necessary to check if there are any differences in the results between smaller and larger domains.

Following this idea, the results of the energy dissipated by the turbines in the model with the extended domain, with open boundary located approximately between Drummore and Barrow-in-Furness, have been

compared with the results from a smaller model, where the boundary is approximately located between Wigtown and Tarn Point (please see figure 5.24

Figure 5.24: Open boundaries for the analysis of the sensitivity of energy extraction to boundary location

The energy dissipated by the tidal farms in each boundary has been approximated by the product of the number of turbines by the energy dissipated at each turbine, that is, the thrust force resulting from applying formula 2.24 by the flow velocity. The latter has been averaged from the velocity results over the elements occupied by the farms given the problems derived from dealing with the large files containing the modelled thrust and velocities at every individual turbine. The estimated energies have been compared for the model domains in table 5.8. The difference is sufficiently small (approximately 6 %) to consider that there is no error or resonance effect introduced by the choice of the location of the open boundary.

5.2.9 Coastal flooding scenario

In order to evaluate the effect of the tidal farms over the levels of flood risk in the Solway Firth estuary by means of the improved model with the extended domain an extreme coastal event has been considered at the open boundary. In this

	Drummore - Barrow	Wigtown - Tarn point	Difference (%)
Energy Farm1 (MW)	114.70	121.25	-5.72
Energy Farm2 (MW)	106.15	112.74	-6.20

Table 5.8: Comparison of the energy dissipated by the tidal farms between different locations of the open boundary.

case, the fluvial flooding analysed in Chapter 4 has not been regarded here due to the lack of available data for the peak discharges at the rivers included in the new domain at the current time of the preparation of this Chapter.

The boundary conditions consist of the 200-year return period event, formed by the highest astrological tide plus a storm surge component. The same process as the one indicated in section 4.3.3 has been followed to produce the peak water level forcing the open sea boundary. The GIS information provided by the Environment Agency was used to identify the 200-year return period levels at the points in the edges of the boundary (nearby Drummore and Duddon Bar). Information from the United Kingdom Hydrographic Office [2012] was used to identify the date and time when the highest astronomical tide would be happening at the standard port (Liverpool), which is the same as in the initial model. Then, the base tide at each edge was predicted by means of the MIKE 21 toolbox and scaled with the surge curve in order to reach the extreme level. In this case, the surge curves applied to each point were:

- Surge curve 30: Heysham - Fleetwood to Haverigg Point (Morecambe Bay, Duddon Estuary), for Duddon Bar.
- Surge curve 33 Portpatrick - Isle of Withorn to Girvan, for Drummore.

Finally, the water levels were interpolated and applied over the open

boundary. The simulation covered a period between 6th February of 2013 at 12:00 hours and 13th February of 2013 at 12:00. It consisted of 672 time steps of 900 seconds, in order to allow the model to spin-up during the first three days, with the peak of the flooding scenario centred within the other four days. A high order scheme was used both for the spatial and temporal discretisation of the governing equations with a critical CFL number of 1. The bed roughness and turbulence were defined according to the values found through the calibration and validation of the model, that is 40 $m^{1/3}/s$ for the inverse of the Manning's coefficient and 0.28 for the Smagorinsky coefficient.

Regarding the tidal farms, the turbines were included in the model as described in point 5.2.6. As was mentioned in Chapter 2, the correction factor given by Waldman et al. [2015] depends on the water depth. In a tidal environment, the water depth is changing with time and would be influenced by the presence of the potential tidal farms. The values of the correction factor would need to be updated at each time step and they would equally influence the results of the next time steps. As the current version of MIKE 21 does not allow for the retrofit of the correction factor according to the internal results of water depths over the tidal cycle, in this study some simplifications have been assumed. The correction factor applied to the turbine representation in the improved model of the Solway Firth has been calculated taking into account the results of minimum water depth from the simulations without turbines in the area of the tidal farms during the period of the simulation. The results for the water depths in the model without farms have been statistically treated to identify the minimum values over the simulation period. Next these minimum values have been extracted for the elements that would be occupied by the turbines and the lowest value within them has been identified and used for the calculation of the correction factor. During the period of the coastal flooding scenario, a few locations inside the area of the tidal farm have been found to have a water depth close to the diameter of the turbine, maybe due to the extreme nature of the water levels. Therefore, the maximum limit of the

correction factor (4.0) has been used for all the turbines in the tidal farms. This criterion responds to the idea of staying on the safety side in terms of the results or representing the worst case. Both the parallel and staggered layouts have been used in the simulations with the tidal farms and the results for the maximum water levels have been compared with the ones from the model without turbines.

5.2.10 Results

The changes over the peak water levels induced by tidal farms in the parallel and staggered configurations under the coastal flooding scenario in the improved model can be seen in figures 5.25 to 5.28.

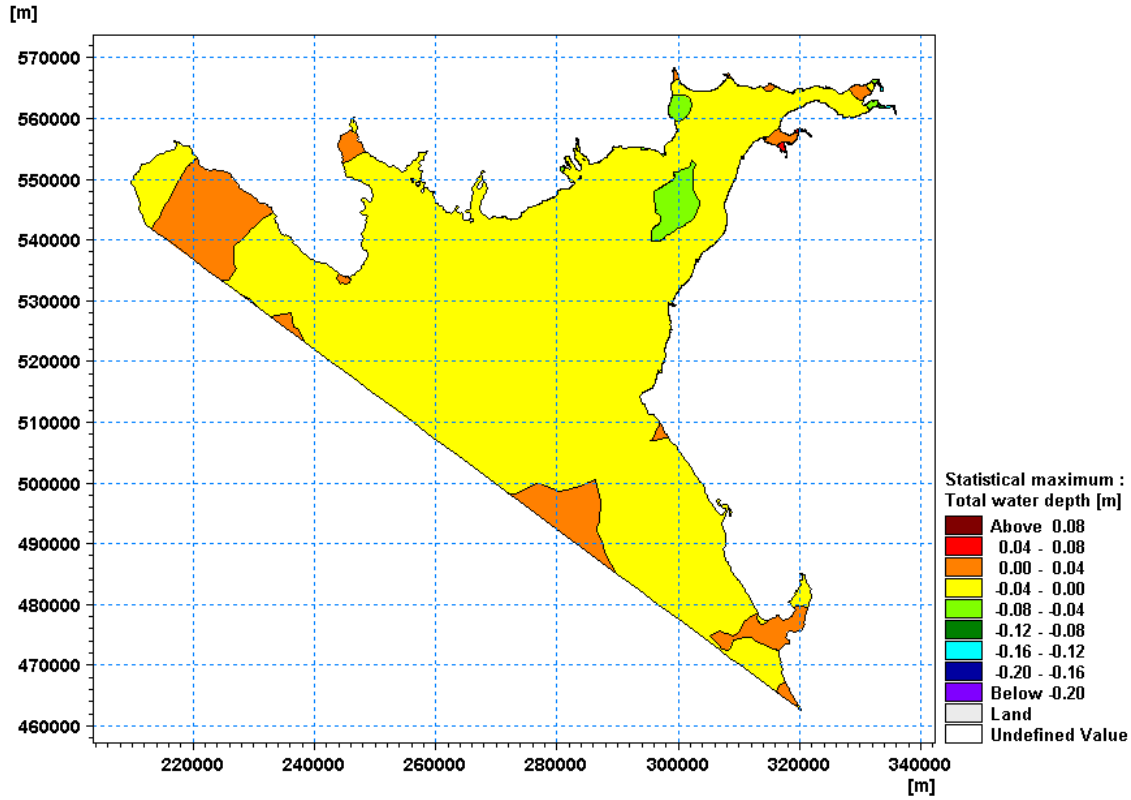

Figure 5.25: Differences (m) in peak water levels between the situations with and without tidal farms in a parallel layout under a coastal flooding scenario

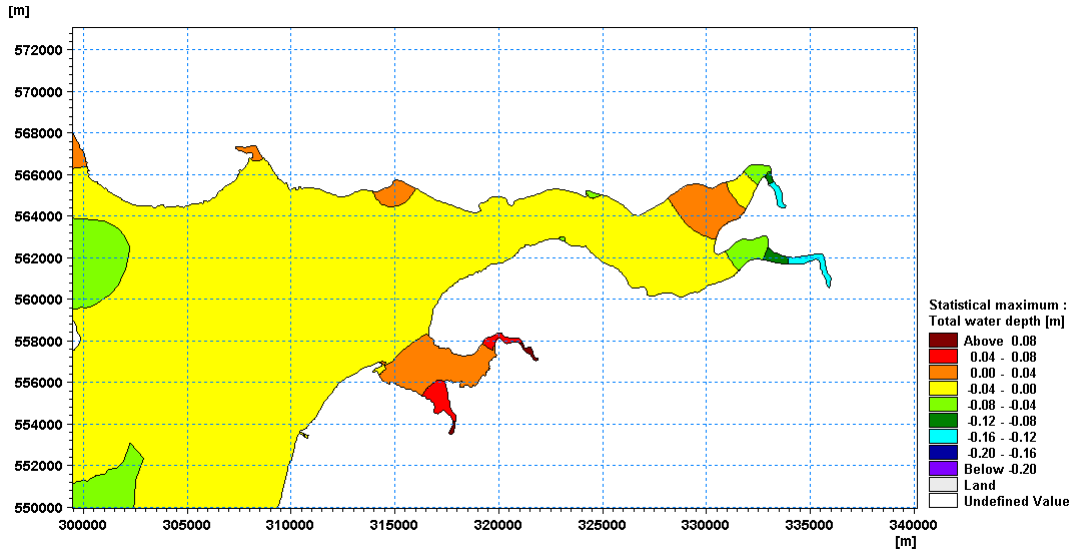

Figure 5.26: Close-up view of the upper estuary. Differences (m) in peak water levels between the situations with and without tidal farms in a parallel layout under a coastal flooding scenario

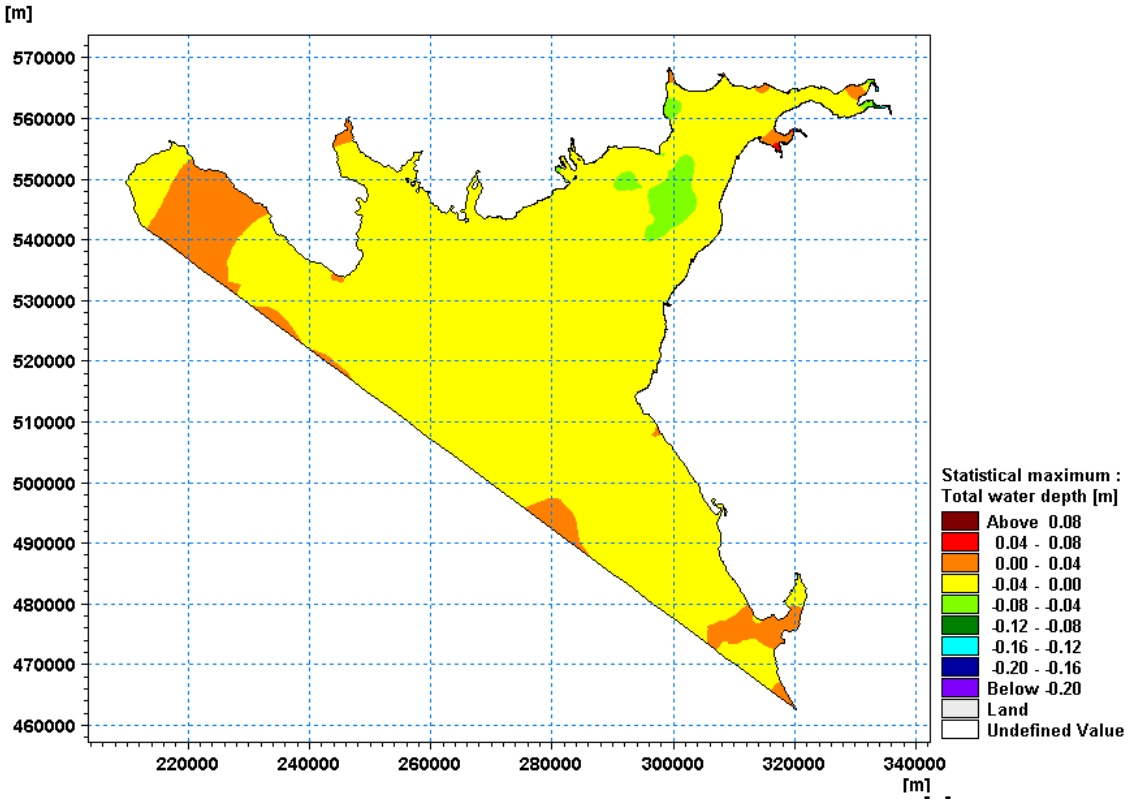

Figure 5.27: Differences (m) in peak water levels between the situations withand without tidal farms in a staggered layout under a coastal flooding scenario

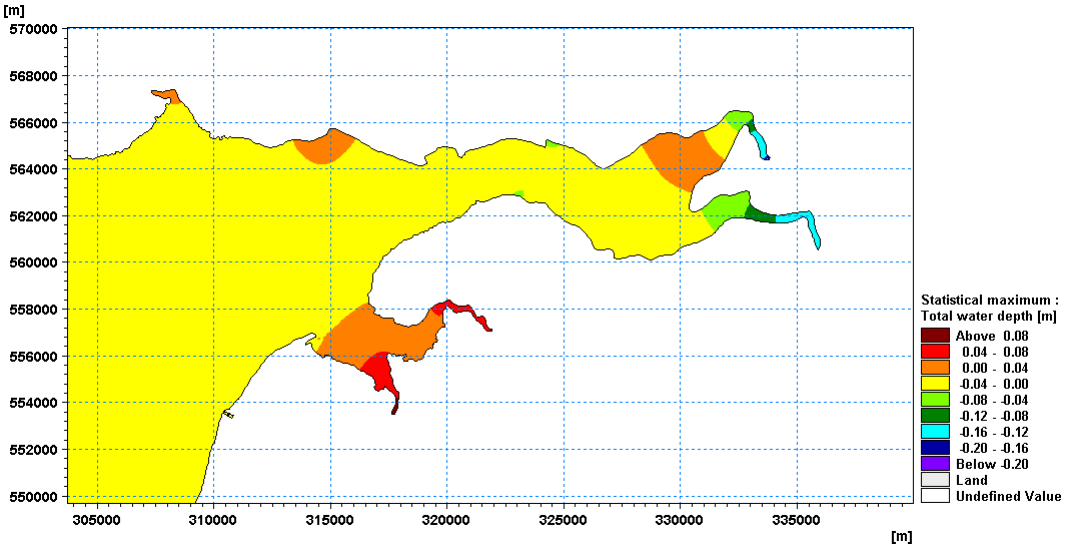

Figure 5.28: Close-up view of the upper estuary. Differences (m) in peak water levels between the situation with and without tidal farms in a staggered layout under a coastal flooding scenario

The maximum changes happen at the rivers in the upper estuary. The maximum increase of peak levels for the parallel farm happens at the river Wampool whereas the maximum decrease occurs at the river Eden. For the staggered layout, the maximum increase and decrease of peak levels are located at the rivers Waver and Esk, respectively. Negative values mean a decrease and positive values indicate an increase in water levels due to the tidal farms.

The maximum increase and decrease in peak water levels during the coastal flooding scenario due to the presence of tidal farms in both configurations (parallel and staggered) are shown in table 5.9. It can be highlighted that the decrease is larger than the increase in both cases, which is positive from the point of view of the flood risk, and that the maximum increase is under the dm scale and therefore does not represent a significant contribution to the flooding hazards in the area of the estuary.

When comparing these results with the ones obtained for the same scenario in Chapter 4, it seems logical that the effect of the farms has become higher due to the fact that the farm size is larger, amongst other factors. The initial and the

Layout	Coastal flooding scenario	
	Max increase	**Max decrease**
Parallel	0.094	-0.155
Staggered	0.091	-0.161

Table 5.9: Maximum changes (m) in peak water levels with tidal farms in the coastal flooding scenario.

improved model have been proved to illustrate examples about how very large tidal farms could affect peak water levels under extreme events in a real case.

5.2.11 Comparison with idealised model

The maximum differences in low tides with and without the turbines present have been extracted from the results of the improved model of the Solway Firth, as well as the locations where these changes happen, following the same method than for the peak levels. The purpose is to compare these results and the ones related to the high tide levels with the results from the idealised case presented in Chapter 3 in order to demonstrate its validity. It must be noted that the results from the initial model of the estuary have not been considered here because the bathymetry and the data used for the calibration of the bed roughness presented substantial errors.

Tables 5.10 and 5.11 show the comparison of results between both models.

Although the numerical values of the results in table 5.10 cannot be directly compared between the models because the boundary conditions and the size of the tidal farm are different, some parallelism can be found between the main trends identified from these results:

- Regarding the impact on low tide levels, in both models the maximum decrease is more significant than the increase, which could lead to a

Model	Difference low tides (m)		Difference high tides (m)	
	Max increase	Max decrease	Max increase	Max decrease
Idealised	0.014	0.667	0.076	0.418
Detailed	0.083	0.560	0.094	0.155

Table 5.10: Maximum changes (m) in low and peak water levels with a tidal farm present in the idealised and improved model of the Solway Firth.

Model	Difference low tides - locations		Difference high tides - locations	
	Max increase	Max decrease	Max increase	Max decrease
Idealised	I	F	M	H
Detailed	I	F	I	H

Table 5.11: Locations of the maximum changes (m) in low and peak water levels with a tidal farm present in the idealised and improved model of the Solway Firth. (H: head of the estuary; I: inner part; F: Farm; M: mouth of the estuary)

potential creation of new intertidal areas. The locations of these changes are also similar between them, consisting of the inner part of the estuary and the area within the tidal farm for the increase and decrease, respectively.

- The maximum changes in high tide levels due to the tidal farm also reflect similar trends in both models, where the decrease of peak levels is higher than the increase, meaning a reduction of flood risk levels at some parts of the estuary. In this case, the maximum decrease occurs at the head of the estuary in both models while the maximum increase varies from the mouth of the estuary for the idealised model to the inner part for the detailed model. Maybe this could be due to the different level of complexity of the bathymetry between both models.

This comparison demonstrates the validity of the simplified model for its use

as a tool during initial assessments of the impacts of tidal farms on water levels in estuaries or in cases where the data for the creation of more detailed models are scarce.

5.3 Conclusions

This Chapter shows that there is an important influence of the input data over the model results. The use of the new bathymetry affected the potential location of tidal farms and the associated impacts, while the change in observed datasets for the calibration resulted in a different value for the bed roughness, compared to the initial model.

Another conclusion that can be extracted is that the choice of the open limits in models with clamped boundary conditions has to be considered carefully in order to avoid errors due to wave reflection and miscalculation of the energy dissipated by the turbines.

In light of the results obtained in this Chapter for the improved model of the Solway Firth previously described, the main conclusions are that:

- For all configurations of the tidal farm, the maximum decrease of peak water levels (related to the reduction of flood risk) is bigger than the maximum increase (associated with the loss of intertidal areas), although both values are in the same order of magnitude.

- Staggered configurations seem to provoke a higher impact than the parallel ones, being more noticeable in the maximum reduction of peak water levels, which could lead to loss of intertidal regions that become permanently dry.

- In this case, the strongest effects on water levels are more localised towards the rivers at the inner part of the estuary. Differences with the results from the previous Chapter could be related to the influence of the topography on the results.

Chapter 6

Discussion and conclusions

The main objective of this thesis, which was the assessment of the impact that tidal farms could have on flood risk when they are deployed in estuaries, has been achieved as follows. A 2D numerical model (MIKE 21) has been used to simulate the hydrodynamic conditions and the effect of large groups of turbines on the water levels in several cases based on real estuaries in the UK.

Initially, the representation of an individual turbine in MIKE 21 was compared with experimental and CFD results and good agreement was found between the results of the thrust force and flow field with the use of a correction factor, which was defined in previous studies. This way, the objective of integrating the results from the CFD model based on the experiments of the MRL turbine was accomplished.

Secondly, idealised models have been used for the sensitivity analysis of the geometry of the estuary over the impact that a tidal farm could have on water levels. This specific analysis has not been carried out before, although the benefits of these models in terms of reduced computational costs and identification of the underlying physical trends have been acknowledged in the existing literature.

Finally, the generic methodology provided in this thesis has been

demonstrated against a fully detailed model of a real case in the UK (Solway Firth Estuary). This is the first study of this kind done on that specific location, although it has been already considered for tidal range energy extraction in previous publications. This research reveals that the Solway Firth provides a good example for the validation of the methodology because it combines strong currents to be harnessed for electricity production with high levels of flood risk.

An initial model of the Solway Firth, based on the available bathymetry at that stage of the research, was run over three different flooding scenarios, two sizes of the tidal farm and two configurations of the turbines inside the array, providing a novel evaluation of these parameters in regards to the impact of the farm on peak water levels. When a more realistic bathymetry dataset was found, the Solway Firth model was simulated again, resulting in new features for the tidal farms. A coastal flooding scenario as well as two array layouts were tested in this case with the same purpose than the initial model. The results of both models were discussed and some agreement was found between them and with previous studies investigating the effects of tidal arrays on water levels.

One of the advantages of the methodology followed in this thesis lies in the fact that it is generic and, therefore, it can be applied to other turbine designs, locations and kind of impacts. Besides, the implementation of the turbines in the model as individual structures around which the computational mesh is refined will allow the definition of different turbine loadings based on optimisation techniques in the future. In this regard, a Python script which has been created for this thesis as a generic tool to include large numbers of turbines in the current version of MIKE 21. It is shown in the appendices and it can be used, modified and improved by other users.

It is also worthy to mention some limitations and changes which appeared during the development of this thesis:

- The initial bathymetry of the Solway Firth model included significant errors as well as lack of coverage at the inner part of the estuary and the only measurements of current speed available in the estuary were taken at a particular depth.
- It was not possible to validate the Solway Firth model with observed measurements from the 200-year return period events. Therefore, validation was done against the base tidal levels (highest astronomic tide) without the surge component.

Despite these issues, reliable results have been obtained through this thesis.

6.1 Discussion of results

A discussion of the results obtained in the different parts of this thesis is presented. Some comparisons with results from previous studies have also been included. The analysis carried out here has been used to draw the conclusions and define the lines for future research.

6.1.1 Idealised estuaries

From the sensitivity analysis carried out in 3 some ideas can be discussed in relation to the influence of channel geometry on the impact of tidal farms on water levels in estuaries:

- The impacts of the farm increase with the length of the estuary. Considering the tidal farm as an artificial friction in the channel, this idea agrees with the results from a 1D analytical model developed by Prandle [1985], which shows that the tidal response to a frictional increase is directly proportional to the length of the estuary.

- The effects of the farm are inversely proportional to the width and depth of the estuary. This may be due to the fact that blockage effects increase the performance of the turbines [Nishino & Willden, 2012a] and, therefore, higher turbine loadings provoke higher impacts, as reported in section 3.5.3.
- The impacts of the farm are smaller for cases with longitudinal width variation compared to those with a constant width. According to Prandle [1985], an increase in the natural friction of a channel with constant depth and variable width leads to a less resonant behaviour, which could be connected to the previous idea.
- Estuaries with a longitudinal depth variation receive stronger impacts from the farm than the equivalent cases with a constant width. An explanation can be found in the fact that the sensitivity of the tidal response in an estuary to an increase in friction is inversely proportional to the depth at the head of the estuary, as presented in the study by Prandle [1985]. A steeper longitudinal slope means a shallower depth at the estuary head and, thus, more sensitivity to the impact of the farm.
- Cross sections with a more horizontal lateral slope for the same area register a higher impact of the tidal farm. This could be also related to the blockage effects. Apart from this, the shape of the cross section also has an influence, which can be noted from the comparison of results between rectangular, trapezoidal and triangular cross-sections.

Some of the environmental implications of the impact of tidal farms on water levels are those related to flood risk levels, occuring during peak tides, and the extension of intertidal areas, which are delimited by the low and high tide levels. In this sense, it was found that in the presence of the tidal farm:

- The decrease in high tide levels is larger than the increase in most of the cases, which is in agreement with the results from the models carried out by Ahmadian & Falconer [2012] and Fallon et al. [2014] for different tidal arrays in the Bristol Channel and Shannon estuary, respectively. This would have a potential positive effect on flood risk levels and loss of intertidal areas in some parts of the estuaries.
- For the majority of the cases, the increase in low tide levels results in higher values than the increase, leading to permanent submersion of the intertidal areas at some regions.
- When comparing between the overall effects on low and high tide levels, it must be noticed that the effect is generally less pronounced for the decrease of high tides than for the increase of low tide levels. This trend is also found in the results from the study by Nash et al. [2014], in which the flushing characteristics , the tidal regime and the intertidal areas of the Shannon estuary with tidal arrays are analysed by means of a detailed numerical model. Therefore, the tidal farm considered here has a general effect of attenuation of the tidal range with a possible reduction on flood risk and a more noticeable potential impact on intertidal areas.

  Regarding the locations where each kind of impact could happen within the estuary a generalisation cannot be made, given the high dependency of those locations on the geometry of the channel. However, without differentiating between impacts on flood risk or intertidal areas it can be said that most of the changes happen at the mouth of the estuary followed by the outer part and the area upstream the tidal farm.

  In terms of the time when high and low tides happen with or without the tidal farm present, it has been found that any changes would occur during the same time step (15 minutes) for all cases. In contrast, in the study by Nash et al. [2014] the time lag could reach up to 1.28

hours for the denser array. However, the reason for such a different result could lie in the fact that the array was extended over the whole width of the estuary and that maximum the installed capacity, which has not been specified, could be significantly high compared to the one used for the idealised models in this thesis.

In relation to the impact of different turbine loadings, it was found that the maximum changes in a case with constant cross section over the estuary length increase with a higher drag coefficient of the turbines and stay in the same order of magnitude (cm) even for unrealistically high loadings of the turbines.

When comparing the impact of the farm between a resonant and non resonant case without bed friction higher changes appeared for the resonant case, the increase being higher for the low tides with potential effects on the permanent inundation of inter-tidal areas. The decrease of high tide levels was also significant, which could lead to attenuation of the flood risk levels. The effect on tidal range was also analysed for both cases showing that the reduction of tidal range was significant in the resonant case at some parts of the domain whereas the increase was not observed at any location. In the non resonant case there was a small increase of the tidal range at some areas and a higher decrease at other locations, which was smaller than in the resonant case by one order of magnitude. These results were different from the ones derived by Draper [2011] from a 1D model with a tidal fence, maybe due to the fact that the fence crossed the entire width of the estuary while the block farm in the 2D model only partially occupied the estuary width. These differences between block farms and tidal fences were also mentioned in the study by Y. Chen et al. [2014].

An idealised model of the Solway Firth estuary has also been included at the end of the chapter in order to validate the use of

these models against the results of a detailed numerical model based on real conditions of the bathymetry and observed measurements of the hydrodynamic conditions. Although the boundary conditions and the size of the tidal farm are different between the idealised and the detailed models, some parallelisms can be found between the results:

* Regarding the impact on low tide levels, in both models the maximum decrease is more significant than the increase, which could lead to a potential creation of new intertidal areas.
* The maximum changes in high tide levels due to the tidal farm also reflect similar trends: the decrease of peak levels is higher than the increase, meaning a reduction of flood risk levels at some parts of the estuary.
* The locations of these changes are also similar between them, although some differences can be found for the location maximum decrease of high tide levels, maybe be due to the complex bathymetry in the detailed model.

Although the existing studies on tidal stream energy extraction in idealised models of estuaries are focused on tidal fences and, therefore, the results are not entirely comparable, it was thought of interest to include a summary here of the results obtained in those studies:

* In the work by Draper [2011], it was indicated that an increase in the tidal range could happen in those cases with a length larger than the resonant one when a fence was deployed at one quarter of the wave-length from the mouth of the estuary. This conclusion is extracted from a 1D simplified analytical model which neglects bed friction and considers a rectangular shape of the bay.
* According to the study carried out by Y. Chen et al. [2014] with a 3D model of an idealised estuary with varying depth and width

over the length and a rectangular cross-section, when a tidal fence or a group of them are deployed in the estuary both the low and high tides are increased along the central or longitudinal axis of the model.

* From the results of the idealised model of a stratified estuary connected by a narrow channel to an ocean basin, developed by Yang & Wang [2015], when a tidal farm occupying the entire cross-section of the channel is deployed the effects on the water elevations at a point inside the estuary are small (from the graphs it can be seen that low tides are slightly increased while high tides decrease in a similar way).

6.1.2 Solway Firth models

This thesis presents a methodology to delimit the effects of very large groups of tidal stream turbines on flood risk levels in estuaries. As part of the methodology, a fully detailed numerical model of the estuary of interest in the undisturbed conditions has to be created first in order to identify the most suitable locations for the tidal farm, which is then introduced in the model. The impacts on flood risk levels are determined by the difference on peak water levels with and without turbines present in the estuary. One of the advantages of the numerical model is the possibility to combine its results with tools for the assessment of tangible damages from floodings. An example could be found in the tool presented by Hammond et al. [2012] which provides the classification of damages to properties through the use of flood risk maps, like the ones produced in MIKE21. Another future application of this methodology could be the assessment of the impact of tidal farms on the extension of intertidal areas and associated wildlife habitats in estuaries through the analysis of changes to high and low tide levels, as shown in Chapter 3.

In this thesis, the aforementioned methodology has been demonstrated against a real estuary in the UK, the Solway Firth. Despite the errors present in the bathymetry of the initial model of the Solway Firth, it was found of interest to analyse the results in the frame of the theoretical nature of this research. As the model was tested for different numbers of turbines, configurations and flooding scenarios, it provided new insights about the impact of tidal farms on flood risk levels in the estuary:

* In general, the maximum reduction of peak levels occurred at the inner part of the estuary whereas the maximum increase happened in the outer area.
* The decrease of peak water levels was higher than the increase for every case under all scenarios.
* When comparing the results between different scenarios, in general, the effect of the farm on the increase on peak levels was higher in the fluvial flooding scenario while the decrease was more noticeable during the coastal flooding.
* From the analysis of different array configurations, it was found that, in most of the cases, the staggered arrays had a bigger effect than the parallel ones.
* Regarding the size of the farm, the effects increased with the number of turbines, as expected, but the relationship was not linear.

In the improved model simulations were run with the a more realistic bathymetry and the locations and size of the tidal farms were modified in comparison with the initial model. The model domain had to be enlarged in order to avoid wave reflections at the open boundary and only the coastal flooding scenario was analysed. The results show that:

* The maximum changes in peak water levels happened in small

areas close to the river boundaries at the upper estuary, for both cases.

* The maximum decrease of peak water levels was larger than the maximum increase in every case and the magnitude of these maximum changes was approximately on the scale of decimeters.
* The staggered array showed a bigger reduction and a similar increase in peak water levels than the parallel layout.

Although the results are not completely comparable between the initial and the improved model some differences and parallelisms can be identified for the same scenario and array layout:

* In the initial model, the locations of the effects were more clearly divided between the inner and the outer estuary whereas in the improved model most of the estuary showed no change or a decrease and the increase of peak levels were sparsely distributed.
* The values for the maximum increase and decrease of peak levels are closer in the improved model than in the initial model, where these changes are in different orders of magnitude.
* In both models, the staggered layouts showed bigger impacts.

In terms of previous studies investigating the effect of tidal arrays on water levels in estuaries some agreement can be established:

* In the study carried out by Ahmadian & Falconer [2012], three different shapes of an array of 1000 turbines were tested in a DIVAST model of the Bristol channel. The maximum changes in peak water levels are in the scale of a few centimeters and the decrease of peak water levels happened in the inner part of the estuary, similarly to the results obtained for the 1024 turbines farm in chapter 4.

* Fallon et al. [2014] created a DIVAST model of the Shannon estuary with three different array densities over the same area, consisting of 600, 2400 and 9600 turbines, approximately. The authors found that the high water levels were decreased at four positions (inside and outside the array as well as in the inner and outer parts of the domain), which generally agrees with the results for the improved model of the Solway Firth. The fact that the decrease of high water levels is larger in the inner part of the estuary than in the outer part can be similarly observed in the results from the improved model of the Solway Firth, although it appears less evidently in the plots included in (chapter 5).

6.2 Conclusions and future research

The conclusions extracted from the results of this thesis as well as the recommendations for future work in this line of research are given as follows.

6.2.1 Turbine representation in MIKE 21

This thesis shows that the use of the correction to the drag force of individual turbines described in subsection 2.4.2 under steady flow conditions, like the ones represented in laboratory and CFD tests, realistically represents the energy dissipated by the turbine. Although the degree of adjustment of flow velocities was found to be very similar between axial and cross-flow designs, some differences were found in the representation of the thrust force between different turbine types.

However, in real flow applications, where water levels change significantly with time, there is a limitation of the use of the correction factor in the current version of MIKE 21. The correction is not

implemented internally in the source code and therefore it does not vary according to the water levels from previous time steps, which would be equally affected by the retrofitted values of the turbine loading.

6.2.2 Idealised estuaries

Following, some conclusions are drawn from the results of this thesis in relation to the impact of a tidal farm deployed in a central location of a set of idealised models based on real estuaries in the UK.

* The geometry of the estuary has an influence on the impact of a tidal farm on water levels compared over those of the undisturbed state, which can be explained by the combination of two main effects:
  - The blockage of the channel increases the performance of the turbines and, consequently, the magnitude of the impacts.
  - The sensitivity of the tidal response to the friction induced by the tidal farm is directly proportional to the length and inversely proportional to the depth at the head of the estuary.
* This study shows that environmental aspects, such as the existence of intertidal areas and flood risk levels, are affected by the tidal farm as follows:
  - The increase of low tide levels is predominant, with consequences for the permanent inundation of intertidal habitats.
  - The decrease of high tide levels is the second important effect in most of the scenarios., leading to a potential loss of intertidal areas, which become permanently dry regions, and a positive net effect over flood risk levels.
* The mouth of the estuary is most frequently affected than other

areas in the scenarios considered, although the strong dependency of the results on the geometry suggests that care has to be taken before generalisation in this sense.

* Changes on time for high and low tides lie within a frame of 15 minutes, without substantial effects on associated activities, such as navigation.
* It can be also concluded that a higher loading or drag coefficient of the turbines generally increases the impacts.

6.2.3 Demonstration case study - Solway Firth

It must be highlighted that the accuracy of the bathymetric data affects the choice for the location and features of the tidal farm and, consequently, the impact of the tidal farm on the estuary.

From the results of both models, it can also be concluded that the effects of the tidal farms on the decrease of peak tide levels are generally higher than the increase, for both models of the Solway Firth under different scenarios, layouts and sizes of the tidal farms. This effect would result in permanently dry conditions at some of the intertidal areas and the reduction of flood risk levels at the coastline, depending on the location.

In terms of the flooding types, this study reveals that there is a dependency of the impact of the farm on the type of event (coastal, fluvial or combined) but the maximum changes in water levels stay in a similar order of magnitude.

Another conclusion is that the relationship between the size of the tidal farm and the effects on peak levels is non-linear.

Regarding the different layouts of the tidal farm considered in both models of the Solway Firth, it is revealed that the staggered configurations produce a higher impact than the parallel ones, mainly

on the decrease of peak levels, associated with the reduction of flood risk and loss of intertidal areas.

6.2.4 Future Research

Regarding the representation of tidal farms in MIKE 21 or any similar 2D model, some suggestions can be made for the topics of future investigation:

* It is important to include the correction factors for the drag force internally into the source code in order to avoid mesh dependency of the results, as presented in this study. This would ensure that the correction is updated at each time step depending on the water levels, which are significantly variable in tidal locations.
* It follows from this that it would also be important to include suitable adaptation of the correction factor for different turbine designs by means of analytical or empirical models. For example, the correction proposed in this study is based in the actuator disk theory, but it is not clear if that would be the best approach for horizontal cross-flow designs, such as the MRL turbine.
* Some improvements to the existing turbulence schemes in the 2D depth-averaged models would be necessary for the purpose of representing the interactions between turbines, being validated with experiments of groups of turbines.
* Experimental or CFD work needs to be done in order to identify the effects of group of turbines on water levels and compare the results with the 2D depth averaged models. It would allow one to delimit the differences between 2D and 3D models and check what the penalty is on the accuracy of the results when the

computational time is reduced by means of the 2D models. In this sense, maybe future research in coastal modelling could be oriented towards affordable 3D models or coupling of 2D and 3D models.

In reference to the estuarine modelling, some ideas can be considered for further research:

* From the analysis of the idealised models of estuaries it was found that tidal farms could have an impact on the intertidal areas. Therefore, a logical continuation of the research done in this thesis could be oriented towards the identification of the implied changes to intertidal areas and associated habitats. The generic methodology presented in this study can be adapted for that purpose and applied to the Solway Firth or any other location. In the case of the Solway Firth, it presents one of the most extense intertidal regions in the UK and it is declared Natural Protection Area, therefore it would provide a suitable case study.
* Another aspect that would need to be investigated in the future is the assessment of the impact of tidal farms on morphological changes in estuaries or other coastal areas. Sandflats can be regarded as natural flooding protections. In relation to this thesis, given the fact that the geometry of the estuary has an influence on the impact of tidal farms on water levels, it would be interesting to simulate the changes induced by the turbines on the seabed morphology and delimit the resulting effects on flood risk. The sand transport modules of MIKE 21 or any other similar software could be used for that purpose. The time horizon for this kind of analysis could be the service life of the tidal farms and issues such as sea level rise due to climate change would need to be considered. For the calibration of the model it would

be necessary to use observations of estuarine changes, thus restricting the analysis to certain locations.

* Taking into account that the hydrodynamic models used in this thesis considered only the tidal forcing, further investigations are suggested introducing wave conditions, which represent a significant power resource around the UK. For example, it would be of interest to compare the results of peak water levels between the hydrodynamic model with and without including the waves.
* Considering the effect of tidal farms on the increase of low tides in estuaries, derived from the results of the idealised models in this thesis, some consequences could be derived in relation to groundwater flooding or soil saturation conditions affecting the overland flooding in the surrounding catchments. Therefore, this topic is of interest for future evaluation.

Finally, there are some points related to the broader optimisation project, in which this thesis is framed, that can be suggested as a future work:

* The estuary modelling could be used to test a group of tidal farm layouts obtained in the optimisation process as possible solution for the maximum energy extraction. It would allow one to determine which are the layouts with minimum impact on peak water levels.
* Instead of using the same turbine loading for the whole farm, simulations could be performed with different values calculated as optimal solutions for maximising the energy output.

Appendix A

Python script for tidal farms in MIKE 21

A.1 Parallel layout

```
import math
import numpy as np

cols =  # number of columns
rows =  # number of rows

n = rows*cols # number of turbines

deltax=  # longitudinal spacing between turbines
deltay=  # transverse spacing between turbines

x1=  # x coordinate of the centre of the first turbine in the farm
y1=  # y coordinate of the centre of the first turbine in the farm

alpha =   # main flow direction (angle in radians referred to horizontal absolute axis)

a = np.linspace(1, n, n).reshape(cols,rows)

d =  #turbines diameter

cd =  #drag coefficient

cf = #correction factor

with open("C:/User/farm_parall.txt", "a") as f: # route to the text file where the tidal
farm will be written
    f.write ("         [TURBINES] \n")
    f.write ("            Touched = 1 \n")
    f.write ("            MzSEPfsListItemCount = ")
    f.write (repr(n))
    f.write ("\n")
    f.write ("            format = 0 \n")
    f.write ("            number_of_turbines = ")
    f.write (repr(n))
    f.write ("\n")
    f.write ("            output_type = 1 \n")
    f.write ("            output_frequency = 1 \n")
    f.write ("            output_file_name = 'turbine_data.dfs0' \n") # user-defined file
    name for turbine outputs
    f.close()

for i in range(cols):
    for j in range(rows):
        print x1+(math.cos(alpha)*(j)*deltax-math.sin(alpha)*(i)*deltay)    #horizontal
        coordinates of the turbines in the farm
        print y1+(math.sin(alpha)*(j)*deltax+math.cos(alpha)*(i)*deltay)     #vertical
        coordinates of the turbines in the farm
        with open("C:/User/farm_parall.txt", "a") as f: # route to the text file where the
        tidal farm will be written
            f.write ("            [TURBINE_")
            f.write (repr(int(a[i,j])))
            f.write ("]\n")
            f.write ("              Name = 'turbine")
```

```
f.write (repr(int(a[i,j])))
f.write ("' \n")
f.write ("               include = 1 \n")
f.write ("               coordinate_type = ")
f.write ("'")

f.write('PROJCS["British_National_Grid",GEOGCS["GCS_OSGB_1936",DATUM["D_OSGB_1936"
,SPHEROID["Airy_1830",6377563.396,299.3249646]],PRIMEM["Greenwich",0],UNIT["Degree
",0.0174532925199433295]],PROJECTION["Transverse_Mercator"],PARAMETER["False_Eastin
g",400000],PARAMETER["False_Northing",-100000],PARAMETER["Central_Meridian",-2],PA
RAMETER["Scale_Factor",0.999601272],PARAMETER["Latitude_Of_Origin",49],UNIT["Meter
",1]]') # Map projection in British National Grid System/ User defined
f.write ("' \n")
f.write ("               x =")
f.write (repr(x1+(math.cos(alpha)*(j)*deltax-math.sin(alpha)*(i)*deltay)))
f.write (" \n")
f.write ("               y = ")
f.write (repr(y1+(math.sin(alpha)*(j)*deltax+math.cos(alpha)*(i)*deltay)))
f.write (" \n")
f.write ("               description = 1 \n")
f.write ("               orientation = 90 \n")
f.write ("               diameter = ")
f.write (repr (d))
f.write (" \n")
f.write ("               centroid = -10 \n")
f.write ("               drag_coefficient = ")
f.write (repr (cd))
f.write (" \n")
f.write ("               [TABLE] \n")
f.write ("                  number_of_directions = 2 \n")
f.write ("                  minimum_direction = 0 \n")
f.write ("                  maximum_direction = 360 \n")
f.write ("                  number_of_speeds = 2 \n")
f.write ("                  minimum_speed = 0 \n")
f.write ("                  maximum_speed = 10 \n")
f.write ("                  cd_1 = 0.4, 0.4 \n")
f.write ("                  cd_2 = 0.4, 0.4 \n")
f.write ("                  cl_1 = 0, 0 \n")
f.write ("                  cl_2 = 0, 0 \n")
f.write ("               EndSect  // TABLE \n")
f.write (" \n")
f.write ("               [CORRECTION_FACTOR] \n")
f.write ("                  Touched = 1 \n")
f.write ("                  type = 1 \n")
f.write ("                  format = 0 \n")
f.write ("                  constant_value = ")
f.write(repr (cf))
f.write (" \n")
f.write ("                  file_name = || \n")
f.write ("                  item_number = 1 \n")
f.write ("                  item_name = '' \n")
f.write ("                  type_of_soft_start = 2 \n")
f.write ("                  soft_time_interval = 0 \n")
f.write ("                  reference_value = 0 \n")
```

```
            f.write ("                  type_of_time_interpolation = 1 \n")
            f.write ("               EndSect  // CORRECTION_FACTOR \n")
            f.write (" \n")
            f.write ("            EndSect  // TURBINE_")
            f.write (repr(int(a[i,j])))
            f.write (" \n")
            f.write (" \n")
            f.close()


with open("C:/User/farm_parall.txt", "a") as f: # route to the text file where the tidal
farm will be written
    f.write ("         EndSect  // TURBINES \n")
```

A.2 Staggered layout

```
import math
import numpy as np

cols1 =  # number of columns (odd position)
rows1 =  # number of rows (odd position)

cols2 =  # number of columns (even position)
rows2 =  # number of rows (even position)

n = rows1*cols1 # number of turbines (odd position)
m = rows2*cols2 # number of turbines (even position)

deltax1= # longitudinal spacing between turbines (odd position)
deltay1= # transverse spacing betwee turbines (even position)

deltax2= # longitudinal spacing between turbines (even position)
deltay2= # transverse spacing between turbines (even position)

x1=
y1=  #coordinates of first turbine (first row and column)

x2=
y2= #coordinates of second turbine (second row and column)

alpha =    # flow direction (angle in radians refered to horizontal absolute axis)

a = np.linspace(1, n, n).reshape(cols1,rows1)
b = np.linspace(n+1,n+m,m).reshape(cols2,rows2)

d =  # turbines diameter

cd =  #drag coefficient

cf = #correction factor

with open("C:/User/farm_parall.txt", "a") as f: # route to the text file where the tidal
farm will be written
    f.write ("         [TURBINES] \n")
    f.write ("            Touched = 1 \n")
    f.write ("            MzSEPfsListItemCount = ")
    f.write (repr(n+m))
    f.write ("\n")
    f.write ("            format = 0 \n")
    f.write ("            number_of_turbines = ")
    f.write (repr(n+m))
    f.write ("\n")
    f.write ("            output_type = 1 \n")
    f.write ("            output_frequency = 1 \n")
    f.write ("            output_file_name = 'turbine_data.dfs0' \n") # user-defined file
    name for turbine outputs
    f.close()

for i in range(cols1):
```

```
for j in range(rows1):
    print x1+(math.cos(alpha)*(j)*deltax1-math.sin(alpha)*(i)*deltay1)    # horizontal
    coordinates
    print y1+(math.sin(alpha)*(j)*deltax1+math.cos(alpha)*(i)*deltay1)     #vertical
    coordinates
    with open("C:/User/farm_parall.txt", "a") as f: # route to the text file where the
    tidal farm will be written
        f.write ("            [TURBINE_")
        f.write (repr(int(a[i,j])))
        f.write ("]\n")
        f.write ("               Name = 'turbine")
        f.write (repr(int(a[i,j])))
        f.write ("' \n")
        f.write ("               include = 1 \n")
        f.write ("               coordinate_type = ")
        f.write ("'")

        f.write('PROJCS["British_National_Grid",GEOGCS["GCS_OSGB_1936",DATUM["D_OSGB_1936"
        ,SPHEROID["Airy_1830",6377563.396,299.3249646]],PRIMEM["Greenwich",0],UNIT["Degree
        ",0.01745329251994295]],PROJECTION["Transverse_Mercator"],PARAMETER["False_Eastin
        g",400000],PARAMETER["False_Northing",-100000],PARAMETER["Central_Meridian",-2],PA
        RAMETER["Scale_Factor",0.999601272],PARAMETER["Latitude_Of_Origin",49],UNIT["Meter
        ",1]]')
        f.write ("' \n")
        f.write ("               x =")
        f.write (repr(x1+(math.cos(alpha)*(j)*deltax1-math.sin(alpha)*(i)*deltay1)))
        f.write (" \n")
        f.write ("               y = ")
        f.write (repr(y1+(math.sin(alpha)*(j)*deltax1+math.cos(alpha)*(i)*deltay1)))
        f.write (" \n")
        f.write ("               description = 1 \n")
        f.write ("               orientation = 90 \n")
        f.write ("               diameter = ")
        f.write (repr (d))
        f.write (" \n")
        f.write ("               centroid = -10 \n")
        f.write ("               drag_coefficient = ")
        f.write (repr (cd))
        f.write (" \n")
        f.write ("               [TABLE] \n")
        f.write ("                  number_of_directions = 2 \n")
        f.write ("                  minimum_direction = 0 \n")
        f.write ("                  maximum_direction = 360 \n")
        f.write ("                  number_of_speeds = 2 \n")
        f.write ("                  minimum_speed = 0 \n")
        f.write ("                  maximum_speed = 10 \n")
        f.write ("                  cd_1 = 0.4, 0.4 \n")
        f.write ("                  cd_2 = 0.4, 0.4 \n")
        f.write ("                  cl_1 = 0, 0 \n")
        f.write ("                  cl_2 = 0, 0 \n")
        f.write ("               EndSect  // TABLE \n")
        f.write (" \n")
        f.write ("               [CORRECTION_FACTOR] \n")
        f.write ("                  Touched = 1 \n")
```

```
            f.write ("                  type = 1 \n")
            f.write ("                  format = 0 \n")
            f.write ("                  constant_value = ")
            f.write(repr (cf))
            f.write (" \n")
            f.write ("                  file_name = || \n")
            f.write ("                  item_number = 1 \n")
            f.write ("                  item_name = '' \n")
            f.write ("                  type_of_soft_start = 2 \n")
            f.write ("                  soft_time_interval = 0 \n")
            f.write ("                  reference_value = 0 \n")
            f.write ("                  type_of_time_interpolation = 1 \n")
            f.write ("               EndSect  // CORRECTION_FACTOR \n")
            f.write (" \n")
            f.write ("            EndSect  // TURBINE_")
            f.write (repr(int(a[i,j])))
            f.write (" \n")
            f.write (" \n")
            f.close()

for i in range(cols2):
    for j in range(rows2):
        print x2+(math.cos(alpha)*(j)*deltax2-math.sin(alpha)*(i)*deltay2)    # horizontal
        coordinates
        print y2+(math.sin(alpha)*(j)*deltax2+math.cos(alpha)*(i)*deltay2)     #vertical
        coordinates
        with open("C:/User/farm_parall.txt", "a") as f: # route to the text file where the
        tidal farm will be written
            f.write ("            [TURBINE_")
            f.write (repr(int(b[i,j])))
            f.write ("]\n")
            f.write ("               Name = 'turbine")
            f.write (repr(int(b[i,j])))
            f.write ("' \n")
            f.write ("               include = 1 \n")
            f.write ("               coordinate_type = ")
            f.write ("'")

            f.write('PROJCS["British_National_Grid",GEOGCS["GCS_OSGB_1936",DATUM["D_OSGB_1936"
            ,SPHEROID["Airy_1830",6377563.396,299.3249646]],PRIMEM["Greenwich",0],UNIT["Degree
            ",0.0174532925199433295]],PROJECTION["Transverse_Mercator"],PARAMETER["False_Eastin
            g",400000],PARAMETER["False_Northing",-100000],PARAMETER["Central_Meridian",-2],PA
            RAMETER["Scale_Factor",0.999601272],PARAMETER["Latitude_Of_Origin",49],UNIT["Meter
            ",1]]')
            f.write ("' \n")
            f.write ("               x =")
            f.write (repr(x2+(math.cos(alpha)*(j)*deltax2-math.sin(alpha)*(i)*deltay2)))
            f.write (" \n")
            f.write ("               y = ")
            f.write (repr(y2+(math.sin(alpha)*(j)*deltax2+math.cos(alpha)*(i)*deltay2)))
            f.write (" \n")
            f.write ("               description = 1 \n")
            f.write ("               orientation = 90 \n")
            f.write ("               diameter = ")
```

```
            f.write (repr (d))
            f.write (" \n")
            f.write ("               centroid = -10 \n")
            f.write ("               drag_coefficient = ")
            f.write (repr (cd))
            f.write (" \n")
            f.write ("               [TABLE] \n")
            f.write ("                  number_of_directions = 2 \n")
            f.write ("                  minimum_direction = 0 \n")
            f.write ("                  maximum_direction = 360 \n")
            f.write ("                  number_of_speeds = 2 \n")
            f.write ("                  minimum_speed = 0 \n")
            f.write ("                  maximum_speed = 10 \n")
            f.write ("                  cd_1 = 0.4, 0.4 \n")
            f.write ("                  cd_2 = 0.4, 0.4 \n")
            f.write ("                  cl_1 = 0, 0 \n")
            f.write ("                  cl_2 = 0, 0 \n")
            f.write ("               EndSect  // TABLE \n")
            f.write (" \n")
            f.write ("               [CORRECTION_FACTOR] \n")
            f.write ("                  Touched = 1 \n")
            f.write ("                  type = 1 \n")
            f.write ("                  format = 0 \n")
            f.write ("                  constant_value = ")
            f.write(repr (cf))
            f.write (" \n")
            f.write ("                  file_name = || \n")
            f.write ("                  item_number = 1 \n")
            f.write ("                  item_name = '' \n")
            f.write ("                  type_of_soft_start = 2 \n")
            f.write ("                  soft_time_interval = 0 \n")
            f.write ("                  reference_value = 0 \n")
            f.write ("                  type_of_time_interpolation = 1 \n")
            f.write ("               EndSect  // CORRECTION_FACTOR \n")
            f.write (" \n")
            f.write ("            EndSect  // TURBINE_")
            f.write (repr(int(b[i,j])))
            f.write (" \n")
            f.write (" \n")
            f.close()


with open("C:/User/farm_parall.txt", "a") as f: # route to the text file where the tidal
farm will be written
    f.write ("         EndSect  // TURBINES \n")
```

Appendix B

Changes at high/low tides - Idealised estuaries

Positive values: decrease/ Negative values: increase.

Upper image: changes in minimum water levels (low tides)

Lower image: changes in maximum water levels (high tides)

Case 1.b

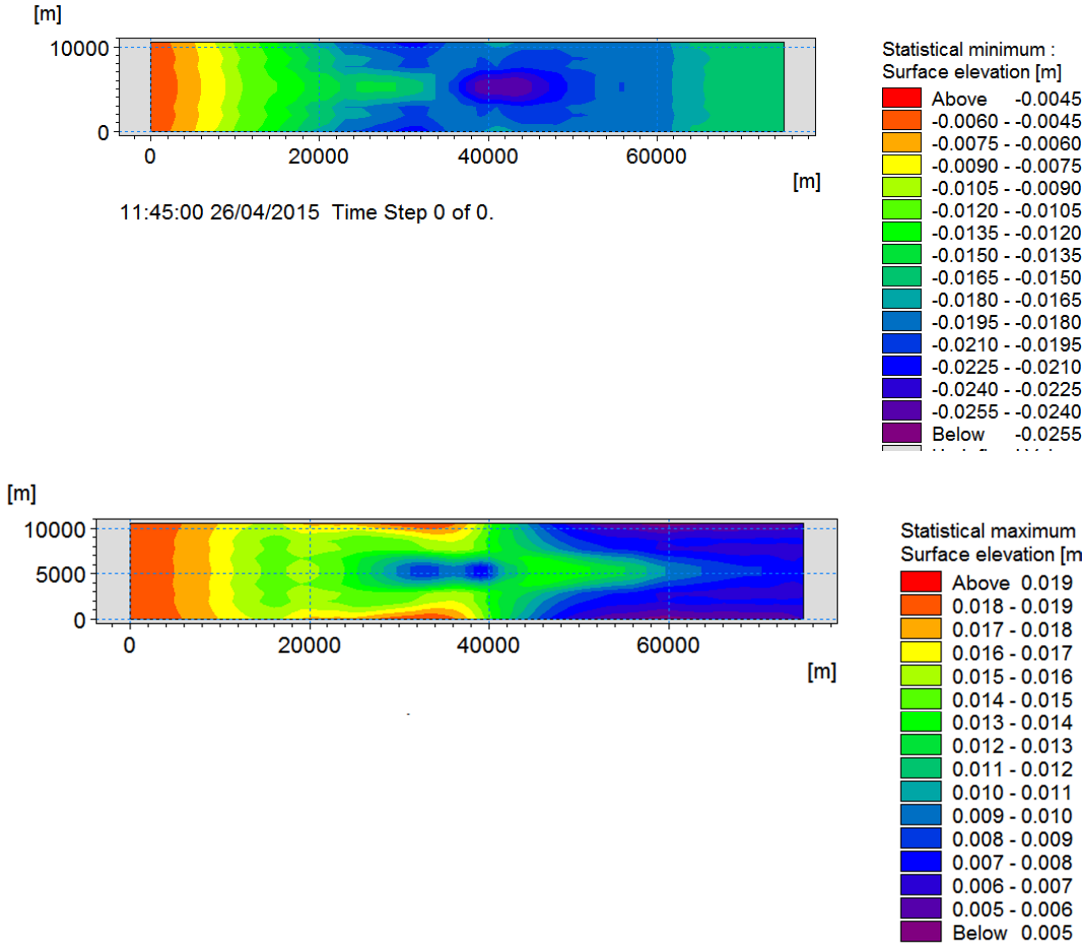

Case 1.c

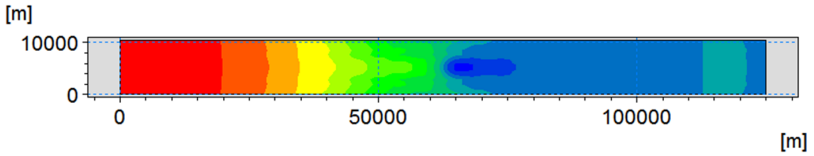
[m]
10000
0
0
50000
100000
[m]

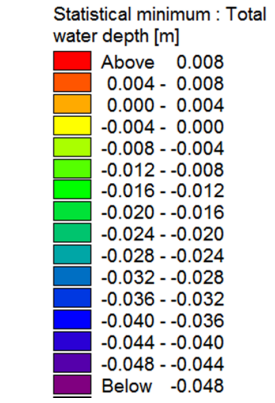
Statistical minimum : Total water depth [m]
Above 0.008
0.004 - 0.008
0.000 - 0.004
-0.004 - 0.000
-0.008 - -0.004
-0.012 - -0.008
-0.016 - -0.012
-0.020 - -0.016
-0.024 - -0.020
-0.028 - -0.024
-0.032 - -0.028
-0.036 - -0.032
-0.040 - -0.036
-0.044 - -0.040
-0.048 - -0.044
Below -0.048

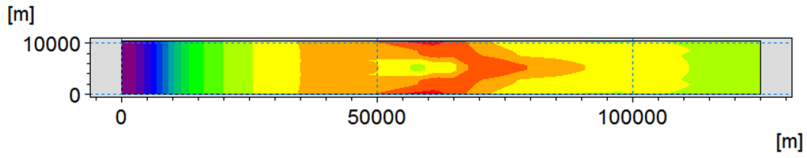
[m]
10000
0
0
50000
100000
[m]

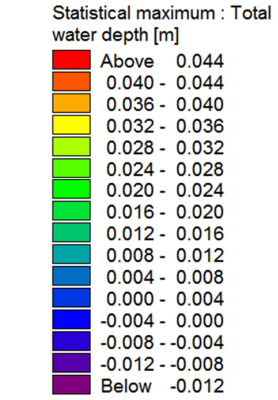
Statistical maximum : Total water depth [m]
Above 0.044
0.040 - 0.044
0.036 - 0.040
0.032 - 0.036
0.028 - 0.032
0.024 - 0.028
0.020 - 0.024
0.016 - 0.020
0.012 - 0.016
0.008 - 0.012
0.004 - 0.008
0.000 - 0.004
-0.004 - 0.000
-0.008 - -0.004
-0.012 - -0.008
Below -0.012

Case 2.a

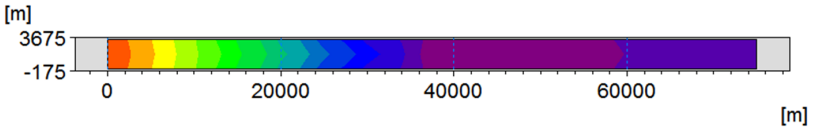

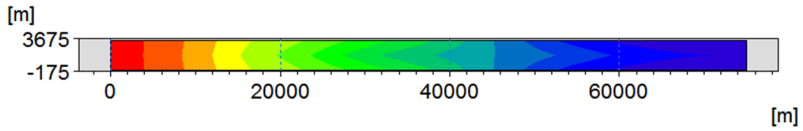

Statistical minimum : Total water depth [m]

- Above -0.008
- -0.016 - -0.008
- -0.024 - -0.016
- -0.032 - -0.024
- -0.040 - -0.032
- -0.048 - -0.040
- -0.056 - -0.048
- -0.064 - -0.056
- -0.072 - -0.064
- -0.080 - -0.072
- -0.088 - -0.080
- -0.096 - -0.088
- -0.104 - -0.096
- -0.112 - -0.104
- -0.120 - -0.112
- Below -0.120

Statistical maximum : Total water depth [m]

- Above 0.120
- 0.114 - 0.120
- 0.108 - 0.114
- 0.102 - 0.108
- 0.096 - 0.102
- 0.090 - 0.096
- 0.084 - 0.090
- 0.078 - 0.084
- 0.072 - 0.078
- 0.066 - 0.072
- 0.060 - 0.066
- 0.054 - 0.060
- 0.048 - 0.054
- 0.042 - 0.048
- 0.036 - 0.042
- Below 0.036

Case 2.c

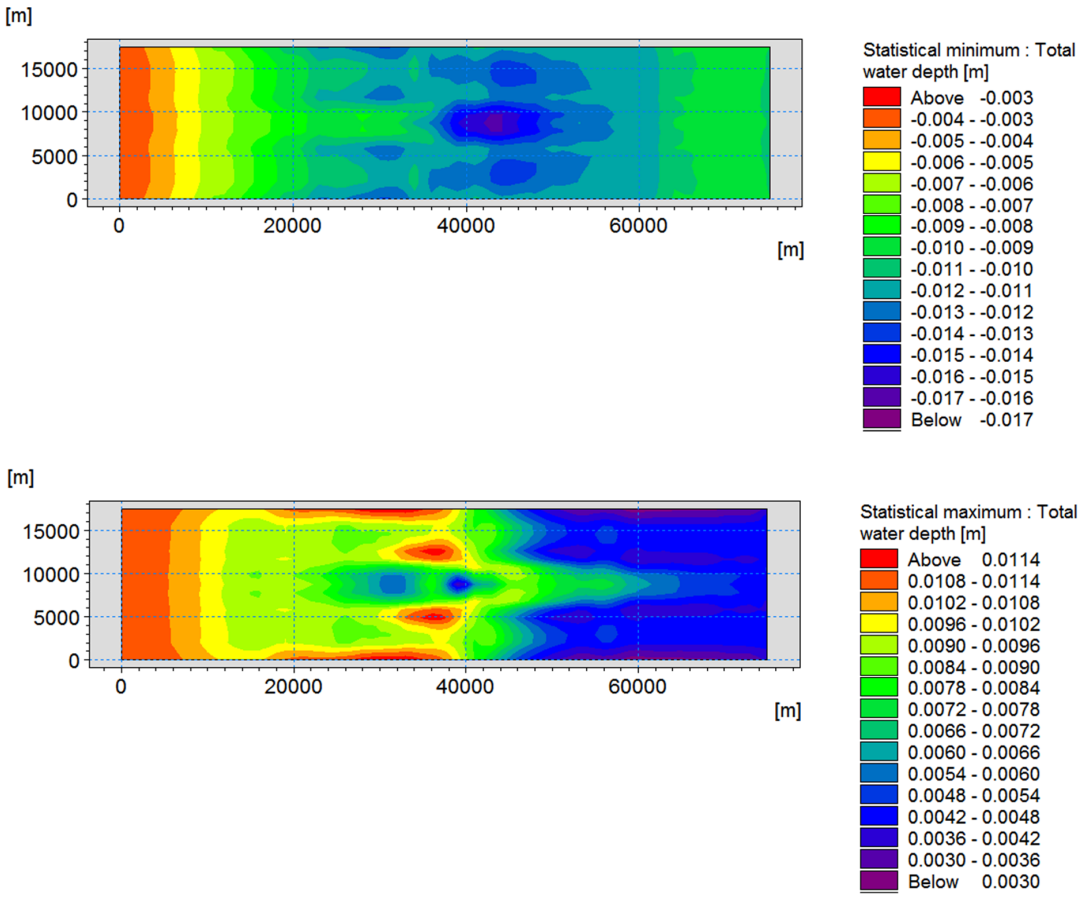
[m]
15000
10000
5000
0
0
20000
40000
60000
[m]
Statistical minimum : Total water depth [m]
Above -0.003
-0.004 - -0.003
-0.005 - -0.004
-0.006 - -0.005
-0.007 - -0.006
-0.008 - -0.007
-0.009 - -0.008
-0.010 - -0.009
-0.011 - -0.010
-0.012 - -0.011
-0.013 - -0.012
-0.014 - -0.013
-0.015 - -0.014
-0.016 - -0.015
-0.017 - -0.016
Below -0.017
[m]
15000
10000
5000
0
0
20000
40000
60000
[m]
Statistical maximum : Total water depth [m]
Above 0.0114
0.0108 - 0.0114
0.0102 - 0.0108
0.0096 - 0.0102
0.0090 - 0.0096
0.0084 - 0.0090
0.0078 - 0.0084
0.0072 - 0.0078
0.0066 - 0.0072
0.0060 - 0.0066
0.0054 - 0.0060
0.0048 - 0.0054
0.0042 - 0.0048
0.0036 - 0.0042
0.0030 - 0.0036
Below 0.0030

Case 2.i

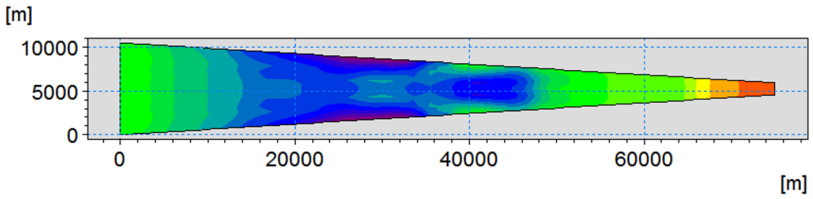
[m]
10000
5000
0
0
20000
40000
60000
[m]

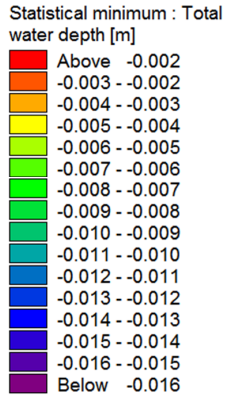
Statistical minimum : Total water depth [m]
Above -0.002
-0.003 - -0.002
-0.004 - -0.003
-0.005 - -0.004
-0.006 - -0.005
-0.007 - -0.006
-0.008 - -0.007
-0.009 - -0.008
-0.010 - -0.009
-0.011 - -0.010
-0.012 - -0.011
-0.013 - -0.012
-0.014 - -0.013
-0.015 - -0.014
-0.016 - -0.015
Below -0.016

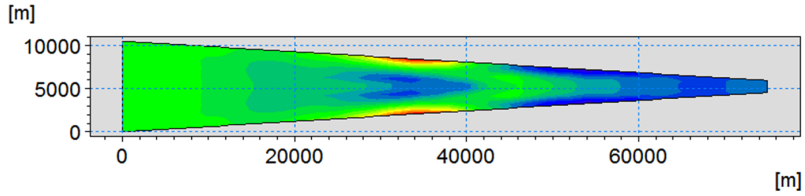
[m]
10000
5000
0
0
20000
40000
60000
[m]

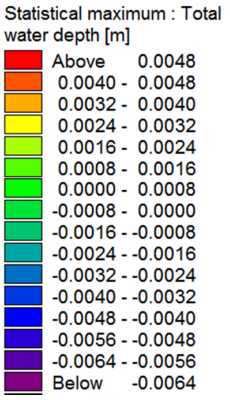
Statistical maximum : Total water depth [m]
Above 0.0048
0.0040 - 0.0048
0.0032 - 0.0040
0.0024 - 0.0032
0.0016 - 0.0024
0.0008 - 0.0016
0.0000 - 0.0008
-0.0008 - 0.0000
-0.0016 - -0.0008
-0.0024 - -0.0016
-0.0032 - -0.0024
-0.0040 - -0.0032
-0.0048 - -0.0040
-0.0056 - -0.0048
-0.0064 - -0.0056
Below -0.0064

Case 2.ii

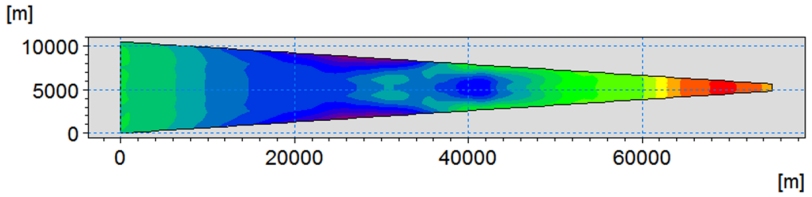
[m]
10000
5000
0
0
20000
40000
60000
[m]

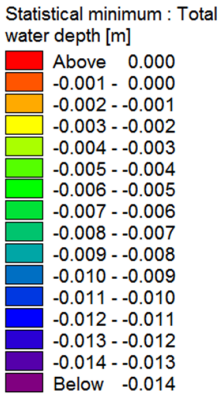
Statistical minimum : Total water depth [m]
Above 0.000
-0.001 - 0.000
-0.002 - -0.001
-0.003 - -0.002
-0.004 - -0.003
-0.005 - -0.004
-0.006 - -0.005
-0.007 - -0.006
-0.008 - -0.007
-0.009 - -0.008
-0.010 - -0.009
-0.011 - -0.010
-0.012 - -0.011
-0.013 - -0.012
-0.014 - -0.013
Below -0.014

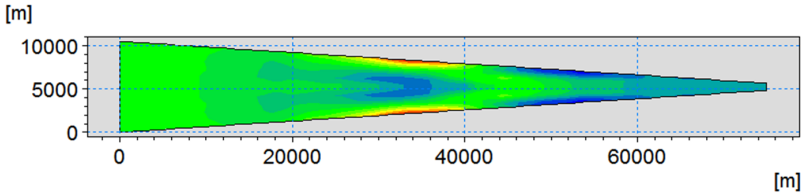
[m]
10000
5000
0
0
20000
40000
60000
[m]

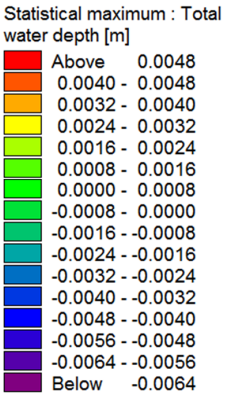
Statistical maximum : Total water depth [m]
Above 0.0048
0.0040 - 0.0048
0.0032 - 0.0040
0.0024 - 0.0032
0.0016 - 0.0024
0.0008 - 0.0016
0.0000 - 0.0008
-0.0008 - 0.0000
-0.0016 - -0.0008
-0.0024 - -0.0016
-0.0032 - -0.0024
-0.0040 - -0.0032
-0.0048 - -0.0040
-0.0056 - -0.0048
-0.0064 - -0.0056
Below -0.0064

Case 2.iii

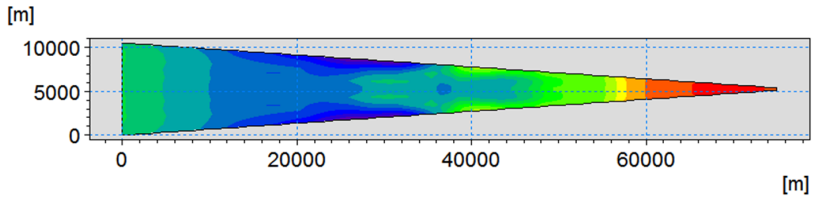
[m]
10000
5000
0
0
20000
40000
60000
[m]

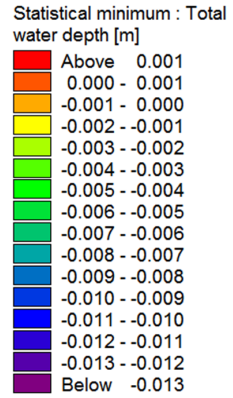
Statistical minimum : Total water depth [m]
Above 0.001
0.000 - 0.001
-0.001 - 0.000
-0.002 - -0.001
-0.003 - -0.002
-0.004 - -0.003
-0.005 - -0.004
-0.006 - -0.005
-0.007 - -0.006
-0.008 - -0.007
-0.009 - -0.008
-0.010 - -0.009
-0.011 - -0.010
-0.012 - -0.011
-0.013 - -0.012
Below -0.013

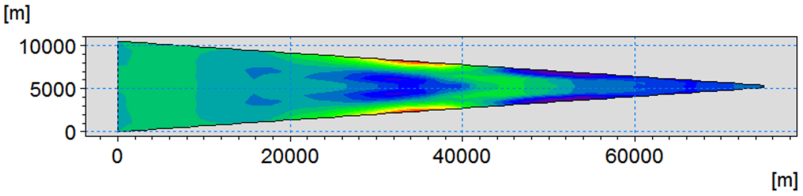
[m]
10000
5000
0
0
20000
40000
60000
[m]

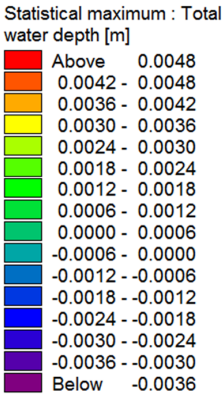
Statistical maximum : Total water depth [m]
Above 0.0048
0.0042 - 0.0048
0.0036 - 0.0042
0.0030 - 0.0036
0.0024 - 0.0030
0.0018 - 0.0024
0.0012 - 0.0018
0.0006 - 0.0012
0.0000 - 0.0006
-0.0006 - 0.0000
-0.0012 - -0.0006
-0.0018 - -0.0012
-0.0024 - -0.0018
-0.0030 - -0.0024
-0.0036 - -0.0030
Below -0.0036

Case 3.a

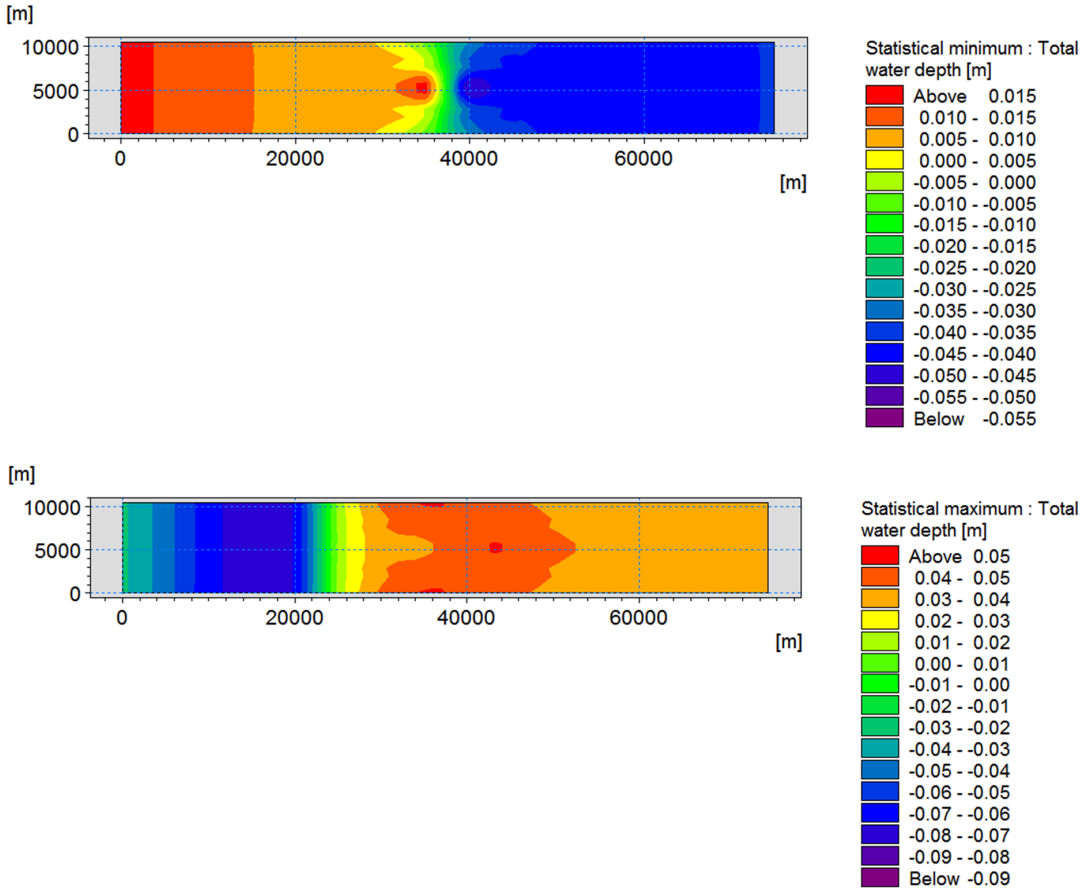
[m]
10000
5000
0
0
20000
40000
60000
[m]
Statistical minimum : Total water depth [m]
Above 0.015
0.010 - 0.015
0.005 - 0.010
0.000 - 0.005
-0.005 - 0.000
-0.010 - -0.005
-0.015 - -0.010
-0.020 - -0.015
-0.025 - -0.020
-0.030 - -0.025
-0.035 - -0.030
-0.040 - -0.035
-0.045 - -0.040
-0.050 - -0.045
-0.055 - -0.050
Below -0.055
[m]
10000
5000
0
0
20000
40000
60000
[m]
Statistical maximum : Total water depth [m]
Above 0.05
0.04 - 0.05
0.03 - 0.04
0.02 - 0.03
0.01 - 0.02
0.00 - 0.01
-0.01 - 0.00
-0.02 - -0.01
-0.03 - -0.02
-0.04 - -0.03
-0.05 - -0.04
-0.06 - -0.05
-0.07 - -0.06
-0.08 - -0.07
-0.09 - -0.08
Below -0.09

Case 3.c

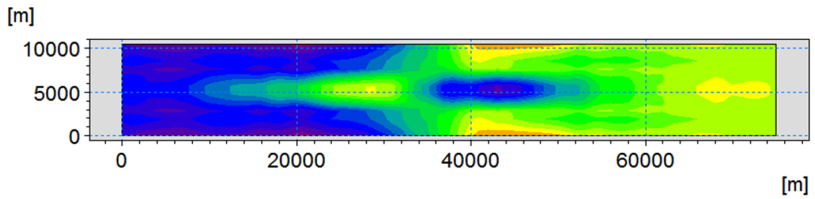

Statistical minimum : Total water depth [m]

Above	-0.0012
-0.0016	-0.0012
-0.0020	-0.0016
-0.0024	-0.0020
-0.0028	-0.0024
-0.0032	-0.0028
-0.0036	-0.0032
-0.0040	-0.0036
-0.0044	-0.0040
-0.0048	-0.0044
-0.0052	-0.0048
-0.0056	-0.0052
-0.0060	-0.0056
-0.0064	-0.0060
-0.0068	-0.0064
Below	-0.0068

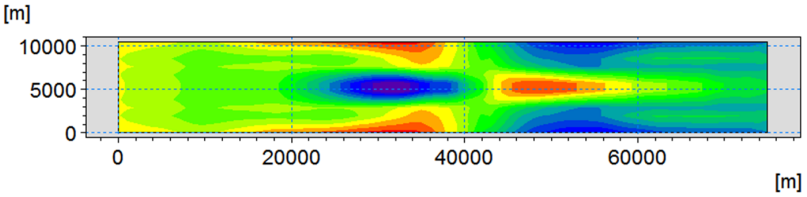

Statistical maximum : Total water depth [m]

Above	0.0036
0.0032	0.0036
0.0028	0.0032
0.0024	0.0028
0.0020	0.0024
0.0016	0.0020
0.0012	0.0016
0.0008	0.0012
0.0004	0.0008
0.0000	0.0004
-0.0004	0.0000
-0.0008	-0.0004
-0.0012	-0.0008
-0.0016	-0.0012
-0.0020	-0.0016
Below	-0.0020

Case 3.i

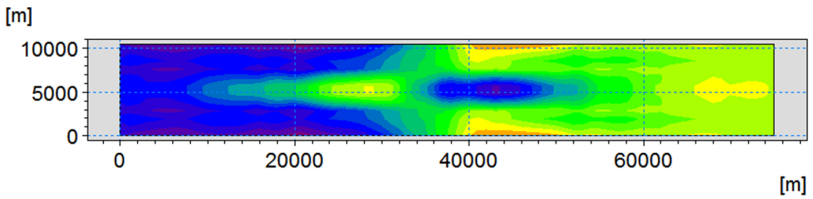
[m]
10000
5000
0
0
20000
40000
60000
[m]

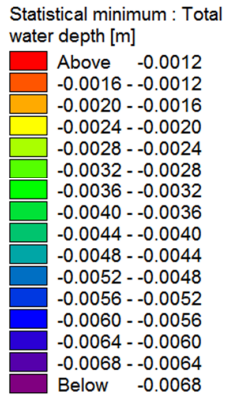
Statistical minimum : Total water depth [m]
Above -0.0012
-0.0016 - -0.0012
-0.0020 - -0.0016
-0.0024 - -0.0020
-0.0028 - -0.0024
-0.0032 - -0.0028
-0.0036 - -0.0032
-0.0040 - -0.0036
-0.0044 - -0.0040
-0.0048 - -0.0044
-0.0052 - -0.0048
-0.0056 - -0.0052
-0.0060 - -0.0056
-0.0064 - -0.0060
-0.0068 - -0.0064
Below -0.0068

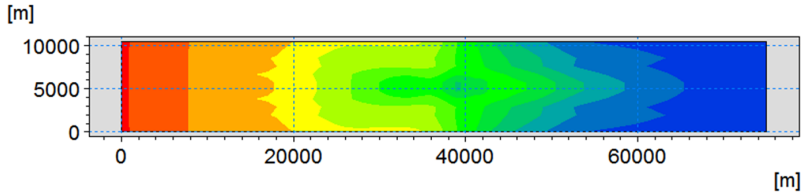
[m]
10000
5000
0
0
20000
40000
60000
[m]

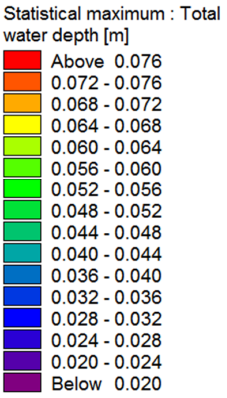
Statistical maximum : Total water depth [m]
Above 0.076
0.072 - 0.076
0.068 - 0.072
0.064 - 0.068
0.060 - 0.064
0.056 - 0.060
0.052 - 0.056
0.048 - 0.052
0.044 - 0.048
0.040 - 0.044
0.036 - 0.040
0.032 - 0.036
0.028 - 0.032
0.024 - 0.028
0.020 - 0.024
Below 0.020

Case3.i-ii

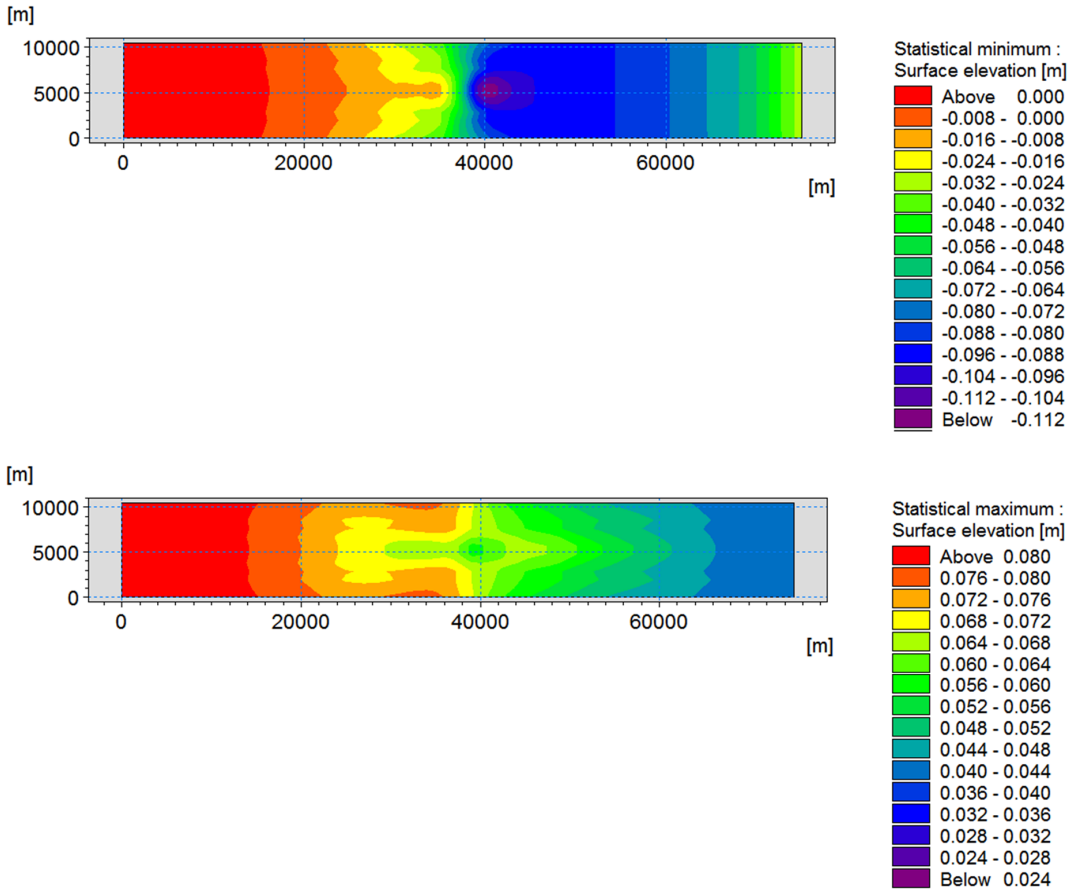
[m]
10000
5000
0
0
20000
40000
60000
[m]
Statistical minimum :
Surface elevation [m]
Above 0.000
-0.008 - 0.000
-0.016 - -0.008
-0.024 - -0.016
-0.032 - -0.024
-0.040 - -0.032
-0.048 - -0.040
-0.056 - -0.048
-0.064 - -0.056
-0.072 - -0.064
-0.080 - -0.072
-0.088 - -0.080
-0.096 - -0.088
-0.104 - -0.096
-0.112 - -0.104
Below -0.112
[m]
10000
5000
0
0
20000
40000
60000
[m]
Statistical maximum :
Surface elevation [m]
Above 0.080
0.076 - 0.080
0.072 - 0.076
0.068 - 0.072
0.064 - 0.068
0.060 - 0.064
0.056 - 0.060
0.052 - 0.056
0.048 - 0.052
0.044 - 0.048
0.040 - 0.044
0.036 - 0.040
0.032 - 0.036
0.028 - 0.032
0.024 - 0.028
Below 0.024

Case 3.ii

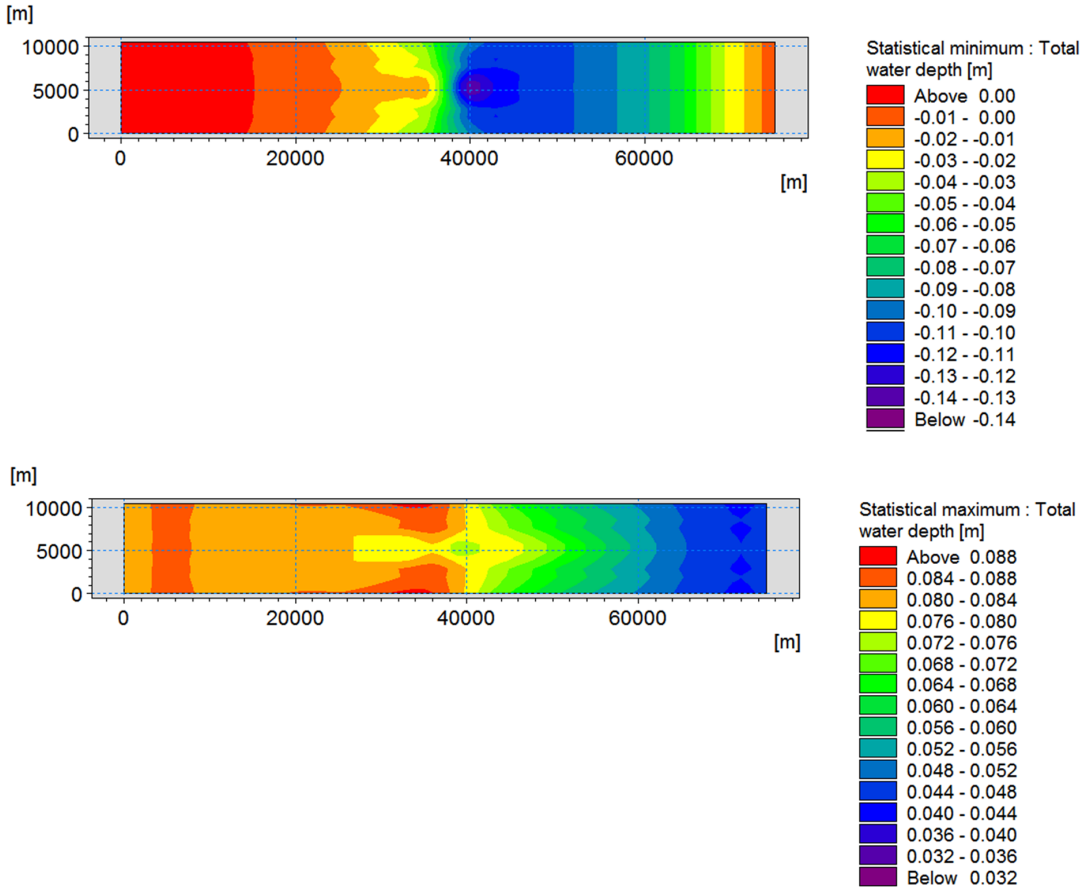
[m]
10000
5000
0
0
20000
40000
60000
[m]
Statistical minimum : Total water depth [m]
Above 0.00
-0.01 - 0.00
-0.02 - -0.01
-0.03 - -0.02
-0.04 - -0.03
-0.05 - -0.04
-0.06 - -0.05
-0.07 - -0.06
-0.08 - -0.07
-0.09 - -0.08
-0.10 - -0.09
-0.11 - -0.10
-0.12 - -0.11
-0.13 - -0.12
-0.14 - -0.13
Below -0.14
[m]
10000
5000
0
0
20000
40000
60000
[m]
Statistical maximum : Total water depth [m]
Above 0.088
0.084 - 0.088
0.080 - 0.084
0.076 - 0.080
0.072 - 0.076
0.068 - 0.072
0.064 - 0.068
0.060 - 0.064
0.056 - 0.060
0.052 - 0.056
0.048 - 0.052
0.044 - 0.048
0.040 - 0.044
0.036 - 0.040
0.032 - 0.036
Below 0.032

Case 3.ii-iii

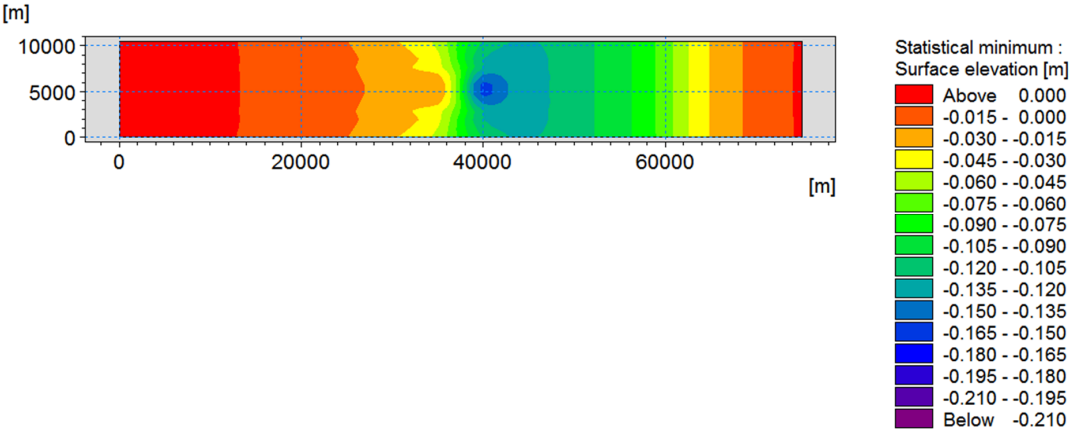
[m]
10000
5000
0
0
20000
40000
60000
[m]
Statistical minimum :
Surface elevation [m]
Above 0.000
-0.015 - 0.000
-0.030 - -0.015
-0.045 - -0.030
-0.060 - -0.045
-0.075 - -0.060
-0.090 - -0.075
-0.105 - -0.090
-0.120 - -0.105
-0.135 - -0.120
-0.150 - -0.135
-0.165 - -0.150
-0.180 - -0.165
-0.195 - -0.180
-0.210 - -0.195
Below -0.210

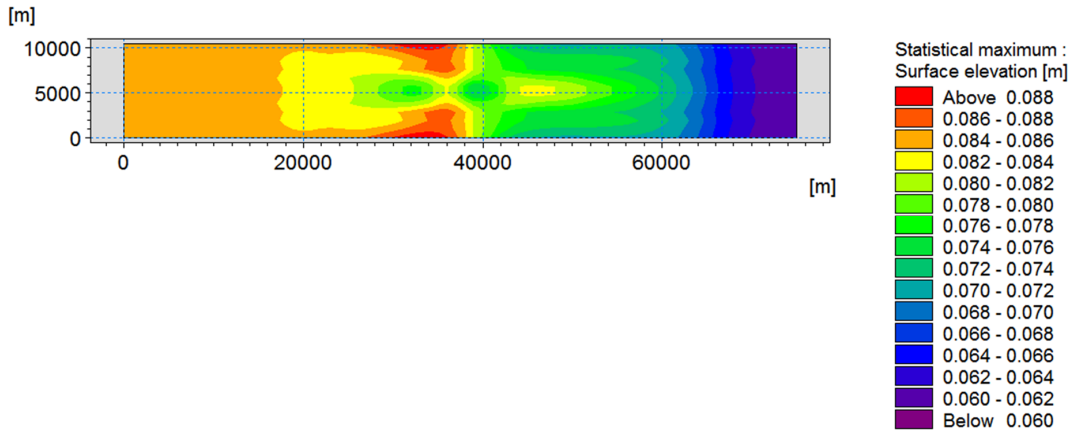
[m]
10000
5000
0
0
20000
40000
60000
[m]
Statistical maximum :
Surface elevation [m]
Above 0.088
0.086 - 0.088
0.084 - 0.086
0.082 - 0.084
0.080 - 0.082
0.078 - 0.080
0.076 - 0.078
0.074 - 0.076
0.072 - 0.074
0.070 - 0.072
0.068 - 0.070
0.066 - 0.068
0.064 - 0.066
0.062 - 0.064
0.060 - 0.062
Below 0.060

Case 3.iii

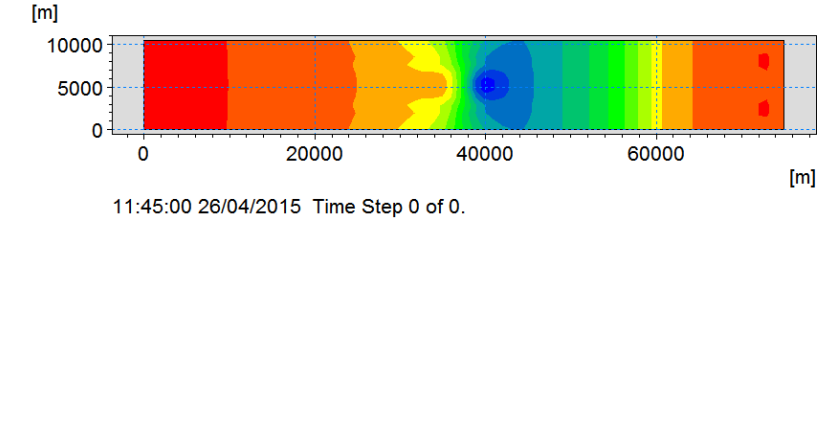
[m]
10000
5000
0
0
20000
40000
60000
[m]
11:45:00 26/04/2015 Time Step 0 of 0.

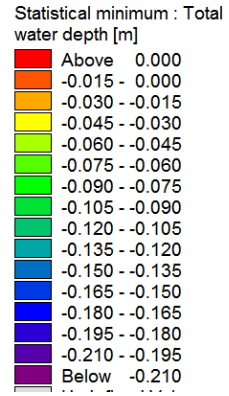
Statistical minimum : Total water depth [m]
Above 0.000
-0.015 - 0.000
-0.030 - -0.015
-0.045 - -0.030
-0.060 - -0.045
-0.075 - -0.060
-0.090 - -0.075
-0.105 - -0.090
-0.120 - -0.105
-0.135 - -0.120
-0.150 - -0.135
-0.165 - -0.150
-0.180 - -0.165
-0.195 - -0.180
-0.210 - -0.195
Below -0.210

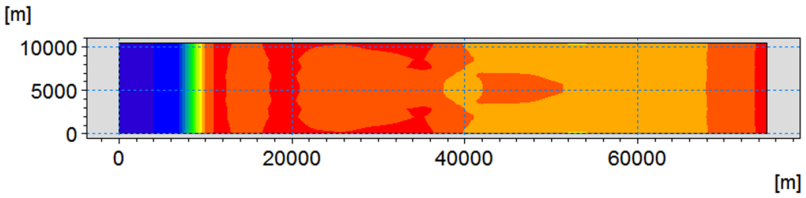
[m]
10000
5000
0
0
20000
40000
60000
[m]

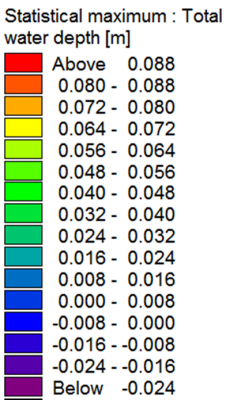
Statistical maximum : Total water depth [m]
Above 0.088
0.080 - 0.088
0.072 - 0.080
0.064 - 0.072
0.056 - 0.064
0.048 - 0.056
0.040 - 0.048
0.032 - 0.040
0.024 - 0.032
0.016 - 0.024
0.008 - 0.016
0.000 - 0.008
-0.008 - 0.000
-0.016 - -0.008
-0.024 - -0.016
Below -0.024

Case 4.a

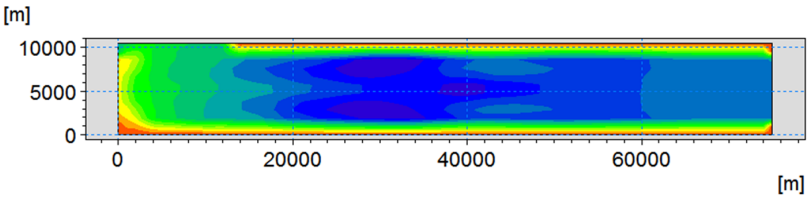
[m]
10000
5000
0
0
20000
40000
60000
[m]

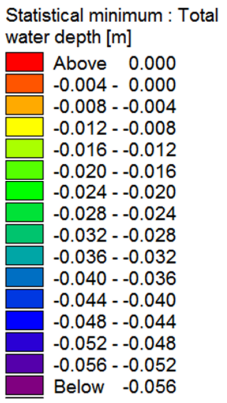
Statistical minimum : Total water depth [m]
Above 0.000
-0.004 - 0.000
-0.008 - -0.004
-0.012 - -0.008
-0.016 - -0.012
-0.020 - -0.016
-0.024 - -0.020
-0.028 - -0.024
-0.032 - -0.028
-0.036 - -0.032
-0.040 - -0.036
-0.044 - -0.040
-0.048 - -0.044
-0.052 - -0.048
-0.056 - -0.052
Below -0.056

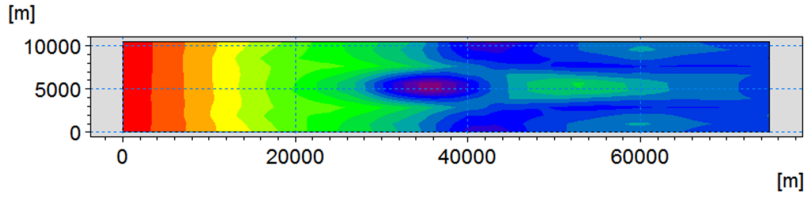
[m]
10000
5000
0
0
20000
40000
60000
[m]

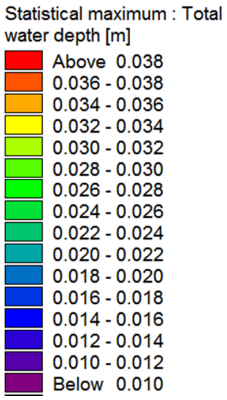
Statistical maximum : Total water depth [m]
Above 0.038
0.036 - 0.038
0.034 - 0.036
0.032 - 0.034
0.030 - 0.032
0.028 - 0.030
0.026 - 0.028
0.024 - 0.026
0.022 - 0.024
0.020 - 0.022
0.018 - 0.020
0.016 - 0.018
0.014 - 0.016
0.012 - 0.014
0.010 - 0.012
Below 0.010

Case 4.b

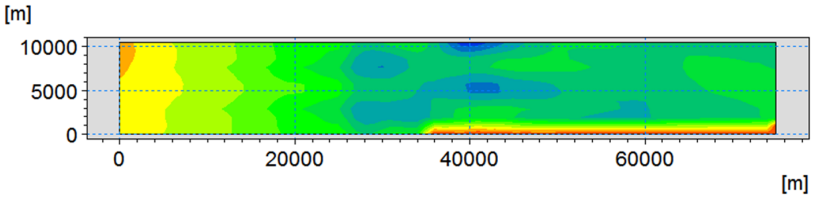
[m]
10000
5000
0
0
20000
40000
60000
[m]

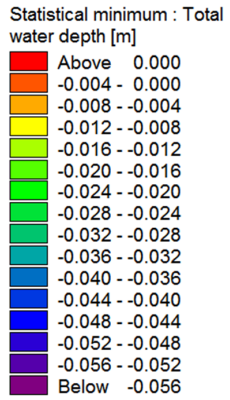
Statistical minimum : Total water depth [m]
Above 0.000
-0.004 - 0.000
-0.008 - -0.004
-0.012 - -0.008
-0.016 - -0.012
-0.020 - -0.016
-0.024 - -0.020
-0.028 - -0.024
-0.032 - -0.028
-0.036 - -0.032
-0.040 - -0.036
-0.044 - -0.040
-0.048 - -0.044
-0.052 - -0.048
-0.056 - -0.052
Below -0.056

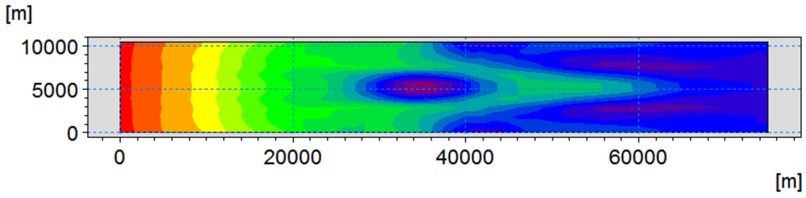
[m]
10000
5000
0
0
20000
40000
60000
[m]

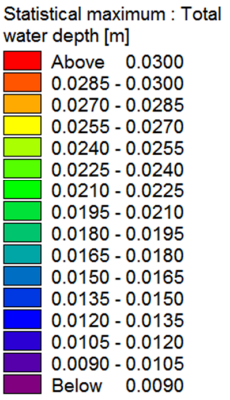
Statistical maximum : Total water depth [m]
Above 0.0300
0.0285 - 0.0300
0.0270 - 0.0285
0.0255 - 0.0270
0.0240 - 0.0255
0.0225 - 0.0240
0.0210 - 0.0225
0.0195 - 0.0210
0.0180 - 0.0195
0.0165 - 0.0180
0.0150 - 0.0165
0.0135 - 0.0150
0.0120 - 0.0135
0.0105 - 0.0120
0.0090 - 0.0105
Below 0.0090

Case 5.a

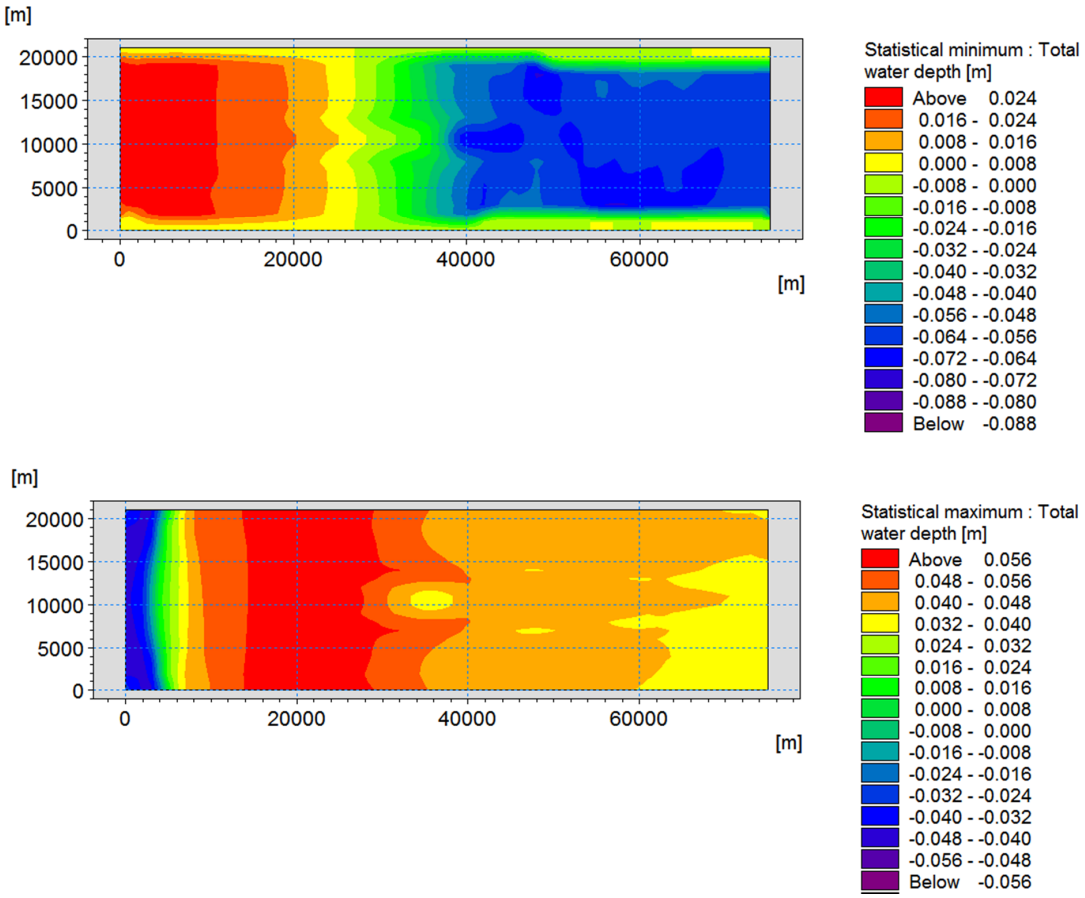
[m]
20000
15000
10000
5000
0
0
20000
40000
60000
[m]
Statistical minimum : Total water depth [m]
Above 0.024
0.016 - 0.024
0.008 - 0.016
0.000 - 0.008
-0.008 - 0.000
-0.016 - -0.008
-0.024 - -0.016
-0.032 - -0.024
-0.040 - -0.032
-0.048 - -0.040
-0.056 - -0.048
-0.064 - -0.056
-0.072 - -0.064
-0.080 - -0.072
-0.088 - -0.080
Below -0.088
[m]
20000
15000
10000
5000
0
0
20000
40000
60000
[m]
Statistical maximum : Total water depth [m]
Above 0.056
0.048 - 0.056
0.040 - 0.048
0.032 - 0.040
0.024 - 0.032
0.016 - 0.024
0.008 - 0.016
0.000 - 0.008
-0.008 - 0.000
-0.016 - -0.008
-0.024 - -0.016
-0.032 - -0.024
-0.040 - -0.032
-0.048 - -0.040
-0.056 - -0.048
Below -0.056

Case 5.b

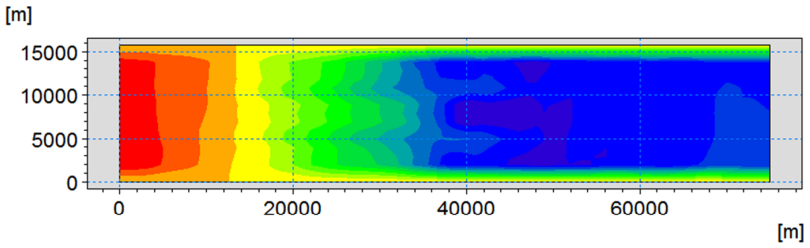
[m]
15000
10000
5000
0
0
20000
40000
60000
[m]

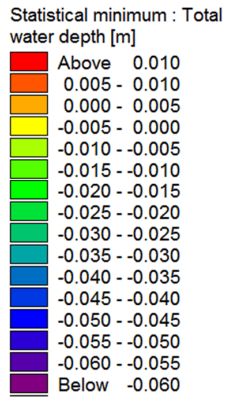
Statistical minimum : Total water depth [m]
Above 0.010
0.005 - 0.010
0.000 - 0.005
-0.005 - 0.000
-0.010 - -0.005
-0.015 - -0.010
-0.020 - -0.015
-0.025 - -0.020
-0.030 - -0.025
-0.035 - -0.030
-0.040 - -0.035
-0.045 - -0.040
-0.050 - -0.045
-0.055 - -0.050
-0.060 - -0.055
Below -0.060

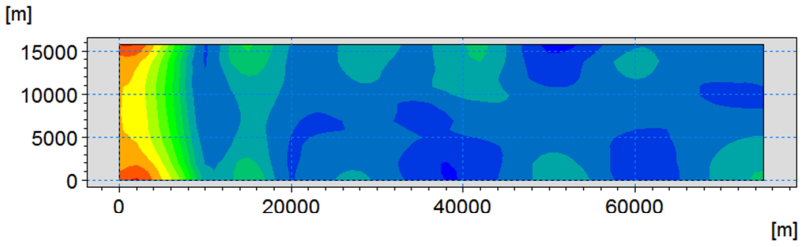
[m]
15000
10000
5000
0
0
20000
40000
60000
[m]

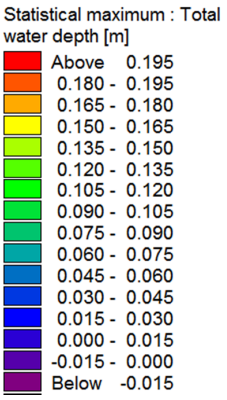
Statistical maximum : Total water depth [m]
Above 0.195
0.180 - 0.195
0.165 - 0.180
0.150 - 0.165
0.135 - 0.150
0.120 - 0.135
0.105 - 0.120
0.090 - 0.105
0.075 - 0.090
0.060 - 0.075
0.045 - 0.060
0.030 - 0.045
0.015 - 0.030
0.000 - 0.015
-0.015 - 0.000
Below -0.015

Case 6.b

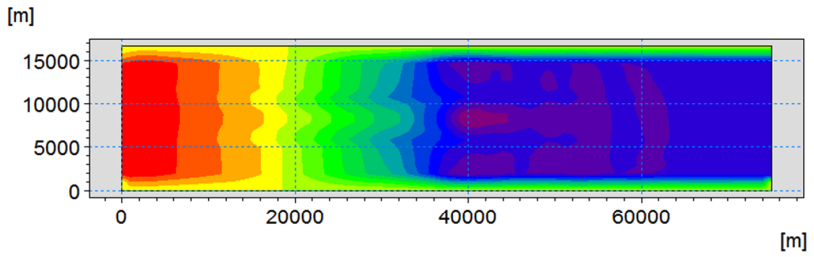
[m]
15000
10000
5000
0
0
20000
40000
60000
[m]

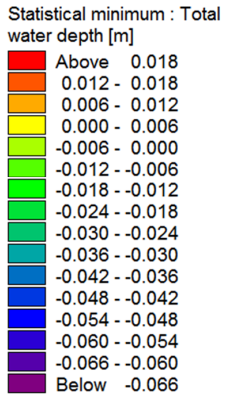
Statistical minimum : Total water depth [m]
Above 0.018
0.012 - 0.018
0.006 - 0.012
0.000 - 0.006
-0.006 - 0.000
-0.012 - -0.006
-0.018 - -0.012
-0.024 - -0.018
-0.030 - -0.024
-0.036 - -0.030
-0.042 - -0.036
-0.048 - -0.042
-0.054 - -0.048
-0.060 - -0.054
-0.066 - -0.060
Below -0.066

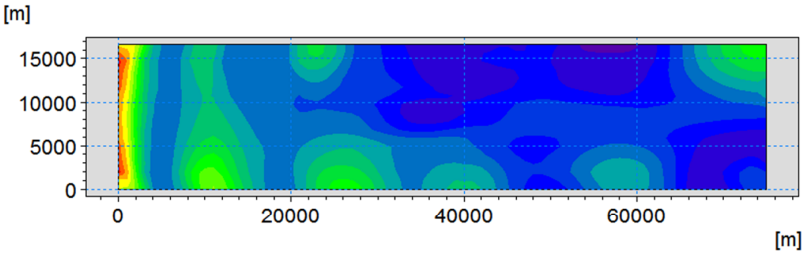
[m]
15000
10000
5000
0
0
20000
40000
60000
[m]

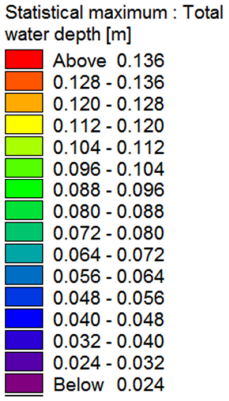
Statistical maximum : Total water depth [m]
Above 0.136
0.128 - 0.136
0.120 - 0.128
0.112 - 0.120
0.104 - 0.112
0.096 - 0.104
0.088 - 0.096
0.080 - 0.088
0.072 - 0.080
0.064 - 0.072
0.056 - 0.064
0.048 - 0.056
0.040 - 0.048
0.032 - 0.040
0.024 - 0.032
Below 0.024

Case 1.b without bed friction

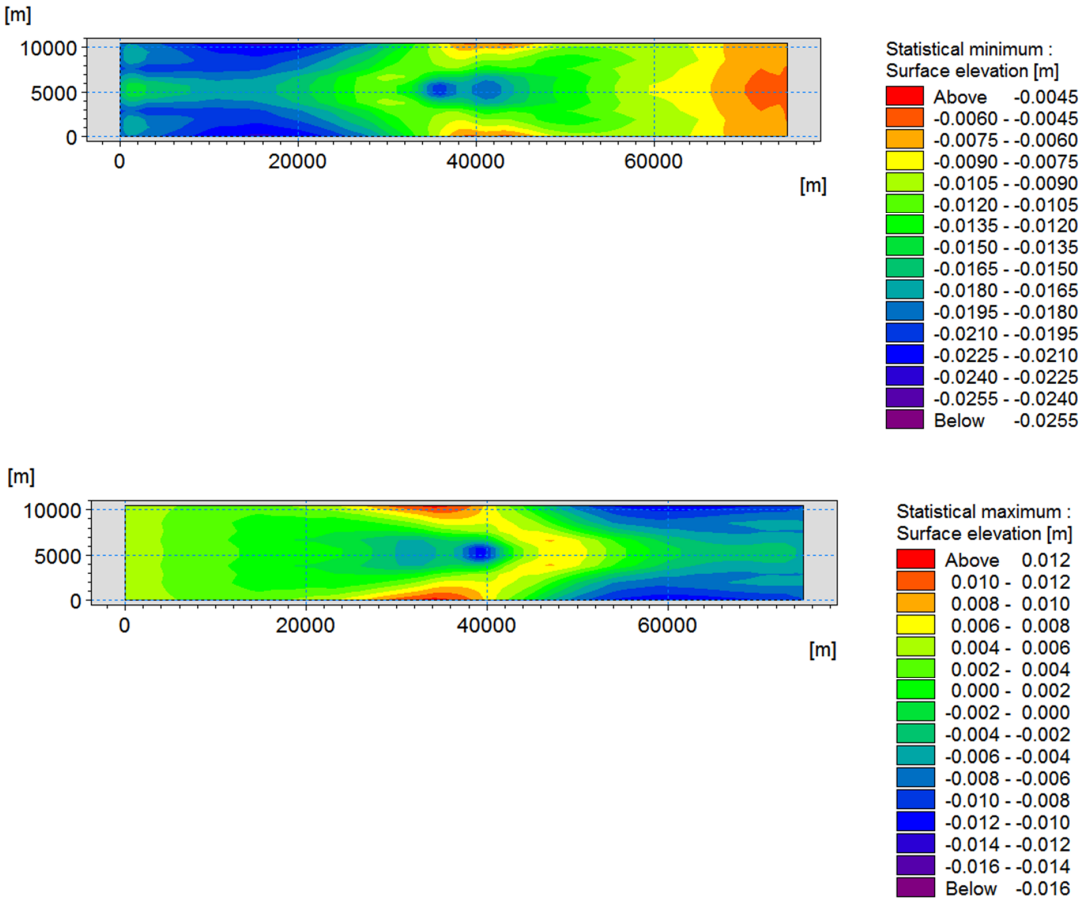

Resonant case (without bed friction)

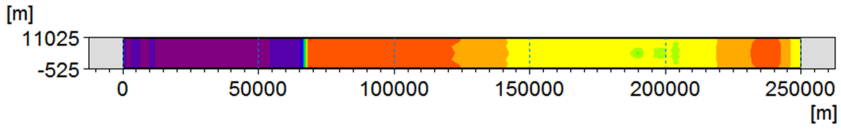

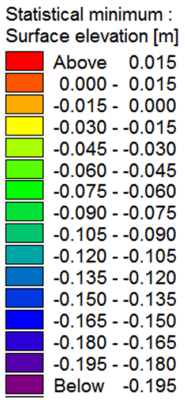

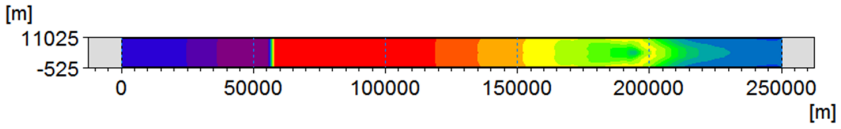

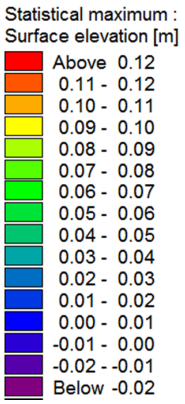

References

ABPmer. (2014). *Atlas of UK Marine Renewable Energy Resources.* Retrieved December 22, 2015 from `http://www.renewables-atlas.info/`.

Adcock, T. A., Draper, S., Houlsby, G. T., Borthwick, A. G., & Serhadlıoğlu, S. (2013). The available power from tidal stream turbines in the Pentland Firth. In *Proceedings of the Royal Society of London A: Mathematical, Physical and Engineering Sciences.* The Royal Society.

Ahmadian, R., Falconer, R., & Bockelmann-Evans, B. (2012). Far-field modelling of the hydro-environmental impact of tidal stream turbines. *Renewable Energy*, *38*(1), 107–116. doi: 10.1016/j.renene.2011.07.005

Ahmadian, R., Falconer, R., & Lin, B. (2010). Hydro-environmental modeling of proposed Severn barrage, UK. *Proceedings of the ICE-Energy*, *163*(3), 107–117.

Ahmadian, R., & Falconer, R. a. (2012). Assessment of array shape of tidal stream turbines on hydro-environmental impacts and power output. *Renewable Energy*, *44*, 318–327. doi: 10.1016/j.renene.2012.01.106

Aldridge, J. N. (1997). Hydrodynamic model predictions of tidal asymmetry and observed sediment transport paths in

Morecambe Bay. *Estuarine, Coastal and Shelf Science*, *44*(1), 39–56.

Andersen, O. B. (1994). Ocean tides in the northern North Atlantic and adjacent seas from ERS 1 altimetry. *Journal of Geophysical Research: Oceans (1978–2012)*, *99*(C11), 22557–22573.

Andersen, O. B. (1999). Shallow water tides in the northwest European shelf region from TOPEX/POSEIDON altimetry. *Journal of Geophysical Research: Oceans (1978–2012)*, *104*(C4), 7729–7741.

Aqua-RET consortium. (2016). *Aquatic Renewable Energy Technologies.* Retrieved July 10, 2016 from `http://www.aquaret.com/indexea3d.html?option=com_content&view=article&id=203&Itemid=344&lang=en`.

Attrill, M. J. (1998). *A rehabilitated estuarine ecosystem: The environment and ecology of the Thames estuary*. Springer Science & Business Media.

Bachant, P., & Wosnik, M. (2014). Reynolds number dependence of cross-flow turbine performance and near-wake characteristics. In *Proceedings of the 2nd Marine Energy Technology Symposium, Seattle, Washington, U.S.A.*

Bachant, P., & Wosnik, M. (2015). Performance measurements of cylindrical-and spherical-helical cross-flow marine hydrokinetic turbines, with estimates of exergy efficiency. *Renewable Energy*, *74*, 318–325.

Bahaj, A., & Myers, L. (2013). Shaping array design of marine current energy converters through scaled experimental analysis. *Energy*, *59*, 83–94.

Bahaj, A., Myers, L., Thomson, M., & Jorge, N. (2007). Characterising the wake of horizontal axis marine current turbines. In *Proceedings of the 7th European wave and tidal energy conference, Porto, Portugal* (p. 9).

Balica, S. F., Popescu, I., Beevers, L., & Wright, N. G. (2013). Parametric and physically based modelling techniques for flood risk and vulnerability assessment: A comparison. *Environmental Modelling & Software*, *41*, 84–92. doi: 10.1016/j.envsoft.2012.11.002

Bartlett, J. (1998). *Quality Control Manual for Computational Estuarine Modelling.* (Tech. Rep.). Environment Agency.

Baston, S., Waldman, S., & Side, J. (2015). *Modelling energy extraction in tidal flows. MASTS Position Paper.* (Vol. 1). Retrieved June 15, 2015 from `http://www.masts.ac.uk/media/126430/140828\_position\_paper\_tidal\_energy\_extraction\_rev2`.

Bates, P. D., Dawson, R. J., Hall, J. W., Horritt, M. S., Nicholls, R. J., & Wicks, J. (2005, sep). Simplified two-dimensional numerical modelling of coastal flooding and example applications. *Coastal Engineering*, *52*(9), 793–810. doi: 10.1016/j.coastaleng.2005.06.001

Blunden, L. S. (2009). *New approach to tidal stream energy analysis at sites in the English Channel* (Doctoral dissertation). University of Southampton.

BODC. (2015). *GEBCO_08 Grid – artefacts in some coastal regions of the Irish Sea,.* Retrieved April 24, 2014 from `http://www.bodc.ac.uk/help_and_hints/errata/gebco/documents/gebco_08_irish_sea.pdf`.

Bonar, P. A., Bryden, I. G., & Borthwick, A. G. (2015). Social and ecological impacts of marine energy development. *Renewable and Sustainable Energy Reviews*, *47*, 486–495.

Borthwick, A. G. (2016). Marine Renewable Energy Seascape. *Engineering*, *2*(1), 69–78.

Brown, J., Joyce, A., Aldridge, J., Young, E., Fernand, L., & Gurbutt, P. (2001). *Further identification and acquisition of bathymetric data for Irish Sea modelling*. Centre for Environment, Fisheries and Aquaculture Science.

Brutto, O. A. L., Nguyen, V. T., Guillou, S., Gualous, H., & Boudart, B. (2015). Reanalyse of an Analytical Model for One Tidal Turbine Wake Prediction. In *Proceedings of the 11th European Wave and Tidal Energy Conference, Nantes, France.*

Bryden, I., Couch, S., Owen, A., & Melville, G. (2007). Tidal current resource assessment. *Proceedings of the Institution of Mechanical Engineers, Part A: Journal of Power and Energy*, *221*(2), 125–135.

Bryden, I. G., Grinsted, T., & Melville, G. T. (2004). Assessing the potential of a simple tidal channel to deliver useful energy. *Applied Ocean Research*, *26*(5), 198–204. doi: 10.1016/j.apor .2005.04.001

Burzel, A., Dassanayake, D. R., & Oumeraci, H. (2012). Spatial modelling of tangible and intangible losses in an integrated risk analysis. *Coastal Engineering Proceedings*, *1*(33), 65.

Carballo, R., Iglesias, G., & Castro, A. (2009). Numerical model evaluation of tidal stream energy resources in the Ría de Muros

(NW Spain). *Renewable Energy*, *34*(6), 1517–1524. doi: 10 .1016/j.renene.2008.10.028

CEFAS. (2008). *Medina Estuary 2008 Sanitary Survey. Classification of bivalve mollusc production areas in England and Wales under EC Regulation No. 854/2004.* (Tech. Rep.). CEFAS.

Centre for Ecology and Hydrology. (2013). *Map of the distribution of gauging stations with flow records on the National River Flow Archive, Scale 1:1540000.* Retrieved December 19, 2014 from `http://nora.nerc.ac.uk/id/eprint/503628`.

Chen, A. S., Djordjevic, S., Leandro, J., & Savic, D. A. (2010). An analysis of the combined consequences of pluvial and fluvial flooding. *Water Sci Technol*, *62*(7), 1491–1498. doi: 10.2166/ wst.2010.486

Chen, S.-N., & Sanford, L. P. (2009a). Axial Wind Effects on Stratification and Longitudinal Salt Transport in an Idealized, Partially Mixed Estuary. *Journal of Physical Oceanography*, *39*(8), 1905–1920.

Chen, S.-N., & Sanford, L. P. (2009b). Lateral circulation driven by boundary mixing and the associated transport of sediments in idealized partially mixed estuaries. *Continental Shelf Research*, *29*(1), 101–118.

Chen, W.-B., Liu, W.-C., & Hsu, M.-H. (2013). Modeling evaluation of tidal stream energy and the impacts of energy extraction on hydrodynamics in the Taiwan Strait. *Energies*, *6*(4), 2191–2203.

Chen, Y., Lin, B., & Lin, J. (2014). Modelling tidal current energy extraction in large area using a three-dimensional estuary model. *Computers & Geosciences*, *72*, 76–83.

Chua, V. P., & Xu, M. (2014). Impacts of sea-level rise on estuarine circulation: An idealized estuary and San Francisco Bay. *Journal of Marine Systems*, *139*, 58–67.

Consul, C. A., Willden, R. H., & McIntosh, S. C. (2013). Blockage effects on the hydrodynamic performance of a marine cross-flow turbine. *Phil. Trans. R. Soc. A*, *371*(1985), 20120299.

Cousineau, J., Nistor, I., & Cornett, A. (2012). Hydrodynamic impacts of tidal power lagoons in the Bay of Fundy. *Coastal Engineering Proceedings*, *1*(33), 69.

Creech, A. C. (2009). *A three-dimensional numerical model of a horizontal axis, energy extracting turbine: an implementation on a parallel computing system* (Doctoral dissertation). Heriot-Watt University.

Creech, A. C., Früh, W.-G., & Maguire, A. E. (2013). High-resolution CFD modelling of Lillgrund Wind farm. In *International Conference on Renewable Energies and Power Quality (ICREPQ13), Bilbao, Spain* (Vol. 11).

Croft, N., Lin, B., Williams, A., Mason-Jones, A., Fidler, R., Loman, J., ... Evans, P. (2010). Tidal turbine deployment in the Bristol Channel: a case study. *Proceedings of the ICE - Energy*, *163*(3), 93–105. doi: 10.1680/ener.2010.163.3.93

Cummins, P., & Garrett, C. (2005). The power potential of tidal currents in channels. *Proceedings of the Royal Society A: Mathematical, Physical and Engineering Sciences*, *461*(2060), 2563–2572. doi: 10.1098/rspa.2005.1494

Cummins, P. F. (2013). The extractable power from a split tidal channel: An equivalent circuit analysis. *Renewable Energy*, *50*, 395–401.

Davidson, N., & Buck, A. (1997). *An inventory of UK Estuaries, volume 1: Introduction and Methodology*. Joint Nature Conservation Committee.

Davies, A. M., & Lawrence, J. (1995). Modeling the effect of wave-current interaction on the three-dimensional wind-driven circulation of the eastern Irish Sea. *Journal of Physical Oceanography*, *25*(1), 29–45.

Defne, Z., Haas, K. A., & Fritz, H. M. (2011). Numerical modeling of tidal currents and the effects of power extraction on estuarine hydrodynamics along the Georgia coast, USA. *Renewable Energy*, *36*(12), 3461–3471. doi: 10.1016/j.renene.2011.05.027

DHI. (2012a). MIKE21 FLOW MODEL FM Hydrodynamic Module User Guide. *Denmark: DHI Water & Environment*.

DHI. (2012b). MIKE 21 & MIKE 3 FLOW MODEL Hydrodynamic Module Scientific Documentation. *Denmark: DHI Water & Environment*.

DHI. (2012c). MIKE21 Tidal Analysis and Prediction Module Scientific Documentation. *Denmark: DHI Water & Environment*.

Divett, T., Vennell, R., & Stevens, C. (2013). Optimization of multiple turbine arrays in a channel with tidally reversing flow by numerical modelling with adaptive mesh. *Phil. Trans. R. Soc. A*, *371*(1985), 20120251.

Doodson, A. T. (1921). The harmonic development of the tide-generating potential. *Proceedings of the Royal Society of London. Series A, Containing Papers of a Mathematical and Physical Character*, *100*(704), 305–329.

Draper, S. (2011). *Tidal stream energy extraction in coastal basins* (Doctoral dissertation). University of Oxford.

Draper, S., Adcock, T. A., Borthwick, A. G., & Houlsby, G. T. (2014). An electrical analogy for the Pentland Firth tidal stream power resource. In *Proc. R. Soc. A* (Vol. 470, p. 20130207). The Royal Society.

Draper, S., Houlsby, G., Oldfield, M., & Borthwick, A. (2010). Modelling tidal energy extraction in a depth-averaged coastal domain. *IET renewable power generation*, *4*(6), 545–554.

Draper, S., & Nishino, T. (2014). Centred and staggered arrangements of tidal turbines. *Journal of Fluid Mechanics*, *739*, 72–93.

EA, & DEFRA. (2015). *The Estuary Guide.* Retrieved July 29, 2015 from `http://www.estuary-guide.net/`.

Easton, M., Woolf, D., & Pans, S. (2010). An operational hydrodynamic model of a key tidal energy site: Inner Sound of Stroma, Pentland Firth (Scotland, UK). In *Proceedings of the 3rd International Conference on Ocean Energy, Bilbao, Spain.*

EDINA Marine Digimap Service . (2015a). *HydroSpatial One [SHAPE geospatial data], Scale 1:25000.* Retrieved August 13, 2015 from `http://digimap.edina.ac.uk`.

EDINA Marine Digimap Service . (2015b). *HydroView Chart [TIFF geospatial data], Scale 1:10000, Tile: 1346-0 w.* Retrieved August 11, 2015 from `http://digimap.edina.ac.uk`.

EDINA Marine Digimap Service . (2015c). *HydroView Chart [TIFF geospatial data], Scale 1:10000, Tile: 2013-3 w.* Retrieved August 11, 2015 from `http://digimap.edina.ac.uk`.

Ekman, M. (1993). A concise history of the theories of tides, precession-nutation and polar motion (from antiquity to 1950). *Surveys in geophysics*, *14*(6), 585–617.

EMEC. (2013). *Feasibility Study for a Marine Energy Test/ Generating Facility in West Cumbria* (Tech. Rep.). European Marine Energy Centre.

Environment Agency. (2015). *Risk of Flooding from Rivers and Sea.* Retrieved October 10, 2015 from `http://watermaps.environment-agency.gov.uk/wiyby/wiyby.aspx?topic=floodmap#x=323585&y=563228&scale=5`.

Falconer, R. A., Xia, J., Lin, B., & Ahmadian, R. (2009). The Severn Barrage and other tidal energy options: Hydrodynamic and power output modeling. *Science in China Series E: Technological Sciences*, *52*(11), 3413–3424. doi: 10.1007/s11431-009-0366-z

Fallon, D., Hartnett, M., Olbert, A., & Nash, S. (2014). The effects of array configuration on the hydro-environmental impacts of tidal turbines. *Renewable Energy*, *64*(0), 10 - 25. doi: http://dx.doi.org/10.1016/j.renene.2013.10.035

Fallon, D., & Nash, S. (2012). The Effects of Array Configuration on the Hydro-environmental Impacts of Tidal Turbines..

Finlay, L., Couch, S. J., & Ingram, D. M. (2009). Numerical modelling of the response of tidal resonance to the presence of a barrage. In (Vol. 4).

Flather, R. (1976). A tidal model of the northwest European continental shelf. *Mem. Soc. R. Sci. Liege*, *10*(6), 141–164.

Flather, R., & Heaps, N. (1975). Tidal computations for Morecambe Bay. *Geophysical Journal International*, *42*(2), 489–517.

Fontanazza, C. M., Freni, G., & Notaro, V. (2012). Bayesian inference analysis of the uncertainty linked to the evaluation of potential flood damage in urban areas. *Water Sci Technol*, *66*(8), 1669–1677. doi: 10.2166/wst.2012.359

Funke, S. W., Farrell, P. E., & Piggott, M. (2013). Tidal turbine array optimisation using the adjoint approach. *arXiv preprint arXiv:1304.1768*.

Garrett, C. (1975). Tides in gulfs. In *Deep Sea Research and Oceanographic Abstracts* (Vol. 22, pp. 23–35). Elsevier.

Garrett, C., & Cummins, P. (2007). The efficiency of a turbine in a tidal channel. *Journal of fluid mechanics*, *588*, 243–251.

Garrett, C., & Cummins, P. (2013). Maximum power from a turbine farm in shallow water. *Journal of Fluid Mechanics*, *714*, 634–643. doi: 10.1017/jfm.2012.515

Garrett, C., & Greenberg, D. (1977). Predicting changes in tidal regime: The open boundary problem. *Journal of Physical Oceanography*, *7*(2), 171–181.

Gebreslassie, M. G. (2012). *Simplified CFD modelling of tidal turbines for exploring arrays of devices* (Doctoral dissertation). University of Exeter.

Gebreslassie, M. G., Sanchez, S. O., Tabor, G. R., Belmont, M. R., Bruce, T., Payne, G. S., & Moon, I. (2016).

Experimental and CFD Analysis of the Wake Characteristics of Tidal Turbines. *International Journal of Marine Energy*. doi: http://dx.doi.org/10.1016/j.ijome.2016.07.001

Gebreslassie, M. G., Tabor, G. R., & Belmont, M. R. (2012). CFD simulations for investigating the wake states of a new class of tidal turbine. *Journal of Renewable Energy and Power Quality*, *10*(241).

Gebreslassie, M. G., Tabor, G. R., & Belmont, M. R. (2013a, feb). Numerical simulation of a new type of cross flow tidal turbine using OpenFOAM Part I: Calibration of energy extraction. *Renewable Energy*, *50*, 994–1004. doi: 10.1016/j.renene.2012.08.065

Gebreslassie, M. G., Tabor, G. R., & Belmont, M. R. (2013b, feb). Numerical simulation of a new type of cross flow tidal turbine using OpenFOAM Part II: Investigation of turbine-to-turbine interaction. *Renewable Energy*, *50*, 1005–1013. doi: 10.1016/j.renene.2012.08.064

Gebreslassie, M. G., Tabor, G. R., & Belmont, M. R. (2015). Investigation of the performance of a staggered configuration of tidal turbines using cfd. *Renewable Energy*, *80*, 690–698.

Godin, G. (1972). The analysis of tides. *University of Toronto Press*, *1*.

Godin, G. (1993). On tidal resonance. *Continental Shelf Research*, *13*(1), 89–107.

Great Britain Dept. for Communities and Local Government. (2009). *Planning Policy Statement 25: development and flood risk practice guide*. TSO. Retrieved from `http://books.google.co.uk/books?id=m-TMSAAACAAJ`

Gurbutt, P. (1993). *Ituna: A model of the Solway Firth*. Ministry of Agriculture, Fisheries and Food, Directorate of Fisheries Research.

Hammond, M. J., Chen, A. S., Djordjevic, S., Butler, D., Khan, D. M., Rahman, S., & Haque, A. (2012). The development of a flood damage assessment tool for urban areas..

Hardisty, J. (2007). *Estuaries: monitoring and modeling the physical system*. Wiley Online Library.

Hardisty, J. (2009). *The analysis of tidal stream power*. John Wiley & Sons.

Harleman, D. R., & Abraham, G. (1966). *One-dimensional analysis of salinity intrusion in the Rotterdam Waterway*. Waterloopkundig Laboratorium.

Harleman, D. R., & Thatcher, M. L. (1974). Longitudinal dispersion and unsteady salinity intrusion in estuaries. *La Houille Blanche*(1-2), 25–33.

Harrison, M., Batten, W., Myers, L., & Bahaj, A. (2010). Comparison between CFD simulations and experiments for predicting the far wake of horizontal axis tidal turbines. *IET Renewable Power Generation*, *4*(6), 613–627.

Hasegawa, D., Sheng, J., Greenberg, D. A., & Thompson, K. R. (2011). Far-field effects of tidal energy extraction in the Minas Passage on tidal circulation in the Bay of Fundy and Gulf of Maine using a nested-grid coastal circulation model. *Ocean Dynamics*, *61*(11), 1845–1868. doi: 10.1007/s10236-011-0481-9

Hibma, A., De Vriend, H., & Stive, M. (2003). Numerical modelling of shoal pattern formation in well-mixed elongated estuaries. *Estuarine, Coastal and Shelf Science*, *57*(5), 981–991.

Hibma, A., Stive, M., & Wang, Z. (2004). Estuarine morphodynamics. *Coastal Engineering*, *51*(8), 765–778.

Hofschreuder, B. (2012). *Flood protection and marine power in the Wash estuary, United Kingdom: Technical and economical feasibility study* (Doctoral dissertation). TU Delft, Delft University of Technology.

Houlsby, G., Draper, S., Oldfield, M., et al. (2008). Application of linear momentum actuator disc theory to open channel flow. *Report no. OUEL*, *2296*(08).

Hunt, S., Bryan, K. R., & Mullarney, J. C. (2015). The influence of wind and waves on the existence of stable intertidal morphology in meso-tidal estuaries. *Geomorphology*, *228*, 158–174.

Intergovernmental Oceanographic Commission. (2010). *The International Thermodynamic Equation of Seawater 2010: Calculation and Use of Thermodynamic Properties. Man. Guides Ser., vol. 56, UN Educ., Sci. and Cult. Organ., Paris.* Retrieved December 12, 2015 from `http://unesdoc.unesco.org/images/0018/001881/188170e.pdf`.

Joint Nature Conservation Committee . (2016). *Solway Firth site details.* Retrieved March 30, 2016 from `http://jncc.defra.gov.uk/protectedsites/sacselection/sac.asp?EUCode=UK0013025`.

Kadiri, M., Ahmadian, R., Bockelmann-Evans, B., Rauen, W., & Falconer, R. (2012). A review of the potential water quality impacts of tidal renewable energy systems. *Renewable and*

Sustainable Energy Reviews, *16*(1), 329–341. doi: 10.1016/j.rser.2011.07.160

Kalyanapu, A. J., Judi, D. R., McPherson, T. N., & Burian, S. J. (2012). Monte Carlo-based flood modelling framework for estimating probability weighted flood risk. *Journal of Flood Risk Management*, *5*(1), 37–48. doi: 10.1111/j.1753-318X.2011.01123.x

Karsten, R., McMillan, J., Lickley, M., & Haynes, R. (2008). Assessment of tidal current energy in the Minas Passage, Bay of Fundy. *Proceedings of the Institution of Mechanical Engineers, Part A: Journal of Power and Energy*, *222*(5), 493–507.

Kramer, S. C., & Piggott, M. D. (2016). A correction to the enhanced bottom drag parameterisation of tidal turbines. *Renewable Energy*, *92*, 385 - 396. doi: http://dx.doi.org/10.1016/j.renene.2016.02.022

Kramer, S. C., Piggott, M. D., Hill, J., Kregting, L., Pritchard, D., & Elsaesser, B. (2014). The modelling of tidal turbine farms using multi-scale, unstructured mesh models. In *Proceedings of the 2nd International Conference on Environmental Interactions of Marine Renewable Energy Technologies,(EIMR2014), Stornoway, Scotland.*

Lalander, E., & Leijon, M. (2011). In-stream energy converters in a river–Effects on upstream hydropower station. *Renewable energy*, *36*(1), 399–404.

Lalander, E., Thomassen, P., & Leijon, M. (2013). Evaluation of a model for predicting the tidal velocity in fjord entrances. *Energies*, *6*(4), 2031–2051.

Lamb, H. (1932). *Hydrodynamics 6th ed.* Cambridge Univ Press.

Lambkin D. (2016). *A Review of the Bed Roughness Variable in MIKE21 FLOW MODEL FM, Hydrodynamic (HD) and Sediment transport (ST) modules.* Retrieved January 16, 2014 from `http://faq.dhigroup.com/images/FAQ164/Bottom_roughness_parameter_study.pdf`.

Lane, A., & Prandle, D. (2007). Changing flood risks in estuaries due to global climate change: forecasts from observations, theory and models. *International Journal of Applied Mathematics and Engineering Sciences*, *1*(1), 69–88.

Leslie, H., & Palmer, M. (2015). Examining the Impacts of Tidal Energy Capture from an Ecosystem Services Perspective. *Marine Technology Society Journal*, *49*, 97-114. doi: http://dx.doi.org/10.4031/MTSJ.49.1.6

Lewis, J. K., Hsu, Y. L., & Blumberg, A. F. (1994). Boundary forcing and a dual-mode calculation scheme for coastal tidal models using step-wise bathymetry. In *Estuarine and Coastal Modeling III: Proceedings of the 3rd International Conference. Am. Soc. Civil Eng., Oak Brook, Illinois, U.S.A.* (pp. 422–431).

Liang, D., Xia, J., Falconer, R. A., & Zhang, J. (2014). Study on tidal resonance in Severn Estuary and Bristol Channel. *Coastal Engineering Journal*, *56*(01), 1450002.

Lighthill, J. (2001). *Waves in fluids*. Cambridge university press.

Lin, B., Ahmadian, R., & Falconer, R. (2010). Hydro-environmental modeling of proposed Severn barrage, UK. *Proceedings of the ICE - Energy*, *163*(3), 107–117. doi: 10.1680/ener.2010.163.3.107

Lin, J., Sun, J., Liu, L., Chen, Y., & Lin, B. (2015). Refined representation of turbines using a 3D SWE model for predicting distributions of velocity deficit and tidal energy density. *International Journal of Energy Research*, *39*(13), 1828–1842.

Luo, J., Li, M., Sun, Z., & O'Connor, B. A. (2013). Numerical modelling of hydrodynamics and sand transport in the tide-dominated coastal-to-estuarine region. *Marine Geology*, *342*, 14–27.

Macdonald, D., Dixon, A., Newell, A., & Hallaways, A. (2012). Groundwater flooding within an urbanised flood plain. *Journal of Flood Risk Management*, *5*(1), 68–80. doi: 10.1111/j.1753-318X.2011.01127.x

Malki, R., Masters, I., Williams, A. J., & Croft, T. N. (2014). Planning tidal stream turbine array layouts using a coupled blade element momentum–computational fluid dynamics model. *Renewable Energy*, *63*, 46–54.

Martin-Short, R., Hill, J., Kramer, S., Avdis, A., Allison, P., & Piggott, M. (2015). Tidal resource extraction in the Pentland Firth, UK: Potential impacts on flow regime and sediment transport in the Inner Sound of Stroma. *Renewable Energy*, *76*, 596–607.

Maskell, E. (1963). *A theory of the blockage effects on bluff bodies and stalled wings in a closed wind tunnel* (Tech. Rep. No. ARC-R/M-3400). Aeronautical Research Council.

Maskell, J., Horsburgh, K., Lewis, M., & Bates, P. (2013). Investigating River-Surge Interaction in Idealised Estuaries. *Journal of Coastal Research*, *30*(2), 248–259.

Masters, I., Malki, R., Williams, A. J., & Croft, T. N. (2013). The influence of flow acceleration on tidal stream turbine wake dynamics: A numerical study using a coupled BEM–CFD model. *Applied Mathematical Modelling*, *37*(16), 7905–7918.

Masters, I., Williams, A., Croft, T. N., Togneri, M., Edmunds, M., Zangiabadi, E., ... Karunarathna, H. (2015). A comparison of numerical modelling techniques for tidal stream turbine analysis. *Energies*, *8*(8), 7833–7853.

McCall, R., Saunders, A., Shepperd, P., & Beadle, R. (2007). *Tidal Power in the UK - Research Report 1: UK Tidal Resource Assessment* (Tech. Rep.). Sustainable Development Commission.

McMillan, A., Batstone, C., Worth, D., Tawn, J., Horsburgh, K., & Lawless, M. (2011). *Coastal flood boundary conditions for UK mainland and islands. Project SC060064/TR2: Design sea levels* (Tech. Rep.).

Miles, J. W. (1971). Resonant response of harbours: an equivalent-circuit analysis. *J. Fluid Mech*, *46*(02), 241–265.

Moore, R. D., Wolf, J., Souza, A. J., & Flint, S. S. (2009). Morphological evolution of the Dee Estuary, Eastern Irish Sea, UK: A tidal asymmetry approach. *Geomorphology*, *103*(4), 588–596.

Morris, D. (2003). *Automation and appraisal of the FEH statistical procedures for flood frequency estimation* (Tech. Rep.). DEFRA.

Mycek, P., Gaurier, B., Germain, G., Pinon, G., & Rivoalen, E. (2014). Experimental study of the turbulence intensity effects

on marine current turbines behaviour. Part I: One single turbine. *Renewable Energy*, *66*, 729–746.

Nash, S., O'Brien, N., Olbert, A., & Hartnett, M. (2014). Modelling the far field hydro-environmental impacts of tidal farms-A focus on tidal regime, inter-tidal zones and flushing. *Computers and Geosciences*, *71*, 20–27.

Natural Power . (2015). *Environmental Statement - Supporting applications for an offshore windfarm at Robin Rigg.* Retrieved December 12, 2015 from http://77.68.107.10/Renewables%20Licensing/Robin_Rigg/ES/Robin%20Rigg%20ES%2028.05.02.pdf.

Nature Conservation Committee. (2014). *UKSeamap 2010.* Retrieved January 19, 2014 from http://jncc.defra.gov.uk/page-5534&LAYERS=PredictedHabitats%2CUKCS.

Néelz, S., & Pender, G. (2010). Benchmarking of 2D hydraulic modelling packages. *Environment Agency*.

Neill, S. P., Litt, E. J., Couch, S. J., & Davies, A. G. (2009). The impact of tidal stream turbines on large-scale sediment dynamics. *Renewable Energy*, *34*(12), 2803–2812. doi: 10 .1016/j.renene.2009.06.015

Nishino, T., & Willden, R. H. (2012a). Effects of 3-D channel blockage and turbulent wake mixing on the limit of power extraction by tidal turbines. *International Journal of Heat and Fluid Flow*, *37*, 123–135.

Nishino, T., & Willden, R. H. J. (2012b). The efficiency of an array of tidal turbines partially blocking a wide channel. *Journal of Fluid Mechanics*, *708*, 596–606. doi: 10.1017/jfm.2012.349

North West Coastal Group. (2012). North West England and North Wales Shoreline Management Plan SMP2. *Halcrow Group Ltd, Swindon, UK.*.

Novák, P., Guinot, V., Jeffrey, A., & Reeve, D. E. (2010). *Hydraulic Modelling An Introduction: Principles, Methods and Applications*. Taylor & Francis.

Parkinson, S., Willden, R., Wickham, A., Stallard, T., & Thomson, M. (2012). Comparison of scale model wake data with an energy yield analysis tool for tidal turbine farms. In *Proceedings of 4th International Conference on Ocean Energy (ICOE), Dublin, Ireland.*

Polagye, B. L. (2009). *Hydrodynamic effects of kinetic power extraction by in-stream tidal turbines*. ProQuest.

Polagye, B. L., & Malte, P. C. (2011). Far-field dynamics of tidal energy extraction in channel networks. *Renewable energy*, *36*(1), 222–234.

Pope, S. B. (2000). *Turbulent Flows*. Cambridge University Press. Retrieved from `http://dx.doi.org/10.1017/CBO9780511840531` (Cambridge Books Online)

Prandle, D. (1980). Modelling of tidal barrier schemes: an analysis of the open-boundary problem by reference to AC circuit theory. *Estuarine and Coastal Marine Science*, *11*(1), 53–71.

Prandle, D. (1985). Classification of tidal response in estuaries from channel geometry. *Geophysical Journal International*, *80*(1), 209–221.

Prandle, D. (2009). *Estuaries: dynamics, mixing, sedimentation and morphology*. Cambridge University Press.

Prandle, D. (2010). *Vulnerability of estuaries to sea level rise stage 1: a review* (Tech. Rep. No. SC080016). Environment Agency.

Prandle, D., & Rahman, M. (1980). Tidal response in estuaries. *Journal of Physical Oceanography*, *10*(10), 1552–1573.

Purvis, M. J., Bates, P. D., & Hayes, C. M. (2008). A probabilistic methodology to estimate future coastal flood risk due to sea level rise. *Coastal Engineering*, *55*(12), 1062–1073. doi: 10 .1016/j.coastaleng.2008.04.008

Rainey, R. (2009). The optimum position for a tidal power barrage in the Severn estuary. *Journal of Fluid Mechanics*, *636*, 497.

Reeve, D., Chadwick, A., & Fleming, C. (2004). *Coastal engineering: processes, theory and design practice*. CRC Press.

Ridgway, J., Bee, E., Breward, N., Cave, M., Chenery, S., Gowing, C., ... Jarrow, A. (2012). *The Mersey Estuary: sediment geochemistry*. British Geological Survey.

Roberts, A., Thomas, B., Sewell, P., Khan, Z., Balmain, S., & Gillman, J. (2016). Current tidal power technologies and their suitability for applications in coastal and marine areas. *Journal of Ocean Engineering and Marine Energy*, *2*(2), 227–245.

Robinson, I. (1981). Tidal power from wedge-shaped estuaries: an analytical model with friction, applied to the Bristol Channel. *Geophysical Journal International*, *65*(3), 611–626.

Roc, T. (2013). *Numerical Modelling for Hydrodynamic Impact and Power Assessments of Tidal Current Turbine Arrays* (Doctoral dissertation). University of Plymouth, Plymouth, UK,.

Roc, T., Conley, D. C., & Greaves, D. (2013). Methodology for tidal turbine representation in ocean circulation model. *Renewable Energy*, *51*, 448–464.

Salter, S., & Taylor, J. M. (2007). Vertical-axis tidal-current generators and the pentland firth. *Proceedings of the Institution of Mechanical Engineers, Part A: Journal of Power and Energy*, *221*(2), 181–199.

Scott, G. (1994). A numerical study of the interaction of tidal oscillations and non-linearities in an estuary. *Estuarine, Coastal and Shelf Science*, *39*(5), 477–496.

Scottish Environment Protection Agency. (2015). *Flood Maps,.* Retrieved October 10, 2015 from `http://map.sepa.org.uk/floodmap/map.htm`.

Shahapure, S. S., Eldho, T. I., & Rao, E. P. (2010). Coastal Urban Flood Simulation Using FEM, GIS and Remote Sensing. *Water Resources Management*, *24*(13), 3615–3640. doi: 10.1007/s11269-010-9623-y

Shapiro, G. I. (2011). Effect of tidal stream power generation on the region-wide circulation in a shallow sea. *Ocean Science*, *7*(1), 165–174. doi: 10.5194/os-7-165-2011

Shaw, E. (1994). *Hydrology in Practice*. CRC Press.

Shell, UK. (1987). The Humber Estuary: Environmental Background. *Shell UK Ltd, London*, 59.

Sleigh, P., Gaskell, P., Berzins, M., & Wright, N. (1998). An unstructured finite-volume algorithm for predicting flow in rivers and estuaries. *Computers & Fluids*, *27*(4), 479–508.

Stringer, R., Hillis, A., & Zang, J. (2016). Numerical investigation of laboratory tested cross-flow tidal turbines and reynolds number scaling. *Renewable Energy*, *85*, 1316–1327.

Sun, X. (2008). *Numerical and experimental investigation of tidal current energy extraction* (Doctoral dissertation). University of Edinburgh.

Sustainable Energy Ireland. (2005). *Tidal and Current Energy Resources in Ireland*. Sustainable Energy Ireland.

Szollosi-Nagy, A., & Zevenbergen, C. (2005). *Urban flood management*. AA Balkema.

Taylor, G. (1921). Tides in the Bristol channel. In *Proceedings of the Cambridge Philosophical Society* (Vol. 20, pp. 320–325).

Townend, I. (2008). Understanding and Managing Morphological Change in Estuaries. *ABPmer Pty Ltd, Carole Park*.

Turnock, S. R., Phillips, A. B., Banks, J., & Nicholls-Lee, R. (2011). Modelling tidal current turbine wakes using a coupled rans-bemt approach as a tool for analysing power capture of arrays of turbines. *Ocean Engineering*, *38*(11), 1300–1307.

United Kingdom Hydrographic Office. (2012). *Admiralty Tide Tables, United Kingdom and Ireland - Including Channel Ports* (Vol. 1). United Kingdom Hydrographic Office.

van der Molen, J., Ruardij, P., & Greenwood, N. (2016). Potential environmental impact of tidal energy extraction in the Pentland Firth at large spatial scales: results of a biogeochemical model. *Biogeosciences*, *13*(8), 2593–2609.

Van Veen, J. (1947). Analogy between tides and AC electricity. *Engineering*, *184*, 498.

Vennell, R. (2010). Tuning turbines in a tidal channel. *Journal of Fluid Mechanics*, *663*, 253–267. doi: 10.1017/s0022112010003502

Vennell, R. (2011). Tuning tidal turbines in-concert to maximise farm efficiency. *Journal of Fluid Mechanics*, *671*, 587–604. doi: 10.1017/s0022112010006191

Vennell, R. (2012). The energetics of large tidal turbine arrays. *Renewable Energy*, *48*, 210–219. doi: 10.1016/j.renene.2012.04.018

Vennell, R., Funke, S. W., Draper, S., Stevens, C., & Divett, T. (2015). Designing large arrays of tidal turbines: A synthesis and review. *Renewable and Sustainable Energy Reviews*, *41*, 454–472.

Villars, M., & Delvigne, G. (2001). Estuarine processes. *Literature review. Final draft prepared for CEFIC. WL. Delft hydraulics Z*, *2725*.

Waldman, S., Baston, S., Side, J., & Miller, C. (2014). Comparison of two types of hydrodynamic model for investigating the environmental impacts of energy extraction from tidal flows. In *Proceedings of Environmental Impacts of Marine Renewables (EIMR) 2014, Stornoway, Isle of Lewis, Outer Hebrides, Scotland.*

Waldman, S., Genet, G., Bastón, S., & Side, J. (2015). Correcting for mesh size dependency in a regional model's representation of tidal turbines. In *Proceedings of the 11th European Wave and Tidal Energy , Nantes, France.*

Walkington, I., & Burrows, R. (2009). Modelling tidal stream power potential. *Applied Ocean Research*, *31*(4), 239–245. doi: 10 .1016/j.apor.2009.10.007

Waters, S., & Aggidis, G. (2016). A World First: Swansea Bay Tidal lagoon in review. *Renewable and Sustainable Energy Reviews*, *56*, 916–921.

Whelan, J., Graham, J., & Peiro, J. (2009). A free-surface and blockage correction for tidal turbines. *Journal of Fluid Mechanics*, *624*, 281–291.

Wolf, J., Walkington, I., Holt, J., & Burrows, R. (2009). Environmental impacts of tidal power schemes. In *Proceedings of the Institution of Civil Engineers-Maritime Engineering* (Vol. 162, pp. 165–177). Thomas Telford Publishing.

Wu, J. (1980). Wind-stress coefficients over sea surface near neutral conditions-A revisit. *Journal of Physical Oceanography*, *10*(5), 727–740.

Wu, J. (1994). The sea surface is aerodynamically rough even under light winds. *Boundary-Layer Meteorology*, *69*(1-2), 149–158.

Wu, Y., Falconer, R., & Uncles, R. (1999). Modelling of water flows and cohesive sediment fluxes in the Humber Estuary, UK. *Marine Pollution Bulletin*, *37*(3), 182–189.

Xia, J., Falconer, R., Lin, B., & Tan, G. (2011, sep). Estimation of future coastal flood risk in the Severn Estuary due to a barrage. *Journal of Flood Risk Management*, *4*(3), 247–259. doi: 10 .1111/j.1753-318X.2011.01106.x

Xia, J., Falconer, R. a., & Lin, B. (2010a). Hydrodynamic impact of a tidal barrage in the Severn Estuary, UK. *Renewable Energy*, *35*(7), 1455–1468. doi: 10.1016/j.renene.2009.12.009

Xia, J., Falconer, R. a., & Lin, B. (2010b). Impact of different operating modes for a Severn Barrage on the tidal power and flood inundation in the Severn Estuary, UK. *Applied Energy*, *87*(7), 2374–2391. doi: 10.1016/j.apenergy.2009.11.024

Xia, J., Falconer, R. a., & Lin, B. (2010c). Impact of different tidal renewable energy projects on the hydrodynamic processes in the Severn Estuary, UK. *Ocean Modelling*, *32*(1-2), 86–104. doi: 10.1016/j.ocemod.2009.11.002

Yang, Z., & Wang, T. (2015). Modeling the effects of tidal energy extraction on estuarine hydrodynamics in a stratified estuary. *Estuaries and Coasts*, *38*(1), 187–202.

Yates, N., Walkington, I., Burrows, R., & Wolf, J. (2013). Appraising the extractable tidal energy resource of the UK's western coastal waters. *Philos Trans A Math Phys Eng Sci*, *371*(1985), 20120181. doi: 10.1098/rsta.2012.0181

Yoshizawa, A., & Horiuti, K. (1985). A statistically-derived subgrid-scale kinetic energy model for the large-eddy simulation of turbulent flows. *Journal of the Physical Society of Japan*, *54*(8), 2834–2839.

Zhao, D., Shen, H., Tabios III, G., Lai, J., & Tan, W. (1994). Finite-volume two-dimensional unsteady-flow model for river basins. *Journal of Hydraulic Engineering*, *120*(7), 863–883.